DEEP CAVITY NOISE REDUCTION BY EXPLOITING THE STRATEGICALLY EMBEDDED AEROACOUSTIC-STRUCTURAL INTERACTION OF ELASTIC PANELS

MUHAMMAD REHAN NASEER

PhD

The Hong Kong Polytechnic University

2025

THE HONG KONG POLYTECHNIC UNIVERSITY

DEPARTMENT OF MECHANICAL ENGINEERING

Deep Cavity Noise Reduction by Exploiting the Strategically Embedded Aeroacoustic-Structural Interaction of Elastic Panels

Muhammad Rehan Naseer

A thesis submitted in partial fulfilment of the requirements for the degree of Doctor of Philosophy

April 2024

Certificate Of Originality

I hereby declare that this thesis is my own work and that, to the best of my knowledge and belief, it reproduces no material previously published or written, nor material that has been accepted for the award of any other degree or diploma, except where due acknowledgment has been made in the text.

_____

Muhammad Rehan Naseer

Abstract

The phenomenon of flow over a rectangular cavity has garnered significant research interest due to its prevalence in diverse engineering applications across the low and high-speed environments. Under specific operating conditions, unsteady flow over a cavity can initiate self-sustained oscillations that couple with acoustic modes within the cavity, leading to pronounced extreme noise response owing to these flow-induced cavity oscillations which can precipitate premature mechanical failures upon longtime exposure. Existing noise reduction strategies, including cavity shape modifications and the use of plasma actuators or leading-edge blow systems, are flow-invasive and often introduce significant disturbances, altering the cavity fundamental flow characteristics. This can result in unintended aerodynamic consequences such as increased turbulence, flow-induced drag, and higher actuation energy requirements, alongside potentially inducing extraneous noise in frequency ranges absent in the original flow. Such implications have not been comprehensively addressed in the existing literature.

This study explores a new passive control method for reducing cavity tonal noise using flow-induced surface vibrations, employing an elastic panel mounted across the cavity walls. The primary objective is to decrease tonal noise while keeping the shear layer over the cavity opening largely unchanged, minimizing any negative impact on cavity aerodynamic performance. The application of an elastic panel is envisaged to invoke aeroacoustic-structural interaction, which could alter the phase and intensity of acoustic waves inside

the cavity, inherently modify the aeroacoustic coupling receptivity pattern at the cavity leading edge and ultimately reduce the cavity noise emission.

In the first part of the study, the concept of utilizing localized surface compliance is tested to suppress deep cavity aeroacoustics at low Mach number with a single elastic panel embedded across the cavity walls. The concept is studied using high-fidelity, two-dimensional Direct Aeroacoustic Simulation at a freestream Mach number of 0.09 and a Reynolds number, based on the cavity length, of 4×10^4. The investigation of the baseline rigid cavity (without panel) case deciphers that the aeroacoustic feedback process in deep cavities consists of five distinct processes, each supported by the corresponding cavity walls. Having confirmed the key aeroacoustic processes in the numerical solution through careful validation and investigation, localized surface compliance in the form of an elastic panel is strategically introduced to target each aeroacoustic constituent process at five different cavity walls. The natural frequency of the panel is set equal to the feedback loop characteristic frequency to facilitate its flow-induced structural resonance for energy absorption. Suppression of cavity noise pressure and power levels by 3.8 dB and 4.8 dB, respectively, is successfully achieved with an aft wall-mounted panel case, together with an unforeseen reduction in cavity drag by almost 19%.

To corroborate the numerical findings and the potential of aeroacoustic suppression induced by the elastic panel, an experiment was conducted in a closed-circuit type open-jet anechoic wind tunnel. The experimental study observed a significant decrease in pressure fluctuations across the cavity base, shear layer, and far-field region with the application of the elastic panel. Additionally, the peak frequency shifted, suggesting a considerable alteration in the shear layer-cavity mode coupling phenomenon in the elastic panel case. Compared to the baseline rigid cavity, the cavity-panel configuration demonstrated a promising reduction in tonal noise by 16.1 dB. The phase pattern across the shear layer and cavity base was also modified in the case of the elastic panel, resulting in reduced noise radiation due to the changed interaction.

Finally, we leverage further noise reduction potential of the cavity-panel configuration by employing a localized surface compliance mechanism realized

through an arrangement of strategically designed multiple elastic panels. Each panel in this arrangement is tailored to target a certain constituent process of the deep cavity aeroacoustic mechanism. With the synergistic action of its flow-induced panel vibration, every panel is expected to maximize noise reduction potential. The underlying principle of the proposed approach is to harness flow-induced panel resonant vibrations, which are set to absorb the incident flow energy to alter or decouple the aeroacoustic feedback mechanisms driving the fluid-resonant oscillations with the combined action of strategically placed panels across the cavity walls. The most effective configuration gives a remarkable noise power reduction of 15 dB from the rigid cavity, inadvertently reducing cavity drag by almost 15%. Simultaneous reduction of both cavity noise and drag is doubly advantageous. In the most effective tested multi-panel configuration, the vertical panel acts to curtail the efficacy of coupling between the growing shear layer and cavity acoustic modes, whose sustenance is further impeded by an acoustically induced resonant panel at the cavity bottom. The proposed methodology is confirmed to be feasible yet effective, holding great potential for fluid-moving applications in which a quiet and energy-efficient cavity configuration is desired.

Research Output / Publications

To date, the following research has been produced, accepted, is in press, or is in preparation.

Book Chapter

Naseer, M. R., Arif, I., and Leung, R. C. K. (2025), "Mitigation of Cavity Noise with Aeroacoustically Excited Surface Panels", In: Doolan, C., Moreau, D., Wills, A. (eds) *Flinovia—Flow Induced Noise and Vibration Issues and Aspects*-IV, FLINOVIA 2023, Springer.

Journal Articles

Naseer, M. R., Arif, I., Leung, R. C. K., and Lam, G. C. Y. (2023), "Suppression of deep cavity aeroacoustics at low Mach number by localized surface compliance", *Physics of Fluids,* 35 (5).

Naseer, M. R., Arif, I., Leung, R. C. K., and Abdullah, A. (2024), " Deep cavity noise suppression by exploiting aeroacoustic–structural interaction of multiple elastic panels". *Physics of Fluids*, 36 (5).

Naseer, M. R., Li, L., Zou J., Leung, R. C. K., Liu, Y., Maryami, R. (2025) Experimental Verification of a Novel Concept for Deep Cavity Noise Suppression through Aeroacoustic-Structural Interaction. (*in preparation*)

Conference proceedings

Naseer, M. R., Arif, I., Lam, G. C. Y., and Leung, R. C. K. (2022), "Effect of Flow-Induced Surface Vibration on Deep Cavity Aeroacoustics", *28th AIAA/CEAS Aeroacoustics 2022 Conference*, AIAA Paper No, 2022-2958.

Naseer, M. R., Arif, I., and Leung, R. C. K. (2022) "Control of flow-induced noise by structural compliance" In *24th International Congress on Acoustics Proceedings*, no. ABS-0899, pp. 169 – 173.

Naseer, M. R., Arif, I., and Leung, R. C. K. (2023), "Utilization of Embedded Surface Compliance for Suppression of Deep Cavity Flow Noise", *INTER-NOISE and NOISE-CON Congress and Conference Proceedings,* 268 (3), 5323-5334.

Naseer, M. R., Li, L., Zou, J., Leung, R. C. K., Liu, Y., and Maryami, R. (2024), "Experimental Study of Deep Cavity Noise Suppression by Surface Compliance", *30th AIAA/CEAS Aeroacoustics 2024 Conference*. AIAA Paper No, 2024-3280.

Other Journal Publications

Naseer, M. R., Uddin, E., Mubashar, A., Sajid, M., Ali, Z., and Akhtar, K. (2020), "Numerical investigation of hydrodynamic and hydro-acoustic performance of underwater propeller operating in off-design flow conditions" *Journal of Marine Engineering & Technology*, 21(4).

Arif, I., Lam, G. C. Y., Leung, R. C. K., and **Naseer, M. R.** (2022), "Distributed surface compliance for airfoil tonal noise reduction at various loading conditions," *Physics of Fluids*, 34(4).

Arif, I., Leung, R. C. K., **Naseer, M. R.** (2023), " A computational study of trailing edge noise suppression with embedded structural compliance" *JASA Express Letter*, 3(2).

Arif, I., **Naseer, M. R.**, Leung, R. C. K., & Salamat, S. (2023), "Control of acoustic scattering of trailing edge flow by distributed compliance." *Physics of Fluids*, 35(10).

Acknowledgements

Alhamdulillah, all praises to Allah, the Most Gracious and the Most Merciful, for endowing me with the strength, determination, sustenance, guidance, and blessings throughout the tenure of my research and the completion of this thesis. The journey to this point would not have been possible without the support and assistance of numerous individuals.

First and foremost, I extend my deepest gratitude to my chief research supervisor, Dr. Randolph C. K. Leung, for his unwavering support, guidance, and encouragement throughout this challenging journey. His invaluable and inspirational advice, gleaned from our extensive discussions, not only helped me navigate through technical challenges but also instilled a profound sense of positivity in my approach. Dr. Leung's inquisitive nature to understand the underlying physical mechanisms behind every outcome has inspired me to become a critical thinker. Completing my PhD journey under his mentorship has not only honed my research skills but also facilitated my growth as a well-rounded individual.

I am immensely grateful to my senior colleagues, Dr. Irsalan Arif and Dr. Garret C. Y. Lam, for their invaluable support in resolving every technical challenge I encountered during my tenure. My heartfelt appreciation extends to my fellow group members, Ali Abdullah and Sanjya Rai, for their time and assistance whenever needed. I am also extremely thankful to my PolyU friends—Imran Mehmood, Zahid Javid, Aamir Mehmood, Husnain Tansar—who have been a constant source of joy. The lasting memories I built with them,

along with our timeouts and hangouts, provided a much-needed respite from the rigors of academic life and helped me recharge throughout my time in Hong Kong.

Most importantly, I extend my heartfelt gratitude to my beloved parents and siblings for their love and support. I am especially indebted to my mother, whose relentless efforts have shaped my academic journey and beyond, also her lifelong dedication to me and my siblings will forever be a beacon of light and inspiration. The emotional support from my family has been invaluable and their continuous prayers and well-wishes have uplifted me in ways beyond imagination. I am also deeply grateful to my wife for her encouragement and motivation during the final stages of my thesis.

Additionally, I would like to express my sincere gratitude to The Hong Kong Polytechnic University for providing the essential resources and a research-conducive environment that enabled me to pursue my PhD without administrative or financial obstacles. I am especially thankful for the opportunities offered by PolyU, from the research exchange program at SUSTech to the generous conference support, which allowed me to present my work at various technical forums.

The support for the present study from the Research Grants Council of the Government of the Hong Kong Special Administrative Region under Grant No. 15208520 is also gratefully acknowledged.

Contents

List of Figures

List of Tables

Abbreviations

CB	Cavity Bottom
CE	Conservation Element
CE/SE	Conservation Element and Solution Element
CFL	Courant–Friedrichs–Lewy condition
CNIS	Courant number insensitive scheme
DAS	Direct Aeroacoustic Simulation
DEP	Cavity – Panel Configuration with Dual Elastic Panel
EP	Elastic Panel
FFT	Fast Fourier Transform
LE	Cavity Leading Edge
N-S	Navier Stokes
NC	Non-Coupled Configuration
NRBC	Non-Reflecting Boundary Condition
PIV	Particle Image Velocimetry
RC	Rigid Cavity
SCNIS	Simplified Courant Number Insensitive Scheme
SE	Solution Element
SEP	Cavity – Panel Configuration with Single Elastic Panel
TE	Cavity Trailing Edge
TEP	Cavity – Panel Configuration with Tripple Elastic Panel

Nomenclature

c	speed of sound
C_{EP}	clastic panel structural damping coefficient
C_D	coefficient of drag
$C_{D,fric}$	coefficient of skin friction drag
$C_{D,form}$	coefficient of form drag
C_p	coefficient of pressure
c_p	specific heat at constant pressure
D	cavity depth
dt	time step size
E	energy
E_{EP}	modulus of elasticity
$\boldsymbol{F}, \boldsymbol{G}, \boldsymbol{U}$	flow flux conservation variables
f	frequency
$(f_{EP})_n$	n^{th} natural frequency of panel vibration mode
h_{EP}	panel thickness
K_{EP}	stiffness of foundation supporting panel
k	wavenumber
L	cavity length
L_{EP}	elastic panel length
M	Mach number
m	Rossiter mode number
N_{EP}	Elastic panel internal tensile stress
n	panel vibration mode number
P_r	Prandtl number
PSD	power spectral density
PWL	sound power level
$\boldsymbol{Q}$	source term
p'	pressure fluctuation
q_x, q_y	heat flux
R	specific gas constant for air

Re_L	Reynolds number based on cavity length
S_{EP}	panel bending stiffness
SPL	sound pressure level
T_{EP}	panel external tension
T	time period
t	time
u, v	velocity components along streamwise and transverse directions
$w, \dot{w}, \ddot{w}$	panel vibration displacement, velocity and acceleration
w_x	first-order spatial derivative of panel displacement
w_{xx}	second-order spatial derivative of panel displacement
w_{xxxx}	fourth-order spatial derivative of panel displacement
Δx	grid size in x direction
Δy	grid size in y direction
β	boundary layer thickness
θ	momentum thickness
ϕ	phase
κ	shear layer vortex convection rate
λ	wavelength
μ	viscosity
$\mathscr{L}$	checkpoints indicator across different cavity wall
$\wp$	reference point of correlation analysis
ρ	density of fluid
ρ_{ref}	reference density
ρ_{EP}	density of panel
ω	vorticity
γ^2	magnitude-squared coherence function between two signals

Subscripts

EP	parameter related to elastic panel
aft	Cavity aft wall mounting
bottom	Cavity bottom wall mounting
front	Cavity front wall mounting
downstream	Cavity downstream wall mounting
upstream	Cavity upstream wall mounting
B	boundary cell
G	ghost cell
s	Shear layer
a	Cavity acoustics
0	cavity leading condition
∞	freestream condition
ref	Reference parameters
rms	root mean square value

Superscripts

–	time averaged value
^	dimensional quantity
$'$	fluctuation component
j	index of time step
n	index of panel mesh point

Chapter 1

Introduction

1.1 Motivation

The flow over a rectangular cavity has garnered significant research interest over the decades due to its prevalent occurrence in various real-world engineering applications. Under a range of operating conditions, the unsteady flow over the cavity excites a self-sustained oscillation that would couple with a cavity acoustic mode to generate intense flow-induced noise. The hazardous nature of this noise carries a multitude of implications, ranging from psychoacoustic damage to the human health and structural fatigue failure of the mechanical systems which might lead to the catastrophic consequences if left untreated.

Noise pollution ranks among the top three environmental pollutants, exerting adverse effects on human health (European and Directorate-General for 2018) , akin to air pollution and exposure to toxic chemicals. Primary sources of this pollution include road traffic, railways, air traffic, and industrial activities (European and Directorate-General for 2018). Even at levels that are non-harmful to hearing, noise pollution can cause a variety of health issues (Stansfeld and Matheson 2003), such as the release of stress hormones (Singh and Davar 2004; European and Directorate-General for 2018), sleep disturbances (Pirrera *et al.* 2010), hypertension, and heart diseases (Harding *et al.* 2013). Additionally, anthropogenic noise pollution significantly impacts wildlife (Kight and Swaddle 2011), leading to health problems similar to those affecting humans. Consequently, managing anthropogenic noise is essential for maintaining healthy ecosystems and human populations.

While noise itself does not inherently pose a risk if maintained within permissible limits, certain types of noise can be particularly harmful. For instance, exposure to low-level white noise has been shown to improve concentration (Söderlund *et al.* 2010; Rausch *et al.* 2014) and have calming effects (Burgio *et al.* 1996). However, the main concern regarding noise pollution is tonal noise, which has a very narrow frequency range compared to broadband noise (Pawłaczyk-Luszczyńska *et al.* 2003). High-frequency noise tends to be more annoying within the human auditory range at comparable sound pressure levels (Björk 1986), whereas low-frequency noise is more problematic due to increased human sensitivity to these frequencies (Berglund *et al.* 1996). Additionally, managing and reducing low-frequency noise is

challenging due to the long wavelengths involved, which can penetrate most barriers designed to dampen or block sound.

Noise, beyond its status as an environmental pollutant, has a myriad of effects on its source, particularly in various mechanical systems. Prolonged exposure can lead to structural fatigue failure, thereby jeopardising the structural integrity of these systems. A significant contributor to noise within mechanical systems is cavity flow noise. Basic shapes in some form of the cavity, which are integral components of various systems across multiple dimensions, are prone to generating excessive noise when flow passes over them. Consequently, there is a pressing need to pinpoint such noise sources and develop strategies for their suppression. Several key applications of cavity flow result in extreme noise responses, thereby providing the impetus for the present study.

When the flow passes open cavities, such as weapon bays, wheel wells, or measurement windows in aeronautical configurations the substantial density and pressure fluctuations induced by the flow can result in optical pathway deviations, elevated sound levels, and intense vibrations, leading to structural fatigue (Cattafesta III *et al.* 2008; Lawson and Barakos 2009, 2011; Liu *et al.* 2024). This poses challenges for military aircraft attempting to deploy stores from internal bays. An exposed undercarriage cavity also contributes to the unsteady flow characteristics. The intricate nature of the flow within the cavity generates aerodynamic loads, pressure fluctuations, and acoustic radiation. Despite the long-standing recognition of this issue, effectively controlling cavity oscillations remains a formidable task. The presence of a cavity can significantly alter the flow field, disrupting the free-stream flow

beneath the aircraft fuselage and creating additional unsteady aerodynamic loads on surrounding components such as landing gear doors, struts, and drag braces.

Aerodynamic noise, often emanating from the gap between train cars and the bogie, is typically attributed to cavity flow, given the structural similarities between these components and various dimensional cavities (Talotte 2000; He *et al.* 2024). As trains are engineered to operate at higher speeds but with minimal noise emission footprints, the mitigation of noise along railway lines has emerged as a significant concern. This is particularly true for aerodynamic noise, which escalates disproportionately, increasing to the sixth power of speed or even higher. Consequently, there is a pressing need to attenuate the noise generated by the train-car gap, which constitutes a substantial portion of the overall noise. This necessitates a comprehensive understanding of the noise generation mechanism in this scenario and the development of effective noise reduction strategies. The current research is thus motivated by the need to explore such mechanism related to the cavity flow and devise innovative the potential solution to mitigate the impact of aerodynamic noise.

Sunroof buffeting is another cavity flow phenomenon that results in elevated interior noise levels (Kook and Mongeau 2002), causing discomfort for vehicle passengers. This phenomenon, which also occurs with side window buffeting in passenger vehicles, is primarily due to an unsteady shear layer in the sunroof or window opening, which triggers an acoustic resonance within the passenger compartment. While practical design solutions for mitigating sunroof buffeting across various wind speeds and geometric configurations are

well-documented, a comprehensive solution that avoids costly design measures remains elusive in the industry. Recently, a buffeting suppression method was tested using a deflector, but its effectiveness varied across car designs. Therefore, it could not be assumed to be universally effective. Hence, to reliably predict a vehicle propensity for buffeting which closely resembles a deep cavity, it is crucial to understand the sensitivity of this phenomenon to various noise parameters. This underscores the importance of the current research in contributing to a more nuanced understanding of the underlying mechanism as well as presenting the concept for mitigation.

The self-sustained aeroacoustic pulsations observed in gas transportation systems bear a striking resemblance to deep cavity flow (Bruggeman *et al.* 1989, 1991; Ziada and Bühlmann 1992; Ziada 2010; Wang *et al.* 2024). These pulsations, which are prevalent in numerous technical applications, are propelled by the instability of the flow along the closed branches. The pulsations induced by flow in a pipe with a closed side branch are the outcome of the interaction between the shear layer, which separates the main flow from the stagnant gas in the side branch, and the acoustic field. These pulsations are undesirable not only due to the noise they generate but also due to the potential for mechanical failures within the pipe network. The high amplitude of the acoustic pressure fluctuations can result in mechanical stresses that may lead to fatigue failure.

Impinging shear layers are recognized as a primary contributor to unsteady pressure loading and noise radiation within turbomachinery. This type of noise generation is associated with various flow paths across the structures within the turbomachinery (Ziada *et al.* 2002; Rebholz *et al.* 2016),

encompassing the flow exchange between nozzles and turbines, the flow exchange between impellers and diffusers, the movement of fuel or lubricant over engine cavities, and the impinging wake created by flow past bluff bodies, such as struts and turning vanes on downstream obstacles. Despite their differences, these functionaries in turbomachinery share a commonality in their basic structure and operation, closely mirroring the cavity flow (Lucas. *et al.* 1995). Flow past rectangular or slotted cavities results in self-sustained oscillations of a purely hydrodynamic type, but often, it has the potential to couple these basic instabilities with a resonant acoustic mode within the cavity. In such scenarios, the pressure fluctuations can intensify to such high amplitudes that they may instigate structural failure of engine components. Considering the potential for catastrophic failure, the detection and possible suppression of cavity flow-induced noise becomes an urgent necessity.

The nature of flow-induced oscillations in an open cavity as recorded in the aforementioned applications inspires the need to accurately model the disparate scales of acoustic and vortical disturbances driving the oscillations, and their resultant acoustic generation, is a difficult task as it is challenged by the multiple competing resonant modes of cavity flow oscillation that must be controlled to achieve suppression. All of these factors have established flow-induced cavity oscillations as a canonical control problem in fluid mechanics as well as aeroacoustics that requires special attention.

1.2 Literature Survey

The phenomenon of cavity noise generation has been a subject of extensive research over the years, with scholars striving to comprehend the underlying physics that fluctuates across diverse cavity dimensions and operational conditions. At its core, this phenomenon is a complex interplay of various physical mechanisms, including hydrodynamics, acoustics, and in certain instances, structural dynamics. Therefore, a comprehensive understanding of all the physical processes and their inter-dynamics is crucial for studying cavity tonal noise. In the light of recent advancements in computational and experimental facilities, there have been numerous attempts to devise and implement new methods to mitigate cavity noise generation. The subsequent section provides a concise review of the categorization of cavity flow, the mechanism of tonal noise generation, and some prevalent methods of cavity noise control, while also discussing their respective advantages and drawbacks.

1.2.1 Cavity Flow Classification

Plentovich *et al.* (1993) performed a comprehensive experimental study of cavity flow operating at low to high subsonic freestream Mach numbers ($0.2 \leq M \leq 0.95$) and a wide range of Reynolds numbers ($0.2 - 18 \times 10^6$) based on the cavity length. They classified the characteristics of cavity flow into *open*, *closed*, and *transitional* types and revealed the limits of cavity dimensions expressed in terms of the length-to-depth ratio, L/D, which segregates different types of flow responses anticipated. In the case of open cavity flow ($L/D \lesssim 8$), the shear layer bridges the cavity opening, and its impingement at the cavity trailing edge produces the tonal noise response. In the case of the closed cavity flow regime

($L/D \gtrsim 13$), the incoming flow separates at the cavity leading edge but does not possess enough energy to surpass the cavity opening. So, it reattaches onto the cavity floor before the ejection takes place towards the cavity trailing edge. In this process, no discernible acoustic signature can be produced. When transitional cavity flow occurs, the cavity dimensions lay within $8 \lesssim L/D \lesssim 13$, and the flow possesses partly both the attributions (open and closed) across this range.

One common feature of the flow responses of open cavity flow is the emission of high amplitude tonal noise at discrete frequencies over large broadband levels. The characteristics of noise radiation may be categorised into shallow ($L/D > 1$) and deep cavity configurations ($L/D < 1$). This categorization was first proposed by Covert (1970) and further emphasized by Heller and Bliss (1975), as they noted the pattern of aeroacoustic coupling phenomenon in the latter differs significantly from the former. However, due to the likewise shear layer characteristic motion over the cavity opening and its interaction with the acoustic mode of the cavity volume (transverse or longitudinal mode depending on the dimensions of the cavity), Rockwell and Naudascher (1978) later established that under certain flow conditions, the peculiar flow response of shallow and deep open cavities is a canonical type of fluid-resonant oscillation. In this type of oscillation, the standing waves inside the cavity have a significant influence on the oscillations. This is due to the acoustic reinforcement of the shear layer instabilities at the leading edge of the cavity, which closes the feedback loop, thereby enabling self-sustained resonant flow oscillations. Whereas the fluid dynamic cavity oscillations (as opposed to fluid-resonant oscillations) arise from the inherent instability of the flow, and the resonant acoustic mode does not reinforce the shear layer and vice versa. In this scenario,

the oscillation is predominantly driven by the shear layer, which is excited by the upstream travelling waves generated after the shear layer impingement process at the cavity downstream edge and provides sufficient conditions for an effective feedback loop. Hence it is argued that the feedback phenomenon exists in both cases (fluid-resonant and fluid-dynamic), However, their modus operandi differs from each other in such a way that the shear layer coupled itself with the resonant cavity mode which provides thereby the impetus for the shear layer oscillation in case of fluid resonant oscillation, while the upstream travelling waves triggers the shear layer in case of fluid-dynamic oscillation. The onsetting and the necessary conditions for fluid resonant oscillation to occur has not been yet fully explored in the existing literature which could explain that why such phenomena occurs at certain flow conditions while the fluid dynamic oscillations occurred at other conditions. Some authors have (East 1966; Tam and Block 1978; Yokoyama *et al.* 2020; Ho and Kim 2021) argued that it usually occurs if the cavity natural frequency of the cavity based on its dimensions comes close to the flow frequency then the fluid resonant oscillation could occur, however how the interplay between the cavity natural mode and the flow happens it still requires a rigorous investigation to fully comprehend the phenomenon.

Numerous experiments and numerical studies (Plumblee *et al.* 1962; Rossiter 1964; Sarohia 1977; Rockwell and Naudascher 1978; Plentovich *et al.* 1993; Rowley *et al.* 2002; Bres and Colonius 2008; Sun *et al.* 2017) have been conducted to better understand the fundamental flow physics of open-cavity flow. These studies have examined various flow characteristics under different conditions, including parameters like free stream Mach number, Re_θ, and L/θ_o.

The oscillation frequency captured in these experiments and simulations can vary depending on the aforementioned factors. The behaviour of cavity flow is heavily influenced by external flow features, such as Mach number, Reynolds number, and incoming boundary layer thickness, as well as the geometry of the cavity itself (length, depth, and span). The parameters that control the cavity configuration and flow conditions include cavity aspect ratio (L/D), spanwise extent (Λ/D), reference length to leading-edge momentum thickness ratio (L/θ_0), Reynolds number ($Re_\theta = U\theta_0/\nu$), and free-stream Mach number ($M_\infty = u_\infty/a_\infty$).

1.2.2 Cavity Aeroacoustic Feedback Phenomenon

Rossiter (1964) proposed a mechanism for self-sustaining shallow cavity flow oscillations and devised a simple formula for predicting the dominant oscillation frequencies. In his empirical formulation, he explained the feedback phenomenon that leads to the tonal noise emission in the presence of grazing flow over a shallow cavity. The sustaining process for the feedback loop involves the Kelvin-Helmholtz instabilities of the shear layer, which are amplified as they move downstream. Upon impingement of the shear layer on the cavity trailing edge, acoustic waves are formed, which travel towards the cavity leading edge to prop up further instabilities in the shear layer. The prevalence of this phenomenon has also been reported and validated by several experimental and numerical studies (Plentovich *et al.* 1993; Mendoza 1997; Arya and De 2021; Liu and Gaitonde 2021; Han *et al.* 2022).

Further explaining the feedback phenomenon, Rossiter (1964) performed an extensive set of experiments for two-dimensional rectangular cavities of different length to depth ratio, at different Mach numbers, which

identified a series of discrete frequencies of oscillation. He used the idea of the feedback process to develop a semi-empirical formula to predict the resonant frequencies. Assumption reasonably based on the experimental data were proposed as;

i. There is some connection between the vortex shedding and the acoustic radiation

ii. Acoustic radiation initiates the vortex shedding and that the passage of the vortices over the rear lip of the cavity is responsible for the acoustic radiation.

iii. Frequency of the acoustic radiation is the same as the vortex shedding frequency. If the average speed of the vortices over the cavity is κ times the free-stream speed and sound waves travel upstream in the cavity at a mean speed c,

iv. There is some inherent connection between the synchronized process of the vortex shedding and acoustic radiation.

- At time t = 0, an identified phase of acoustic radiation leaves the rear lip of the cavity. and vortex is $\gamma_v \lambda_v$ behind the rear lip.
- At time $t = t'$, an identified phase of acoustic radiation arrives at the front lip just as a vortex is shed and vortex pattern has moved downstream a distance $\kappa U t'$ in this time interval.
- Therefore, the complete Wavelengths of acoustic radiation and vortex motion involved eq (1.2) and eq (1.3).
- By eliminating t' between (1.2) and (1.3) And substituting for λ_a & λ_v from eq (1.1) and replacing $m_a + m_v$, γ_v and a with the m, γ and c respectively. The final form will be as follows,

$$f = \frac{\kappa U}{\lambda_v} = \frac{c}{\lambda_a} \tag{1.1}$$

$$m_a \lambda_a = L - ct' \tag{1.2}$$

$$m_v \lambda_v = L + \gamma_v \lambda_v + \kappa U t' \tag{1.3}$$

$$S_t = f\frac{L}{U} = \frac{(m+\gamma)}{\left(M + \frac{1}{\kappa}\right)} \tag{1.4}$$

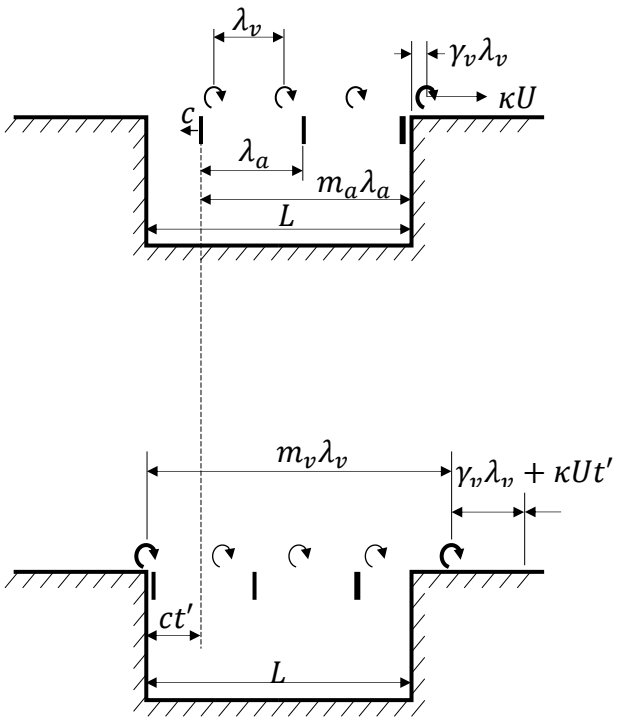

Figure 1.1 Schematic of Rossiter feedback mechanism, redrawn from original script reported by Rossiter (1964).

Heller and Bliss (1975) modified the Rossiter prediction model and proposed the Strouhal number of the m-th Rossiter mode based on cavity length L can be estimated as,

$$St_m = \frac{m - \alpha}{1/\kappa + M_\infty / \sqrt{1 + (r_T/2)(\gamma - 1)M_\infty^2}} \tag{1.5}$$

where r_T is the thermal recovery factor set to unity for low Mach number flow, the quantities κ and α are, respectively, the ratio of average convection speed of disturbances in the shear layer to freestream velocity and the phase delay of

acoustic wave generation at cavity trailing edge from shear layer impingement there. With the prediction given by Eq. (1.5), it is informative to compare the dominant frequencies from the numerical results to ascertain if they are created by the Rossiter modes of the present deep cavity. The two quantities, κ and α, are usually determined and their justifications are heuristic. They are often taken as 0.57 and 0.25 for open cavity flows (Gharib and Roshko 1987; Rowley *et al.* 2002; Sun *et al.* 2017) irrespective of the operating Mach number, which makes the frequency prediction with Eq. (1.5) only valid at high subsonic flow conditions ($M > 0.5$). Thus, the afore-mentioned values of κ and α may not be applicable to the low Mach number flows. Therefore, an accordant estimation for κ and α is necessary to make the empirical calculation of cavity oscillation frequency valid. Secondly, with an appropriate choice of the vortex convection speed and phase delay the above equations becomes deemed valid for the estimation of deep cavity flow oscillation frequency estimation apart form the shallow cavity calculation for which these equations are actually derived from.

For deep cavities, extensive studies (East 1966; Ziada and Bühlmann 1992; Ho and Kim 2021) indicate that the oscillations of the shear layer at the cavity opening activate the acoustic modes within the cavity depth and the synergistic interaction between the flow dynamics and acoustic modes results in noise radiation from deep cavities. While deep cavities operate differently from shallow ones, the Rossiter formula, with appropriate adjustments (Heller and Bliss 1975), remains effective in forecasting the oscillation frequencies within the deep cavity flow field . In Particular, at flow frequencies that align closely with the cavity natural modes, deep cavities set in maximal acoustic resonance (East 1966; Ho and Kim 2021), emphasizing the intricate

relationship between flow dynamics and acoustic responses in cavity flows. (Bruggeman *et al.* 1989) suggested an alternative feedback mechanism for the fluid-resonant oscillation based on Vortex Sound Theory (Howe 2003). This mechanism can be expressed by the following process: acoustic forcing from the resonance on the shear layer at the upstream corner; formation of coherent vortices by the instabilities in the separated shear layer; transfer of energy from the local flow to the acoustic field by the interaction of convective vorticity and the acoustic resonance; and the net energy transfer to the acoustic field determines the amplitude and the phase of the feedback at the upstream corner. Based on this concept, the acoustic resonance in the deep cavity plays an important role in destabilising the shear layer and reinforcing the vortex coalescences. Therefore, this alternative feedback mechanism based on the energy transfer between the vortical (hydrodynamic) and potential (acoustic) fields offers an attractive explanation for the 'lock-on' effect as observed in deep cavity experiments (Elder 1978; Yang *et al.* 2009).

In an attempt to further elucidate the aeroacoustic driving mechanism in deep cavities, Naseer *et al.* (2023b) have revealed that the aeroacoustic feedback process in deep cavities consists of five distinct processes, each of which is supported by the corresponding cavity walls. Firstly, the boundary layer develops at the upstream cavity wall. Upon separating from the cavity leading edge, and with acoustic reinforcement by the reflected acoustic mode supported by the cavity front wall, the shear layer emanates and evolves over the cavity opening. Secondly, vortices of a fully developed shear layer reach the cavity trailing edge, where vortex impingement occurs, supported by the cavity aft wall. Thirdly, the residual eclipsed shear layer vortices convect over the

downstream wall. Afterwards, the high strain impingement of the shear layer at the aft wall produces strong pressure waves directed towards the cavity bottom. Eventually these waves are then reflected back, reinforcing the developing shear layer and closing the feedback loop. Recent studies have also provided insights into the mechanisms of cavity flow-induced noise. Liu *et al.* (2023) investigated Rossiter resonance noise in a low-speed wind tunnel, highlighting the interaction between Rossiter modes and depth resonant modes in locked-on states, offering a modified Rossiter formula that considers phase delay variations with velocity for more accurate predictions. Similarly, Wang *et al.* (2024) explored the interplay of flow and acoustics within tandem deep cavities, focusing on the resonance mechanism between turbulent shear layers and acoustic eigenmodes, advancing our understanding of aeroacoustic interactions in complex cavity configurations. Furthermore, Bourquard (2021) studied the combined effect of thermo- and aeroacoustic instabilities by modelling the phenomena as systems of coupled harmonic oscillators, applying this framework to both the analysis of damper effectiveness in stabilizing unstable acoustic modes and exploring the nonlinear dynamics of damper systems and aeroacoustic instabilities in deep cavities. The results, validated experimentally, highlight the utility of the coupled oscillators approach in understanding and mitigating complex acoustic phenomena.

1.2.3 Cavity Aeroacoustic Suppression Methods

In order to suppress the cavity noise emission due to the aeroacoustic feedback phenomenon at play, approaches are generally categorized into active and passive control methods. Active control involves the external input of energy, either mechanical or electrical, to dynamically adjust actuators that influence

the flow characteristics. Conversely, passive control techniques do not rely on external energy inputs. Numerous successful implementations of active control for mitigating cavity aeroacoustic resonance have been documented across a diverse array of cavity geometries and flow conditions, with a comprehensive review provided by Cattafesta III *et al.* (2008). Both open-loop and closed-loop active control strategies have proven effective in reducing resonant cavity oscillations and their associated tonal noise emissions. Additionally, broadband noise components can be significantly attenuated using sophisticated sensor configurations. Specifically, control-loop methodologies can be tailored to achieve notable suppression, even when cavity flows operate under off-design conditions. However, despite their efficacy in laboratory settings, Cattafesta III *et al.* (2008) noted several critical prerequisites for active control to be viable in real-world applications. These include (i) the development of enhanced physical dynamic models for executing control theories, (ii) the availability of actuators that offer high output, broad bandwidth, and rapid response capable of addressing multi-mode tonal and potentially broadband disturbances, and (iii) a deeper integration of knowledge spanning fluid mechanics, control theory, and transducer technologies. Achieving these requirements presents significant challenges, not least due to the substantial costs involved. Furthermore, the scalability of sensor and actuation systems remains a formidable barrier to the practical application of these advanced control strategies in engineering settings, as discussed by Rowley and Williams (2006).

Passive control strategies mitigate cavity oscillations by altering the development of the shear flow over the cavity, utilizing cost-effective and straightforward devices. These methods often involve geometric modifications

such as the implementation of fixed fences, spoilers, ramps, and passive bleed systems, which can significantly suppress oscillations but may lack the versatility of active control under off-design conditions (Schmit and Raman 2006). Effective passive control mechanisms disrupt cavity resonance through one or more of the following approaches, by (i) altering the mean shear layer trajectory to shift its impingement point downstream of the cavity trailing edge, thereby modifying the interaction with the cavity trailing edge (Arunajatesan *et al.* 2003; Ukeiley *et al.* 2004), (ii) Changing the stability characteristics of the shear layer by adjusting the velocity profiles or fluid properties, which helps prevent the amplification of resonant modes (Ukeiley *et al.* 2003; Arunajatesan *et al.* 2009) and (iii) disrupting the spanwise coherence of the shear layer and its associated Rossiter modes, thereby weakening the resonant feedback mechanism (Arunajatesan *et al.* 2009). Commonly, spoilers and fences are installed on production aircraft to dampen resonant tones within weapon bays, particularly when bay doors are opened. These devices increase the shear-layer thickness, shifting the most unstable shear layer frequencies to lower values. Additionally, spoilers and ramps are used to elevate the mean separation streamline, ensuring that flow reattachment occurs downstream of the cavity trailing edge (Heller and Bliss 1975; Shaw 1979), which diminishes the strength of feedback acoustic waves and Rossiter modes. Furthermore, rods placed in the upstream boundary layer create a mean wake, influencing the development of the cavity mean shear layer (Arunajatesan *et al.* 2003; Milne *et al.* 2013). (Ukeiley *et al.* 2003) explored the effects of rods and variable-height fences, emphasizing the importance of the device impact on the mean gradient of the shear layer in determining attenuation levels. Lai and Luo (2008) also explored the use of dissipative porous media within cavity interiors, demonstrating its

potential in suppressing pressure fluctuations and reducing far-field sound pressure levels.

Recently, a variety of other passive and active techniques aimed at altering the flow dynamics at the leading or trailing edges (Fig. 1(a)) of cavities have been explored to attenuate their Rossiter modes, thereby reducing cavity noise (Lee 2010; Liu and Gómez 2019; Abdelmwgoud and Mohany 2021; Mourão Bento *et al.* 2022). A noteworthy passive approach includes the use of micro-perforated panels (Maury *et al.* 2019), which demonstrated could reduce cavity pressure fluctuations by up to 8 dB in transitional cavity flow regimes, showcasing their effectiveness without altering the fundamental flow characteristics. Sun *et al.* (2019) employed a sequence of flow jets at the cavity leading edge to inject varying momentum flux rates, for the suppression of cavity flow oscillations. Their findings indicated an amplification in the pressure fluctuation over the cavity aft wall at the lower rate of injected momentum flux, however, the reduction was noticed with a significant momentum flux input, inevitably at the expense of a significant increase in the input energy demand. Yokoyama *et al.* (2020) endeavoured to enhance the efficiency of actuation energy in cavity noise reduction by substituting flow jets with continuous and intermittent plasma actuators at the leading edge. Their results demonstrated that considerable noise reduction is achievable with reduced, though still substantial, actuation power input, plateauing with further power increases. Additionally, recent numerical studies by Bacci and Saddington (2023) highlighted the impact of structural modifications, such as introducing a gap between the doors and the cavity edge on a weapon bay model, which showed a strong palliative effect on the aeroacoustic and

structural response, including a notable fluid-acoustic coupling at the first structural mode frequency. Furthermore, Bacci and Saddington (2022) conducted Hilbert–Huang spectral analysis on cavities with fluidic spoilers, revealing that these spoilers significantly mitigate acoustic noise and modify shear layer trajectories, thus altering resonant modes and their interaction with Rossiter–Heller tones in a complex nonlinear manner. It is important to note that these noise suppression methods are intrinsically flow-invasive. Their implementation invariably introduces substantial disturbances to the evolving cavity shear layer, thereby altering the fundamental flow characteristics inherent to the original cavity configuration. This may lead to a range of unintended aerodynamic effects, such as intensified turbulence, increased flow-induced drag, and elevated actuation energy requirements as a result of the traditional treatment for cavity noise reduction. Moreover, these methods may induce extraneous noise in frequency ranges absent in the original flow. Unfortunately, these potential drawbacks have not been comprehensively addressed in the existing literature.

1.3 Proposed Cavity Aeroacoustic Suppression Concept

Passive control strategies usually involve introducing new devices and making geometric modifications to a cavity in order to disrupt the aeroacoustic feedback loop that causes self-sustained flow oscillations and noise radiation. These changes aim to alter the cavity mean flow and its stability characteristics. However, modifying the cavity geometry and dimensions may result in trade-offs such as increased overall drag or adverse mean pressure distributions. An innovative approach involves directly targeting the suppression or elimination

of fluid dynamic and acoustic pressure perturbations within the aeroacoustic feedback loop, rather than through changes to the cavity geometry. This can be achieved by integrating localized surface compliance, specifically through the use of elastic panels flush-mounted on the cavity walls. These panels are designed to resonate near their natural frequencies when exposed to the dynamic and acoustic pressures within the cavity, potentially leading to structural resonance.

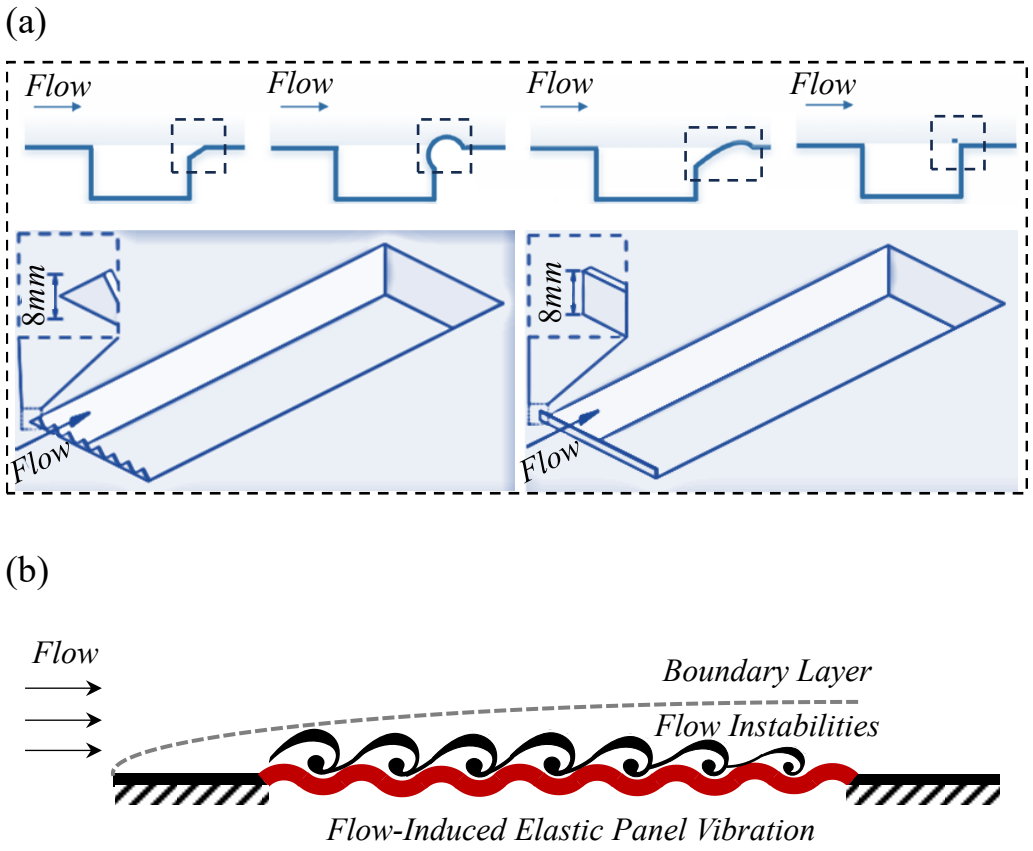

Figure 1.2 (a) Traditional cavity noise reduction techniques (reproduced from Saddington *et al.* (2016); Liu and Gómez (2019) with the permission of the authors). (b) The novel cavity noise suppression concept proposed in Naseer *et al.* (2023b).

This concept draws inspiration from earlier experimental and numerical studies practiced on different aerodynamic structures, such as those by Luk *et al.* (2004), who investigated the aerodynamic and structural resonance of an

elastic airfoil subjected to periodic pressure perturbations from upstream cylindrical vortex generators. Their results demonstrated that when the airfoil excitation frequency aligns closely with one of its fluid-loaded natural frequencies, it exhibits structural resonance and may enter a state of limit cycle oscillation. Consequently, the airfoil absorbs kinetic energy from the incoming excitation, sustaining its flow-induced resonant vibration primarily through reactive energy absorption, with minimal energy dissipation due to viscous effects and structural damping.

Building on this understanding, there is potential to leverage similar energy absorption phenomena to mitigate the impact of shear layer perturbations on the cavity trailing edge and the acoustic perturbations feeding back to the leading edge as well as the cavity bottom where the incident acoustic waves get reflected. These perturbations are crucial in forming the resonant Rossiter modes and the subsequent aeroacoustic feedback loop. Numerical studies by Arif *et al.* (2020b); Arif *et al.* (2020a); Arif *et al.* (2022) have already demonstrated the feasibility of using elastic panels to weaken the aeroacoustic feedback loop and reduce tonal noise without compromising the aerodynamic performance of airfoils, as evidenced by the unchanged time-averaged streamlines. Furthermore, the use of compliant surfaces has been explored for other applications such as delaying the laminar-turbulent transition and reducing skin-friction drag in high Reynolds number wall-bounded flows (Carpenter *et al.* 2001; Gad-el-Hak 2002). However, the current study represents the first attempt to utilize compliance technology specifically for reducing cavity resonance and its associated aeroacoustic effects.

1.4 Objectives of the Present Study

Driven by the challenges of cavity noise and the limitations of existing noise reduction methods, this study introduces a novel approach aimed at mitigating cavity tonal noise. We propose a unique passive noise suppression strategy that employs localized surface compliance in the form of an elastic panel. The concept is rooted in utilizing flow-induced resonant panel vibration to absorb flow energy and alter the aeroacoustic feedback mechanisms that drive fluid-resonant oscillations within a deep cavity. The proposed methodology offers two primary advantages. First, the resonant panel vibratory displacement is intentionally maintained smaller than typical cavity dimensions, ensuring minimal distortion of local streamlines. Second, the panel utilizes a reactive mechanism to absorb flow oscillation energy, potentially leaving cavity drag unaffected. This approach is designed to suppress cavity noise while preserving the original flow characteristics of the cavity.

To investigate and validate the efficacy of this concept, the study employs direct aeroacoustics simulation (DAS) using the Conservation Element and Solution Element (CE/SE) method, complemented by extensive wavenumber-frequency analysis for precise panel design. The elastic panel is strategically configured to resonate at the dominant Rossiter frequency of the cavity, optimizing energy absorption and strategically placed to target various aeroacoustic feedback and coupling processes. This comprehensive study aims to provide a detailed aeroacoustic-structural interaction analysis to evaluate the effectiveness of the proposed noise suppression strategy and its impact on cavity flow characteristics. Additionally, we assess the flow dynamics

implications of our control method, a critical aspect often overlooked in existing literature. With these considerations in mind, the study sets forth the following objectives:

- To investigate the potential for tonal noise reduction through localized flow-induced vibration of an elastic panel mounted on various cavity walls.
- To develop a comprehensive panel design methodology, including specifications for its placement, length, and tuning frequency, to ensure effective resonance with the flow and suppression of flow fluctuations energy.
- To elucidate the fundamental aeroacoustic coupling phenomena in deep cavities and the aeroacoustic-structural interactions through which the elastic panel mitigates or even eliminates the aeroacoustic feedback loop, thereby achieving significant noise reduction.
- To design and implement an experimental setup to verify the single wall-mounted elastic panel effectiveness in reducing cavity noise emissions and to experimentally study the modification the aeroacoustic feedback loop responsible for extreme cavity noise.
- To enhance the noise reduction capabilities of the developed approach by employing multiple elastic panels for more effective tonal noise suppression.

1.5 Structure of the Thesis

The remainder of the thesis is organized as follows.

Chapter 2 provides details on the numerical techniques employed in the study. It discusses the implementation of the Conservation Element and Solution Element (CE/SE) method to solve the unsteady Navier-Stokes (N-S) equations, including the boundary conditions applied. A subsection on the aeroacoustic-structural coupling is presented, which outlines how these interactions are incorporated into the numerical framework. Additionally, this chapter covers the computational domain setup, grid generation, grid independence studies, and the validation of the numerical scheme to ensure accuracy and reliability in simulations.

Chapter 3 introduces the concept of using localized surface compliance to suppress deep cavity aeroacoustics at low Mach numbers. The core idea revolves around the local absorption of energy from the aeroacoustic processes that support the self-sustained feedback loop responsible for tonal noise generation. Employing high-fidelity, two-dimensional direct aeroacoustic simulation, the chapter details the strategic introduction of an elastic panel across the different cavity walls, its design considerations, and its impact on noise suppression. The natural frequency of the panel is tuned to match the characteristic frequency of the feedback loop, enhancing its energy absorption capabilities. Results demonstrating significant reductions in noise pressure levels and cavity drag, as well as comprehensive wavenumber-frequency analyses, are discussed to elucidate the mechanisms behind the observed noise generation and suppression.

Chapter 4 details the experimental work conducted to verify the numerical findings concerning the effectiveness of the elastic panel strategy in aeroacoustic suppression. Experiments were carried out in a low-velocity, closed-circuit, open-jet wind tunnel. The experimental setup is described, highlighting the controlled environment that mimics the conditions modelled in the simulations. Different cavity configurations, including both rigid and panel-modified setups, were tested at different flow velocities. This chapter emphasizes the methodological approach and experimental techniques used to capture the crucial interactions between the shear layer oscillations and cavity acoustic modes, providing a comprehensive evaluation of the acoustic response under varied aerodynamic conditions.

Chapter 5 reports on advanced numerical studies investigating a novel methodology for passive suppression of deep cavity noise using multiple elastic panels. The study, conducted at low freestream Mach and Reynolds numbers, explores various cavity-panel configurations using Direct Aeroacoustic Simulation (DAS) coupled with a panel dynamic solver. Each configuration is designed to harmonize the panel natural frequencies with the characteristic aeroacoustic processes of the cavity to promote effective energy absorption. This chapter presents the significant noise power and drag reduction achieved. In-depth spatio-temporal analyses elucidate the complex interplay between cavity flow, panel vibration responses, and cavity acoustic modes, culminating in comprehensive noise reduction across all studied configurations. The feasibility and effectiveness of the proposed methodology suggest its substantial potential for applications requiring quiet and energy-efficient cavity configurations.

Chapter 6 provides a summary of the research achievements and the conclusions derived from the study. It also offers recommendations for future research in this field.

Chapter 2

Physical Models and Numerical Solution

This chapter delineates the numerical methodologies utilized in the current investigation and the strategies for their application. The current study focuses on the attenuation of tonal noise emanating from cavity flow, which entails the intricate interplay of unsteady airflow, the vibrational behaviour of panel structures, and acoustic phenomena. A numerical framework that can accurately capture these complex interactions across both aerodynamic and acoustic domains is imperative. Consequently, the direct aeroacoustic simulation (DAS) technique has been selected for its proficiency in resolving the interdependent dynamics of unsteady cavity aerodynamics and acoustics with high fidelity. For the execution of DAS, the conservation element and solution element (CE/SE) method is employed to tackle the unsteady compressible Navier-Stokes (N-S) equations. The non-linear interrelation between flow perturbations and the structural dynamics of the panel is

addressed through a monolithic scheme, as developed by Fan *et al.* (2018). The following sections will explain the numerical methods, their underlying mathematical formulations, and the nuances of their practical implementation in greater detail.

2.1 Aeroacoustic Model

The present problem of interest involves the investigation of an aeroacoustic phenomenon arising from unsteady airflow over a deep cavity. Recognizing that the acoustical phenomena are essentially manifestations of unsteady motions within a compressible fluid medium (Crighton 1981), it becomes imperative to utilize a numerical method adept at concurrently resolving both the unsteady flow dynamics, the resultant acoustic waves and the interaction between the former and later. While there are hybrid methodologies that segregate the resolution of flow dynamics from acoustics into distinct stages (Singer *et al.* 2000), these approaches fail to adequately represent the nonlinear interplay between the hydrodynamic and acoustic domains. Therefore, the numerical framework of choice for this investigation is the Direct Aeroacoustic Simulation (DAS) for its inherent ability to precisely simulate both the flow and acoustic characteristics. The DAS methodology involves the simultaneous solution of the unsteady compressible Navier-Stokes (N-S) equations alongside the equation of state, ensuring a comprehensive treatment of the coupled aerodynamic and acoustic fields. The utility of the DAS method within the field of aeroacoustic research has been substantiated through numerous studies encompassing a diverse array of applications. These include investigations into the acoustic characteristics of airfoils, the dynamics of jet flows, and the complex behaviour within cavities and duct systems (Gloerfelt *et al.* 2003; Desquesnes *et al.* 2007;

Jones 2008; Lam *et al.* 2014b). The current unsteady flow problem of the open cavity flow is described by the two-dimensional compressible Navier-Stokes equations and adheres to the ideal gas law, which is applicable to calorically perfect gases. For the sake of generality, all primitive flow and panel variables are described in their non-dimensional form unless otherwise mentioned. The two-dimensional normalized N–S equations in strong conservation format can be written as,

$$\frac{\partial \boldsymbol{U}}{\partial t} + \frac{\partial(\boldsymbol{F} - \boldsymbol{F}_v)}{\partial x} + \frac{\partial(\boldsymbol{G} - \boldsymbol{G}_v)}{\partial y} = 0, \tag{2.1}$$

The solution vector U, pressure and viscous flux vectors (F, G, F_v, G_v) are defined by:

$$\boldsymbol{U} = [\rho \;\; \rho u \;\; \rho v \;\; \rho E]^T, \tag{2.2}$$

$$\boldsymbol{F} = [\rho u \;\; \rho u^2 + p \;\; \rho uv \;\; (\rho E + p)u)]^T \tag{2.3}$$

$$\boldsymbol{F_v} = \left[0 \;\; \tau_{xx} \;\; \tau_{xy} \;\; \tau_{xx}u + \tau_{xy}v - q_x\right]^T (1/Re), \tag{2.4}$$

$$\boldsymbol{G} = [\rho v \;\; \rho uv \;\; \rho v^2 + p \;\; (\rho E + p)v)]^T, \tag{2.5}$$

$$\boldsymbol{G_v} = \left[0 \;\; \tau_{xy} \;\; \tau_{yy} \;\; \tau_{xy}u + \tau_{yy}v - q_y\right]^T (1/Re), \tag{2.6}$$

where the flow normal and shear stresses are given as,

$$\tau_{xx} = \left(\frac{2}{3}\right)\mu\left(2\frac{\partial u}{\partial x} - \frac{\partial v}{\partial y}\right), \tau_{xy} = \mu\left(2\frac{\partial u}{\partial y} - \frac{\partial v}{\partial x}\right), \tau_{yy} = \left(\frac{2}{3}\right)\mu\left(2\frac{\partial v}{\partial y} - \frac{\partial u}{\partial x}\right).$$

thermal fluxes are calculated by:

$$q_x = [\mu/(\gamma - 1)PrM^2](\partial T/\partial x), q_y = [\mu/(\gamma - 1)PrM^2](\partial T/\partial y).$$

the Reynolds number $Re_{\hat{L}}$ based on the cavity length $\hat{L}$, Mach number M and Prandtl number Pr are calculated as:

$$M = \hat{u}_\infty/\hat{c}_\infty, Re_{\hat{L}} = \hat{\rho}_\infty\hat{u}_\infty\hat{L}/\hat{\mu}_\infty, Pr = \hat{c}_\infty\hat{\mu}_\infty/\hat{k}_\infty = 0.71.$$

the total energy E and pressure p are calculated by:

$$E = p/\rho(\gamma - 1) + (u^2 + v^2)/2, p = \rho T/\gamma M^2$$

the spatial coordinates x and y, time t, density ρ, pressure p, and velocities u and v are non-dimensionalized as:

$x = \hat{x}/\hat{L},\ y = \hat{y}/\hat{L}, t = \hat{t}\hat{u}_\infty/\hat{L}, \rho = \hat{\rho}/\hat{\rho}_\infty, p = \hat{p}/(\hat{\rho}_\infty \hat{u}_\infty^2), u = \hat{u}/\hat{u}_\infty$ and $v = \hat{v}/\hat{u}_\infty$

variables with a hat (^) denote dimensional quantities, while the subscript "∞" signifies freestream conditions. The reference dimension is defined by the cavity length $\hat{L}$ in this study.

2.1.1 Conservation Element and Solution Element Method (CE/SE)

For the implementation of Direct Aeroacoustic Simulation (DAS), a numerical method that is both highly accurate and exhibits low numerical dissipation is essential. This requirement stems from the significant disparities in energy and length scales between the domains of flow dynamics and acoustics (Lam *et al.* 2014b). Excessive numerical dissipation can introduce artificial behaviours, potentially distorting the propagation of delicate acoustic waves within the flow field and leading to substantial errors in the context of the current study. One strategy to mitigate such effects is the adoption of high-order numerical schemes (Visbal and Gordnier 2004). Although effective, these schemes are computationally intensive. Traditional high-order finite-difference methods, previously employed in aeroacoustic research (Desquesnes *et al.* 2007; Jones *et al.* 2010), demand intricate numerical treatments to achieve desired accuracy, which can be challenging to implement in complex scenarios such as shock wave interactions. Additionally, finite-difference approaches rely heavily on uniform grids, rendering them less suitable for intricate geometries (Anderson 2009). While the finite element method offers advantages for complex configurations, it too is computationally demanding due to extensive

matrix operations. The finite volume method, another prevalent approach, necessitates the evaluation of flux across each mesh surface, involving comprehensive numerical computations and often the introduction of artificial viscosity, which further escalates computational demands and poses difficulties in handling complex geometries. The space-time Conservation Element and Solution Element (CE/SE) method, pioneered by (Chang 1995), presents an effective alternative that circumvents these challenges. Distinguished by its robustness and precision, the CE/SE method upholds strict conservation principles within the Navier-Stokes (N-S) equations across both spatial and temporal dimensions (Lam *et al.* 2014b). In contrast to conventional numerical frameworks based on finite volume and finite element methods, the CE/SE method amalgamates the handling of space and time into a unified computational process. Since its introduction, the CE/SE method has been successfully leveraged in simulations involving various aeroacoustic phenomena, shock interactions, and jet noise concerns (Loh *et al.* 2001; Venkatachari *et al.* 2008; Lam and Leung 2018). Lam *et al.* (2014a) accurately employed the CE/SE method to dissect complex aeroacoustic interplays at varying flow speeds within duct environments. More recently, Arif *et al.* (2022) applied the CE/SE method with notable success in delineating the aeroacoustic behavior of airfoil flow and deciphering the acoustic feedback mechanisms integral to airfoil tonal noise generation. Their work underscores the formidable capacity of the scheme to concurrently resolve the intricacies of flow dynamics and acoustic phenomena with high accuracy.

2.1.2 Mathematical Formulation of CE/SE

The CE/SE method is engineered in such a way as to enable the accurate calculation of flow flux across the finite control volume surfaces in Euclidean space. This scheme establishes two pivotal constructs: the conservation element (CE), which represents the finite control volume in space-time, and the solution element (SE), where the flow solutions are stored. By defining the CE and SE appropriately, the flow flux calculation can be directly determined from the flow quantities at the CE surface centroid, thus circumventing the need for complex flux reconstruction typically required in finite volume methods.

The CE/SE method utilizes the concept of the conservation element (CE) to enforce flux conservation within the control volume in the space-time domain. The flux evaluation across the surface draws upon the solution element (SE), which is based on the Taylor expansion of solutions around the solution point. This approach simplifies the computational procedure by eliminating the need for flux reconstruction and does not rely on methods such as the characteristics method or other constraints. Its foundation on Taylor series expansion renders it non-dissipative, neutrally stable, and adaptable to both uniform and unstructured meshes. Although inherently a first-order method, its accuracy extends up to second-order (Lam *et al.* 2014b). Thus, it is expected to be more efficient than high-order finite-difference schemes, which are computationally demanding in terms of both execution time and memory usage. This approach prioritizes the strict conservation of physical laws while providing a unified framework for spatial and temporal discretization—fundamentally differing from traditional finite-difference and finite-element methods. The combination of these features makes the CE/SE method an

excellent choice for solving the complex aeroacoustics associated with cavity noise with optimal computational resource use. For a comprehensive explanation of the CE/SE method, readers are referred to Lam (2012). The subsequent discussion in this thesis will provide an overview of the mathematical foundations of the method.

Consider the Euclidean space characterized by spatial coordinates x and y, and time t.The Navier-Stokes equations in strong conservation form is represented as:

$$\nabla \cdot \boldsymbol{K} = 0 \tag{2.7}$$

where $\nabla\cdot$ denotes the divergence operator in Euclidean space and $\boldsymbol{K} = [\boldsymbol{F} - \boldsymbol{F_v}, \boldsymbol{G} - \boldsymbol{G_v}, \boldsymbol{U}]$. Applying Gauss divergence theorem, Equation (2.7) is reformulated as:

$$\oint_{S(V)} \boldsymbol{K} \cdot ds = 0 \tag{2.8}$$

with $ds = [\Delta x, \Delta y, \Delta t]$ signifying the differential surface element vector, and $S(V)$ representing the surface enclosing an arbitrary space-time region V within the Euclidean space. The computational domain is discretized into triangulated grids, as depicted in Figure 2.1. Here, grid BDF with its centroid G is showcased, while A, C, and E denote the centroids of adjacent grids.

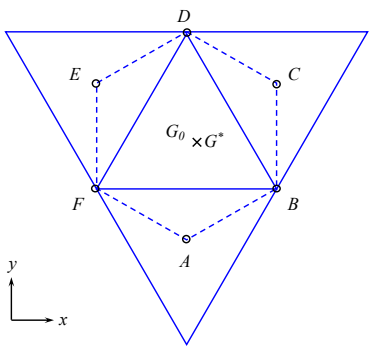

Figure 2.1 Schematic of triangulate grids. A, C, E and G are the centroids of the grids; B, D and F are the nodes; $G*$ is the solution point; and - - - is the boundary of CE.

The conservation element (CE) is formed by connecting the nodes of a grid to the centroids of adjacent grids, thus creating the boundary ($ABCDEF$). The centroid of this hexagon, labelled as G^*, also serves as the solution point. Due to grid non-uniformity, G^* and G may not coincide. The hexagon is extended along the time dimension to create a hexagonal prism, which defines the CE. The conservation of flux is enforced across this CE. Figure 2.2 illustrates the CE, denoted by $CE(G^*, n)$, where G^* represents the spatial location and n is the $n-th$ time level.

Adjacent to the solution point, a solution element (SE) is established, as shown in Figure 2.3. The flow variables $\boldsymbol{\phi}(\boldsymbol{X})$ which could represent $\boldsymbol{U}(\boldsymbol{X}), \boldsymbol{F}(\boldsymbol{X}), \boldsymbol{F_v}(\boldsymbol{X}), \boldsymbol{G}(\boldsymbol{X})$, or $\boldsymbol{G_v}(\boldsymbol{X})$ at location $\boldsymbol{X}(x, y, t)$ within the $SE(G^*, n)$ are computed via first-order Taylor series expansion from the solution point G^*:

$$\boldsymbol{\phi}(\boldsymbol{X}) = \boldsymbol{\phi}_{G^*} + (x - x_{G^*})(\boldsymbol{\phi}_x)_{G^*} + (y - y_{G^*})\left(\boldsymbol{\phi}_y\right)_{G^*} + (t - t_{G^*})(\boldsymbol{\phi}_t)_{G^*}, \quad (2.9)$$

where the subscripts x, y and t denote the partial derivatives with respect to the spatial coordinates x and y, and the temporal coordinate t, respectively. The viscous terms, $\boldsymbol{F_v}(\boldsymbol{X})$ and $\boldsymbol{G_v}(\boldsymbol{X})$ are approximated by their constant values at the solution point G^*. Consequently, the Navier-Stokes equations can be succinctly expressed as:

$$(\boldsymbol{U}_t)_{G^*} = -(\boldsymbol{F}_x)_{G^*} - (\boldsymbol{G}_x)_{G^*} \quad (2.10)$$

The flow quantities $\boldsymbol{K}(\boldsymbol{X})$ are approximated at the solution point $G^*$by:

$$\boldsymbol{K}(\boldsymbol{X})_{G^*} \equiv [\boldsymbol{F}(\boldsymbol{X})_{G^*} - \boldsymbol{F}_v(\boldsymbol{X})_{G^*}, \boldsymbol{G}(\boldsymbol{X})_{G^*} - \boldsymbol{G}_v(\boldsymbol{X})_{G^*}, \boldsymbol{U}(\boldsymbol{X})_{G^*}] \quad (2.11)$$

In this manner, all fluxes through the planes in the SE and the flow variables can be precisely determined based on the values at the solution point G^*.

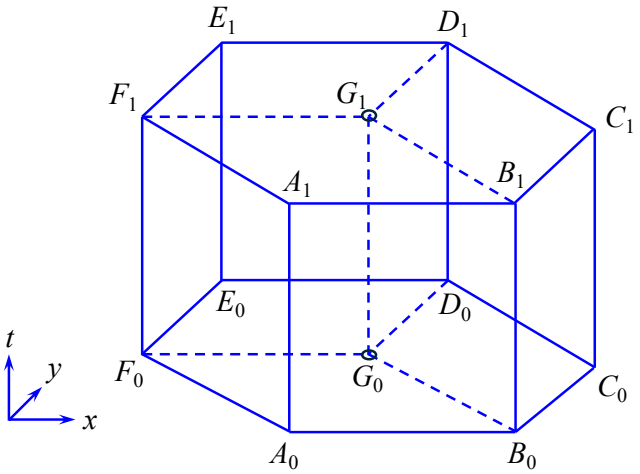

Figure 2.2 Schematic of the conservation element $\boldsymbol{CE}(\boldsymbol{G}^*, \boldsymbol{n})$. - - - is the boundary of $\boldsymbol{SE}(\boldsymbol{G}^*, \boldsymbol{n})$.

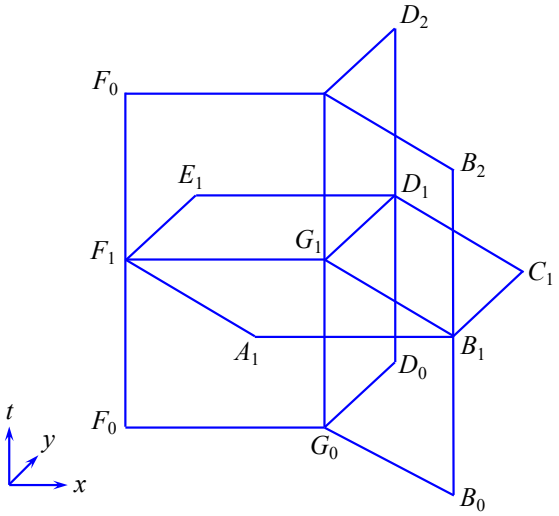

Figure 2.3 Schematic of the solution element $\boldsymbol{SE}(\boldsymbol{G}^*, \boldsymbol{n})$.

2.1.3 Advancement of the Solution in Time

Within the Conservation Element and Solution Element (CE/SE) framework, flow quantities are represented by conservation variables and their spatial derivatives, making the iterative advancement of $\boldsymbol{U}, \frac{\partial \boldsymbol{U}}{\partial x}$ and $\frac{\partial \boldsymbol{U}}{\partial y}$ central to this method. This section elucidates the process of updating these variables within a conservation element $CE(G^*, n)$. Consider the hexahedral conservation element $A_1B_1G_1F_1 - A_0B_0G_0F_0$ as depicted in Figure 2.4(a). The flux traversing the surface $A_1B_1B_0A_0, A_1F_1F_0A_0$ and $A_0B_0G_0F_0$ of $CE(G^*, n)$ is computed as:

$$\Upsilon_1^{n-1/2} = \Upsilon_{A_1B_1B_0A_0} + \Upsilon_{A_1F_1F_0A_0} + \Upsilon_{A_0B_0G_0F_0} \tag{2.12}$$

Here, each flux component through the CE is determined by multiplying the flow variable values at the centroid of the surface by the corresponding area vector:

$$\Upsilon_{A_1B_1B_0A_0} = \boldsymbol{K}\left(\chi_{A_1B_1B_0A_0}\right)_{A^*} \cdot \boldsymbol{S}_{A_1B_1B_0A_0}$$

$$\Upsilon_{A_1F_1F_0A_0} = \boldsymbol{K}\left(\chi_{A_1F_1F_0A_0}\right)_{A^*} \cdot \boldsymbol{S}_{A_1F_1F_0A_0},$$

$$\Upsilon_{A_0B_0G_0F_0} = \boldsymbol{K}\left(\chi_{A_0B_0G_0F_0}\right)_{A^*} \cdot \boldsymbol{S}_{A_0B_0G_0F_0},$$

The centroid χ for each surface is derived by geometric means:

$$\chi_{A_1B_1B_0A_0} = \left(t^{n-1/4}, \frac{1}{2}\left(x_{A_1} + x_{B_1}\right), \frac{1}{2}\left(y_{A_1} + y_{B_1}\right)\right),$$

$$\chi_{A_1F_1F_0A_0} = \left(t^{n-1/4}, \frac{1}{2}\left(x_{A_1} + x_{F_1}\right), \frac{1}{2}\left(y_{A_1} + y_{F_1}\right)\right),$$

$$\chi_{A_0B_0G_0F_0} = \left(t^{n-1/2}, \frac{1}{4}\left(x_{A_0} + x_{B_0} + x_{G_0} + x_{F_0}\right), \frac{1}{4}\left(y_{A_0} + y_{B_0} + y_{G_0} + y_{F_0}\right)\right).$$

The outward normal vector $\boldsymbol{S}$ for each plane can be calculated by:

$$\boldsymbol{S}_{A_1B_1B_0A_0} = \frac{dt}{2}\left(y_{B_1} - y_{A_1}, x_{A_1} - x_{B_1}, 0\right)$$

$$\boldsymbol{S}_{A_1F_1F_0A_0} = \frac{dt}{2}\left(y_{F_1} - y_{A_1}, x_{A_1} - x_{F_1}, 0\right)$$

$$\boldsymbol{S}_{A_0B_0G_0F_0} = \frac{dt}{2}\left(0, 0, -S_{A_0B_0G_0F_0}\right)$$

where $S_{A_0B_0G_0F_0}$ is the area of the plane $A_0B_0G_0F_0$. The flow quantities $\boldsymbol{K}$ at point A^* are estimated as:

$$\boldsymbol{K}\left(\chi_{A_1B_1B_0A_0}\right)_{A^*} = \begin{bmatrix} \boldsymbol{U}\left(\chi_{A_1B_1B_0A_0}\right)_{A^*} \\ \boldsymbol{F}\left(\chi_{A_1B_1B_0A_0}\right)_{A^*} - \boldsymbol{F}_v\left(\chi_{A_1B_1B_0A_0}\right)_{A^*} \\ \boldsymbol{G}\left(\chi_{A_1B_1B_0A_0}\right)_{A^*} - \boldsymbol{G}_v\left(\chi_{A_1B_1B_0A_0}\right)_{A^*} \end{bmatrix}^T \tag{2.13}$$

$$\boldsymbol{K}\left(\chi_{A_1F_1F_0A_0}\right)_{A^*} = \begin{bmatrix} \boldsymbol{U}\left(\chi_{A_1F_1F_0A_0}\right)_{A^*} \\ \boldsymbol{F}\left(\chi_{A_1F_1F_0A_0}\right)_{A^*} - \boldsymbol{F}_v\left(\chi_{A_1F_1F_0A_0}\right)_{A^*} \\ \boldsymbol{G}\left(\chi_{A_1F_1F_0A_0}\right)_{A^*} - \boldsymbol{G}_v\left(\chi_{A_1F_1F_0A_0}\right)_{A^*} \end{bmatrix}^T \tag{2.14}$$

$$\boldsymbol{K}\left(\chi_{A_0B_0G_0F_0}\right)_{A^*} = \begin{bmatrix} \boldsymbol{U}\left(\chi_{A_0B_0G_0F_0}\right)_{A^*} \\ \boldsymbol{F}\left(\chi_{A_0B_0G_0F_0}\right)_{A^*} - \boldsymbol{F}_v\left(\chi_{A_0B_0G_0F_0}\right)_{A^*} \\ \boldsymbol{G}\left(\chi_{A_0B_0G_0F_0}\right)_{A^*} - \boldsymbol{G}_v\left(\chi_{A_0B_0G_0F_0}\right)_{A^*} \end{bmatrix}^T \tag{2.15}$$

It is assumed that all the viscous terms remain constant at the solution point A^*, because over a small spatial and temporal domain, the variation in the viscous terms is negligible, so by making this assumption, the numerical calculation becomes efficient with minimal error:

$$\boldsymbol{F}_v\left(\chi_{A_1B_1B_0A_0}\right)_{A^*} = \boldsymbol{F}_v\left(\chi_{A_1F_1F_0A_0}\right)_{A^*} = \boldsymbol{F}_v\left(\chi_{A_0B_0G_0F_0}\right)_{A^*} \tag{2.16}$$

$$\boldsymbol{G}_v\left(\chi_{A_1B_1B_0A_0}\right)_{A^*} = \boldsymbol{G}_v\left(\chi_{A_1F_1F_0A_0}\right)_{A^*} = \boldsymbol{G}_v\left(\chi_{A_0B_0G_0F_0}\right)_{A^*} \tag{2.17}$$

A corresponding methodology can be applied to the third conservation element configured as a hexahedron $D_1E_1F_1G_1 - D_0E_0F_0G_0$, as depicted in Figure 2.4(c). Finally, the top surface area of the conservation element $CE(G^*, n)$, illustrated in Figure 2.4(d), is quantified as:

$$S_{top} = S_{A_1B_1C_1D_1E_1F_1} = S_{A_0B_0G_0F_0} + S_{C_0D_0G_0B_0} + S_{D_0E_0F_0G_0} \tag{2.18}$$

The efflux through this top surface is articulated as:

$$Y_{top}^n = S_{top} \cdot \boldsymbol{U}_G^n \tag{2.19}$$

To enforce flux conservation within $CE(G^*, n)$, the following condition is imposed:

$$\Upsilon_{top}^{n} + \Upsilon_{1}^{n-\frac{1}{2}} + \Upsilon_{2}^{n-\frac{1}{2}} + \Upsilon_{3}^{n-\frac{1}{2}} = 0 \tag{2.20}$$

Subsequently, the conservation variables at the n-th time level are ascertained by:

$$\Upsilon_{G^*}^{n} = -\frac{\Upsilon_{1}^{n-1/2} + \Upsilon_{2}^{n-1/2} + \Upsilon_{3}^{n-1/2}}{S_{top}} \tag{2.21}$$

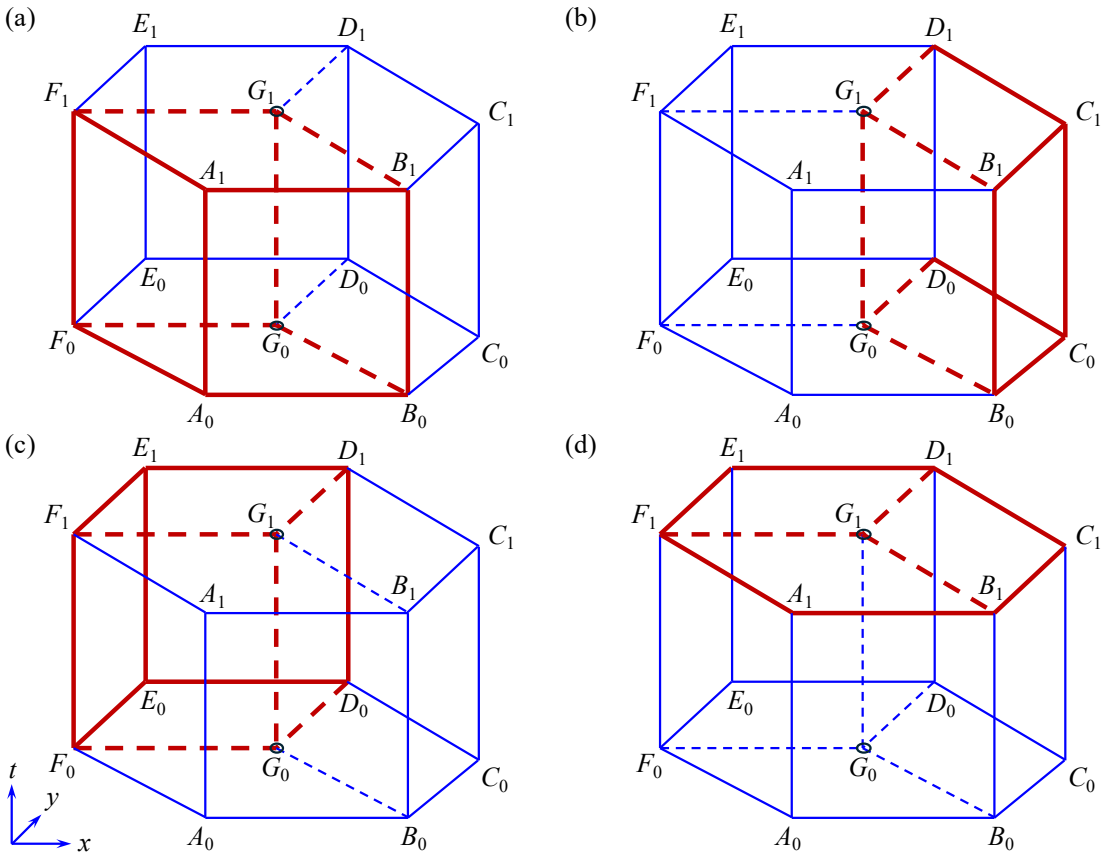

Figure 2.4 Schematic of conservation element of hexahedron. (a) $A_1B_1G_1F_1 - A_0B_0G_0F_0$, (b) $B_1C_1D_1G_1 - B_0C_0D_0G_0$, (c) $D_1E_1F_1G_1 - D_0E_0F_0G_0$ and (d) $A_1B_1C_1D_1E_1F_1$.

Following the determination of $\boldsymbol{U}$, the spatial derivatives $\frac{\partial \boldsymbol{U}}{\partial x}$ and $\frac{\partial \boldsymbol{U}}{\partial y}$ are calculated. Chang *et al.* (1999) proposed a scheme that leverages a central finite difference method to estimate gradients at the solution points of adjacent elements. Yet, this method exhibited significant numerical dissipation, especially in areas with varying Courant-Friedrichs-Lewy (CFL) conditions

such as boundary layers, due to its sole dependence on elementary mathematical operations devoid of physical context. To surmount these deficiencies, Chang and Wang (2002) introduced a Courant number insensitive scheme (CNIS), which utilizes the local CFL number as a dissipation modulator to enhance the fidelity of acoustic wave representation. Despite its effectiveness in resolving small-scale perturbations, the CNIS incurs a high computational demand due to its reliance on six adjacent elements to construct the numerical domain of dependence. In pursuit of computational efficacy, the current study adopts the Simplified Courant Number Insensitive Scheme (SCNIS) developed by Yen and Wagner (2005). SCNIS judiciously reduces computational demands while preserving the ability to accurately capture subtle flow perturbations. The methodology behind SCNIS is outlined below.

Consider an element outlined by the planes $A_1B_1G_1F_1, B_1C_1D_1G_1$ and $D_1E_1F_1G_1$, with their centroids labelled as M_1, M_2, and M_3 respectively, as presented in Figure 2.5. Intermediate points indexed by $P_i, i = 1,2,3$, are placed linearly between the centroids M_i and their respective solution points N_i. The positions of P_i are determined as follows:

$$P_i = M_i + CFL\ (N_i - M_i) \tag{2.22}$$

Figure 2.6 showcases the numerical domain of dependence for the solution element $SE(G^*, n)$. The analytical domain of dependence is symbolized by a circle centered at $(x, y) = 1/2(-udt, -vdt)$ from the origin G^*, with a radius $r = cdt$. The stability of the numerical solution is ensured when this analytical domain is entirely enclosed within the numerical domain of

dependence. For instance, considering the side A^*C^*as illustrated in Figure 2.7, the stability criterion is satisfied if:

$$CFL_1 = \frac{|G^*S| + |G^*T|}{|G^*Q|} = dt\,\frac{\sqrt{u^2+v^2}cos\,(\varphi-\alpha)+c}{|G^*Q|} \leq 1 \tag{2.23}$$

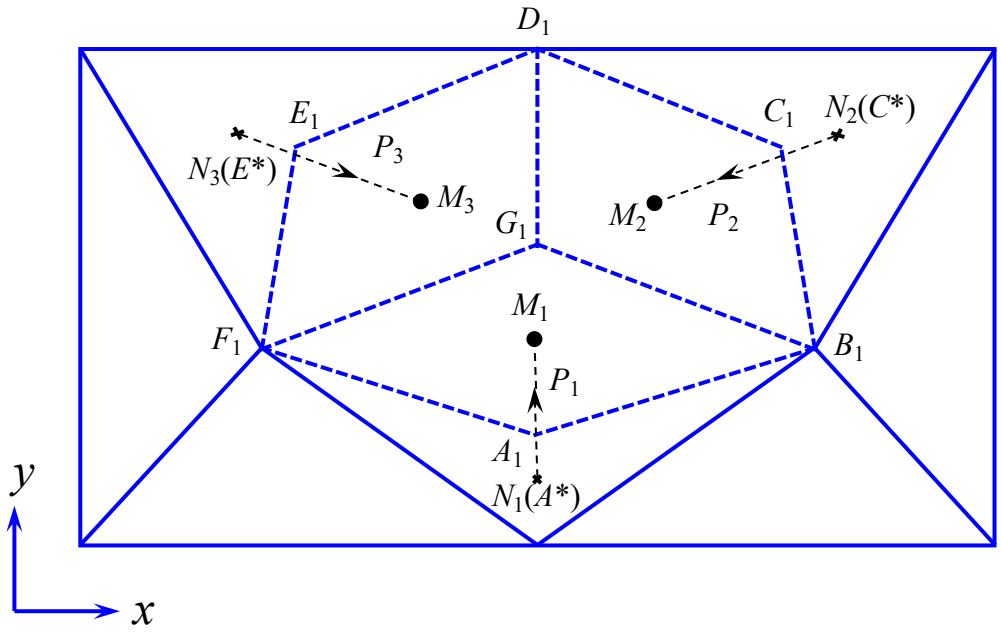

Figure 2.5 Definition of P_i

For the remaining sides, C^*E^* and E^*A^*, the CFL numbers, CFL_2 and CFL_3, are derived in a manner analogous to CFL_1. The most restrictive local CFL condition is then chosen as:

$$CFL = max(CFL_1, CFL_2, CFL_3) \tag{2.24}$$

This selection dictates the location of points P_i. It is crucial to note that the centroid of the triangular region formed by $\triangle P_1P_2P_3$ does not align with the solution point G^*. To reconcile this, a translational adjustment is made such that the centroid of $\Delta P_1P_2P_3$ aligns with G^*:

$$\underline{P_i} = P_i + \left(G^* - \frac{\sum_{i=1}^{3} P_i}{3}\right) \tag{2.25}$$

At the n-th timestep, the conservation variables at the point $\underline{P_i}$ are calculated by:

$$\boldsymbol{U}_{\underline{P_i}}^{n} = \boldsymbol{U}_{N_i^*}^{n-1/2} + \delta x_{\underline{P_i}} \left(\frac{\partial \boldsymbol{U}}{\partial x}\right)_{N_i^*}^{n-1/2} + \delta y_{\underline{P_i}} \left(\frac{\partial \boldsymbol{U}}{\partial y}\right)_{N_i^*}^{n-1/2} + \frac{dt}{2}\left(\frac{\partial \boldsymbol{U}}{\partial t}\right)_{N_i^*}^{n-1/2}, \qquad (2.26)$$

where $\delta x_{\underline{P_i}} = x_{\underline{P_i}} - x_{N_i^*}$ and $\delta y_{\underline{P_i}} = y_{\underline{P_i}} - y_{N_i^*}$ denote the differences in the x and y coordinates between the adjusted point $\underline{P_i}$ and the solution point $y_{N_i^*}$. The spatial derivatives between the solution point G^* and corresponding P_i are computed using a central difference scheme:

$$\left(\frac{\partial \boldsymbol{U}^i}{\partial x}\right)_{G^*}^{n-1/2} = \frac{\Delta_x^i}{\Delta^i}, \qquad \left(\frac{\partial \boldsymbol{U}^i}{\partial y}\right)_{G^*}^{n-1/2} = \frac{\Delta_y^i}{\Delta^i} \qquad (2.27)$$

with determinants defined as:

$$\Delta^1 = \begin{vmatrix} \delta x^1 & \delta y^1 \\ \delta x^2 & \delta y^2 \end{vmatrix}, \Delta^2 = \begin{vmatrix} \delta x^2 & \delta y^2 \\ \delta x^3 & \delta y^3 \end{vmatrix}, \Delta^3 = \begin{vmatrix} \delta x^3 & \delta y^3 \\ \delta x^1 & \delta y^1 \end{vmatrix} \qquad (2.28)$$

and similarly

$$\Delta_x^1 = \begin{vmatrix} \delta \boldsymbol{U}^1 & \delta y^1 \\ \delta \boldsymbol{U}^2 & \delta y^2 \end{vmatrix}, \Delta^2 = \begin{vmatrix} \delta \boldsymbol{U}^2 & \delta y^2 \\ \delta \boldsymbol{U}^3 & \delta y^3 \end{vmatrix}, \Delta^3 = \begin{vmatrix} \delta \boldsymbol{U}^3 & \delta y^3 \\ \delta \boldsymbol{U}^1 & \delta y^1 \end{vmatrix},$$

$$\Delta_y^1 = \begin{vmatrix} \delta \boldsymbol{U}^1 & \delta x^1 \\ \delta \boldsymbol{U}^2 & \delta x^2 \end{vmatrix}, \Delta^2 = \begin{vmatrix} \delta \boldsymbol{U}^2 & \delta x^2 \\ \delta \boldsymbol{U}^3 & \delta x^3 \end{vmatrix}, \Delta^3 = \begin{vmatrix} \delta \boldsymbol{U}^3 & \delta x^3 \\ \delta \boldsymbol{U}^1 & \delta x^1 \end{vmatrix},$$

$$\delta x^i = x_{\underline{P_i}} - x_{G^*}, \delta y^i = y_{\underline{P_i}} - y_{G^*}, \delta \boldsymbol{U}^i = \boldsymbol{U}_{\underline{P_i}} - \boldsymbol{U}_{G^*}, i = 1,2,3.$$

Here, δx^i, δy^i, and $\delta \boldsymbol{U}^i$ represent the differences in the x and y coordinates, and the conservation variable $\boldsymbol{U}$, between the adjusted points $\underline{P_i}$ and the solution point G^*, respectively. The spatial derivatives of the conservation variables are then synthesized by weighting the contributions from each surrounding

element, with $\beta > 0$ serving as a weighting exponent, and $W^1 = \xi_2\xi_3, W^2 = \xi_1\xi_3$ and $W^3 = \xi_1\xi_2$ as the weighting factors derived from the gradients.

$$\left(\frac{\partial \boldsymbol{U}}{\partial x}\right)^n_{G^*} = \frac{\sum_{i=1}^{3} \left(W^i\right)^\beta \left(\frac{\partial \boldsymbol{U}^i}{\partial x}\right)^n_{G^*}}{\sum_{i=1}^{3} \left(W^i\right)^\beta} \tag{2.29}$$

$$\left(\frac{\partial \boldsymbol{U}}{\partial y}\right)^n_{G^*} = \frac{\sum_{i=1}^{3} \left(W^i\right)^\beta \left(\frac{\partial \boldsymbol{U}^i}{\partial y}\right)^n_{G^*}}{\sum_{i=1}^{3} \left(W^i\right)^\beta}. \tag{2.30}$$

$$\xi_i = \sqrt{\left(\left(\frac{\partial \boldsymbol{U}^i}{\partial x}\right)^n_{G^*}\right)^2 + \left(\left(\frac{\partial \boldsymbol{U}^i}{\partial y}\right)^n_{G^*}\right)^2}, i = 1,2,3$$

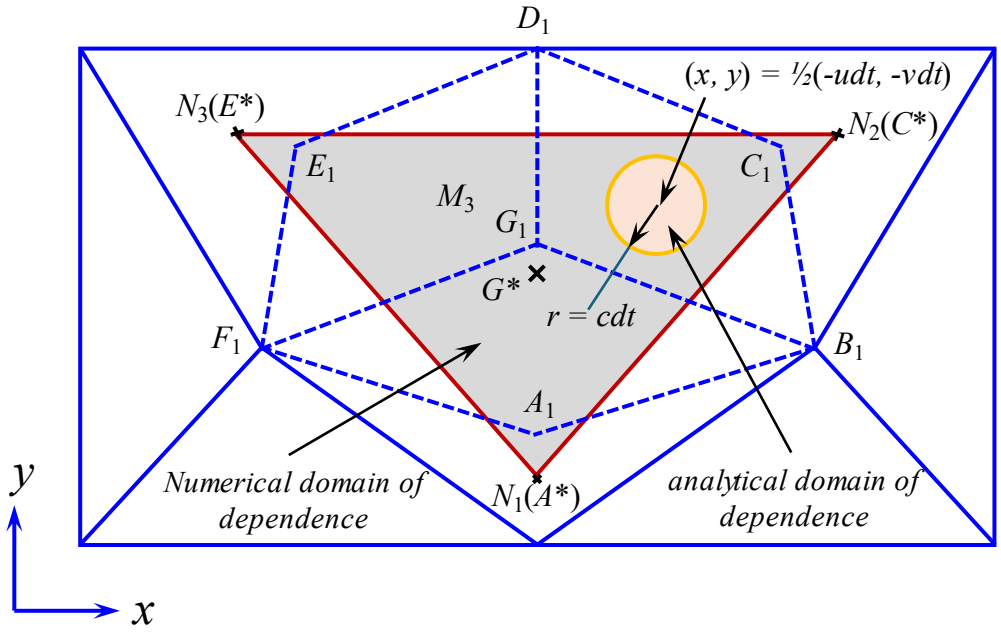

Figure 2.6 Schematic of analytical domain of dependence and analytical domain of dependence.

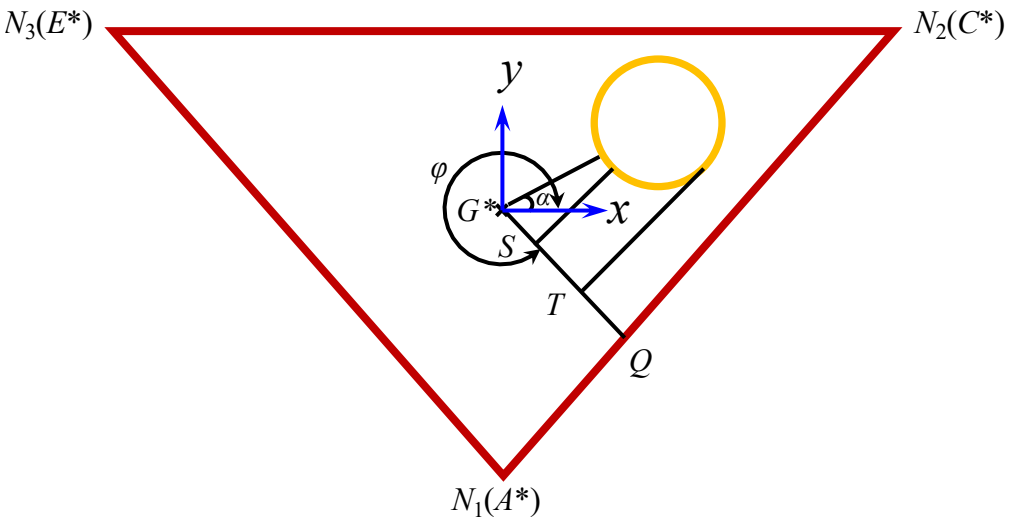

Figure 2.7 Illustration of stability criterion.

2.1.4 Formulation of Boundary Conditions

In the context of Direct Aeroacoustic Simulation (DAS), the careful selection and implementation of boundary conditions are of paramount importance due to the finite dimensions of the computational domain. Inadequate domain scaling or the application of inconsistent boundary conditions can introduce substantial errors into the numerical analysis. Therefore, the establishment of boundary conditions necessitates meticulous consideration and a deep comprehension of the underlying physical phenomena.

Within the CE/SE methodology, boundary conditions are enforced using the ghost cell strategy. This approach consists of extending the computational mesh beyond the domain boundaries by creating ghost elements, which are essentially reflections of the boundary elements. The solutions on these ghost elements are then judiciously prescribed based on the type of boundary condition being implemented. The boundary elements of the conservation element (CE) and solution element (SE) are constructed using the geometric

data from these ghost cells. Depending on the nature of the boundary conditions, appropriate solution values are designated to the solution points of the ghost cells, thereby allowing for the accurate computation of flux at each timestep.

The non-reflecting boundary condition (NRBC) is of particular significance in DAS, as it is designed to minimize the impact of the boundary on the computational domain. Any numerical reflections originating from the boundary have the potential to adversely affect the flow field and, especially the acoustics associated with the cavity flow. In the CE/SE framework, the NRBC facilitates the seamless exit of the flux from the interior of the physical domain (Loh 2003). Two prevalent variations of NRBC are utilized in CE/SE. Type I NRBC specifies that the solution and spatial gradients in the ghost cell are directly inherited from the boundary cell:

$$\boldsymbol{U}_G = \boldsymbol{U}_B, \left(\frac{\partial \boldsymbol{U}}{\partial x}\right)_G = \left(\frac{\partial \boldsymbol{U}}{\partial x}\right)_B, \left(\frac{\partial \boldsymbol{U}}{\partial y}\right)_G = \left(\frac{\partial \boldsymbol{U}}{\partial y}\right)_B . \tag{2.31}$$

Here, the subscripts G and B denote the ghost and boundary cells, respectively. Type I NRBC is commonly employed in supersonic flow scenarios (Loh and Hultgren 2006) because the flow velocity greatly exceeds the speed of sound, ensuring that the flow properties of the ghost cell, as dictated by the boundary cell, do not engender any spurious reflections. Type II NRBC, on the other hand, sets the solution and spatial gradients in the ghost cell based on the free-stream conditions and the values from the boundary cell:

$$\rho_G = \rho_\infty, u_G = u_B, v_G = v_B, p_G = p_\infty \tag{2.32}$$

$$\left(\frac{\partial \boldsymbol{U}}{\partial x}\right)_G = \left(\frac{\partial \boldsymbol{U}}{\partial x}\right)_B, \left(\frac{\partial \boldsymbol{U}}{\partial y}\right)_G = \left(\frac{\partial \boldsymbol{U}}{\partial y}\right)_B \tag{2.33}$$

For the no-slip boundary condition at an isothermal wall, which is a fundamental condition in CE/SE simulations, the variables at the ghost cell are set as follows:

$$\rho_G = \rho_B, u_G = 0, v_G = o, p_G = p_B \tag{2.34}$$

These stipulations ensure that the tangential velocities are nullified at the wall, corresponding to the physical reality of a viscous fluid adhering to a solid boundary.

2.2 Structural solver

The present study utilizes flow-induced elastic panel vibration as a means to suppress the deep cavity aeroacoustics. Hence, the panel dynamics are modeled by the one-dimensional plate equation (Dowell 1974) , normalized by the flow reference variables in Section 2.1, as,

$$D_{EP}\frac{\partial^4 w}{\partial x^4} - (T_{EP} + N_x)\frac{\partial^2 w}{\partial x^2} + \rho_{EP}h_{EP}\frac{\partial^2 w}{\partial t^2} + C\frac{\partial w}{\partial t} + K_{EP}w = p_{ex} \tag{2.35}$$

where p_{ex} represents the net pressure across the panel of length $L_{EP} = \hat{L}_{EP}/\hat{L}$ with material density $\rho_{EP} = \hat{\rho}_{EP}/\hat{\rho}_0$ and having the thickness $h_{EP} = \hat{h}_{EP}/\hat{L}$, $D_{EP} = \widehat{D}_{EP}/\left(\hat{\rho}_0\hat{u}_0^2\hat{L}^3\right)$ represents the bending stiffness, $N_x = (E_{EP}h_{EP}/2L_{EP})\int_0^{L_{EP}} (\partial w/\partial x)^2 dx$ is the tangential internal stress due to tensile loading, $T_{EP} = \hat{T}_{EP}/\left(\hat{\rho}_0\hat{u}_0^2\hat{L}\right)$ is the resultant tensile stress per unit length in the x-direction, $E_{EP} = \hat{E}_{EP}/(\hat{\rho}_0\hat{u}_0^2)$ is the elastic modulus, $C_{EP} = \hat{C}_{EP}/(\hat{\rho}_0\hat{u}_0)$ is the panel structural damping coefficient, and $K_{EP} = \widehat{K}_{EP}\hat{L}/(\hat{\rho}_0\hat{u}_0)$ is the stiffness of the panel foundation. Flexible panels can be categorized based on their thickness-to-length ratio (h_p/L_p) into four distinct types: membranes ($h_p/L_p <$ 1/50), stiff plates (1/50 < h_p/L_p< 1/10, where "plate" typically refers to a stiff

plate in engineering contexts), moderately thick plates ($1/10 < h_p/L_p < 1/5$), and thick plates ($h_p/L_p > 1/5$). For moderately thick and thick plates ($h_p/L_p > 1/10$), a comprehensive three-dimensional stress analysis is essential to achieve accurate results, and thus, these are excluded from the current study. In the case of stiff plates with $h_p/L_p \leq 1/50$, the bending stiffness primarily governs the restoring force, rendering tensile forces negligible, i.e., $(T_x + N_x) = 0$. Conversely, for membranes, tensile forces predominate, and flexural resistance is insignificant, with $D_{EP} = 0$. Additionally, in-plane shear stress can be disregarded as lateral motion at any point on the membrane is minimal when deflections are small relative to thickness ($w/h_p \leq 0.2$). Under these conditions, panel motion can be considered linear, allowing the omission of nonlinearity terms, with $N_x = 0$, and the tensile force on the middle surface remains constant, aligning with the small-deflection theory. However, when $w/h_p \geq 0.2$, panel motion becomes nonlinear, necessitating the application of large-deflection theory. In such scenarios, nonlinear tensile forces become dominant, particularly when $w/h_p \geq 1$ (Dowell 1975, Szilard 2004).We have considered a very thin elastic panel which mimics a membrane, therefore, bending stiffness D_{EP} panel internal tension N_{EP} and are taken as effectively zero (Arif *et al.* 2022; Naseer *et al.* 2023b).

The dynamical behaviour of the panel is resolved using a standard finite difference scheme, which discretizes the panel into a uniform grid with spatial increment Δx. The spatial derivatives of the panel displacement w are calculated employing a second-order central difference method (Hayek 2010):

$$\frac{\partial w^{n,j}}{\partial x} = w_x^{n,j} = \frac{1}{2\Delta x}\left(w^{n+1,j} - w^{n-1,j}\right), \tag{2.36}$$

$$\frac{\partial^2 w^{n,j}}{\partial x^2} = w_{xx}^{n,j} = \frac{1}{\Delta x^2}\left(w^{n+1,j} - 2w^{n,j} + w^{n-1,j}\right), \tag{2.37}$$

$$\frac{\partial^4 w^{n,j}}{\partial x^4} = w_{xxxx}^{n,j} = \frac{1}{\Delta x^4}\left(w^{n+2,j} - 4w^{n+1,j} + 6w^{n,j} - 4w^{n-1,j} + w^{n+2,j}\right), \tag{2.38}$$

where subscript j indicates the j -th timestep and n denotes the n-th grid point. Temporal derivatives are computed as:

$$\frac{\partial w^{n,j}}{\partial t} = \dot{w}^{n,j} = \frac{1}{2\Delta t}\left(w^{n,j+1} - w^{n,j-1}\right), \tag{2.39}$$

$$\frac{\partial^2 w^{n,j}}{\partial t^2} = \ddot{w}^{n,j} = \frac{1}{\Delta t^2}\left(w^{n,j+1} - 2w^{n,j} + w^{n,j-1}\right), \tag{2.40}$$

Incorporating these discrete approximations into Equation 2.35, the displacement w for the subsequent timestep is determined by:

$$w^{n,j+1} = \frac{4\rho_p h_p w^{n,j} + \left(-2\rho_p h_p + C\Delta t\right)w^{n,j-1} + 2\Delta t^2 B}{2\rho_p h_p + C\Delta t}. \tag{2.41}$$

Here, B encompasses the external pressure and the contributions from tension and bending terms, expressed as $B = p_{ex} + (T_x + N_x)w_{xx}^{n,j} - Dw_{xxxx}^{n,j} - K_p w^{n,j}$. Subsequently, the state of all panel elements $\boldsymbol{W} = [w, \dot{w}, \ddot{w}]^T$ is updated at each timestep.

2.2.1 Boundary Conditions

For the interface between the fluid domain and the oscillating panel, the tangential flow condition is met by aligning the flow velocity component in the y-direction with the panel dynamic behaviour:

$$v = \dot{w} + u\frac{\partial w}{\partial x} \tag{2.42}$$

The condition for the normal pressure gradient, ensuring the continuity of velocity and momentum across the fluid-structure boundary, is expressed as:

$$\frac{\partial p}{\partial y} = \rho \frac{\partial v}{\partial t} + \rho u \frac{\partial v}{\partial x} \tag{2.43}$$

In this investigation, which primarily considers the influence of fluid inertia, convective terms are neglected. Consequently, the tangency and normal pressure gradient conditions simplify to:

$$v - \dot{w} = 0, \tag{2.44}$$

$$\frac{\partial p}{\partial y} = \rho \ddot{w}. \tag{2.45}$$

The net pressure acting upon the vibrating panel is derived from the differential pressure across its surfaces:

$$p_{\text{ex}} = p_{\text{panel},b} - p_{\text{panel},a} \tag{2.46}$$

Here, $p_{\text{panel},a} = p_a + \rho_a \ddot{w}^n(\delta_a - w^n)$ and $p_{\text{panel},b} = p_b - \rho_b \ddot{w}^n(\delta_b + w^n)$, where δ represents the offset from the panel surface in the undeformed state as indicated in Figure 2.8. At each time step, the fluid domain deformation is evaluated based on the panel displacement. Typically, the fluid domain mesh is updated to avoid any strained elements that might lead to under resolved solutions (So *et al.* 2003). However, this remeshing process is computationally intensive as it requires updating all mesh points within the domain. Leveraging the unique feature of the CE/SE method where flow solutions are calculated at discrete solution points (Lam 2012) and considering small panel displacements, the deformation of the fluid domain can be accounted for using a more straightforward methodology inspired by the immersed boundary method (Vitturi *et al.* 2007).

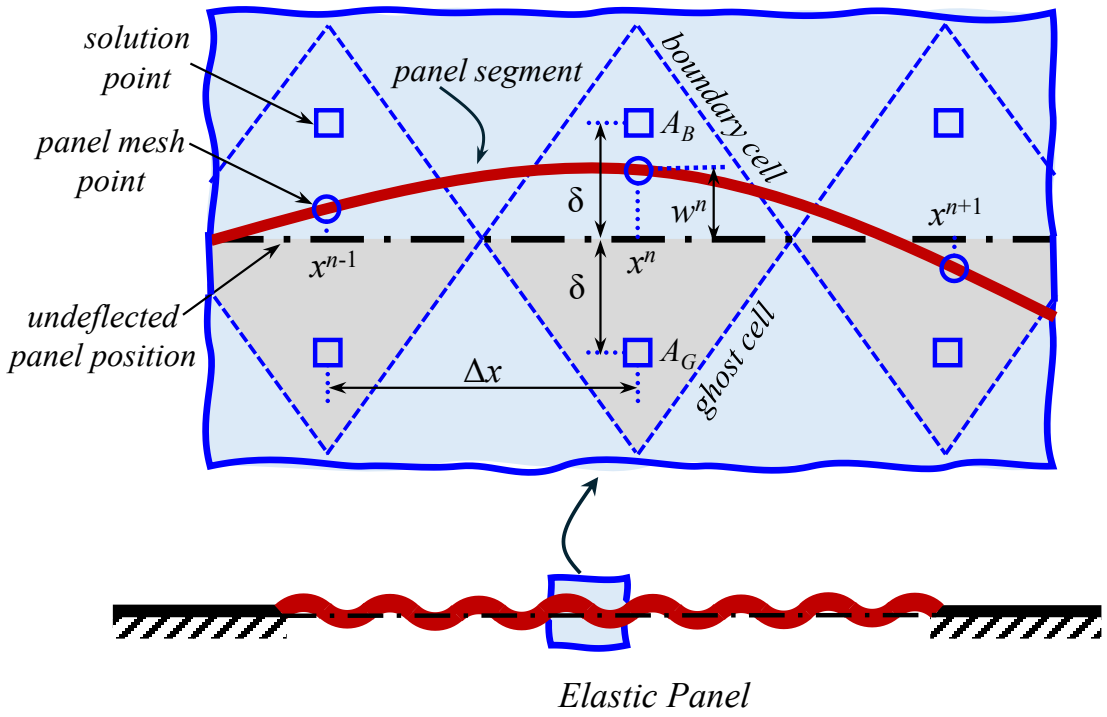

Figure 2.8 Schematic of mesh at fluid-panel interface.

In the CE/SE approach, solution points do not coincide precisely with the actual physical boundary of the fluid domain. Instead, the boundary conditions are effectively imposed by introducing a mirror ghost cell behind the boundary, such as A_G in Figure 2.8. Flow variables are then prescribed at the ghost cell to implicitly satisfy the desired conditions at the actual panel location through interpolation between the boundary and ghost cells. For rigid boundaries, the ghost cell is assigned a normal velocity $v_G = -v_B$ and a corresponding normal gradient $v_{x,G} = -v_{x,B}$ to uphold the no-penetration condition. The tangential velocity at the ghost cell is set to match the boundary cell, $u_G = U_B$, with an opposing gradient $u_{y,G} = -u_{y,B}$. Given that the panel displacement is minor compared to the offset δ of the solution point A_B, the normal velocity v_G can be approximated as:

$$\frac{v_G - \dot{w}^n}{\delta + w^n} = \frac{\dot{w}^n - v_B}{\delta - w^n} \tag{2.47}$$

The derivatives of v_G and $p_G$in the normal direction are congruent with those at the fluid-panel interface:

$$p_{y,G} = -\rho_B \ddot{w}^n \tag{2.48}$$

Using a first-order finite difference approximation, these quantities are expressed as:

$$p_G = p_B - 2\delta p_{y,G} \; and \; v_{y,G} = \frac{v_B - v_G}{2\delta} \tag{2.49}$$

For an isothermal panel, all flow variables at the ghost cell are determined by:

$$u_G = u_B, u_{x,G} = u_{x,B}, u_{y,G} = -u_{y,B} \tag{2.50}$$

$$v_G = \dot{w}^n + \frac{\delta + w^n}{\delta - w^n}(\dot{w}^n - v_B), v_{x,G} = v_{x,B}, v_{y,G} = \frac{v_B - v_G}{2\delta} \tag{2.51}$$

$$p_G = p_B - 2\delta\rho_B \ddot{w}^n, p_{x,G} = p_{x,B}, p_{y,G} = \rho_B \ddot{w}^2 \tag{2.52}$$

In the integrated fluid-structure system, the mesh for the fluid domain aligns with that of the panel, and each solution point on the panel is situated next to a corresponding point within the fluid domain, as indicated in Figure 2.8. To achieve a second-order central difference approximation for the fourth-order spatial derivative, a quartet of adjacent points around each solution point is required. However, at the borders specifically at the first and last points, denoted as $n = 1$ and n' (where n' is the total count of panel solution points) this condition is not naturally met. To address this, supplemental ghost points are instituted at both ends of the panel, labelled as $n = -1$ and $n = n' + 2$, along with two boundary nodes at $n = 0$ and $n = n' + 1$. Edge constraints, such as pinned or clamped conditions, are then applied. Under the pinned-pinned boundary scenario, both the displacement and the bending moment are nullified at the boundary nodes. This is mathematically represented as:

$$w^{0,j} = w^{n'+1,j} = w_{xx}^{0,j} = w_{xx}^{n'+1,j} = 0. \tag{2.53}$$

Consequently, the ghost points are defined symmetrically relative to the nearest interior points:

$$w^{-1,j} = -w^{1,j}, w^{n'+2,j} = -w^{n',j}. \tag{2.54}$$

For the clamped-clamped boundary condition, the displacement and its first spatial derivative are set to zero at the boundary nodes:

$$w^{0,j} = w^{n'+1,j} = w_{x}^{0,j} = w_{x}^{n'+1,j} = 0. \tag{2.55}$$

This leads to a reflection of the interior points at the ghost points:

$$w^{-1,j} = w^{1,j}, w^{n'+2,j} = w^{n',j}. \tag{2.56}$$

The second-order spatial derivatives at the panel edges, using Taylor series expansion, are expressed as:

$$w_{xx}^{1,j} = \frac{1}{\Delta x^2}\left(-4w^{1,j} + \frac{4}{3}w^{2,j}\right), w_{xx}^{n',j} = \frac{1}{\Delta x^2}\left(-4w^{n',j} + \frac{4}{3}w^{n'-1,j}\right), \tag{2.57}$$

The fourth-order spatial derivatives are similarly calculated as:

$$\begin{aligned} w_{xxxx}^{1,j} &= \frac{1}{\Delta x^4}\left(C'w^{1,j} - 8w^{2,j} + \frac{8}{5}w^{3,j}\right), \\ w_{xxxx}^{2,j} &= \frac{1}{\Delta x^4}\left(-8w^{1,j} + 8w^{2,j} + \frac{24}{5}w^{3,j} + \frac{8}{7}w^{4,j}\right), \\ w_{xxxx}^{n',j} &= \frac{1}{\Delta x^4}\left(C'w^{n',j} - 8w^{n'-1,j} + \frac{8}{5}w^{n'-2,j}\right), \\ w_{xxxx}^{n'-1,j} &= \frac{1}{\Delta x^4}\left(-8w^{n',j} + 8w^{n'-1,j} - \frac{24}{5}w^{n'-2,j} + \frac{8}{7}w^{n'-3,j}\right). \end{aligned} \tag{2.58}$$

Here, the coefficient C' equals 16 for the pinned-pinned boundary condition and 32 for the clamped-clamped condition, reflecting the increased stiffness at the clamped edges.

2.2.2Integration of Aeroacoustic Solution and Structural Dynamics

The intricate interaction between aerodynamic fluctuations and structural dynamics of the panel is achieved using a monolithic scheme, as formulated by (Fan *et al.* 2018). This holistic strategy involves the inclusion of all physical domains within the reformulated governing equations, followed by a simultaneous discretization that solves the domains in unison. This approach treats the fluid-structure system as an indivisible unit and incorporates the influence of panel dynamics into an additional source term within the CE/SE numerical framework. This system is then iteratively solved using a Newton method, which offers a more rapid convergence compared to traditional partitioned strategies. The inherent stability of monolithic coupling scheme guarantees accurate time-resolved solutions (Greenshields and Weller 2005), and its efficacy has been confirmed through its application to fluid-structural interactions within Newtonian incompressible fluids. The scheme reliability has undergone rigorous validation against benchmark problems in aeroacoustic-structural interaction, proving its capability to resolve couplings of varied complexities with precision (Fan *et al.* 2015; Fan *et al.* 2018). Only a concise exposition of its mathematical underpinnings is offered in this section.

Consider the stresses imparted on two small control volumes of fluid, one situated above and the other below an elastic panel segment as illustrated in Figure 2.9. The initial height of each control volume in its undeflected state is denoted by δ, while $l(t)$ signifies the control volume height as modulated by panel vibrations over time. The notations a and b tag the variables above and below the panel, correspondingly. The stress σ emanating from the fluid-panel

interface is factored into the fluid momentum equation in the normal direction. These influences are encapsulated as a source term $\boldsymbol{Q}$ on the right side of Equation 2.1:

$$\frac{\partial \boldsymbol{U}}{\partial t} + \frac{\partial(\boldsymbol{F} - \boldsymbol{F}_v)}{\partial x} + \frac{\partial(\boldsymbol{G} - \boldsymbol{G}_v)}{\partial y} = \boldsymbol{Q}, \tag{2.59}$$

Where $Q1 = 0$, $Q2 = 0$, $Q3 = -\frac{\partial p}{\partial y}$, $Q4 = -v\frac{\partial p}{\partial y}$ at the fluid-structure interface and zero elsewhere. All elements of $\boldsymbol{Q}$ are intricately linked to the panel dynamic behaviour.

The net external force exerted on the panel is given by:

$$p_{ex} = \sigma_{panel,b} - \sigma_{panel,a} = \left(p_{panel,b} - \frac{M}{Re}\tau_{yy,b}\right) - \left(p_{panel,a} - \frac{M}{Re}\tau_{yy,a}\right) \tag{2.60}$$

Thus, the equation governing panel dynamics (Equation 2.35) can be reformulated to incorporate the external forces as a function of the source term $\boldsymbol{Q}$.

$$S_{EP}\frac{\partial^4 w}{\partial x^4} - (T_{EP} + N_{EP})\frac{\partial^2 w}{\partial x^2} + \rho_{EP}h_{EP}\frac{\partial^2 w}{\partial t^2} + C_{EP}\frac{\partial w}{\partial t} + K_{EP}w =$$

$$\left(p_{panel,b} - \frac{M}{Re}\tau_{yy,b}\right) - \left(p_{panel,a} - \frac{M}{Re}\tau_{yy,a}\right). \tag{2.61}$$

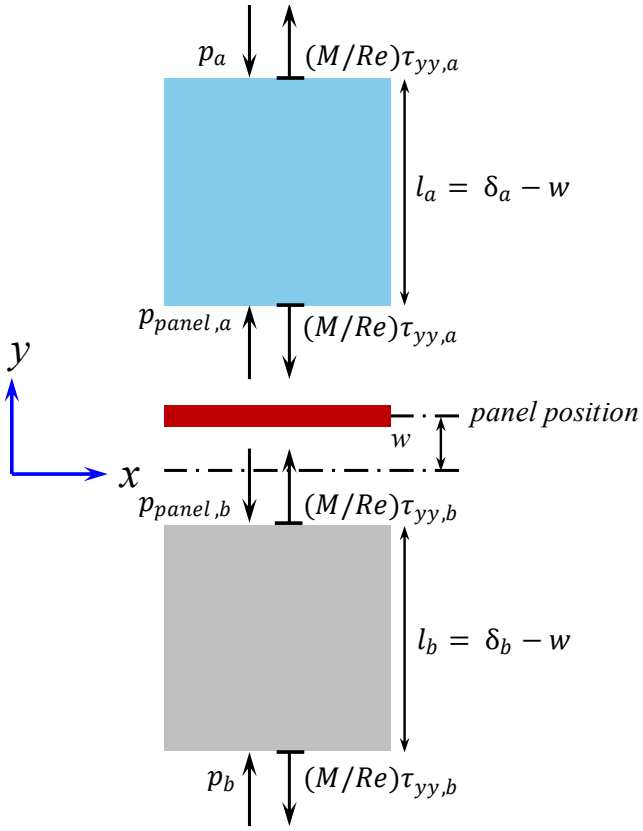

Figure 2.9 Forces balance on control volume.

The source term $\boldsymbol{Q}$ in Equation 2.59 depends on the solution vector $\boldsymbol{U}$, which means it cannot be directly resolved. Therefore, Newton iterative method is employed to determine $\boldsymbol{U}$ (Loh 2005). The term $\partial \boldsymbol{U}/\partial t$ in Equation 2.59 is denoted as:

$$\frac{\partial \boldsymbol{U}}{\partial t} = \boldsymbol{Q} - \boldsymbol{H}', \tag{2.62}$$

where $\boldsymbol{H}'$ represents the spatial flux divergence terms.

$$\boldsymbol{H}' = \frac{\partial(\boldsymbol{F} - \boldsymbol{F}_v)}{\partial x} + \frac{\partial(\boldsymbol{G} - \boldsymbol{G}_v)}{\partial y}.$$

For time-stepping at the j-th timestep, the solution vector is obtained by approximating $\partial \boldsymbol{U}/\partial t = \Delta \boldsymbol{U}/\Delta t$:

$$\frac{\partial \boldsymbol{U}}{\partial t} = \boldsymbol{Q} - \boldsymbol{H}' \tag{2.63}$$

The local homogeneous solution $\boldsymbol{U}_H$ when $\boldsymbol{Q} = 0$ is utilized to negate $\boldsymbol{H}'$. Consequently, Equation 2.63 is expressed as:

$$\boldsymbol{U}_j - \Delta t \boldsymbol{Q}(\boldsymbol{U}_j) - \boldsymbol{U}_{j,H} = \boldsymbol{\Phi}(\boldsymbol{U}_j) = 0 \tag{2.64}$$

The solution $\boldsymbol{U}_j$ of this implicit equation is resolved via Newton method as depicted in Figure 2.10 by iterating the following update:

$$\boldsymbol{U}_{j,k+1} = \boldsymbol{U}_{j,k} - \left(\frac{\partial \boldsymbol{\Phi}}{\partial \boldsymbol{U}}\right)^{-1} \boldsymbol{\Phi}(\boldsymbol{U}_{j,k}) \tag{2.65}$$

In this context, k represents the iteration index, and $\partial \boldsymbol{\Phi} / \partial \boldsymbol{U}$ is the Jacobian matrix, which is defined as:

$$\frac{\partial \boldsymbol{\Phi}}{\partial \boldsymbol{U}} = \boldsymbol{I} - \left[\Delta t \left(\boldsymbol{Q} + \frac{\partial \boldsymbol{Q}}{\partial \boldsymbol{U}}\right) + \boldsymbol{U}_{j,H} - \boldsymbol{U}_{j-1}\right] \tag{2.66}$$

At each time step j, the homogeneous solution $\boldsymbol{U}_{j,H}$ is computed using the aeroacoustic model and subsequently integrated into Equation 2.65 to initiate the iteration process. The iteration continues until the relative error between two successive iterations falls below the convergence threshold of 10^{-10}. This stringent criterion ensures the accuracy and stability of the numerical solution across each time step. To accurately compute $\boldsymbol{Q}$ and $\frac{\partial \boldsymbol{Q}}{\partial \boldsymbol{U}}$ as specified in Equation 2.66, it is essential to ascertain both the pressure above and below the panel, as well as the associated pressure gradients. These quantities are derived from the dynamics of the panel and are articulated in terms of the variable $\boldsymbol{U}$. This formulation is elaborately detailed in the work of Fan (2018), providing a comprehensive methodological framework for integrating these elements into the overall model.

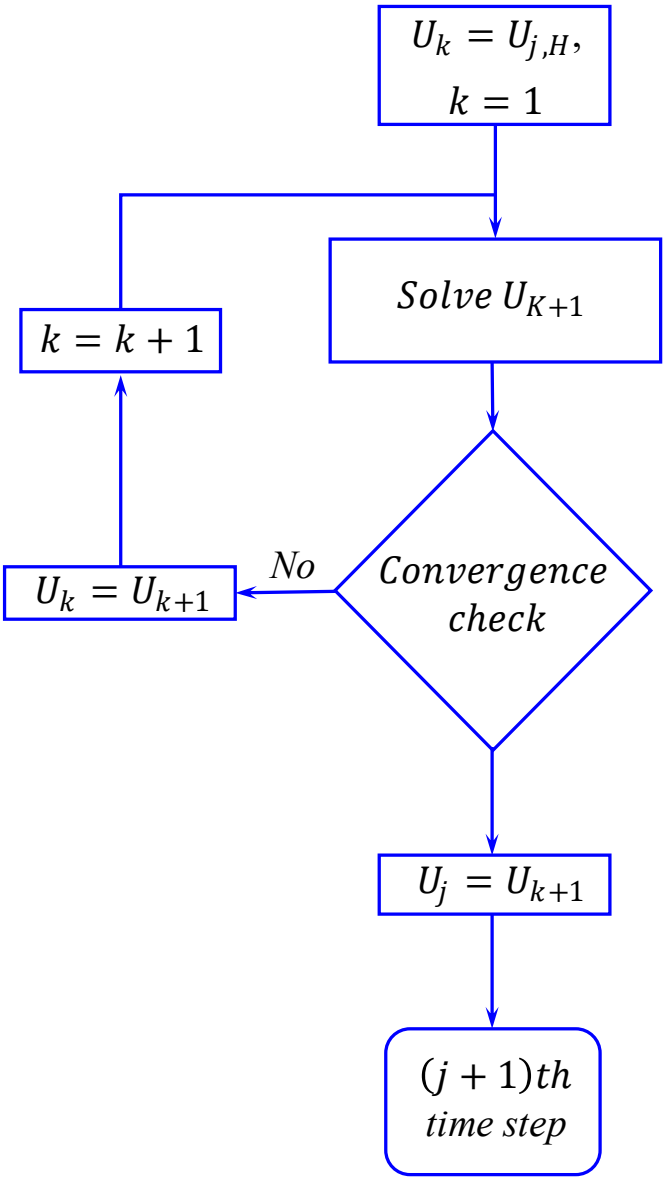

Figure 2.10 Newton's method iterative procedure.

2.3 Numerical Setup for Deep Cavity Open Flow

For the present study, a deep cavity is considered for its popularity in various fluid mechanical systems and susceptibility to flow-induced noise generation over a wide range of system operational conditions (Rockwell and Naudascher 1978; Ziada *et al.* 2002). That has attracted many experimental studies in cavity noise generation since then. The experiments carried out by . Yokohama *et al.* (2016, 2017 and 2020), with a cavity of length-to-depth ratio L/D = 0.4 in open flow with freestream velocities ranging from 15 to 45 ms^{-1}, have vindicated the aforesaid problem. As shown in Figure 2.12, an exceptionally high noise response was observed within a limited range of inflow velocity (25 $ms^{-1} \leq u_{\infty} \leq$ 35 ms^{-1}) in contrast to the lower sound pressure level (*SPL*) at 15 ms^{-1} and 45 ms^{-1}. As such, we take the parameters of these experiments as a reference for the present numerical study. A deep cavity with L/D = 0.4 exposed to u_{∞} = 30 ms^{-1} is considered for its highest acoustic radiation in the experiments.

It is noteworthy to mention that the development of flow past open cavity is three-dimensional in nature. However, the influence of the flow three-dimensionality to the overall sustained fluid-resonant oscillation depends on the flow Mach number and the cavity configuration. Yokohama *et al.* (2016 and 2017) carried out extensive measurements of the developing flow, at same low Mach number as in present study, past a three-dimensional deep cavity of same sectional length-to-depth ratio as the present study and spanwise length equal to 7.5 times cavity length. Their measurements of spanwise fluctuating velocities at different streamwise locations along the cavity shear layer exhibit high degree of spatial coherency covering more than 80% of the center part of

cavity spanwise length. Same level of spatial coherency was also observed in the cavity noise radiation. On the other hand, in an extensive three-dimensional calculation of a flow, at a Mach number twice the one in the present study, past another deep cavity of similar sectional length-to-depth ratio but a shorter spanwise length equal to cavity length (Ho & Kim 2021), the results show similar high degree of spatial coherency in velocity fluctuations along cavity spanwise direction and its noise radiation. Sun *et al.* (2017) carried out extensive calculations of shallow cavities at various subsonic Mach numbers higher than that in the present study. Their results show that the shear evolution pattern (which they referred as Rossiter mode) is strongly coherent along the spanwise direction and find it as dominant mode across different cavity configurations. In view of all these observations, it is decided to carry out two dimensional calculations for the present study for the sake of saving computational resources.

The schematic sketch of the physical problem is illustrated in Figure 2.11, where the cavity leading edge is placed at the origin. A uniform flow of M = 0.09 and $Re = 4 \times 10^4$ based on cavity length is allowed to enter the computational domain from the left. Combined sliding and no-slip boundary conditions are prescribed on the solid wall upstream of the cavity. A laminar boundary layer is allowed to emerge from the change-over location at x = -4.1 and grow naturally to give momentum thickness θ/L = 0.0071 at the cavity leading edge. A buffer zone stretching from physical to computational domain boundaries is applied around the physical domain to suppress any contamination due to erroneous numerical acoustic reflection. Non-reflective boundary condition proposed by Lam *et al.* (2014a) is specified at the outflow (x = 52) and transverse (y = 51)

domain boundaries. The cavity and its upstream and downstream walls ($-4.1 \leq x \leq 52$) are made rigid with no-slip boundary conditions, while the domain length, running from the inlet to the point of boundary layer formation ($-17.5 \leq x \leq -4.1$), adopts the sliding wall boundary condition.

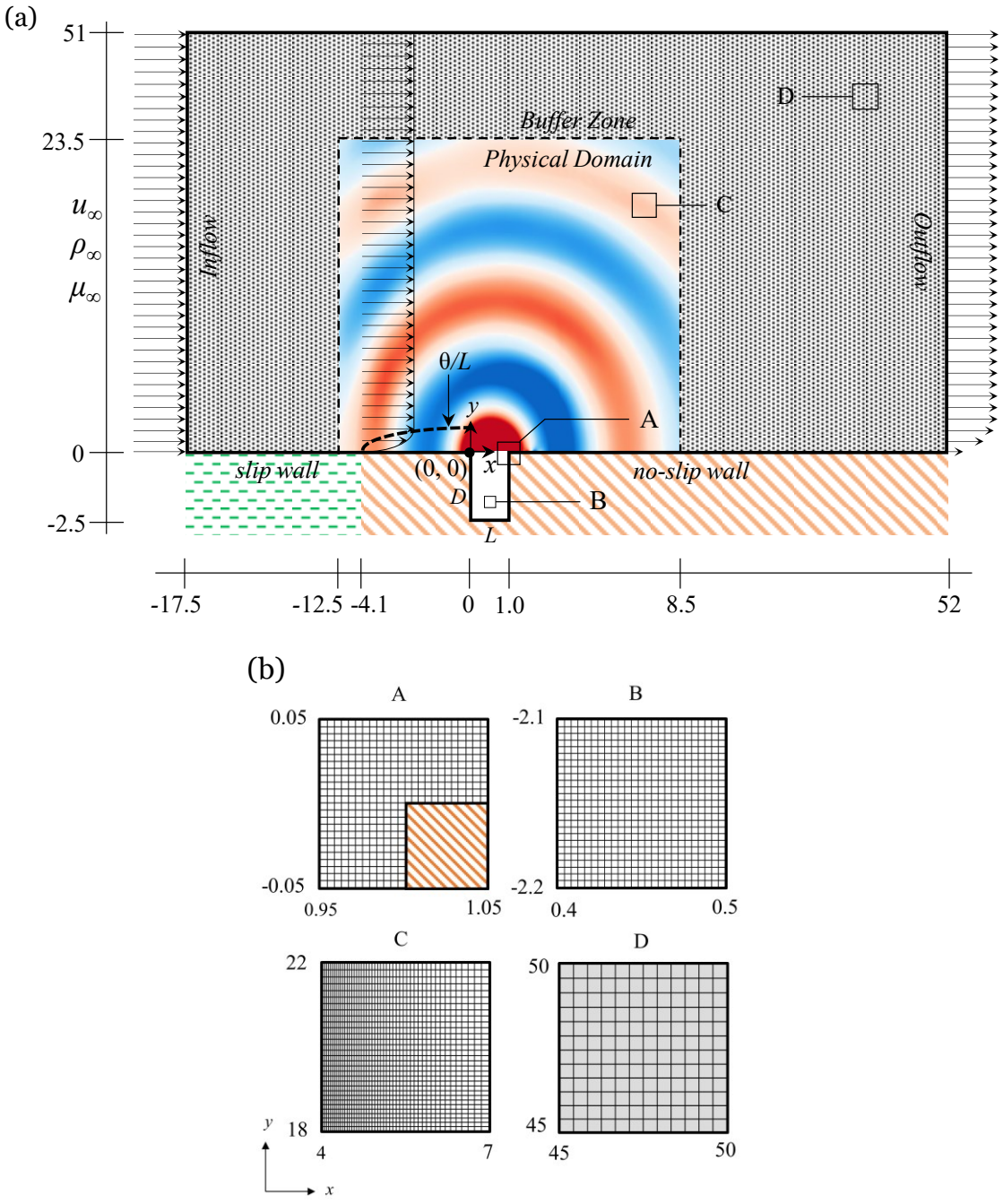

Figure 2.11 (a) Schematic sketch of the physical problem (not to scale). (b) Zoomed views of selected regions A, B, C and D within grid *G*2 are given on the right.

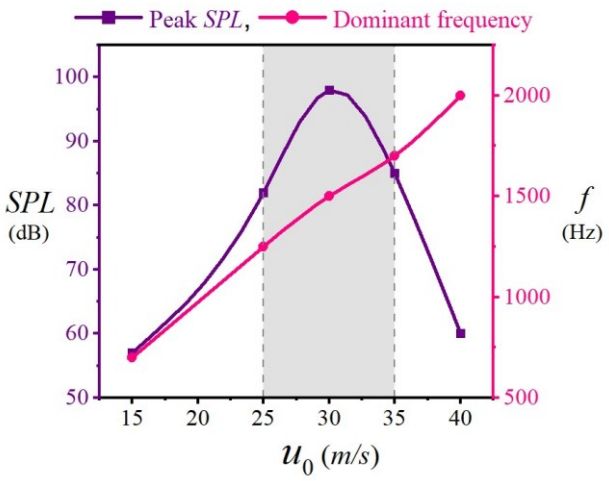

Figure 2.12 Experimental acoustic response of deep cavity flow from Yokoyama *et al.* (2016b, 2017, 2020).

2.3.1 Validation of Rigid Cavity Baseline Result

A structured grid is generated using quadrilateral mesh elements. In the application of the CE/SE scheme, a mesh element diagonally splits into four triangular elements, which makes the actual number of mesh elements four times the original size. The mesh size around the critical locations of the cavity, including leading and trailing edges (A in Figure 2.11) and the cavity inside (B), are refined with special considerations for sufficiently resolving the boundary layer evolution and subsequent acoustic propagation. A grid convergence study has been carried out using three different computational grids, namely *G*1, *G*2 and *G*3, to evaluate the influence of mesh resolution in capturing the accurate flow dynamics and acoustics. Table I provides information on the mesh sizes for each grid. Grid *G*2 is generated by the refinement of *G*1, whereas the subsequent refinement of *G*2 generates Grid *G*3, and the level of refinement of each preceding mesh is equal to ~ 0.5, specifically at the critical locations around the cavity. Hence the total number of mesh elements delivered by *G*1, *G*2 and *G*3 are 1.48, 2.74 and 4.97 million, respectively.

Figure 2.13 illustrates the time history and spectra of the pressure fluctuation $p'(x,y,t) = p(x,y,t) - \bar{p}(x,y)$, where $\bar{p}(x,y)$ is the time-averaged pressure, captured at the cavity bottom (x, y) = (0.5, -2.5), at cavity opening (0.5, 0) and a location far away from the cavity (6.75, 21.5), for $G1$, $G2$ and $G3$. The selection of these locations is made in such a way that allows analyzing the overall mesh resolution effects encompassing the highly unsteady regions in the shear layer and cavity bottom as well as the far field location where the acoustic radiation is anticipated. Evidently, p' is fairly periodic irrespective of the mesh resolution and the location of capture except for the difference in its magnitude $|p'|$. The numerical solutions of $G2$ and $G3$ stay close to each other with only a 12.1% difference, and the results appear greatly converged for these two grid configurations. However, the $G1$ exhibits a significant difference in $|p'|$ by 14.6% with reference to the $G3$. On the other hand, the acoustic pressure spectra are dominated by only one frequency f_1 = 0.925 in all three grid configurations, which stipulates that the main flow and acoustic features might are captured even with the coarser mesh, although the magnitude of p' is compromised. Therefore, grid $G2$, with a total number of mesh elements of 2.74 million, is chosen in the present study for its best compromise between the accuracy and the saving of available computational resources, as the further mesh refinement beyond $G2$ gives no discernible impact on the quality of the results.

In the present study, every calculation is sufficiently advanced until a time-stationary solution is reached. Afterward, the time-marching of the solution is continued for a time episode equivalent to the 80 flow convective cycles for eventual flow dynamic and acoustic analyses. All the calculations are carried out in a parallel computing facility with 494 CPU cores for

approximately 48000 CPU hours for each case. To analyze the aeroacoustic characteristics, 2000 virtual probes are placed along the cavity walls at a separation of ~ 0.01 from each other. Furthermore, a total of 5400 circumferential virtual probes are placed around the cavity at radii r = 10 for the analysis of the cavity acoustic radiation.

Table 2.1 Mesh parameters (minimum mesh size/maximum mesh size).

Mesh	Physical domain					Buffer zone
no. of elements	$x < -4$	$-4 \le x \le 5$	$x > 5$	$-2.5 \le y \le 0.5$	$y > 0.5$	Along x, y
$G1$ (Coarse) 1.48×10^6	0.012/0.12	0.006/0.012	0.012/0.15	0.006/0.006	0.006/0.12	0.006/1.5
$G2$ (Medium) 2.74×10^6	0.008/0.08	0.004/0.008	0.008/0.1	0.004/0.004	0.004/0.08	0.004/1.02
$G3$ (Fine) 4.97×10^6	0.004/0.04	0.002/0.004	0.004/0.75	0.002/0.002	0.002/0.04	0.002/0.75

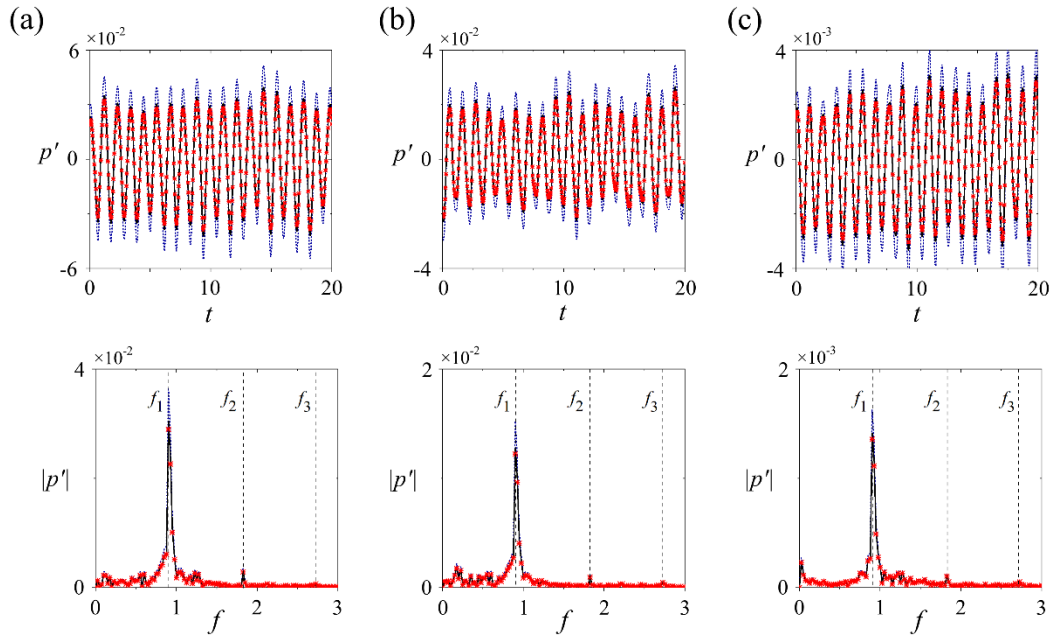

Figure 2.13 Effect of grid resolution on the temporal evolution (top row) and spectra (bottom row) of pressure fluctuation p' measured at (a) cavity bottom, (b) cavity opening and (c) far away from the cavity. ..... , $G1$; ——— , $G2$; —×— , $G3$.

To validate the numerical scheme, a comparison of sound pressure level $SPL = 20 \times \log_{10}(p'/p_{ref})$ is carried out between the numerical values and the available experimental data. The reference pressure p_{ref} is the ISO recommended value (= 20μPa) for the sound level (Bies *et al.* 2017). In addition, the extensive measurements of cavity flow fields in Yokoyama *et al.* (2016, 2017 and 2020) show that the evolution of the large-scale structures in the shear layer covering the cavity opening is highly coherent along cavity spanwise dimension so quasi-two-dimensionality can be assumed for cavity flow and acoustic radiation. Similar features are also observed in a recent comprehensive three dimensional numerical study by Ho and Kim (2021). Therefore, it is decided to assume two dimensionality of the flow problem so that the present study can proceed at a reasonable computational cost. In order to achieve a more accordant comparison between experimental noise measurement and the present numerical results, we adopt the formulation proposed by Kato and Ikegawa (1991) and also implemented by (Kusano *et al.* 2020) for the estimation of *SPL* accounting for all noise generation along entire cavity spanwise length L_{span} which is given as $SPL = SPL_{\mathrm{DAS}} + 10\log_{10}(L_{span}/\pi R)$ where the subscript DAS means the present numerical result, R is the receiver distance from the cavity and L_{span} is taken from the experiments of Yokoyama and his co-workers. Figure 2.14 shows three frequencies emerge in numerical cavity noise spectrum at a far location (x, y) = (6.75, 21.5) with dominant f_1 = 0.925, its second harmonic f_2 = 1.85 and third harmonic f_3 = 2.775. They give a constant deviation difference from experimental noise responses by 1.6% in vis-à-vis comparison (Table 2.2). The difference in *SPL* at

these frequencies are +0.6 dB, +4.8 dB and +3.5 dB respectively from experimental values.

It is worth noting that when a flow past a cavity, a shear layer emanates from the cavity leading edge, convects across the cavity opening and impinges on the cavity trailing edge. The impingement produces an acoustic wave that travels back to the cavity leading edge and modifies the cavity shear layer formation (Rockwell and Naudascher 1978). Such kind of feedback mechanism leads to the occurrence of a spectacular self-sustained flow oscillation across cavity opening, known as Rossiter mode (Rossiter 1967), which acts as the primary noise generation process for open cavity flow. Heller and Bliss (1975) modified the Rossiter prediction model and proposed the Strouhal number of the m-th Rossiter mode based on cavity length L can be estimated as, $St_m = (m - \alpha)/\left(1/\kappa + M_\infty/\sqrt{1 + (r_T/2)(\gamma - 1)M_\infty^2}\right)$, where r_T is the thermal recovery factor set to unity for low Mach number flow, the quantities κ and α are, respectively, the ratio of average convection speed of disturbances in the shear layer to freestream velocity and the phase delay of acoustic wave generation at cavity trailing edge from shear layer impingement there. With the prediction given by the above equation, it is informative to compare the dominant frequencies from the numerical results to ascertain if they are created by the Rossiter modes of the present deep cavity. The two quantities, κ and α, are usually determined and their justifications are heuristic. They are often taken as 0.57 and 0.25 for open cavity flows (Gharib and Roshko 1987; Rowley *et al.* 2002; Sun *et al.* 2017) irrespective of the operating Mach number, which makes the frequency prediction only valid at high subsonic flow conditions ($M > 0.5$). Thus, the afore-mentioned values of κ and α may not be applicable to the

present study flow condition (M = 0.09). Therefore, we choose to obtain an estimate of κ ~ 0.508 from the FFT analysis of DAS solution of rigid cavity as detailed in the discussion in Chapter 3 together with Figure 3.4. We take the recommendation of α = 0 from the studies of subsonic flow past deep cavity (Forestier *et al.* 2003; Larchevêque *et al.* 2003; El Hassan *et al.* 2008). With these values of κ and α set, we find the dominant frequency f_1 agrees fairly well with the St_2 = 0.972 obtained from the above equation. One must realize that the *SPL* at f_1 is much stronger than those of f_2 and f_3 by more than 22 dB. Therefore, it can be said that only the second Rossiter mode (m = 2) is successfully excited and captured in the present numerical study. Similar observations are obtained from the reference experiments (Figure 2.14). In summary, all the aforementioned good agreements between experimental data in the literature and present numerical results validate and verify the capability of DAS calculation in properly preserving the characteristics of the flow dynamic and acoustic responses of the chosen deep cavity in the study.

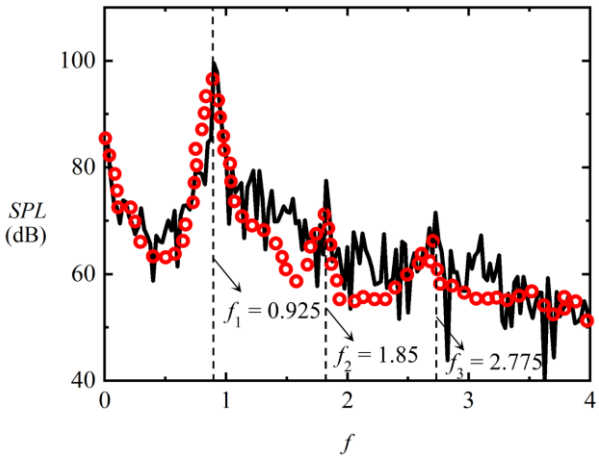

Figure 2.14 Comparison of acoustic spectra at (x, y) = (6.75, 21.5) obtained from the experiment of Yokoyama *et al.* (2016b, 2017 and 2020) and the calculation with *G*2. ——, *Present Study*; ○, *Experiments*.

Table 2.2 Comparison of acoustic characteristics captured at (x, y) = (6.75, 21.5). The value in brackets shows the relative changes of the numerical results from respective experimental values.

	Current Study	Yokoyama *et al.*, (2016b, 2017, 2020)	Rossiter frequency (Heller *et al.*, 1975)
m = 1:	f_1 = 0.925(-1.6%) SPL_1 = 99.6 (+0.6)	f_1 = 0.94 SPL_1 = 99	St_2 = 0.972
m = 2:	f_2 = 1.85 (-1.6%) SPL_2 = 76.8 (+4.8)	f_2 = 1.88 SPL_2 = 72	
m = 3:	f_3 = 2.775 (-1.6%) SPL_3 = 71.5 (+3.5)	f_3 = 2.82 SPL_3 = 68	

2.3.2Validation of Aeroacoustic-Structural Interaction Model

To validate the aeroacoustic-structural model used in this study, the comprehensive validation framework established by Harris (2018) has been adopted. The experimental study by Choy and Huang (2005) on a drum-like silencer with low Mach number flow serves as the benchmark, providing transmission loss for comparison with the numerical results.

The drum-like silencer, a type of duct silencer, was developed based on Huang's (1999) theoretical framework. It features a flexible membrane-based duct segment that reflects noise within the flow duct. Two opposing side-branch cavities, covered with flexible panels, enhance noise attenuation and minimize external sound radiation. The numerical results show strong agreement with experimental data, particularly in capturing spectral variations of transmission loss, demonstrating the accuracy of the present numerical methodology. To examine the role of viscosity, additional simulations were performed using an inviscid flow assumption, employing Euler equations with a sliding-wall boundary condition.

Figures 2.15 compares the acoustic responses of viscous and inviscid solutions against experimental data. In the absence of flow (M=0, Figure 2.15(a)), both solutions overlap, indicating minimal viscous influence. However, with the flow at M=0.03 (Figure 2.15(b)), the inviscid solution overpredicts transmission loss, particularly between f=0.5–0.6 and at f=0.32. This discrepancy increases at M=0.045 (Figures 2.15(c-d)), where the inviscid solution deviates by 5.7 dB from experimental data, whereas the viscous solution shows only a 0.5 dB difference. These results highlight the necessity of incorporating viscosity in numerical models for accurate aeroacoustic-structural predictions. The improved agreement with experimental data underscores the critical role of viscosity in capturing the underlying physics of the interaction.

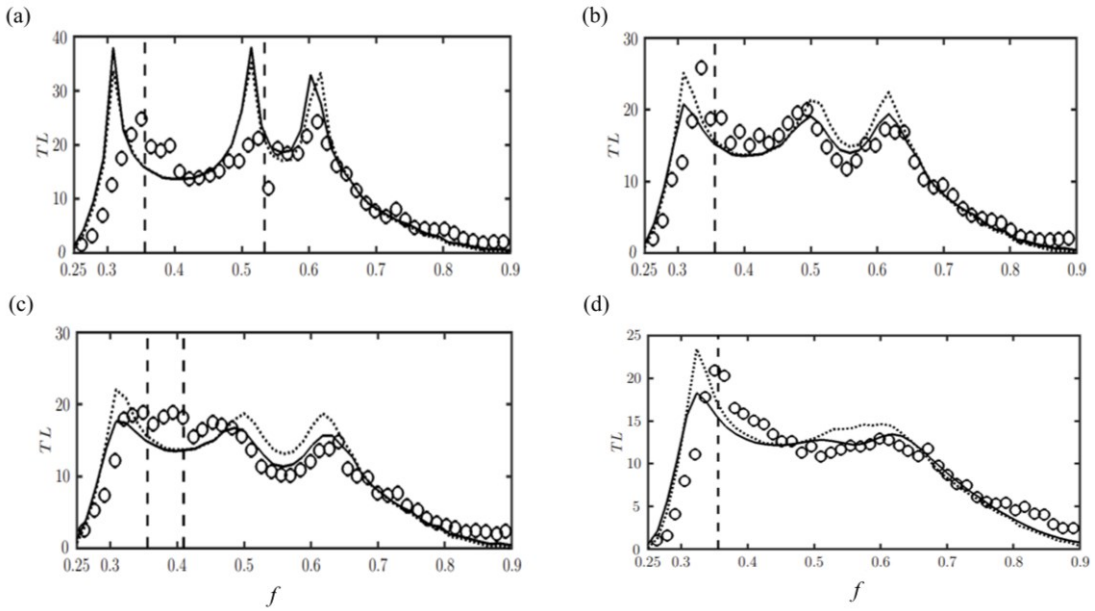

Figure 2.15 From Harris (2018), comparison of the *TL* spectrum of numerical result to experimental data with (a) T = 0.108 and M = 0, (b) T = 0.108 and M = 0.03, (c) T = 0.108 and M = 0.045 and (d) T = 0.116 and M = 0.045. – – –, duct mode frequency; —, numerical result with viscous flow; · · · · · ·, numerical result with inviscid flow; O, experimental data (Choy and Huang 2005).

The influence of cavities beneath the flexible panel on the aeroacoustic-structural interaction was also examined (Harris (2018)) by comparing cases with and without cavities. To prevent panel deflection due to static pressure differences, the external and internal duct pressures are assumed to be identical in the steady state.

Figure 2.16 shows that the panel response is primarily governed by the first five in-vacuo modes, with cavity having a minor effect on the modes. The frequency spectrum indicates that without cavities, the response is concentrated around f=1, with peaks at f=1.016 and f=1.059. When cavities are present, the dominant response shifts to f=1.176, with a smaller peak at f=0.985. Overall, the results suggest that aeroacoustic simulations can be performed without the cavity-backed panel, with only a slight frequency shift as a trade-off. This approach is advantageous in reducing computational costs, as it eliminates the need for a significant number of mesh elements required to model the cavity-backed panel.

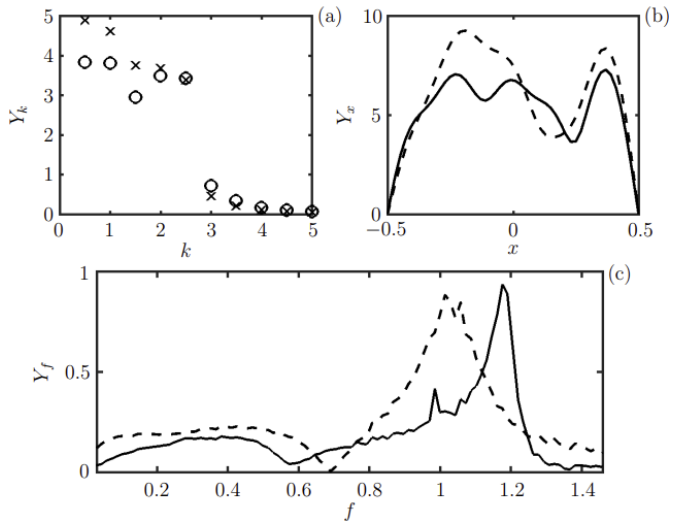

Figure 2.16 From Harris (2018), panel responses with T = 0.116 and M = 0.045. (a), the modal spectrum of panel mobility Y_k. (b), the distributions of panel mobility amplitude Y_x. (c), the averaged frequency spectrum of panel mobility Y_f on the whole panel. O and —, with cavities; × and – – –, without cavities.

Chapter 3

Suppression of Deep Cavity Aeroacoustics using Flow-Compliant Single Elastic Panel

In this chapter a unique concept of utilizing localized surface compliance is proposed to suppress deep cavity aeroacoustics at low Mach number. The core idea is to provide the local absorption of energy of the aeroacoustic processes supporting the cavity flow self-sustained feedback loop responsible for the overall tonal noise generation. The concept is studied using high-fidelity, two-dimensional direct aeroacoustic simulation at a freestream Mach number 0.09 and a Reynolds number, based on the cavity length, of 4×10^4. Having confirmed the replication of all key aeroacoustic processes in the numerical solution through careful validation, localized surface compliance in the form of an elastic panel is strategically introduced to modify every process for cavity noise

suppression. The panel natural frequency is set equal to the feedback loop characteristic frequency to facilitate its flow-induced structural resonance for energy absorption. Suppression of cavity noise pressure and power levels by 3.8 dB and 4.8 dB, respectively, is successfully achieved, together with an unforeseen reduction in cavity drag by almost 19%. Comprehensive wavenumber-frequency analyses of the coupled aeroacoustics and flow-induced panel vibration are conducted to uncover the physical mechanism of noise suppression. The results show that the same type of aeroacoustic feedback loop occurs, but its efficacy is significantly reduced due to the exhaustion of aeroacoustic process energy to the flow-induced vibrating panel. While the present study is conducted with a fixed set of flow and panel parameters, applicable primarily within the subsonic flow regime, its objective is not to examine the influence of inflow conditions on cavity noise behaviour. Instead, the focus is on validating a novel concept for cavity tonal noise suppression. This approach does not require altering panel parameters for each flow condition but rather ensuring that the panel's natural localized vibration frequency complying with the dominant flow frequency—a criterion that can be met regardless of the specific combination of panel structural properties such as length, thickness, or density. The proposed concept is confirmed to be feasible in terms of giving remarkable cavity noise and drag suppression, yet it retains the basic problem geometry intact, which is considered important in many practical applications.

3.1 Rigid Cavity Aeroacoustics

In Chapter 2 we noticed a favourable agreement of the sound pressure spectra derived from the present time-stationary solution with the measured results, it is however important to ensure that the present numerical study is able to correctly capture the key physical processes responsible for the aeroacoustics of the rigid cavity on which the subsequent proposed idea of suppression is based.

The temporal variations of flow pressure fluctuation p' captured across the cavity are illustrated in Figure 3.1. Periodic flow fluctuations along the shear layer region and inside the cavity are evident. For ease of illustration, the snapshots of flow dynamics are set to begin at the moment of weakest pressure inside the cavity (Figure 3.1(b)). Each successive subplot is uniformly chosen at $T/4$ difference within one period of fluctuation, $T = 1/f_1$, and captured at (x, y) = (0.5, -2.5) at the dominant Rossiter frequency as appeared in Figure 3.8. Figure 3.1(a) shows a series of concentrated periodic pressure fluctuations convecting across the cavity opening which is attributed to the peculiar flow dynamics along cavity opening.

Figure 3.2 shows a fluctuating shear layer emanating from the cavity leading edge and forms a series of large-scale vortical flow structures while convecting downstream as a result of Kelvin-Helmholtz instabilities. When a large-scale vortical structure impinges on the cavity trailing edge, the strong flow-structure interaction leads to the formation of separating flow from the downstream flat wall of the cavity. Simultaneously the intensified strain rate in the vicinity of the trailing edge produces a secondary large-scale vortical structure that is stretched and swept down into the cavity (i.e., at $t = T/2$). As the secondary vortical structure detaches from the downstream corner, the

strain rate there is relieved, and the high vorticity region shrinks as the flow develops with the downwash along the cavity aft wall. Further development of the shear layer stems from the repeated formation and impingement of newly formed large-scale vortical structures on the cavity downstream corner. It is important to note that the impingement of vortical structure onto the cavity trailing edge constitutes a peculiar type of vortex-corner interaction that produces an intense flow pressure fluctuation of dipolar character (Tang and Rockwell 1983).

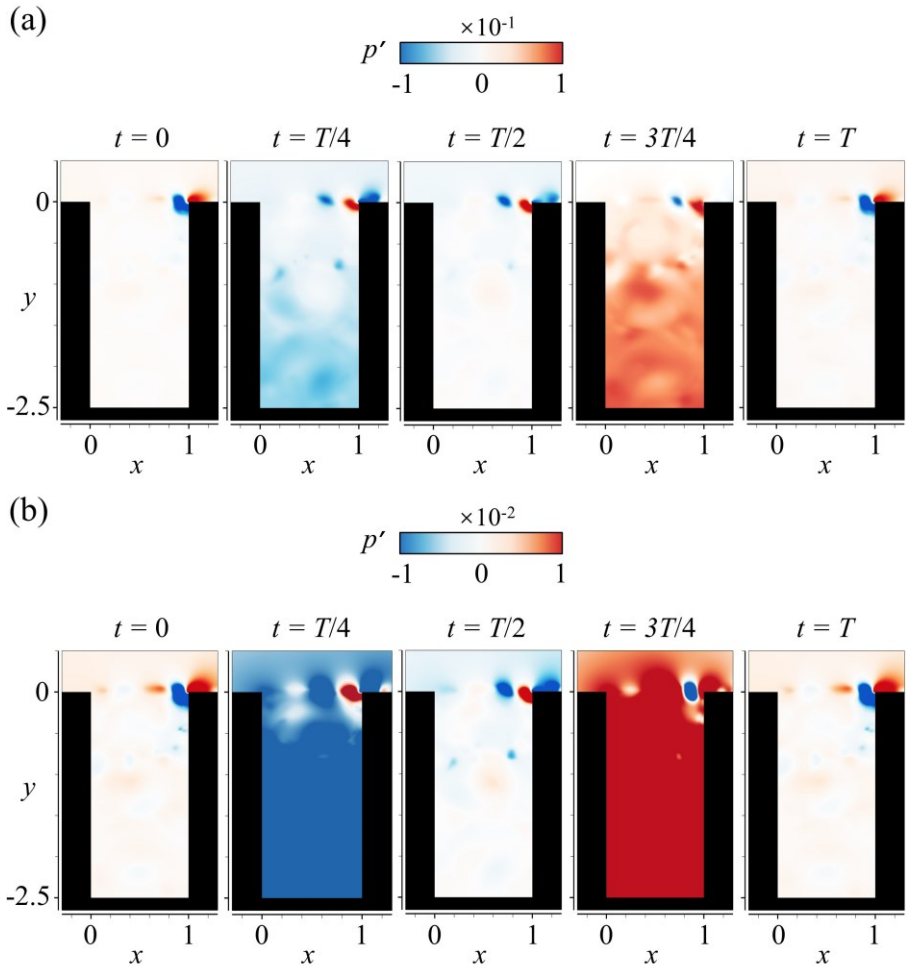

Figure 3.1 Instantaneous pressure fluctuation p' around the cavity and the fluctuation scale disparity distinguishes (a) shear layer vortex strength and (b) emergence of the cavity mode.

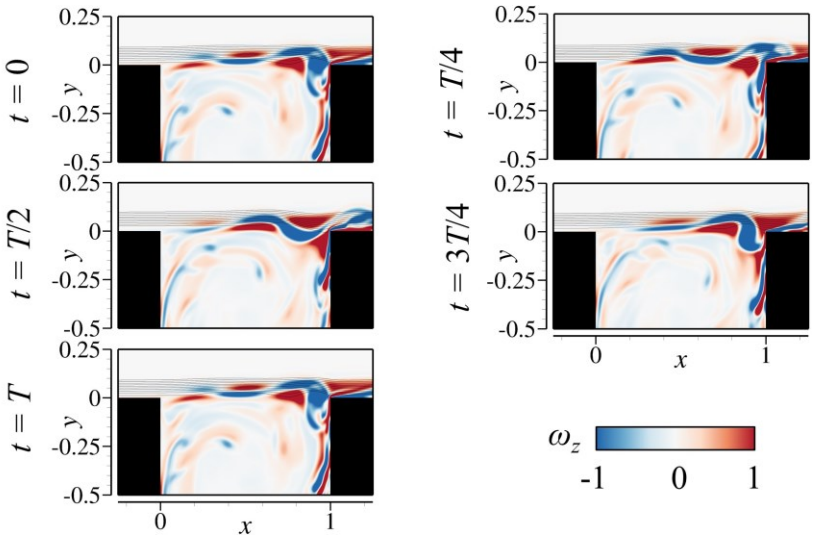

Figure 3.2 Instantaneous vorticity of shear layer development near the cavity opening region.

The pressure inside the cavity fluctuates in a clear alternating pattern in time with a spatial extent almost filling up the entire cavity (Figure 3.1(b)). The strength of the pressure fluctuation is almost two orders of magnitude weaker than that along the shear layer region. Such disparity in magnitude is typical in low Mach number aeroacoustics (Dowling and Williams 1983) and the pressure fluctuation inside the cavity is likely acoustic. It is interesting to note that a strong rarefaction (pressure lower than $\bar{p}$) is released at the moment of formation of the downwash secondary vortex and the separating flow at the cavity trailing edge. A strong compression (pressure greater than $\bar{p}$) is released after these two flow processes are complete. The observations are consistent with the numerical study of a deep cavity of similar size (Ho and Kim (2021). The pressure fluctuations are believed to constitute the acoustic resonance within the cavity which is responsible for driving acoustic waves away from the cavity (Figure 3.3). An acoustic wavefront is created at the cavity opening once the cavity pressure fluctuation has attained its minimum or maximum magnitude (i.e., at $t = T/4$ or $3T/4$ in Figure 3.1(b)). The wavelength of acoustic waves tends to be ~11.03, much longer than the dimensions of the cavity. Such disparity in length scale is characteristic in all low Mach number aeroacoustic problems (Dowling and Williams 1983). The manifestation of characteristic length and magnitude disparity in the numerical solutions provides further evidence of the correctness and accuracy of the present numerical approach.

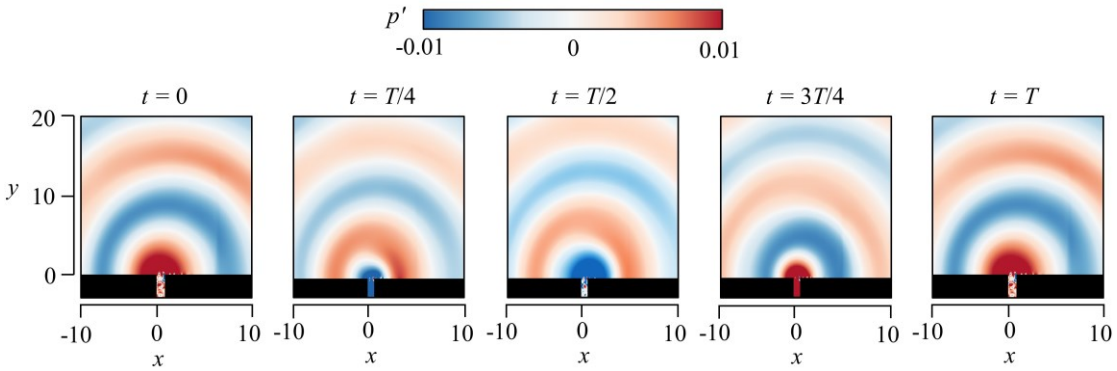

Figure 3.3 Instantaneous pressure fluctuations around the cavity.

It has to be noted that the DAS solutions generally contain acoustic and flow dynamic fluctuations, but their differentiation is not obvious. This fact creates difficulty in determining the dominant physics, whether acoustic or flow dynamic, in the solutions. It is especially true in the region of cavity opening, where the acoustics are generated by the underlying unsteady flow fluctuations. To circumvent this difficulty, the combined technique for differentiation and extraction of acoustic and flow dynamic contributions in time-stationary DAS fluctuation solutions developed by Lam *et al.* (2013) is applied. In essence, it involves using the two-dimensional wavenumber-frequency spectrum ($k - f$, where k is wavenumber) for extracting the phase speeds of various fluctuation contributions followed by delineating the associated phase relationships based on the principle of the two-microphone method (Leung *et al.* 2007). Figure 3.4(a) shows the $k - f$ spectrum of pressure fluctuation along a vertical line ($-2.5 \leq y \leq 0$) from the cavity bottom center $(x, y) = (0.5, -2.5)$. At every location on the line, the Fast Fourier Transform (FFT) analysis with Hamming window and zero data overlapping is applied to a temporal solution of 10^6 samples of temporal solution. The figure shows a symmetric pattern with respect to the line $k = 0$ with two peak contributions at frequency $f = 0.925$ and wavenumbers $k/2\pi = \pm 0.0838$. The phase speeds deduced from the slopes of two straight

lines spanning from the peaks of the spectrum to the origin are equal to ±11.03 ~ $\pm 1/M$ for M = 0.09, but there is no signal detected along the straight lines corresponding to flow convective propagation. Furthermore, Figure 3.4(b) shows only one signal corresponding to convective phase speed ~ 0.508 along the downstream. These observations give two important deductions. Firstly, the upward and downward propagating pressure fluctuations inside the cavity are purely acoustic in nature. Secondly, the flow fluctuation across cavity opening is purely driven by the developing shear layer, and there is no acoustic feedback wave from the shear layer impingement propagating upstream as observed in previous studies with shallow cavities (Rossiter 1967; Heller and Bliss 1975; Tam and Block 1978; Rowley *et al.* 2002). However, these two types of fluctuations might interact to give aeroacoustic coupling in the flow.

The variations of the phase relationship of pressure fluctuations along the vertical line (- 2.5 ≤ y ≤ 5) through the cavity bottom center are explored with reference to the pressure fluctuation at location (x, y) = (6.75, 21.5) far away from the cavity. The results are illustrated in Figure 3.4(c). Phase unwrapping is applied to ensure the smoothness of the data. Three regimes of phase relationship can be discerned. The first regime concerns the constant phase difference ϕ observed from the cavity bottom to $y \sim -1$, which suggests the two acoustic waves along the depthwise direction are responsible for the cavity mode resonance. The second regime concerns the spatial variation of ϕ in region $y \geq 0$. There is a sharp reduction in ϕ, and its variation settles to a fairly linear one beyond $y \sim 0.5$. The linearity signifies an outgoing pressure fluctuation from cavity opening, and its approximate gradient ϕ of variation can be used to deduce the fluctuation phase speed with the approach of Schumacher

et al. (2014) and Lam and Leung (2018). A phase difference of $\pi/2$ indicates a traversal over one-quarter of fluctuation wavelength λ /4 ~ 2.867, giving a phase speed of ~11.02 at the dominant Rossiter frequency f_1 observed with the propagating fluctuation. Therefore, only pure acoustic wave propagates outside the cavity, which is consistent with Figure 3.4. The third regime lies within the region of -1 ≤ y ≤ 0.5, which shows a very different variation of ϕ. It reflects that the corresponding pressure fluctuations are no longer purely acoustic in nature but highly affected by the convecting shear layer across cavity opening, giving rise to substantial nonlinear aeroacoustic interaction. Thus, this regime is aeroacoustic in nature. Figure 3.4(d) shows the phase difference ϕ of pressure fluctuation, with respect to the same location (x, y) = (6.75, 21.5), along the cavity opening (i.e., y = 0). A fairly linear variation is evident within 0.1 ≤ x ≤ 0.85, and its gradient gives a phase speed of ~ 0.508, which is comparable to the convective speed of the shear layer at the cavity opening. This shows that the pressure fluctuation in this range of x is solely dominated by the evolving shear layer. The nonlinear variations of ϕ in the vicinity of two cavity edges reveal strong aeroacoustic interaction. All the variations of ϕ just discussed are similar to a recent study of the aeroacoustics of a cavity flushed mounted in a thick airfoil at a similar Mach number (Lam and Leung 2018). It is interesting to see that all the findings from the present analysis of the DAS flow fluctuations outline a physical picture of acoustic and aeroacoustic interactions of cavity flow that is consistent with the study of Ho and Kim (2021) even though the methods of analysis are different. In what follows, the pressure fluctuations p' in acoustic (i.e., the first and second regimes) and aeroacoustic regimes (i.e. the third regime) are indicated as p'_a and p'_s respectively.

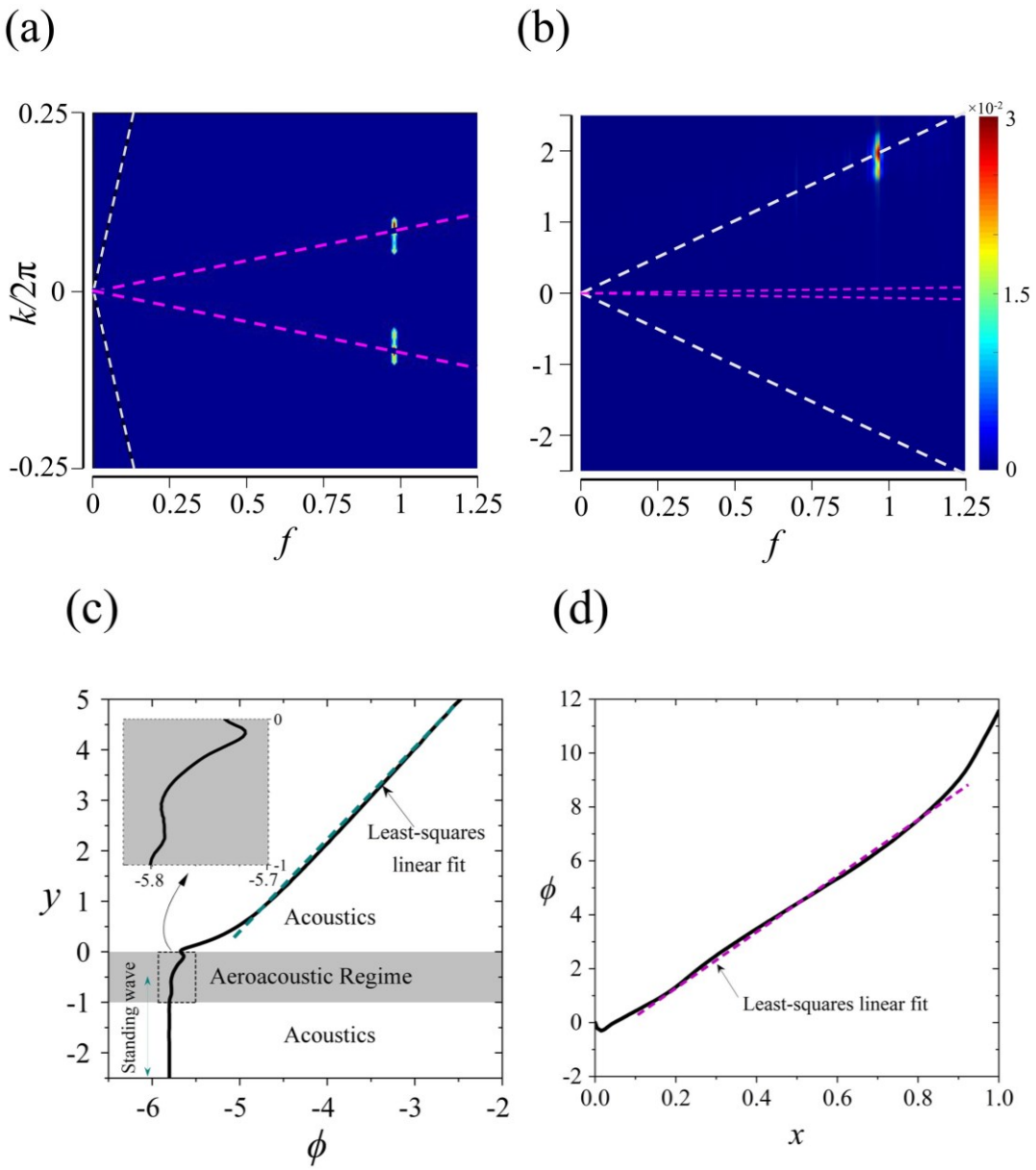

Figure 3.4 Identification of dominant physical processes of cavity flow. (a) Wavenumber-frequency spectra of depthwise cavity pressure fluctuation, violet and white dashed lines give convective and acoustic phase speeds, respectively. (b) Wavenumber-frequency spectrum across cavity opening. (c) The phase difference between the acoustic signal at location (x, y) = (6.75, 21.5) and the line running vertically through the cavity at x = 0.5. (d) The phase difference between the acoustic signal at location (x, y) = (6.75, 21.5) and pressure signals across the cavity opening at y = 0.

The pressure fluctuations p_s' and p_a' along cavity opening and cavity base, respectively, are extracted for FFT analysis, and their magnitudes at the dominant frequency f_1 are illustrated in Figure 3.5(a). The uniform magnitude $|p_a'|$ along cavity bottom confirms the acoustic waves responsible for cavity

mode are essentially planer and one dimensional along the depthwise direction. The magnitude $|p_s'|$ across cavity opening generally increases along the downstream direction due to the growth of shear layer vortices. Its pronounced rate of increase within $x \geq 0.8$ may be attributed to high unsteadiness resulting from the impingement of large-scale vortices on the downstream cavity edge (Figure 3.2). Figure 3.5(b) presents the coherence $\gamma^2(f_1) = |P_{sa}(f_1)|^2 / P_s(f_1)P_a(f_1)$ between p_s' along $y = 0$ and p_a' at the cavity bottom center, where $P_s(f_1)$ and $P_a(f_1)$ are the power spectral densities of p'signals for the shear layer and the acoustic mode respectively, and $P_{sa}(f_1)$ is the cross power spectral density between the signals. The coherence reveals that the pressure fluctuations are highly correlated at the dominant frequency, which implies strong coupling between the shear layer evolution and cavity mode resonance. A clearer picture of such aeroacoustic coupling is obtained from a study of the phase difference $\phi_f = \phi_s - \phi_a$ between p_s' and p_a' fluctuations at varying streamwise location x across cavity length where the phases ϕ_s and ϕ_a are determined from FFT with respect to the same reference value (Figure 3.5(c)). The almost zero difference between ϕ_s and ϕ_a within $x < 0.65$ indicates high constructive coherence between p_s' and p_a', which reflects the high receptivity of developing shear layer and cavity interior acoustics. Such receptivity is significantly lost within $0.65 \leq x \leq 1$, which reflects the dominance of the vortex impingement in the flow development. The entire unsteady coupling between the developing shear layer and cavity mode observed from the present numerical solutions is found to agree highly favorably with the findings of Ho and Kim (2021) despite a slightly different *M* and *Re*.

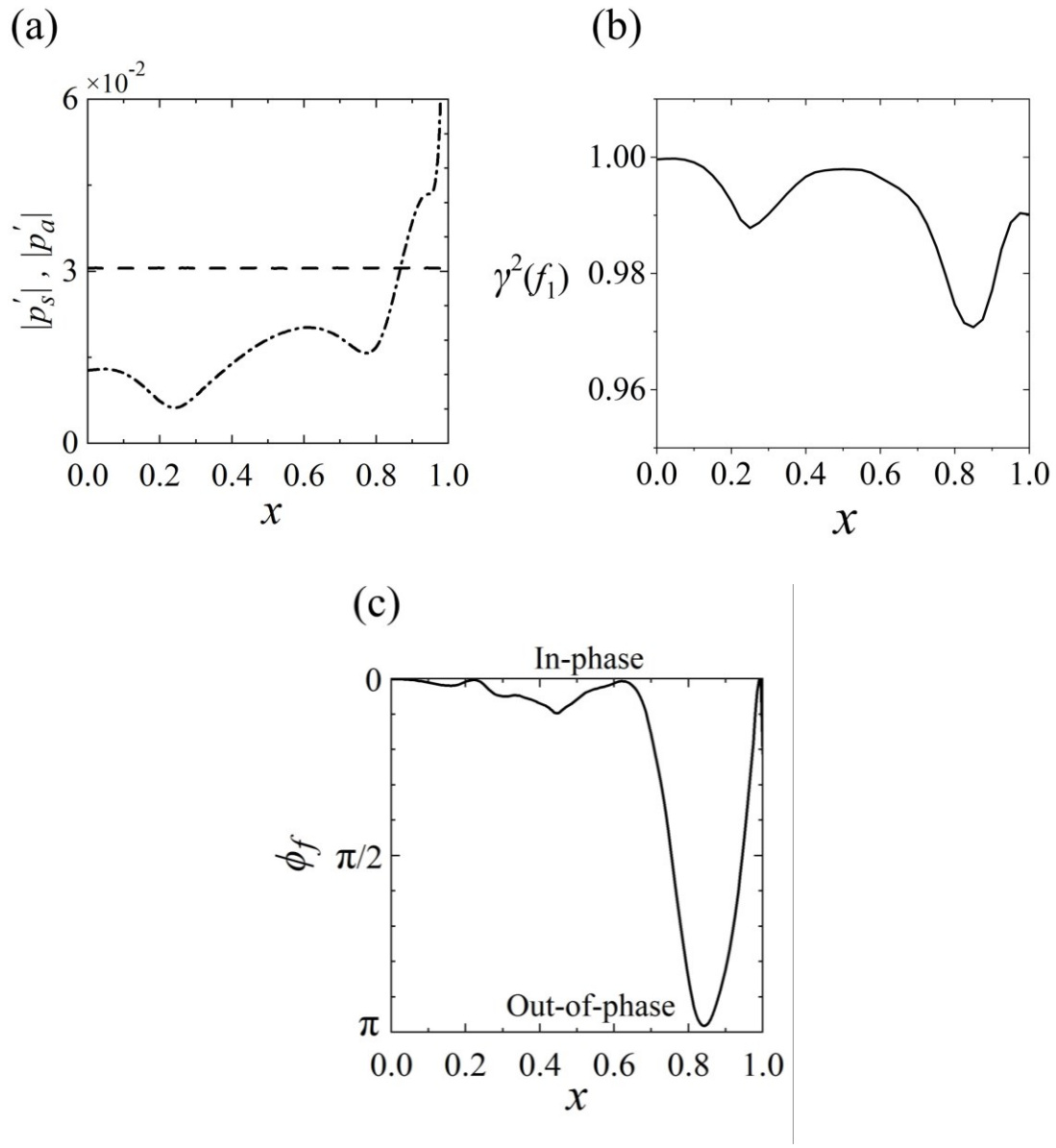

Figure 3.5 Shear layer-cavity mode interaction. (a) Streamwise variation of FFT pressure fluctuation across the cavity opening ($|p_s'|, - \cdot -$) and cavity bottom wall ($|p_a'|, - - -$) at dominant frequency f_1. (b) Coherence between $p_s'(t)$ along y = 0 and $p_a'(t)$ at cavity bottom center (x, y) = (0.5, -2.5). (c) Streamwise phase difference variation ϕ_f between acoustic pressure fluctuations $|p_a'|$ and shear layer pressure fluctuations $|p_s'|$ across the cavity opening.

3.2 Design Of Elastic Panel

The primary aim of the present study is to explore the feasibility of suppressing the tonal noise generated by a deep cavity using a flow-induced vibrating elastic panel. Two major design parameters of the elastic panel, namely its mounting location and structural properties, uphold the key to achieving the said purpose. For the panel to work effectively and sustain its vibration through the flow-induced loadings, the identification of potential locations for an optimal performance requires a careful examination of the evolution of flow oscillations involved in the baseline rigid deep cavity, hereafter indicated as *RC* case. Therefore, the potential locations mounting the elastic panel are identified by deciphering the sequence and nature of the events taking place in the *RC* case.

In the previous section, we extracted key relationships from the pressure fluctuations created by various underlying physical processes contributing to the aeroacoustic feedback for cavity noise radiation. The evidence presented helps to delineate the interactions of these processes and to seek their possible modification through our conceived ideas of elastic panel installation for the ultimate cavity noise reduction. The dominant processes identified are briefly summarized in Figure 3.6(a) & (b). An upstream boundary layer separates from the cavity leading edge of the deep cavity and gives rise to a shear layer (process [a]) which is amplified upon convecting across the cavity opening as a result of Kelvin-Helmholtz instability. As discussed in the previous section, the initial growth of the shear layer might be modified by the acoustic wave reflected from the cavity bottom through a certain aeroacoustic coupling (process [b]). The shear layer eventually impinges on the cavity trailing edge and splits into

unsteady vorticity that downwashes along the cavity aft wall as well as undergoes further flow separation and reattachment on the horizontal wall downstream, producing strong pressure fluctuations due to intense flow-structure interaction there (process [e]). The aeroacoustic interaction of these pressure fluctuations will radiate an acoustic wave towards the cavity bottom (process [d]), which combines its reflected wave there to form a standing wave at the selected cavity mode (process [c]). As shown in the previous section, there is no direct acoustic feedback through the shear layer excited by shear layer impingement; the processes [b] and [d] are believed to be the major contributors to the aeroacoustic coupling between the shear layer and cavity mode as similar to the views upheld by (Ho and Kim 2021).

3.2.1 Panel Location

The locations supporting various characteristic flow processes [a] to [e] are considered for elastic panel mounting (Figure 3.6(a) & (b)). Each panel is envisaged to act as an absorber of the energy of aeroacoustic/acoustic fluctuation of the flow process(es) concerned in such a way that the interaction with the target process will give lower cavity noise radiation. The intended actions produced by the panels are described as follows: panel *EP*1 is to modify the upstream boundary layer growth (process [a]) via flow-induced vibration; panel *EP*2 is to weaken the aeroacoustic coupling between shear layer growth and incident acoustic excitation (process [b]) via aeroacoustic-structural interaction; panel *EP*3 is to weaken the formation of the standing wave inside the cavity (process [c]) via acoustic-structural interaction; panel *EP*4 is to suppress the aeroacoustic production due to impinging shear layer (process [d]) on the panel via aeroacoustic-structural interaction; and the panel *EP*5 is to

weaken the pressure fluctuation in the vicinity of cavity trailing edge (process [e]) via flow-induced vibration. A summary of the rationale taken, and the respective panel locations are given in Table 3.1.

It must be emphasized that the mounting of all panels is targeted to modify the intricate physical processes responsible for the aeroacoustic coupling between the shear layer and cavity mode. It never aims to physically encroach the original cavity flow characteristics, so the chamfering of the cavity edges or other shape transformations as practiced previously (Saddington *et al.* 2016; Liu and Gómez 2019; Sato *et al.* 2019; Yokoyama *et al.* 2020) are not required. In fact, the proposed novel idea respects and preserves the prevalent flow processes by keeping the basic cavity shape intact and, at the same time, presents the possibility of noise reduction with strategic modification of aeroacoustic coupling through flow-induced panel vibration.

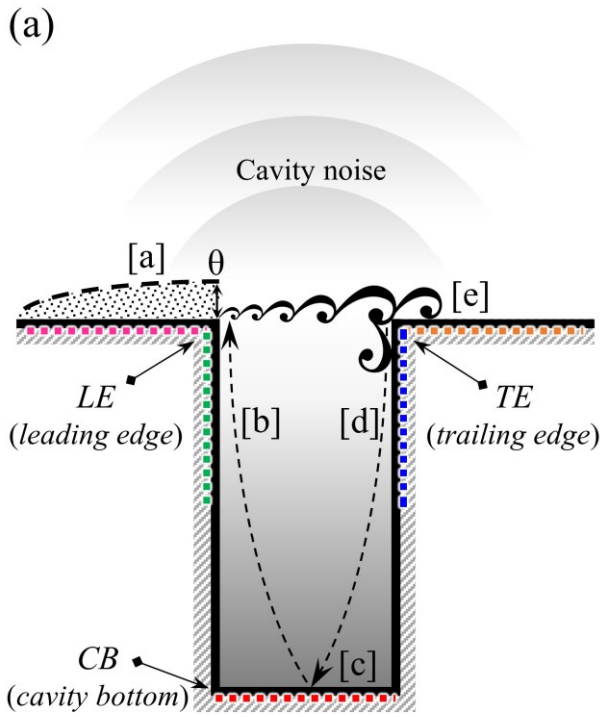

Figure 3.6 Delineation of the physical processes leading to cavity noise generation and their corresponding elastic panel mounting locations. (a) Schematic of shear layer–cavity mode interaction involving the triad of *LE-TE-CB* and supported by flow processes from [a] to [e]. (*continued next page*)

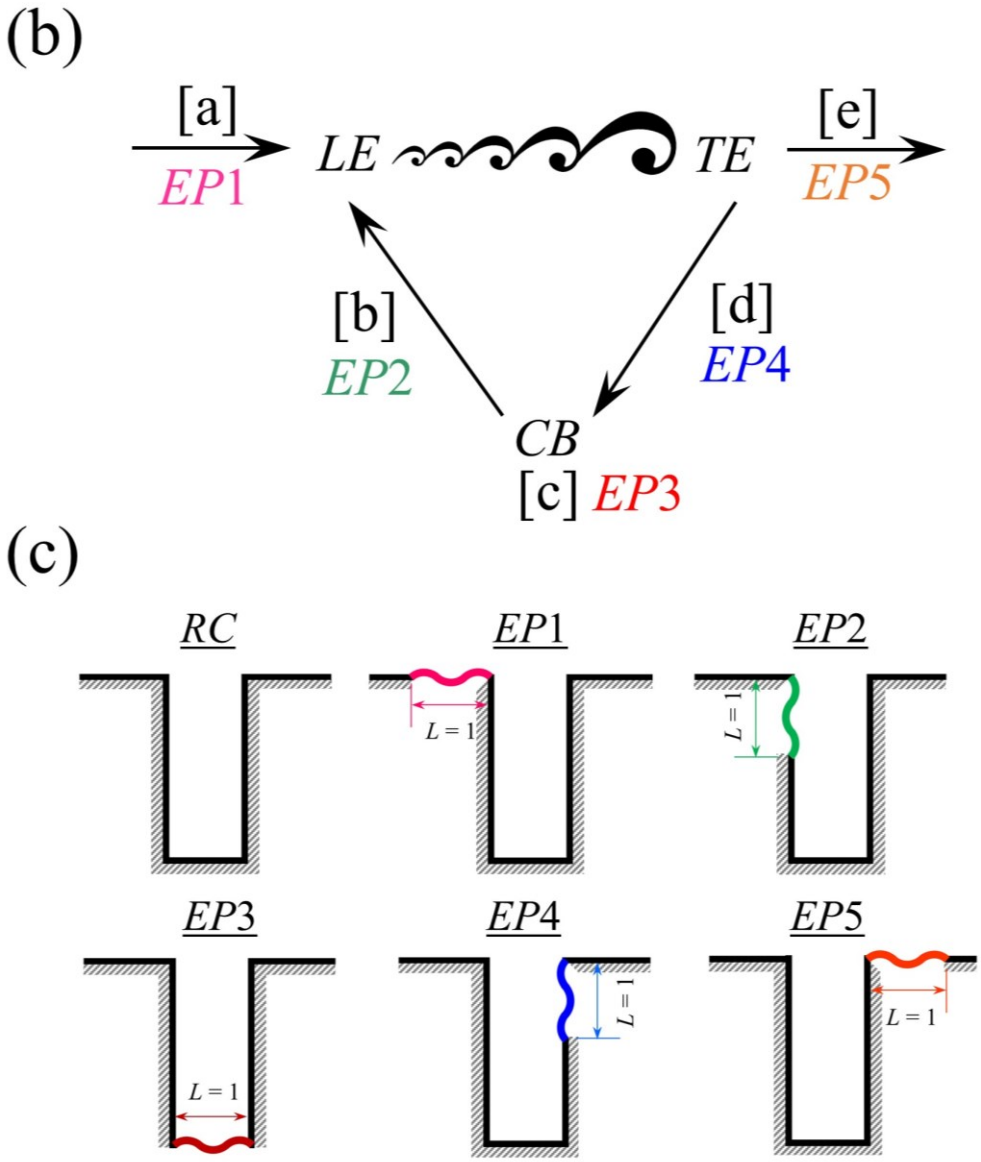

Figure 3.6 (*Continued from previous page*), (b) Contribution of the processes to the shear layer – cavity mode interaction. (c) Selected locations of panels.

Table 3.1 The rationale for the selection of panel locations.

	Leading Edge (*LE*)		Cavity Bottom (*CB*)	Trailing Edge (*TE*)	
Target flow process	[a] Boundary layer growth	[b] Acoustically excited shear layer growth	[c] Cavity standing wave formation	[d] Cavity mode excitation by shear layer impingement	[e] Unsteady flow after shear layer impingement
Proposed panel location	*EP*1 $-1 \le x \le 0$ $y = 0$	*EP*2 $x = 0$ $-1 \le y \le 0$	*EP*3 $0 \le x \le 1$ $y = -2.5$	*EP*4 $x = 1$ $-1 \le y \le 0$	*EP*5 $1 \le x \le 2$ $y = 0$
Imparted panel control mode	Flow-induced vibration	Aeroacoustic – Structural	Acoustic – Structural	Aeroacoustic – Structural	Flow-induced vibration

3.2.2Panel Structural Properties

Table 3.2 lists the selected parameters for all panels in the present study. The dominant flow frequency of the *RC* case is taken to be the primary parameter for consideration in the selection of panel structural properties. To accomplish the intended flow-induced panel resonance for the control purpose, the natural modal resonant frequency of every elastic panel is made the same as the dominant flow frequency. This is achieved by changing the thickness and the tension of the elastic panel accordingly. This has to be emphasized that the natural frequencies of a strongly coupled structure-fluid system are influenced by fluid loading, with the panel experiencing inertial effects due to its higher structural wavenumber compared to the acoustic wavenumber. This results in a slight reduction in its natural frequency from the in-vacuo value, therefore taking into account the effect of fluid loading, the non-dimensional frequency of the n^{th} mode of the panel vibration, clamped at both ends, can be estimated by Eq. (3.1) (Blevins 2015). All panels are assumed to be made up of elastomeric material like silicon rubber (Naseer *et al.* 2022).

$$(f_{EP})_n = \frac{n}{2L}\sqrt{\frac{T_{EP}}{\rho_{EP}h_{EP}}}\Big/\sqrt{1+\frac{L_{EP}}{\pi n \rho_{EP}h_{EP}}} \quad , \tag{3.1}$$

where L_{EP}, ρ_{EP}, T_{EP} and h_{EP} denote the length, density, tension, and thickness of the elastic panel, respectively and C_{EP} denotes the damping coefficient employed . In the present study, the designed frequency of the panel is taken at its third mode (n = 3) for meeting the natural dominant cavity flow frequency as well as the consideration of panel fabrication practicality.

Table 3.2 Elastic panel configuration and its fluid-loaded natural frequencies.

Material	L_{EP}	ρ_{EP}	T_{EP}	h_{EP}	n	C_{EP}	$(f_{EP})_1$	$(f_{EP})_2$	$(f_{EP})_3$	$(f_{EP})_4$
Silicon Rubber	1	833.45	6.37	0.02	3	0.05	0.308	0.62	0.925	1.237

3.3 Deep Cavity Aeroacoustics with Elastic Panel

Figure 3.7 shows a comparison of cavity noise spectra captured at the location $(x, y) = (6.75, 21.5)$ far from the cavity. Tonal noise prevails in all cases, showing that the original coupling between the developing shear layer and cavity mode is not radically changed or destroyed in the presence of elastic panels. For *EP*1 and *EP*2, a mild noise reduction of 1.4 dB and 1.1 dB is observed at the dominant frequency $f = 0.925$, the same as in the *RC* case. The same dominant frequency also prevails in the *EP*5 case but gives a noise amplification of 2.6 dB instead. For *EP*3 and *EP*4, a remarkable noise reduction of 3.6 dB and 3.8 dB is observed, respectively, but they occur at a different dominant frequency $f = 1.25$, which is 35% higher than the *RC* value. Figure 3.8(a) shows the snapshots of instantaneous pressure fluctuation for all the configurations captured at the moment when the acoustic rarefaction hits the cavity bottom. As illustrated, the overall cavity noise radiation pattern in all the cases is similar to the *RC* case (Figure 3.3(b)). The *EP*3 and *EP*4 cases slightly skew the directivity along the downstream direction with new maximum radiation at an angle of ~ 45° from the downstream horizontal wall (Figure 3.8(b)). The extent of azimuthal noise reduction of *EP*1 and *EP*2 and the noise amplification of *EP*5 are fairly uniform (Figure 3.8(c)). However, the extent of noise reduction of *EP*3 and *EP*4 shows some variations. The effectiveness of noise reduction and amplification of elastic panel can be illustrated with the change of sound power level $\Delta PWL = 10\log_{10}(W_{EP}/W_{RC})$ in dB of cavity noise radiation where $W = \int_0^{\pi} p'_{rms}\, d\theta$ and the results are illustrated in Table 3.3. A significant sound power reduction of almost 5 dB is possible with EP3 and *EP*4, but *EP*5 gives a very strong sound power enhancement by 3.3 dB. In summary, all these phenomena firmly reveal that the panels installed in the vicinity of the leading edge and cavity bottom

(Figure 3.6) give rise to mild and significant cavity noise reduction, respectively. In the vicinity of the trailing edge, where the impingement of the shear layer dominates, a panel installed inside the cavity gives significant noise reduction, but one outside the cavity gives noise amplification instead. The physical mechanisms responsible for the observed phenomena are analyzed and discussed in forthcoming sections.

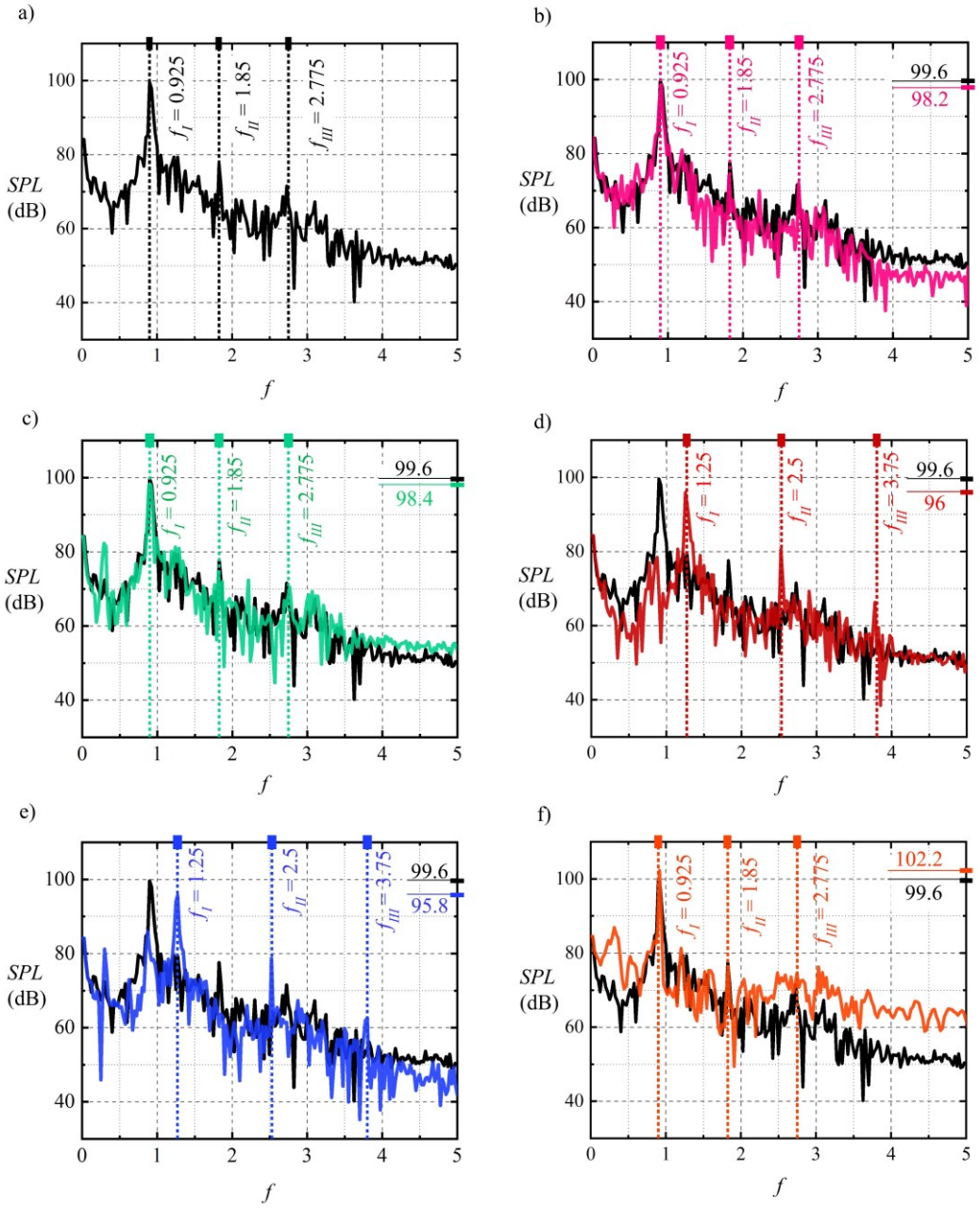

Figure 3.7 Comparison of acoustic spectra at $(x, y) = (6.75, 21.5)$. The markers at the right indicate peak values.(a) *RC*; (b) *EP1*; (c) *EP2*; (d) *EP3*; (e) *EP4*; (f) *EP5*. Solid Black line: *RC*, Colour lines: *EP* cases.

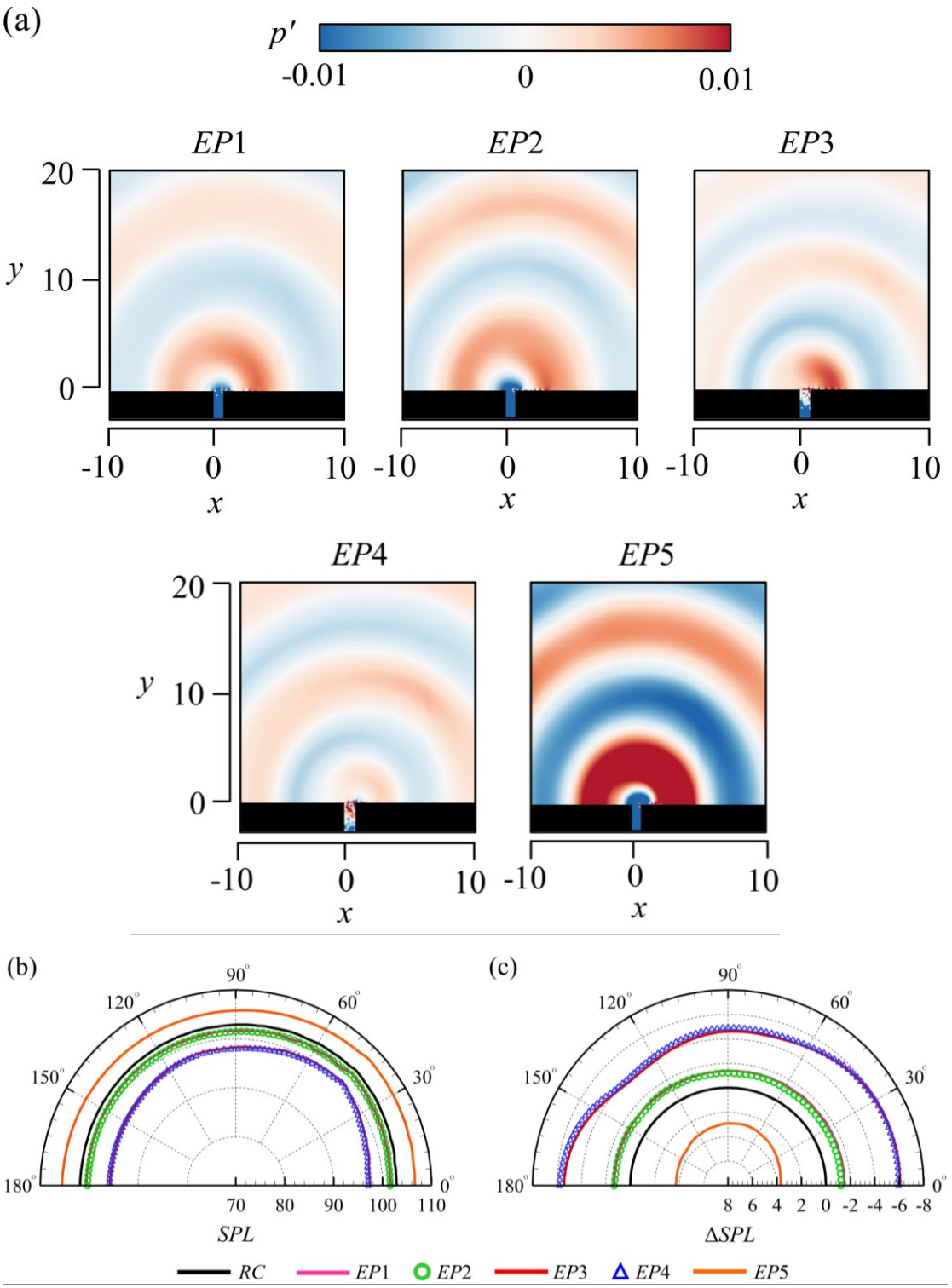

Figure 3.8 (a) Instantaneous acoustic pressure fluctuations of all cases. (b) Azimuthal distribution of peak *SPL* at r = 10. (c) Azimuthal *SPL* change, $\Delta SPL = 20\log_{10}(p'_{EP}/p'_{RC})$ at r = 10.

Table 3.3 Change sound power level due to elastic panels.

Cases	*EP*1	*EP*2	*EP*3	*EP*4	*EP*5
Δ*PWL* (dB)	− 1.3	− 1.1	− 4.6	− 4.8	+3.2

Figure 3.9 depicts the distribution of the time-averaged coefficient of pressure, $\bar{C}_p = 2(\bar{p} - p_\infty)/\rho_\infty u_\infty^2$, along all the cavity walls. For all *EP* cases, the distribution is similar to the *RC* case, each of which shows roughly uniform wall pressure and sudden spikes at locations on the vertical walls very close to the cavity leading edge and trailing edge. Generally, the retention of $\bar{C}_p$ distribution in all *EP* cases infers that the introduction of an elastic panel does not induce significant change to the normal pressure force on the walls. There is an observable $\bar{C}_p$ deviation of *EP*5 from the *RC* by ~19.1% (along -0.5 ≥ y ≥ -1.25) and ~19.4% (along -0.5 ≤ y ≤ 0) on the front and aft walls, respectively, which reflects a more vigorous shear layer dynamics, resulting in the overall noise amplification. Moreover, it is interesting to see the effects of elastic panels on the time-averaged drag acting on the cavity (Table 3.4), calculated as $\bar{C}_D = 2\bar{F}_d/\rho u^2 l_{(x,y)}$, , where $\bar{F}_d = \bar{F}_{form} + \bar{F}_{fric}; \bar{F}_{form} = -\int_{-2.5}^{0} p(0,y)\,dy + \int_{-2.5}^{0} p(1,y)\,dy;$ $\bar{F}_{fric} = \int_0^1 \tau(x,-2.5)\,dx$. In all cases, the coefficient of skin friction drag, $\bar{C}_{D,fric}$ is two orders of magnitudes weaker than that of form drag $\bar{C}_{D,form}$ so the latter is the major contributor to total cavity drag $\bar{C}_D$. The cases *EP*1, *EP*2, *EP*3 and *EP*4 give less total drag, up to 20% lesser than the *RC*. On the contrary, *EP*5 increases total drag by almost 20%. Evidently, the proposed use of an elastic panel for noise reduction is achieved without any sacrifice in the cavity aerodynamics at all. In fact, it provides the aerodynamic benefit of lower cavity drag. That makes the present idea superior to those attempted before (Lang and Johnson 2010; Sanmiguel-Rojas *et al.* 2011). It is interesting to note that similar aeroacoustic benefits are also observed in the study of using flow-induced elastic panels for airfoil tonal noise reduction (Arif *et al.* 2022).

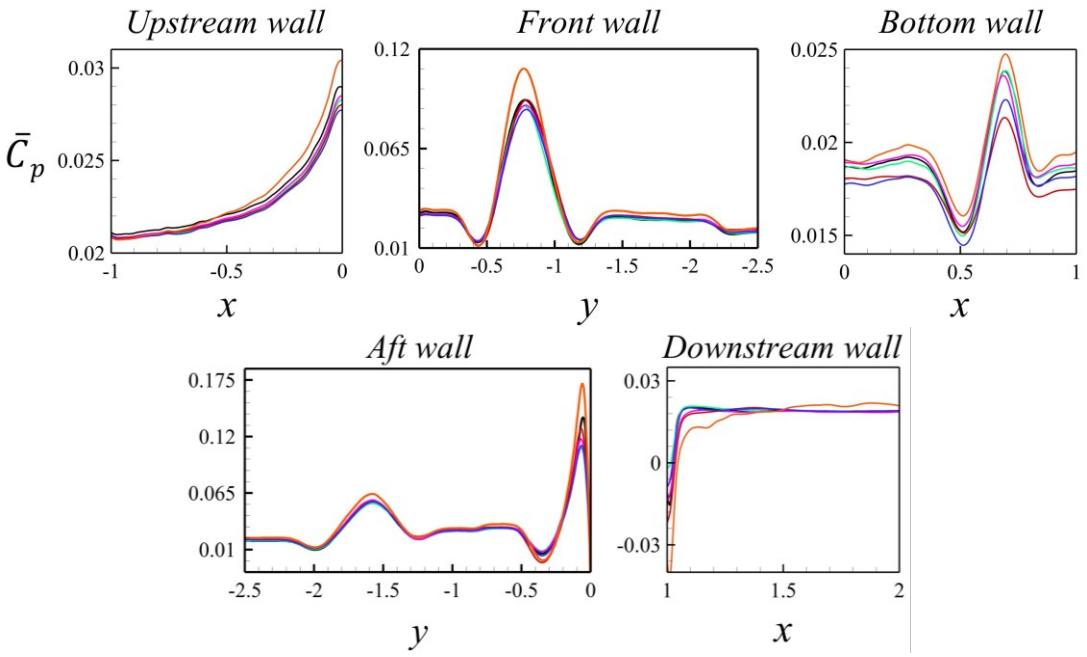

Figure 3.9 Coefficients of pressure along the cavity walls. ____ , *RC*; ____ , *EP*1; ____ , *EP*2; ____ , *EP*3; ____ , *EP*4; ____ , *EP*5.

Table 3.4 Skin friction drag, form drag and total drag comparison of all cavity configurations. Values in brackets show the percentage deviations from the *RC* case.

	Skin friction drag, $\bar{C}_{D,fric}$	*Form drag,* $\bar{C}_{D,form}$	*Total drag,* $\bar{C}_D$
RC	5.68×10^{-5}	1.70×10^{-3}	1.76×10^{-3}
*EP*1	6.38×10^{-5} (+12.2%)	1.42×10^{-3} (-16.7%)	1.48×10^{-3} (-15.7%)
*EP*2	6.50×10^{-5} (+14.4%)	1.69×10^{-3} (-0.7%)	1.75×10^{-3} (-0.2%)
*EP*3	5.48×10^{-5} (-3.6%)	1.59×10^{-3} (-6.4%)	1.64×10^{-3} (-6.4%)
*EP*4	6.48×10^{-5} (+14.1%)	1.36×10^{-3} (-20.2%)	1.42×10^{-3} (-19.1%)
*EP*5	6.31×10^{-5} (+11.1%)	2.03×10^{-3} (+19.1%)	2.09×10^{-3} (+18.1%)

3.4 Modification of Cavity Noise Generation Mechanism

The variation of cavity noise observed in *EP*1 to *EP*5 cases implies that the coupling of the shear layer and the cavity mode of *RC* is greatly modified by the new possibility of acoustic- and/or aeroacoustic-structural interaction given by the elastic panel. To uncover the underlying physical mechanisms leading to the amplified and reduced cavity noise, the phase relationships of pressure fluctuations along cavity opening (i.e., along $0 \leq x \leq 1$ and $y = 0$) at dominant peak frequencies in all cases are examined carefully with reference to that at cavity bottom center, using the same approach as carried out in Section 3.1. It should be reminded that the discussions in Section 3.1 firmly establish that the pressure fluctuations across the cavity opening and at the cavity bottom are purely aerodynamic and acoustic in nature, so the same respective symbols, p'_s and p'_a, are used in forthcoming discussions.

Figure 3.10(a) shows the coherence between the p'_s and p'_a fluctuations for all cases. The *EP*1 and *EP*2 cases maintain more or less the same high level of coherence as *RC* along the significant part of the cavity opening length. So, the same type of coupling between the developing shear layer and the cavity mode (i.e., processes [b] and [d] in Table 3.1) exists as observed in the *RC*. Nevertheless, there is a significant drop in coherence at $x \sim 0.125$ for *EP*3 and *EP*4 cases. Figure 3.10(b) shows the phase difference ϕ_f between the pressure fluctuations. It is interesting to note that the trends of ϕ_f for *EP*1, *EP*2 and *EP*5 cases are similar to the *RC* case, but their magnitudes vary. The acoustic excitation on the shear layer growth around the leading edge ($x < 0.25$) is weaker due to a deviation of ϕ_f from zero, but it becomes effective again for

shear layer growth downstream $0.26 \leq x \leq 0.6$. The values of ϕ_f are smaller than the *RC* case within $0.6 < x \leq 0.8$ but become larger up till the cavity trailing edge for stronger coupling between shear layer impingement and cavity mode in these cases. For *EP*3 and *EP*4 cases, the trends of coherence and ϕ_f of p_s' and p_a' fluctuations together show that the fluctuations are weakly synchronized. Their highly similar variations of ϕ_f give a very different trend from the other cases. Generally, their ϕ_f deviates greatly from zero except at $x \sim 0.25$ and $x \sim 0.7$. Their first minimum $\phi_f = 0.85$ occurs at $x = 0.125$. Given the exceptionally weak coherence at the same x, the fluctuations bear an extremely weak synchronization. At $x = 0.5$ and 0.9, the fluctuations are completely out of phase, so they essentially do not synchronize at all. It is believed that all the observed weakly synchronized fluctuations result in a significant weakening of the inherent coupling between the developing shear layer and cavity mode. The weakened coupling is responsible for the significantly reduced cavity acoustic fluctuation p_a' by 54% of *RC* (Figure 3.10(c)) in contrast with only 16% reduction observed in *EP*1 and *EP*2 cases. It is also responsible for the variations of the shear layer pressure fluctuations p_s' in all cases with panel (Figure 3.10(d)). The p_s' in *EP*1 and *EP*2 cases are consistently weaker than the *RC* case across the entire cavity opening. In *EP*3 and *EP*4 cases, the acoustic excitation on shear layer growth is almost fully suppressed in the vicinity of the cavity leading edge and prominent shear layer growth appears to be delayed to a downstream location $x \sim 0.25$ (supported with forthcoming discussions in conjunction with Figure 3. 11(d) & (e)) . This gives rise to a thinner shear layer of more concentrated vorticity than the *RC* case, so its impingement at the cavity trailing edge produces stronger p_s' fluctuations between $0.65 < x \leq 1$. However, due to

the aforementioned weakened coupling and completely out-of-phase relationship between the shear layer and cavity mode, the stronger pressure fluctuations are not effectively transformed into cavity noise radiation. The stronger pressure fluctuation p_s' in the vicinity of the cavity trailing edge is also observed in the *EP*5 case, which might be attributed to the local flow-panel interaction on shear layer impingement. Such stronger pressure fluctuation not only produces stronger acoustic excitation for more vigorous shear layer growth, an increase in p_s' by ~ 100% at x = 0, but also amplifies cavity noise radiation through the same coupling between the shear layer and cavity mode as the *RC* case.

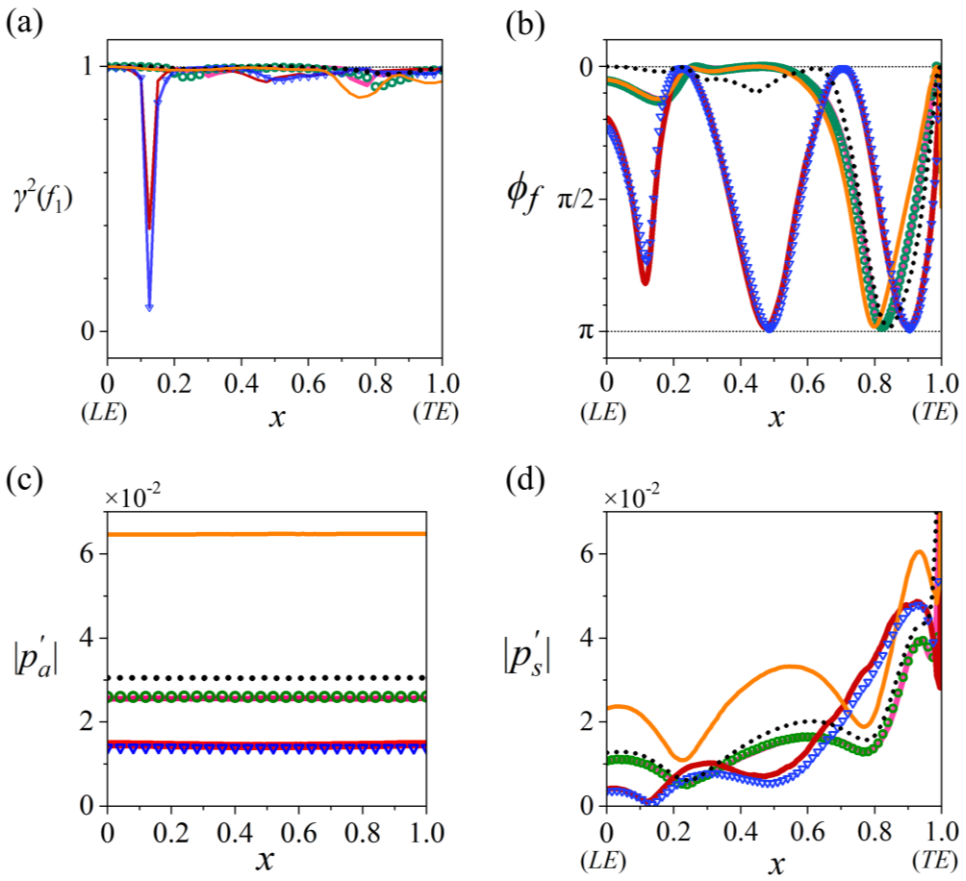

Figure 3.10 (a) Coherence between shear layer pressure p_s' across cavity opening (y = 0) and acoustic pressure p_a' at cavity bottom center. (b) Phase difference between p_s' and p_a'. (c) Variation of FFT transformed p_a' magnitude across the cavity bottom (d) Variation of FFT transformed p_s' magnitude across cavity opening. ..... , *RC*; ——— , *EP*1; ——— , *EP*2; ——— , *EP*3; ——— , *EP*4; ——— , *EP*5.

To apprehend the effects of panels on the coupling between the developing shear layer and the cavity mode, Figure 3.11 depicts the pressure fluctuations along the cavity front and aft walls in all cases, along with the root-mean-square pressure distributions in coloured sub-plots. In the Figure 3.11, only the line plots of FFT transformed pressure magnitudes $|p'|$ are normalized by the FFT transformed acoustic pressure magnitude at the cavity bottom $|p'_a|_{RC}$ of the *RC* case. Evidently, there is a common feature in all the pressure distributions along the walls. Every pressure magnitude outlines a variation in the form of cosine function from its maximum at the cavity bottom, which substantiates the presence of an acoustic standing wave spanning from the cavity bottom. In the *RC* case, the standing wave fills almost the entire cavity, as illustrated by the pressure magnitude variation on the front wall. There is a strong nonlinear pressure variation within y > - 0.5 on the aft wall due to the shear layer impingement. The coupling between the shear layer and cavity standing waves between the walls is evident for the same range of y. These observations agree favourably well with the analysis by Ho and Kim (2021). The associated p'_{rms} distribution of *RC* case clearly shows the separation of acoustic and aeroacoustic regimes for cavity noise development that is consistent with the result of frequency-wave analysis discussed earlier (Figure 3.4(c)). In *EP*1 and *EP*2 cases, the weakening of the coupling between the shear layer and cavity mode is obvious with the shift of the boundary between acoustic and aeroacoustic regions down the cavity depth resulting in shorter standing wave wavelength. In addition, the magnitude of standing waves in these cases is reduced to 20% to 25% of *RC* case, which implies that the acoustics inside the cavity takes less energy from flow fluctuations through coupling to build up.

The coupling further weakens in *EP*3 and *EP*4 cases as their standing wave magnitudes are reduced to 42% to 48% of *RC* case. In addition, their wavelengths are further shortened, which gives a prominent shift of dominant cavity noise frequency from f = 0.925 to f = 1.25. Their associated p'_{rms} distributions show a clearer separation between acoustic and aeroacoustic regions. In the *EP*5 case, the effect of the coupling is so strengthened that it gives a standing wave of a similar wavelength as *RC* (and the same dominant cavity noise frequency) but with a significant increase in magnitude by almost doubling the *RC* value.

A careful study of all the p'_{rms} distributions, as illustrated in Figure 3.11, gives an interesting observation. In *RC*, *EP*2, *EP*3 and *EP*5 cases, along the direction of shear layer development y = 0, the contours of pressure fluctuations show substantial growth at more or less the same location inside the shear layer region. This shows that in all these cases, the coupling between the emerging shear layer and the cavity mode acoustic excitation (process [b] in Figure 3.6) is effective at a location very close to the cavity leading edge. As a result, the occurrence of the associated aeroacoustic coupling processes responsible for Rossiter self-synchronized flow fluctuations are very similar, so all these cases give rise to the same dominant cavity noise frequency f_1 = 0.925 = St_2 from Eq. (3). However, in *EP*3 and *EP*4 cases, the growth of the shear layer appears to be delayed to a location downstream by a distance ~ 0.2 from the cavity leading edge along y = 0. As such, the effective length for shear layer growth in these two cases is effectively shortened to only ~0.8L. If we take this shorter effective shear layer length and the effective κ ~ 0.498 from the ($k - f$) spectra across cavity opening in *EP*3 and *EP*4 cases for the calculation of Eq (3),

it is surprising to see the St_2 obtained is equal to 1.206. Such value of St_2 deviates from the dominant f_1 = 1.25 by only 4.7%. Hence this close agreement implies that the mounting of *EP*3 or *EP*4 panel in the present cavity still allows the original type of Rossiter aeroacoustic coupling (Figure 3.6(b)) to happen but within an effective narrower cavity of the same depth even though all the processes involved in the coupling are suppressed as discussed. This clearly shows that the intended actions of respecting the prevalent flow processes by keeping the basic cavity shape intact with strategic modification of aeroacoustic coupling for overall noise suppression, as stated in Section 3.2, are successfully achieved with *EP*3 and *EP*4 panels.

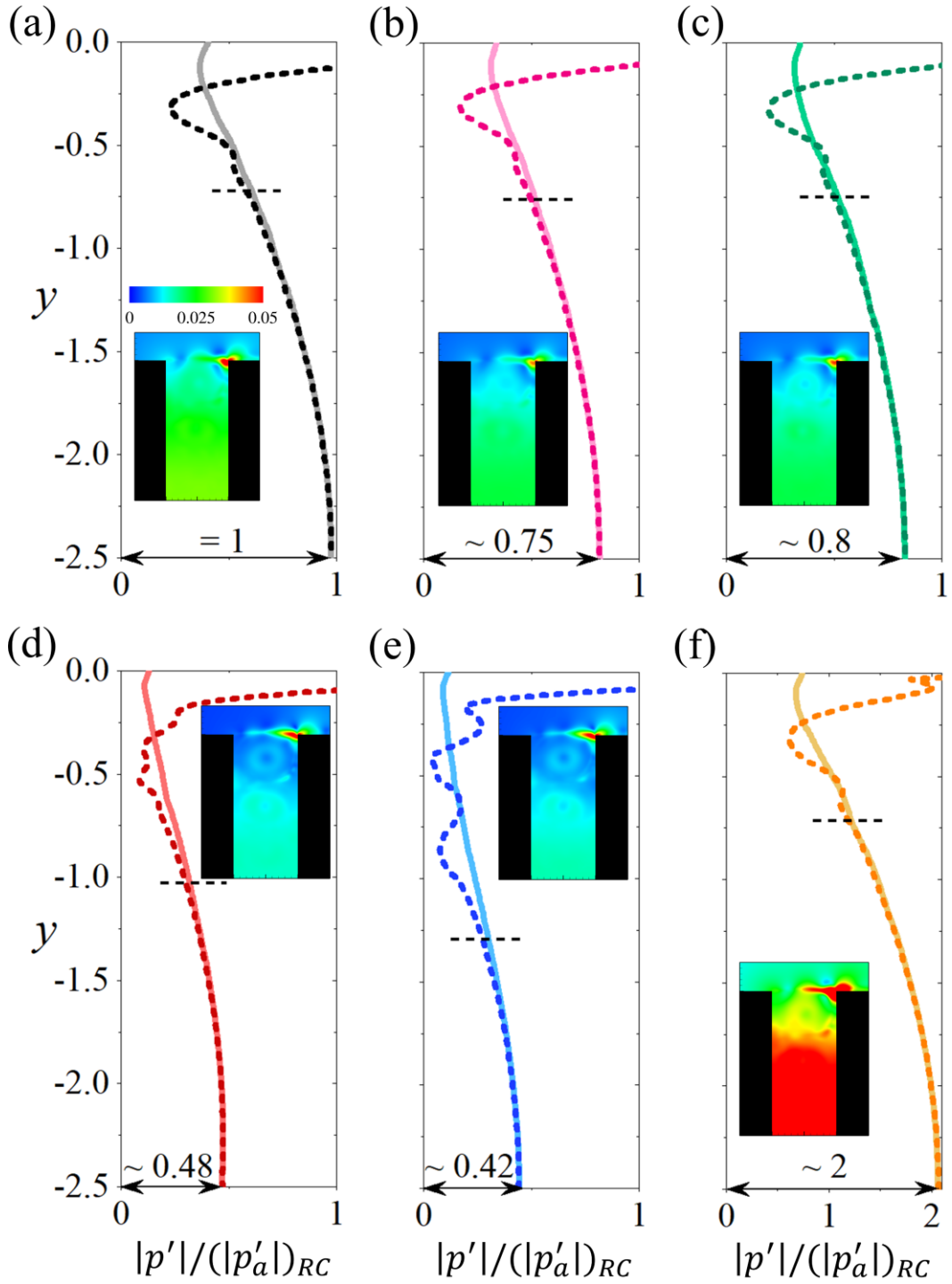

Figure 3.11 FFT transformed pressure fluctuation magnitudes along cavity front (solid line) and aft (dashed line) walls. Every colour plot shows the distribution of root mean squared pressure fluctuation in the respective cases. (a) *RC*, (b) *EP*1, (c) *EP*2, (d) *EP*3, (e) *EP*4 and (f) *EP*5.

3.5 Aeroacoustic-Panel Interaction

It is interesting to see how the acoustically, or aeroacoustically, induced vibration of the elastic panel contributes to the coupling between the developing shear layer and cavity mode in each case. Figure 3.12 shows the time traces (first column) and the corresponding spectra (second column) pressure fluctuations acting at the mid-points of the panels compared with the pressure fluctuations at the same locations in the *RC* case. The figure shows that the aeroacoustic-structural interaction modifies the coupling to a different extent. When the elastic panel is installed near the cavity leading edge, its aeroacoustically-induced vibration is effective in reducing the pressure fluctuation through structural resonance at the designed frequency giving rise to a 20% reduction in magnitude for both *EP*1 and *EP*2 cases. In the *EP*3 case, the acoustically-induced vibration of the elastic panel effectively absorbs incident fluctuation energy at the designed panel frequency from shear layer impingement and leaves much less amount of energy than the *RC* case fed back to close the coupling by excitation of shear layer formation. As a result, the reduction of acoustic pressure on the cavity bottom is as high as 52%. Similarly, the *EP*4 panel case reduces the acoustic pressure fluctuation due to flow-panel interaction by almost 60%. As such, less energy radiates towards the rigid cavity bottom for the formation of a standing wave, so less acoustic energy is fed back to the cavity leading edge to close the coupling. These observations reveal that effective direct absorption of acoustic pressure at the designed panel resonant frequency would leave nonlinear acoustic-structural interaction essentially at frequencies other than panel resonant one to complete the coupling. This might be the reason why a change of dominant radiation frequency prevails in *EP*3

and *EP*4 cases. In the *EP*5 case, the nonlinear aeroacoustic-panel interaction gives a 30% increase in pressure fluctuation magnitude at the designed panel frequency and sizable contributions at other frequency peaks. They give rise to a strong coupling and a much louder cavity noise as a result. The third column of Figure 3.12 depicts the pressure magnitudes along the panels of all cases. The pressure magnitudes in *EP*1 and *EP*2 cases give good support to the delay of shear layer growth due to the modified coupling discussed in the previous section. The significant reduction of acoustic pressure from the panels in *EP*3 and *EP*4 cases is noticeable. In the *EP*5 case, the intensification of pressure fluctuation by nonlinear aeroacoustic-panel interaction is fairly uniform along the panel.

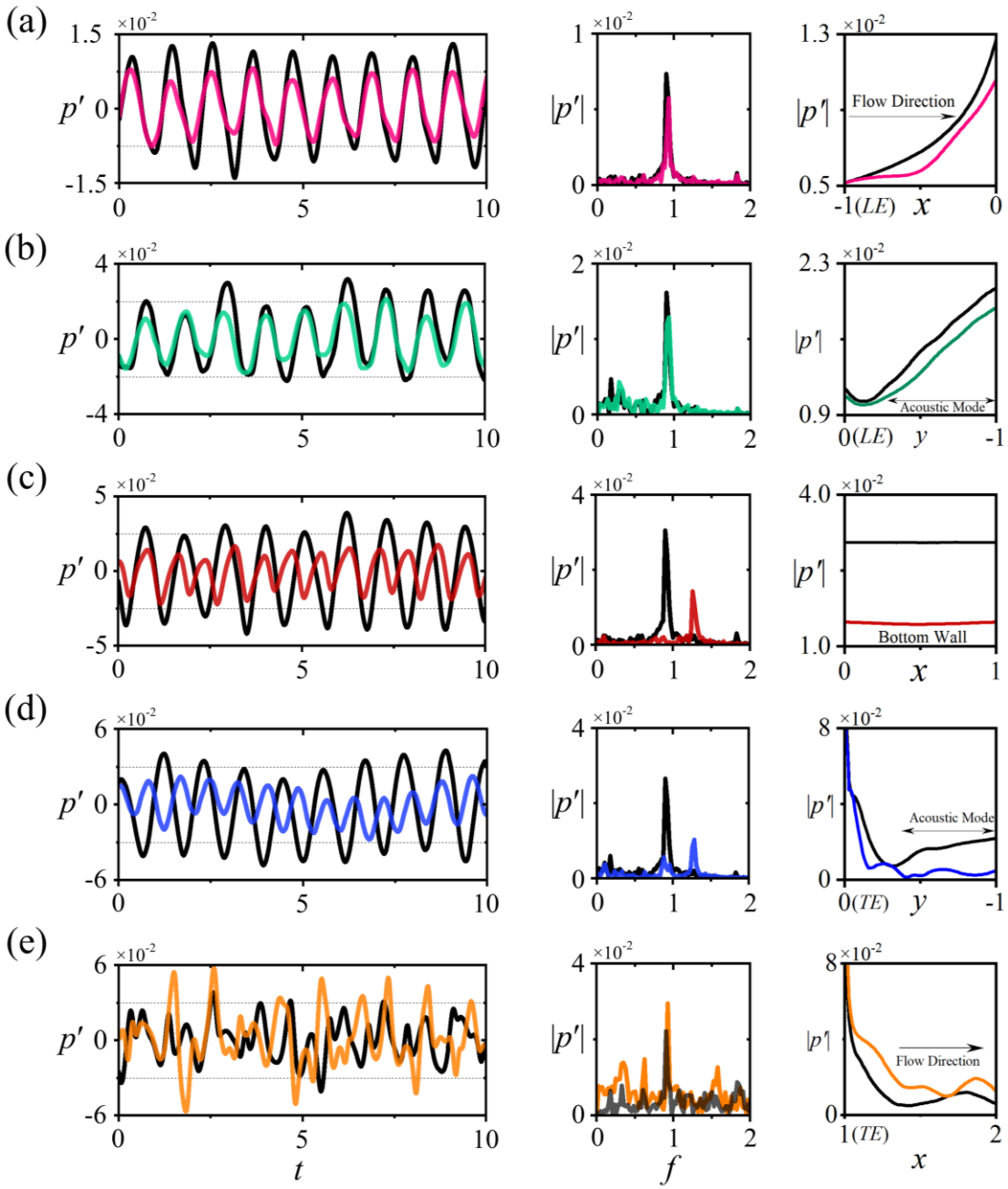

Figure 3.12 Temporal (first column) and spectral (second column) distribution of the pressure instabilities at the midpoint of the flow-panel interface and spatial variance of pressure fluctuation (third column) across the panel length and compared with the rigid wall (in black) of a) *EP*1, b) *EP*2, c) *EP*3, d) *EP*4 and e) *EP*5.

Figure 3.13 shows the temporal displacements of all panels together with their vibratory acceleration spectra obtained from panel mid-points. Evidently, the *EP*1 panel responds to vibrate at the designed resonant frequency. The standing wave pattern in the third fluid-loaded panel resonant mode along the panel persists over time with minor contributions from its two lower-order modes. A similar standing wave pattern prevails in the *EP*2 panel, but it is highly skewed by the emergence of a traveling bending wave bouncing between two ends of the panel at a frequency very close to the first panel resonant mode, which is thus also excited. The *EP*2 panel is entirely embedded in the region for acoustically excited shear layer formation, so it gives a much stronger vibratory response than the *EP*1 panel. These two observations reveal that the panels are able to absorb energy from flow unsteadiness around the cavity leading edge as desired to sustain their resonant vibration. However, the presence of a traveling bending wave in the *EP*2 panel might make its energy absorption by its standing wave counterpart less effective, so the overall modification of the coupling between the shear layer and cavity mode is comparable to the *EP*1 case.

It was illustrated in Section 3.3 that the panels in *EP*3 and *EP*4 cases act to modify the cavity aeroacoustic coupling in such a way that the cavity Rossiter feedback mechanism operates in an effective narrower cavity of the same depth and results in the flow fluctuations dominant frequency shifted from $f = 0.925$ to $f = 1.25$. Coincidently, the new dominant frequency matches the fourth mode of the resonant panel frequency (Table 3.2), but the panel responses in *EP*3 and *EP*4 cases are completely different. The entire length of the *EP*3 panel responds to the incident acoustic excitation in a way that its vibratory displacement is coherent along its length (Figure 3.14). It vibrates like a rigid body rather than

locked into any of its natural panel resonant modes. Nevertheless, a sustained standing wave on the panel is still obvious. Compared to the *EP*1 case, the stronger response of the *EP*3 panel imparts stronger energy absorption for its more effective weakening of feedback processes for closing the coupling and consequently lower overall cavity noise radiation. Its new characteristic frequency of aeroacoustic feedback appears to excite a new cavity mode with a shorter quarter wavelength than in the *EP*1 case (Figure 3.11). Similar observations can be made in the *EP*4 case. Owing to highly unsteady flow-panel interaction upon shear layer impingement, the panel responds to lock its vibration into the fourth panel resonant mode with mild contributions from its second and third modes. Although the panel vibratory response of the *EP*4 panel is stronger, its energy absorption is less effective due to the more complex standing wave pattern of shorter wavelengths, so the weakening of feedback processes for aeroacoustic closing the coupling is comparable to the *EP*3 case. The *EP*5 panel is directly exposed to the strong unsteady pressure fluctuations of the flow after shear layer impingement. It gives a sustained standing wave pattern similar to the *EP*1 case but with the strongest vibratory response among all cases.

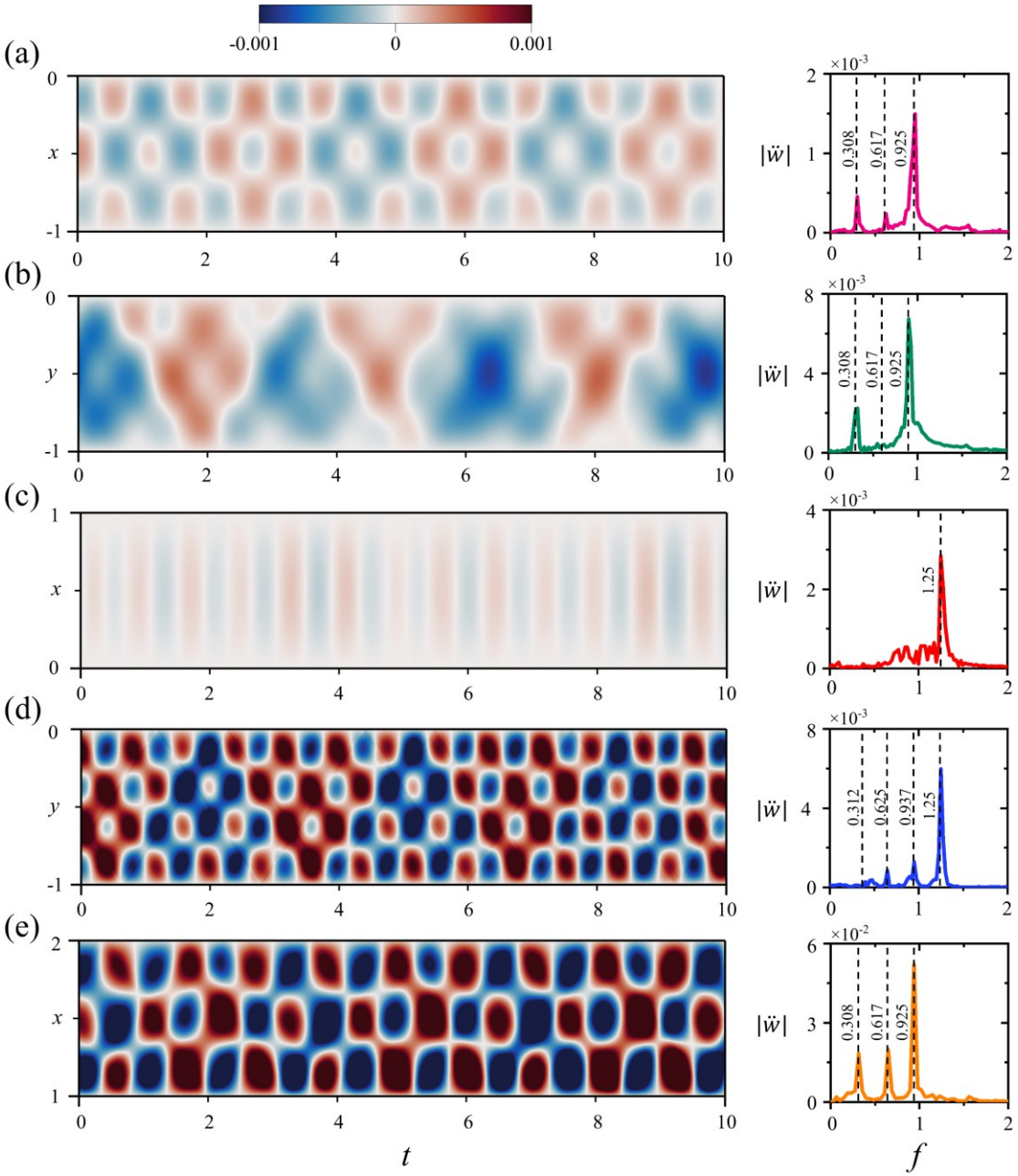

Figure 3.13 Panel vibratory responses. (a) *EP*1. (b) *EP*2. (c) *EP*3. (d) *EP*4. (e) *EP*5. The dashed vertical lines show the first four panel modal frequencies predicted with Eq. (3) with n = 1, 2, 3, and 4.

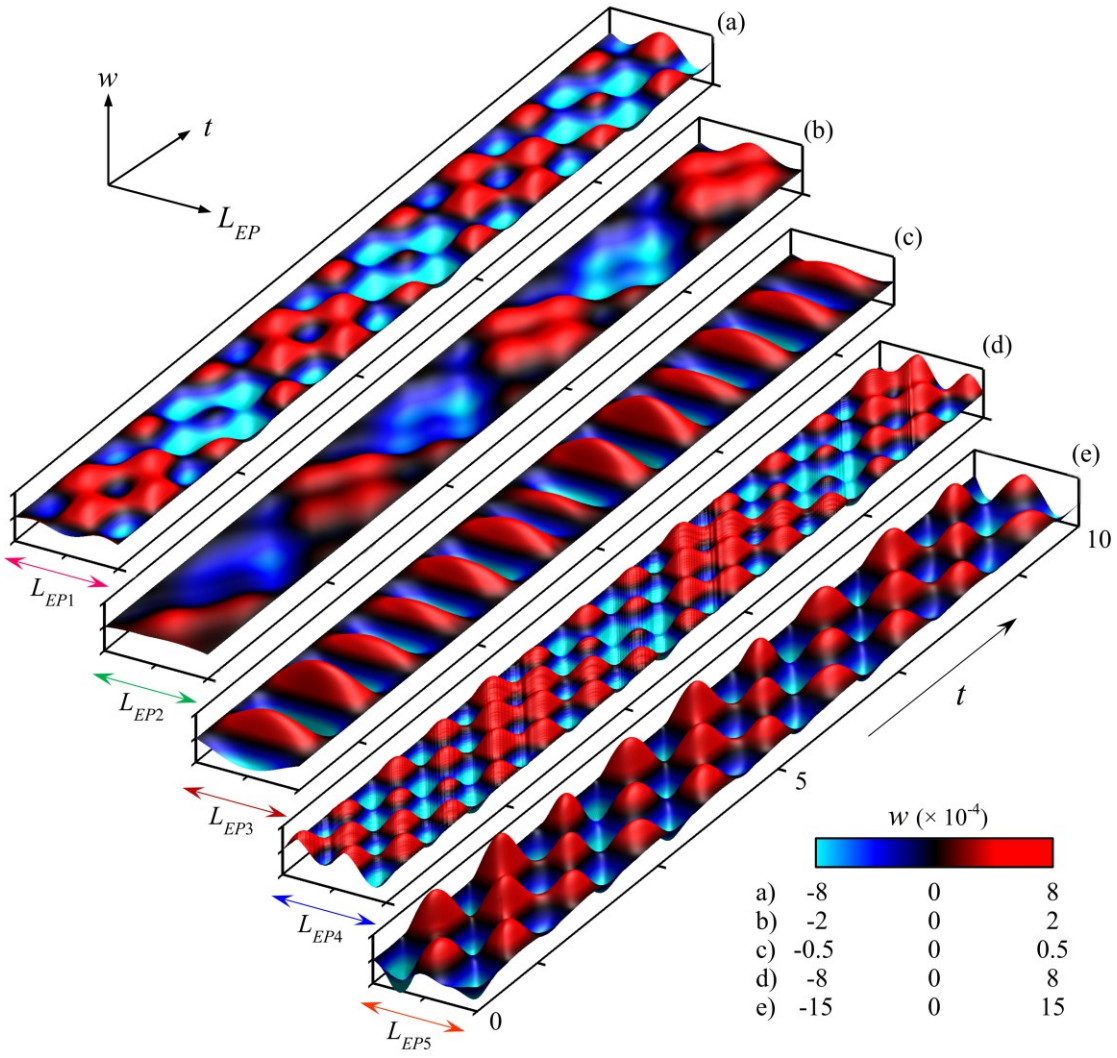

Figure 3.14 Three-dimensional presentation of Elastic panel modal response to the flow-acoustic excitation in space-time domain, a) *EP*1, b) *EP*2, c) *EP*3, d) *EP*4 and e) *EP*5.

3.6 Summary

This paper reports a unique passive control concept for deep cavity noise suppression using localized surface compliance by invoking the flow-induced structural resonance of an elastic panel embedded in cavity walls. The concept is thoroughly studied with the tonal noise response of a deep cavity of the length-to-depth ratio of 0.4 exposed to a flow of Mach number M = 0.09 and Reynolds number $Re = 4 \times 10^4$. The rigid cavity flow characteristics are taken as the basic framework for the elastic panel design. Subsequently, various panel–cavity configurations built on strategically mounted panel locations are attempted to study the effectiveness of the proposed idea for cavity noise suppression.

The spatio-temporal aeroacoustic-structural interaction between the elastic panel and fluid resonant fluctuations of the deep cavity is numerically studied using direct aeroacoustic simulation in two dimensions. After validation with existing experimental results, the numerical solution of flow past a fully rigid deep cavity is thoroughly studied by means of comprehensive wavenumber-frequency analyses. The same type of interaction between the developing shear layer and cavity acoustic mode and its eventual noise radiation to far-field, as reported in existing numerical and experimental works, is identified from the numerical solution. All the five key flow processes of the cavity aeroacoustic feedback are deciphered, namely the boundary layer growth upstream of the cavity leading edge, acoustically excited shear layer growth, cavity acoustic standing wave formation, excitation of cavity mode by shear layer impingement at cavity trailing edge, and the highly unsteady flow subsequent to the shear layer impingement. The elastic panel is assumed to be

made of elastomeric material, and its structural properties are designed to ensure that one of its fluid-loaded natural frequencies is equal to the dominant frequency of the resonant flow fluctuation of the rigid cavity. The panel is then strategically set to be exposed to each of the key flow processes identified so as to ascertain its effects on the modification of every process for cavity noise suppression. Panel structural resonance prevails in all cases. The interaction with the first four flow processes for the cavity aeroacoustic feedback gives noise suppression to a different extent, but that with the fifth process gives noise amplification. Significant noise suppression can be obtained with a panel that is allowed to modify the cavity acoustic standing wave formation or excitation of cavity mode by shear layer impingement at the cavity trailing edge. Both are able to give the reduction in cavity noise pressure level and power level up to 3.8 dB and 4.8 dB, respectively.

An extensive study of the physical mechanism behind the noise suppression cases reveals that the presence of the elastic panel completely alters the aeroacoustic coupling of the key flow processes responsible for cavity flow resonant fluctuation. The coherency between the shear layer growth and cavity mode acoustics, as observed in the rigid cavity, is grossly weakened due to the imposed surface compliance. That results in a change of the dominant frequency of cavity aeroacoustic feedback to a higher value. The loss in coherency is almost complete in the proximity of the cavity leading edge, so the growth of the shear layer is effectively delayed to further downstream of it. It leads to the occurrence of cavity aeroacoustic feedback in an effective narrower cavity of the same depth. The associated flow processes of the aeroacoustic coupling are weakened by the structurally vibrating resonant panel, so the eventual cavity flow noise is reduced. Further analysis of the aeroacoustic-

structural interaction of the panel provides details of how it responds to absorb the flow and acoustic fluctuation energies. Successful noise suppression comes with an unforeseen advantage. The presence of the panel gives rise to a reduction of overall cavity drag by almost 19% from its rigid cavity counterpart, which may helpful in reducing the consumption of flow energy required to drive the cavity flow. Therefore, the present paper confirms the feasibility of the proposed use of strategically placed surface compliance that is not only effective in modifying the fundamental deep cavity tonal noise mechanism but also in achieving noise suppression and drag reduction to the cavity yet retaining the basic problem geometry intact. All these features are considered important in many practical applications.

Chapter 4

Experimental Verification of Deep Cavity Noise Suppression by Surface Compliance

In this chapter we experimentally investigate a novel passive technique for suppressing tonal noise in deep cavities, focusing on the strategic use of surface compliance. An experimental setup was designed, featuring a deep cavity with an elastic panel flush-mounted at the cavity bottom. This experimental study primarily aims to verify a unique concept of cavity noise suppression that has been previously explored numerically in Chapter 3, involving the use of surface compliance, provided by an elastic panel strategically positioned across critical locations on the cavity walls. The core idea hinges on exploiting the aeroacoustic structural interaction, where an elastic panel mounted at the cavity bottom wall is excited by the incident cavity acoustic mode, thereby dissipating its energy into panel vibrations. This interaction is expected to disrupt the aeroacoustic processes within the cavity, thereby influencing the overall noise emissions.

Moreover, this chapter also seeks to experimentally investigate the mechanism of cavity noise reduction through the decoupling of the cavity shear layer and acoustic mode using the described method. A key aspect of this approach is its non-invasive nature, contrasting with traditional methods; it aims to maintain the overall characteristic features of cavity flow while subtly and intuitively altering the interaction between the shear layer and the cavity acoustic mode. Therefore, a detailed exploration of the shear layer dynamics and cavity acoustic mode has also been performed. Lastly, the study will experimentally ascertain the ultimate noise reduction potential of this scheme, which could inform its transition to practical implementation in real-world engineering applications, as we have provided an elaborative design strategy for our novel cavity-panel configuration. Pressure measurements of cavity flow and farfield noise, along with Particle Image Velocimetry (PIV), were utilized to capture the interactions between flow dynamics and the cavity acoustic response. The experimental results demonstrated that the panel effectively altered the aeroacoustic pattern inside the cavity, leading to a noticeable reduction in tonal noise up to 16.1 dB, particularly at specific flow velocities, 20 and 30 ms^{-1}, where the interaction between shear layer oscillations and cavity acoustic modes typically strengthens aeroacoustic resonance. The chapter provides a detailed analysis of the modified aeroacoustic feedback mechanisms due to the introduction of the elastic panel. A comparison of acoustic spectra between the baseline rigid cavity configuration and the modified cavity-panel setup revealed that the panel not only reduced the peak noise levels but also shifted the dominant acoustic frequencies, suggesting a disruption in the typical aeroacoustic coupling processes. These findings highlight the potential of using compliant surfaces to passively control aeroacoustic emissions in practical

applications, offering a promising alternative to more invasive noise mitigation strategies. The experimental campaign was conducted in collaboration with the A3 Lab team at the Southern University of Science and Technology (SUSTech), Shenzhen, as part of the candidate's research exchange program, supported by PolyU.

4.1 Experimental Setup

4.1.1 Aeroacoustic Wind Tunnel

The experimental study is carried out in a low-velocity, closed-circuit, open-jet wind tunnel at the Department of Mechanics and Aerospace Engineering, Southern University of Science and Technology (SUSTech) (Yang *et al.* 2021) as illustrated in Figure 4.1. The test section of the wind tunnel, which corresponds to the nozzle exit, features a rectangular cross-section with dimensions of 600 mm × 550 mm. The wind tunnel is capable of achieving flow velocity up to 70 ms^{-1} within the test section, with an accompanying turbulence intensity of 0.15% in the incoming nozzle flow. The wind tunnel resides inside an anechoic chamber with internal dimensions of 3.8 m × 5.7 m × 3 m (Figure 4.1(a)). To ensure a quasi-two-dimensional flow across the cavity model, a pair of rectangular endplates, each 800 mm in length, are aligned with the nozzle exit. The cavity model is vertically positioned between these plates (Figure 4.2(b), situated 270 mm downstream from the nozzle exit. Consequently, the model is effectively located within the potential core of the nozzle jet flow. The wind tunnel acoustic background noise at 25 ms^{-1} is 20 dB (relative to 20 μPa reference pressure), measured 1m from the center of the jet at 1m vertical height

outside the main flow. The study is carried out with nozzle flow velocities ranging from 10 to 40 ms^{-1} with 5 ms^{-1} increments.

(a) *Experimental Setup*

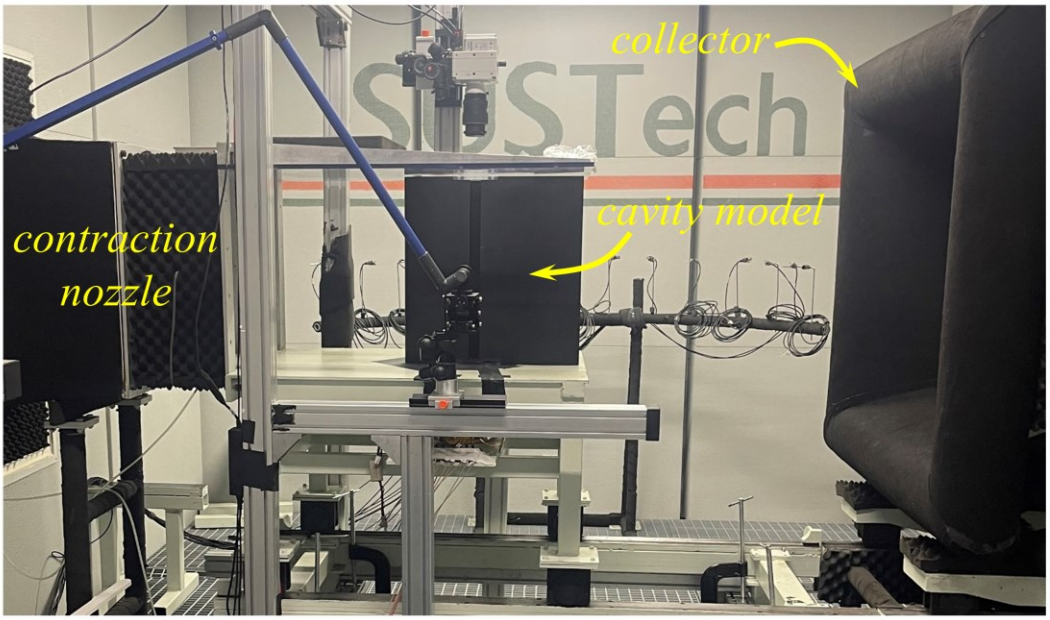

(b) *Schematic of Cavity Flow Model Setup*

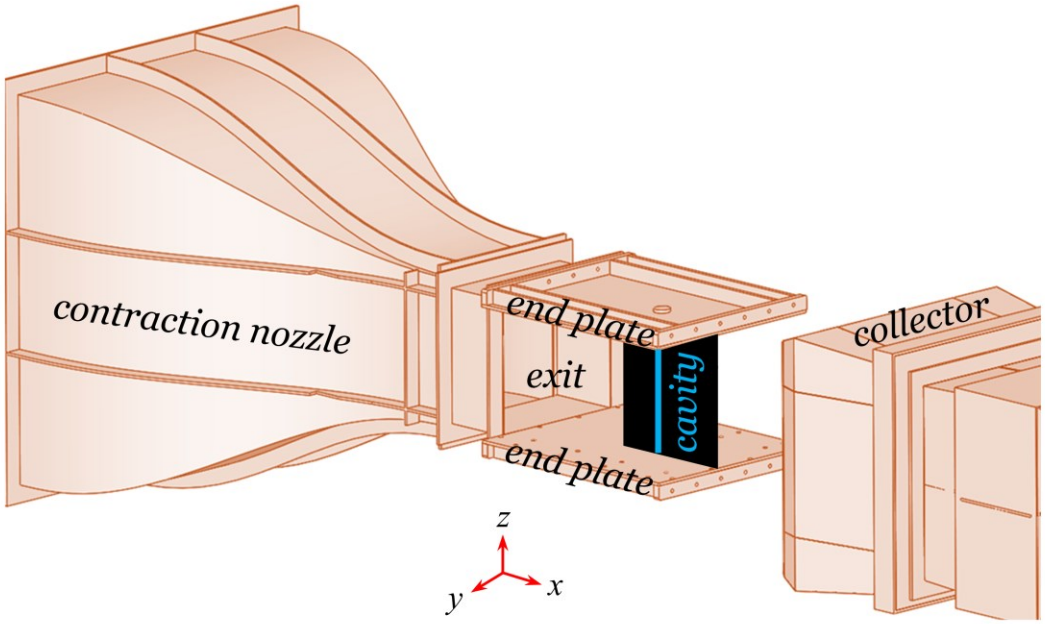

Figure 4.1 Experimental arrangements of open cavity flow, instrumented with surface and far-field microphones and PIV setup in the aeroacoustic wind tunnel (b) schematic diagram depicting the cavity flow model setup.

4.1.2 Cavity Flow Measurements

Characteristic flow pressure measurements are carried out by employing two pressure taps shown as *mic*2 and *mic*3 in Figure 4.2(a), strategically positioned along the cavity median. The first pressure tap is located near the cavity trailing edge at (x, y) = (30 mm, -7.5 mm) while the second pressure tap is located near the cavity bottom at (30 mm, -67.5 mm), as delineated in Figure 4.2(a). The pressure tap *mic*2 is located in the shear layer impingement region to capture the unsteady shear layer signatures of the certain flow and tested rigid cavity/panel configurations. Similarly, *mic*3 is located near the cavity bottom region to capture the acoustic signature of the cavity depthwise mode across the cases. Such a choice of microphone locations is informed by our previous study (Naseer *et al.* 2023b). Each pressure tap featured a Panasonic WM-61A microphone with a 2 mm effective diaphragm diameter. The Panasonic WM-61A microphones, renowned for their extensive application in previous research (Angland *et al.* 2012; Vemuri *et al.* 2020; Maryami and Liu 2024), were selected for their proven fidelity in capturing pressure fluctuations within the 20 Hz to 10 kHz frequency range.

4.1.3 Cavity Noise Measurement

Acoustic signals in the far field were quantified utilizing a Brüel & Kjær Type 4966 free-field microphone (depicted as *mic*1 in the discussion ahead) placed orthogonal to the airflow at a standoff distance of 400 mm from the central axis of the cavity, depicted as *mic*1 in Figure 4.2(a). Data acquisition for both aeroacoustic flow pressure and far-field acoustic emissions was performed concurrently by employing a National Instruments PXI-10420 chassis

equipped with a pair of synchronized 24-bit NI PXI-4496 data acquisition cards, operating at a sampling rate of 51.2 kHz across a duration of 20 seconds. For spectral analysis, the time-series pressure data were transformed into the frequency domain utilizing a Fast Fourier Transform (FFT) algorithm with a Hamming window function and 50% overlap, adhering to Welch method, thus achieving a frequency resolution of 2 Hz. Subsequently, the obtained spectra were processed to yield power spectral density (*PSD*) estimates, denoted with the unit dB/Hz for flow pressure and far-field acoustic fluctuations.

4.1.4 PIV Setup

Cavity acoustic phenomena sprouts from the shear layer evolution and trailing edge impingement, identified as the primary locus of noise generation, is investigated through a high-speed planar Particle Image Velocimetry (PIV) system. The scrutinized measurement domain, encompassing an approximate area of 40 mm × 30 mm, spanned across the area between the cavity leading and trailing edges where the aeroacoustic regime dominates the flow. This region is delineated by the rectangular green illuminated zone presented in Figure 4.2(a) and Figure 4.2(b). PIV experiments were conducted for both cavity configurations (*RC* and *EP*) and free-stream velocities 20 and 30 ms^{-1}. The flow was populated with dioctyl sebacate particles, with a mean diameter of 1μm, to serve as tracer particles. A Photonics Nd:YAG laser, delivering 45 mJ pulses at a repetition rate of 1000 Hz, was strategically placed outside the flow field. Light-sheet optics were utilized at upfront transverse direction of the cavity to illuminate the tracer particles.

Flow field imaging was accomplished using a Phantom VEO410L camera (resolution: 1,280 × 780 pixels, 12-bit, pixel pitch: 20 μm) paired with a Nikon 100 mm lens at an f/4 aperture setting. The camera was positioned approximately 500 mm from the measurement area at mid-span, which yielded an optical magnification of around 0.2. The LaVision DAVIS 10.0 software suite, in conjunction with a LaVision Programmable Time Unit, facilitated the synchronization of laser pulsing and camera triggering, as well as the image acquisition. The PIV system operated at a sampling frequency of 3.05 kHz, capturing images over a 2.72 seconds interval, which resulted in a comprehensive collection of 8297 double-frame images. This comprehensive dataset was subjected to processing through an iterative multipass algorithm, culminating in a final interrogation window dimension of 32 × 32 pixels, with an overlap factor set at 75%. To mitigate the influence of specular reflections from the surface during the PIV procedure, the surface of the cavity-embedded base structure received a matte black coating. Moreover, careful adjustment of the laser illumination incidence angle was performed to optimize the visualization of the seeded flow. This precise alignment of the laser angle was pivotal in reducing the quantity of light directly reflected into the camera sensor, thereby substantially enhancing the quality of the resultant images for PIV evaluation.

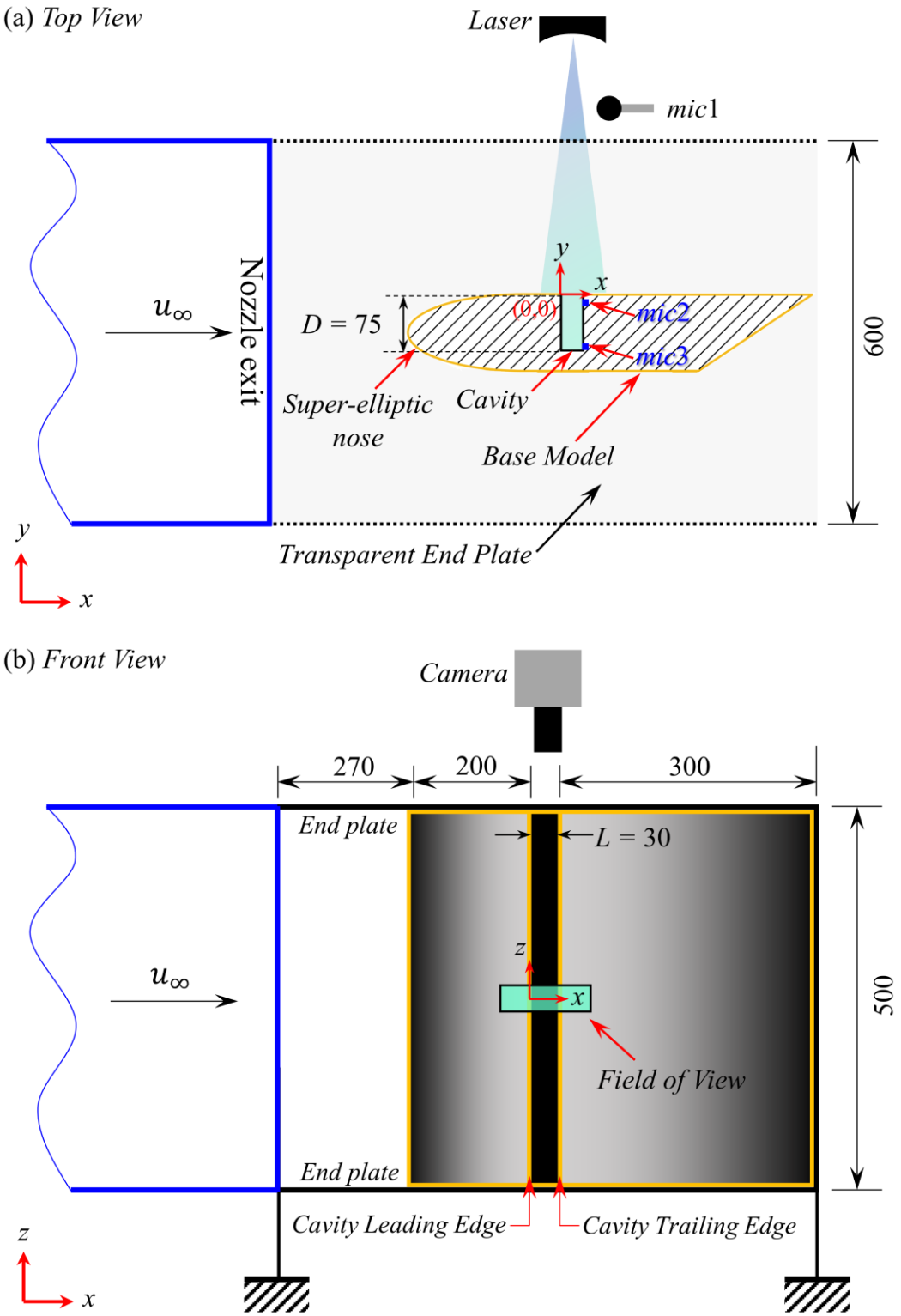

Figure 4.2 Cavity flow model and instrumentation setup, (a) top view, (b) front view. Units for dimension: mm.

4.1.5 Design of Cavity Model and Elastic Panel

An open cavity with length L = 30 mm, depth D = 75 mm and vertical span W = 550 mm is taken. It is prepared in the form of a cutout from a model base structure 530 mm long and 100 mm thick (Figure 4.2(a) and Figure 4.3(c)). Its span is 550 mm which gives a perfect fitting between the two endplates for ensuring two dimensionality of flow around the cavity. The choice of the length-to-depth ratio (L/D = 0.4) is the same as in the numerical study of Naseer *et al.* (2023b). In the present study, a coordinate system is set with its origin positioned at the center point of the leading edge of the cavity. The x-, y- and z-axes are set along the streamwise direction, cavity depth and cavity model span respectively.

The cavity-embedded base structure consists of a 150 mm long super-elliptic nose section following the recommended specifications to avoid flow separation (Narasimha and Prasad 1994). The downstream side of the super-elliptic nose section is connected to a 230 mm long parallel section of 100 mm thickness and a 150 mm long tapered tail section with a 30° apex angle. The trailing edge geometry is inspired by Moreau *et al.* (2012) work as they showed that the sharp-edged flat plate tends to produce broadband noise. Therefore, it was helpful to have a distinguishable cavity tonal noise largely unaffected by the base model noise. A modular experimental rig was manufactured to accommodate both the rigid cavity, identified as *RC*, baseline case (Figure 4.3(a)) as well as the cavity-panel configuration, defined as *EP* in Figure 4.3(c), to verify the aeroacoustic suppression effect. The cavity modular design is actually based on five different parts, the upstream super-elliptic nose, the sharply tapered downstream plate and the former and latter are fixated together

by a bottom plate and two small transparent plates are punched across the base structure to expose the cavity cutout section for the PIV instrumentation. For the *RC* case, a rigid plate of dimension 130 mm × 25 mm × 550 mm is inserted at the cavity bottom.

The specific choice of the mounting location of the elastic panel at the cavity bottom was informed by Naseer *et al.* (2023b). Among the five distinct aeroacoustic processes (each supported by different cavity walls) as shown in Figure 4.3(b) using an elastic panel, two configurations EP_{aft} and EP_{bottom} distinguished themselves by significantly suppressing cavity noise. The case EP_{aft} aimed to pacify the shear layer impingement process at the cavity aft wall, while the case EP_{bottom} focused on mitigating the incident cavity acoustic mode. Comparable in performance, both the configurations showed high effectiveness in noise suppression up to 4.8 dB (Figure 4.3(b). However, the relatively simpler design and easier implementation of the EP_{bottom} panel encouraged its selection for our experimental campaign.

In addition to the panel mounting location, a critical aspect of the panel design strategy is ensuring that the natural frequency of the elastic panel, under fluid loading, matches the dominant flow frequency of the targeted *RC* case and in the current scenario, the targeted frequency is 1585 Hz at a freestream velocity of 30 ms^{-1}, where the cavity generates its maximum acoustic response. To achieve the desired aeroacoustic-structural resonance condition, the fluid-loaded panel natural vibration frequency for the desired mode (n) with fixed-end boundary conditions is calculated using the formula $(f_{EP})_n = (n/2L_{EP})[(T_{EP}/\rho_{EP}h_{EP})/(1 + L_{EP}/\pi n\rho_{EP}h_{EP})]^{0.5}$. While maintaining the panel length L_{EP} equal to the cavity length, adjustments to the thickness h_{EP} and the

applied tension T_{EP} are made to align the panel frequency with the design requirements. In this study, the panel is assumed to be made of an elastomeric material such as a silicone rubber sheet with a thickness of 0.2 mm, following the recommendations from our previous study (Naseer *et al.* 2023b). To configure the experimental setup for *EP*, the rigid bottom plate of *RC* was replaced by a similarly dimensioned elastic panel embedded into the bottom plate. This panel was stretched and secured over two circular rods, fitting snugly into grooves etched across the adjacent cavity plates. A 10 mm gap was maintained beneath the panel to accommodate expected vibrations. The panel backside was exposed to ambient pressure through a series of large-sized holes in the elastic panel bottom plate. Notably, these backside holes also facilitate the insertion of probes for measuring the panel vibration frequency and tension using the Sonic Tension Meter U-550 by Gates Unitta Asia. This design not only ensures effective aeroacoustic interaction but also facilitates the necessary dynamics of the panel.

(a) *RC*

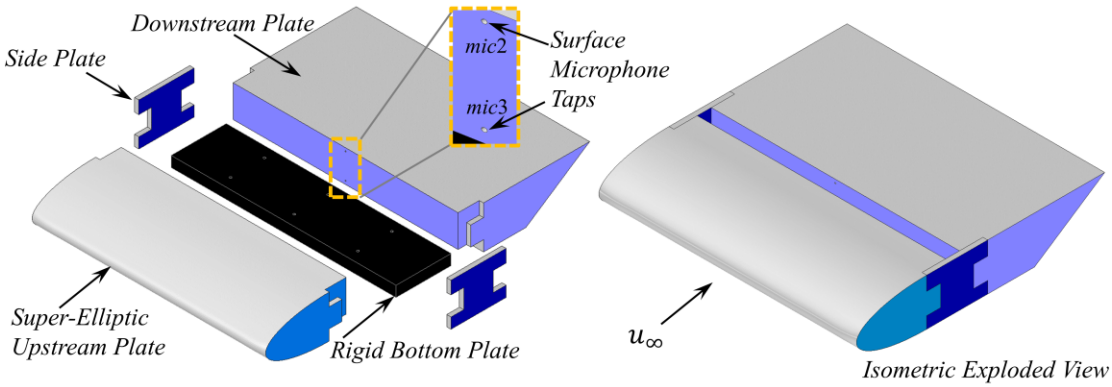

(b) Cavity aeroacoustic processes

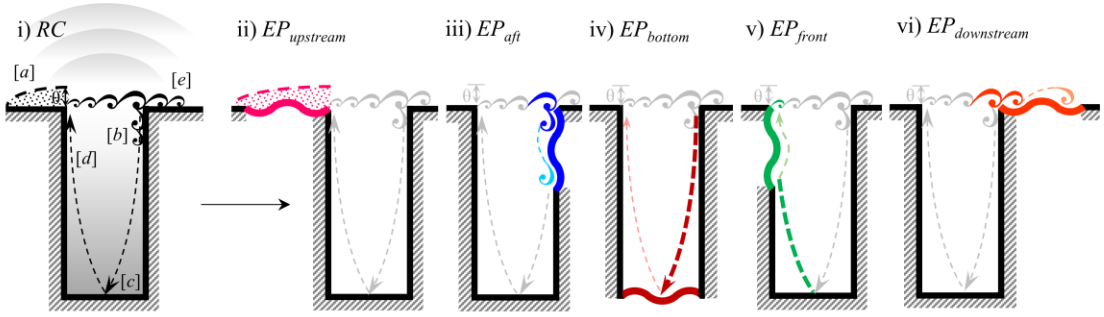

[*a*] *Boundary Layer development* [*b*] *Downwash of impinging Shear Layer* [*c*] *Incident acoustic waves*
[*c*] *Shear layer acoustic reinforcement & Reflected acoustic waves* [*e*] *Downstream vortices convection*

Cases	$EP_{upstream}$	EP_{aft}	EP_{bottom}	EP_{front}	$EP_{downstream}$
Sound Power Level, ΔPWL (dB)	– 1.3	– 4.8	– 4.6	– 1.1	+3.2

(c) *EP*

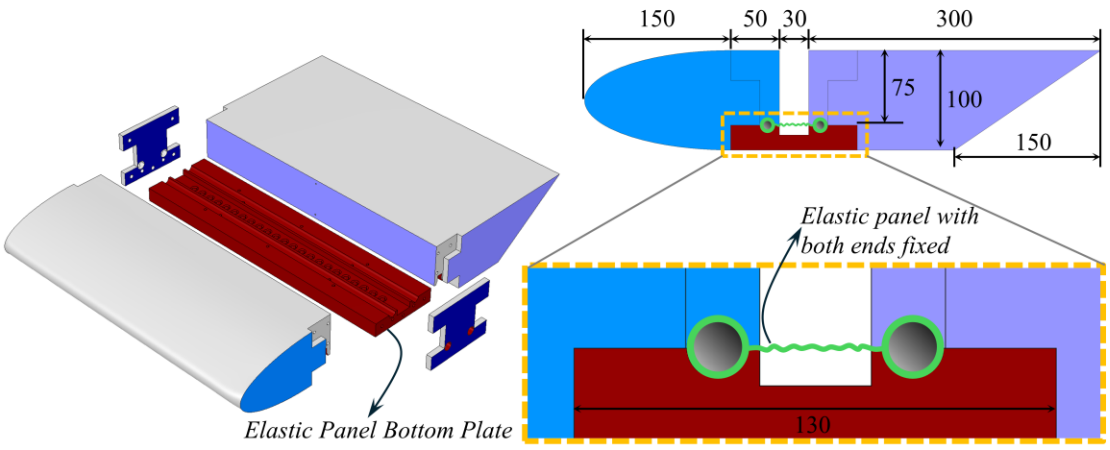

Figure 4.3 Schematic of the physically informed cavity testing model design, (a) exploded views of *RC* modular design, (b) identified physical processes leading to cavity noise generation (Naseer *et al.* 2023b) and the corresponding elastic panel mounting locations for the noise suppression, (c) design of *EP* configuration. Units for dimension: mm.

4.1.6 Boundary Layer Thickness Measurement

Boundary layer thickness specifically at the cavity leading edge (β_0) plays a critical role in the behavior of noise induced by open cavity flow. Accurate measurement of this thickness is essential to ensure that the flow operates within the regime conducive to observing the expected cavity tonal noise behavior. In this context, Sarohia (1977) introduced the parameter, $L\sqrt{Re_{\delta_0}}/\beta_0$ to distinguish between cavity oscillating ($L\sqrt{Re_{\delta_0}}/\beta_0 \gtrsim 0.35 \times 10^3$) and non-oscillating ($L\sqrt{Re_{\delta_0}}/\beta_0 \lesssim 0.35 \times 10^3$) regimes.

For our experimental setup, it was necessary to measure the boundary layer thickness at the leading edge of the cavity. We selected a freestream condition of u_∞ = 30 ms^{-1} (*RC* configuration), where strong acoustic emissions were anticipated, based on our numerical findings (Naseer *et al.* 2023b) which is also vindicated by experimental results ahead shown in Figure 4.5. The boundary layer thickness at the cavity upstream wall, adjacent to the leading edge, was measured using a one-dimensional Dantec hot-wire anemometry streamline pro system. During these measurements, the hot-wire probe was traversed along the transverse direction (y-axis) above the cavity-embedded base structure, with the origin of the axes located at the cavity leading edge.

The hot-wire measurements were conducted at a sampling frequency of 51,200 Hz, with a total sampling time of 20 seconds. The results, as shown in Figure 4.4, display the boundary layer thickness at various probe locations situated at three different points ahead of the cavity leading edge and after the flow passed through the super-elliptic plate of the base structure. A consistent boundary layer thickness of approximately 1.5 mm across these locations

confirms that the boundary layer was fully developed after passing the super-elliptic nose of the base structure. Furthermore, the calculated value of the key parameter, $L\sqrt{Re_{\delta_0}}/\beta_0 \sim 1.1 \times 10^3$, indicates that the cavity flow in this study will operate within the oscillation regime, likely producing a tonal response. This sets the stage to next evaluate the effectiveness of the elastic panel implementation strategy in suppressing such responses.

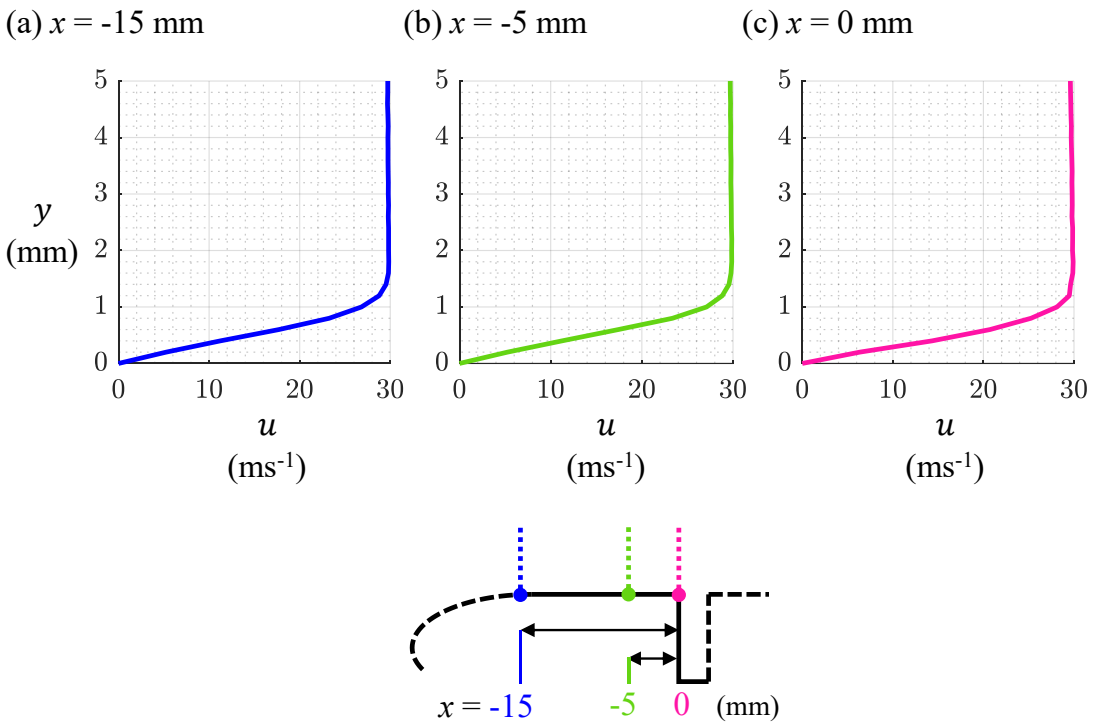

Figure 4.4 Boundary Layer thickness measurements across cavity upstream locations at (a) x = -15 mm, (b) x = -5 mm, (c) x = 0 mm.

4.2 Aeroacoustic characteristics

4.2.1 Rigid Cavity Noise Spectra

Figure 4.5 presents the power spectral density (*PSD*) of acoustic pressure for the *RC* cases, examined across seven free-stream flow velocities (u_∞ = 10, 15, 20, 25, 30, 35 and 40 ms^{-1}). *PSD* is calculated using $PSD\,(\mathrm{dB/Hz}) = 10\log_{10}(p'/p_{ref})$, with reference pressure taken as p_{ref}= 20 μPa and p' is the pressure fluctuation. In order to ascertain the relative impact of base structure noise (absent the cavity feature), the cavity was filled and sealed to render a continuous, uninterrupted plane surface. The comparative analysis reveals that the model noise, with and without the cavity presence, is significantly disparate, exhibiting a difference of up to 40 dB across the relevant frequency range. Moreover, the background noise remains insignificant under all tested free-stream conditions. Given these conditions, the experimental setup offers a robust foundation for investigating cavity-generated noise.

The acoustic signature of the cavity noise features a pronounced tonal peak, indicative of the acoustic and aeroacoustic phenomena occurring inside the cavity confines. The increase in the fundamental frequency of this tonal noise is observed proportionally with the free-stream velocity. Additionally, the broadband noise contribution becomes more prominent across the entire frequency range and is amplified with increasing free-stream velocities. These findings align with the results from prior cavity flow research conducted by (Yokoyama *et al.* 2016; Yokoyama *et al.* 2017), which identified that the peak acoustic response of the cavity occurs at u_∞ = 30 ms^{-1} due to strong aeroacoustic interaction between the shear layer and the cavity acoustic mode. This peak has

been similarly identified in the present experiments, where noise radiation escalates with the free-stream velocity, reaching a tonal peak of 87.4 dB at u_∞= 30 ms^{-1} before reducing to 78.4 dB at u_∞ = 40 ms^{-1}. Instances exhibiting sharp tonal peaks emphasize the predominant influence of aeroacoustic mechanisms in driving the overall noise radiation. However, the coupling strength between the shear layer and acoustic modes varies amongst the cases, influencing the overall acoustic response of the cavity.

Table 4.1 presents a comparison of the peak frequencies obtained from the experimental cases with those calculated using the Heller and Bliss modified Rossiter formula, $f_{Heller\&Bliss}= (m-\alpha)/(\,1/\kappa + M_\infty/(1+(\gamma-1)M_\infty^2/2)^{0.5}\,)$, incorporating a universally chosen set of empirical constants (Heller and Bliss 1975). The comparison reveals a generally good agreement between the experimentally measured Rossiter modes and those predicted by the formula. However, the Heller and Bliss formula tends to overestimate the Rossiter modes with the exception of the condition at a free-stream velocity of 30 ms^{-1}. Deviations between the experimental results and the computed frequencies are ascribed to the application of a uniform set of empirical constants across varying free-stream conditions, which, according to several studies (Yokoyama *et al.* 2020; Naseer *et al.* 2023b), should be custom-fitted for each specific scenario. Additionally, there is a noteworthy comparison between the peak frequencies observed in a previous numerical study of *RC* with a similar aspect ratio (L/D = 0.4) subjected to a free-stream velocity of u_∞= 30 ms^{-1} and its experimental counterpart, with a nominal discrepancy of merely 5%. This congruence further streamlined the numerical and experimental observations.

It is noteworthy that the *RC* noise spectrum for each flow velocity displays a number of tonal peaks corresponding to the Rossiter modes and their higher harmonics. At a freestream velocity of 10 ms^{-1}, there are five tonal peaks, while at 15 ms^{-1} and 20 ms^{-1}, there are three. As the freestream velocity increases, the number of peaks corresponding to the Rossiter modes or their higher harmonics decreases to two or fewer. For velocities of 35 ms^{-1} and 40 ms^{-1}, the prominence of tonal peaks diminishes, and the spectrum assumes a more broadband shape. In summary, the overall cavity flow appears to sustain the aeroacoustic feedback phenomenon, as evidenced by the persistent appearance of Rossiter modes across the range of operating conditions tested.

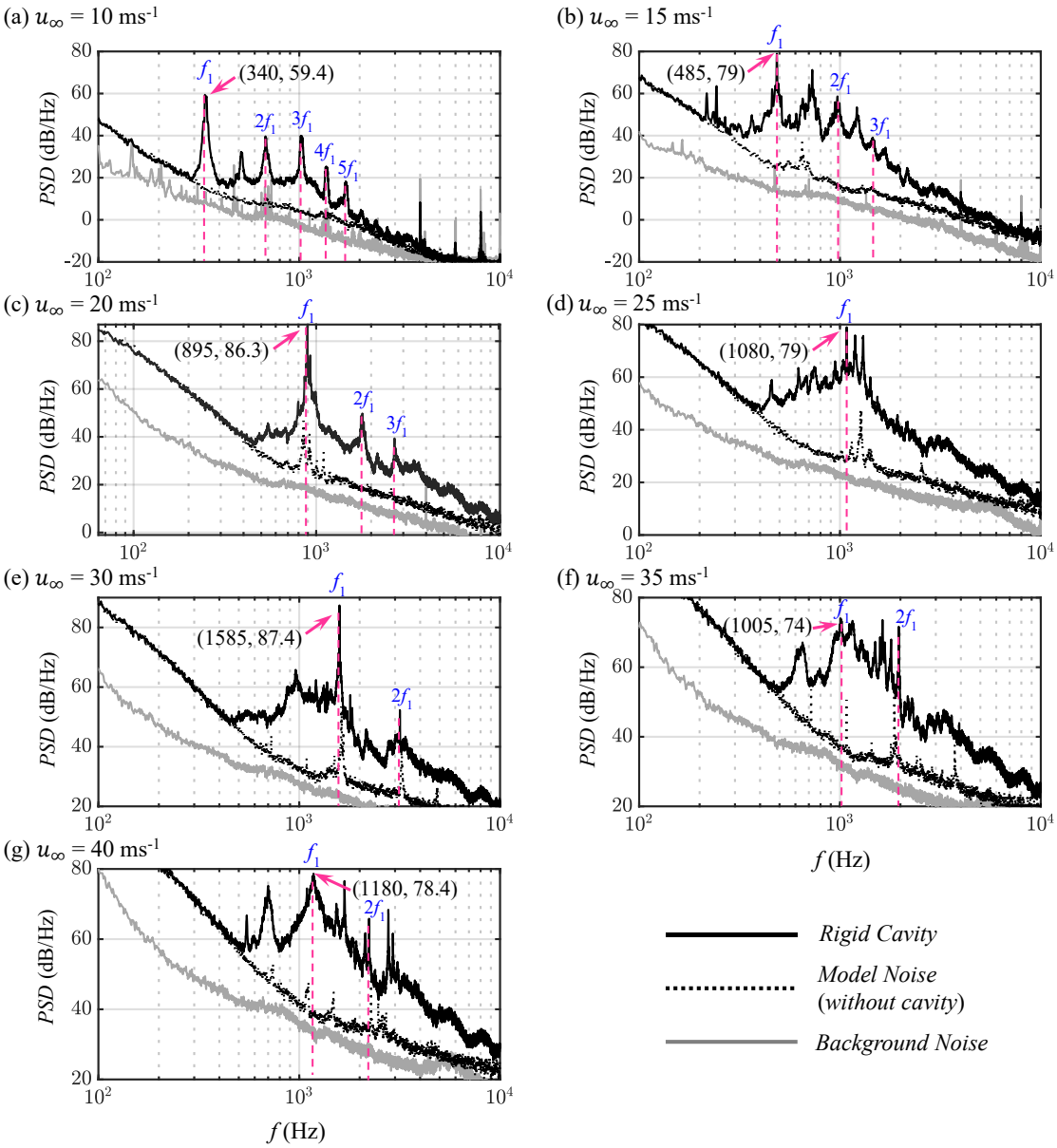

Figure 4.5 Rigid Cavity noise measured at *mic*1 for various freestream flow conditions. The peak frequencies are labelled across each testing case.

Table 4.1 Comparison of experimentally measured peak frequencies with the *Heller & Bliss* formula.

u_∞ (ms^{-1})	m	α	M_∞	k	$f_{H\&B}$ (Hz)	f_{Exp} (Hz)	$\Delta f = \lvert f_{H\&B} - f_{Exp} \rvert / f_{H\&B}$ (%)
10	2	0.25	0.03	0.57	327.1	340	3.9
15	2	0.25	0.045	0.57	486.5	485	0.3
20	3	0.25	0.06	0.57	1011.1	895	11.5
25	3	0.25	0.074	0.57	1253.7	1080	13.8
30	3	0.25	0.09	0.57	1492.5	1585	6.2
35	2	0.25	0.1	0.57	1099.3	1005	8.6
40	2	0.25	0.12	0.57	1246.5	1180	5.3

4.2.2Aeroacoustics of *RC* and *EP* Configurations

The aeroacoustic feedback mechanism, particularly how the coupling between the shear layer and cavity acoustic modes influences noise radiation in deep cavities, has been previously studied theoretically, numerically and experimentally (Elder 1978; Rockwell and Naudascher 1978; Forestier *et al.* 2003; Samimy *et al.* 2007; Yokoyama *et al.* 2017; Ho and Kim 2021; Naseer *et al.* 2023a). Nevertheless, a rigorous experimental study of the corroboration of these aeroacoustic interactions and their precise effect on resultant noise radiation has not been fully elucidated. The primary question remains whether the influence is largely attributable to oscillations within the shear layer or to the acoustic resonant modes within the cavity depth. To elucidate the sequence of events—from the impingement of the shear layer on the cavity to the excitation of the cavity acoustic modes and their consequent interplay leading to noise radiation—a comparative analysis of pressure spectra at three strategically placed probe locations is employed. This comparison aims to dissect their frequency content and associated phenomena. In the following discussion, a total of four representative *RC* configurations are selected as

baselines to gauge the efficacy of their *RC* counterparts in mitigating cavity noise.

To understand the mechanisms of noise generation and attenuation in both the *RC* and *EP* setups, the power spectral density (*PSD*) of pressure signals from the cavity flow and for acoustic fields were simultaneously measured. These measurements were taken using *mic*2 (to characterize the shear layer), *mic*3 (to capture the acoustic mode), and *mic*1 (to observe the far-field noise) and were analyzed in accordance with Heller and Bliss (1975) modified Rossiter formula. Figure 4.6 illustrates the findings for selected *RC* /*EP* configurations under an array of free-stream flow conditions, specifically at velocities of u_∞ = 10, 20, 30, and 40 ms^{-1}.

The power spectral density (*PSD*) spectra for the baseline *RC* conditions manifest a prominent tonal peak at the f_1-tone frequency, consistently observed across measurements of the shear layer, acoustic mode, and far-field noise, agreeing with the fundamental tone depicted in Tabel I. The surface pressure fluctuations captured at *mic*2 and *mic*3, sharing this peak frequency, are the potential contributors and the primary sources of acoustic radiation. For case *RC*10, the peak *PSD* of the shear layer exceeds that of the cavity acoustics, suggesting that the energy transfer from the shear layer impingement at the cavity trailing edge to the cavity acoustic mode is not effectively established. Conversely, in cases *RC*20 and *RC*30, the peak *PSD* of the cavity acoustics overtake that of the corresponding shear layer tone, indicating a proficient transfer of energy from the shear layer to the cavity acoustics, resulting in enhanced acoustic radiation. This enhancement implies the presence of an aeroacoustic feedback resonance mechanism. An additional observation across

the far-field spectra for cases *RC*10, *RC*20, and *RC*30 is that they predominantly mimic the trends of their respective cavity acoustic mode spectra rather than those of the shear layer. Furthermore, the far-field tone remains proportionate with the cavity acoustic mode in *RC*10 or slightly exceeds it in cases *RC*20 and *RC*30. The *RC*40 case, however, exhibits a distinct pattern: the shear layer and cavity acoustic mode possess peak *PSD* tones of equal magnitude, which diverges from trends observed in prior cases. Moreover, the far-field spectral trends and levels do not align with those of the cavity acoustic mode in *RC*40, and the case lacks the sharply defined peaks evident in the other cases. Consequently, this suggests that the aeroacoustic resonance phenomenon diminishes as higher free-stream flow conditions are reached.

Figure 4.6 also presents a comparative analysis of the shear layer, cavity acoustics, and far-field noise spectra for the elastic panel configurations (*EP*10, *EP*20, *EP*30, and *EP*40), measured at the same probe locations as their *RC* counterparts. The spectral examination reveals that *EP*20 and *EP*30 exhibit peak tonal noise reductions of 9.2 dB and 16.1 dB, respectively, relative to their *RC* benchmarks (*RC*20 and *RC*30). In contrast, *EP*10 and *EP*40 configurations do not demonstrate any significant reduction, as their spectra remain largely unaltered. This suggests that the implementation of an elastic panel is effective in conditions (*RC*20 and *RC*30) where strong aeroacoustic interactions—between shear layer oscillations and cavity acoustic modes—are expected to drive fluid resonance within the cavity. However, the panel does not appear to have a discernible impact on other flow conditions (*RC*10 and *RC*40), where the cavity noise is presumed to be predominantly influenced by shear layer oscillations alone (fluid dynamic oscillation).

Apart from *EP*30, spectral analysis across the *EP* and *RC* cases displays a consistent tonal peak frequency pattern in the shear layer, cavity acoustics, and far-field spectra. Whatever frequency is captured by the shear layer is also reflected in the cavity acoustics and far-field noise radiation, indicating a frequency lock-on. This consistency suggests that the implementation of an elastic panel does not induce significant alterations in the aeroacoustic processes for these cases. However, the *EP*30 case stands out, as there is a notable disruption in the aeroacoustic coupling: the shear layer and cavity acoustics do not share the same dominant frequency. This divergence implies a breakdown in the coupling for this case, resulting in disparate dominant frequencies in the shear layer and cavity acoustic spectra.

In summary, it is determined that under certain free-stream flow conditions, specifically for *RC*20 and *RC*30, the deep cavity exhibits a robust acoustic response, with sound pressure levels reaching 86.3 dB and 87.4 dB, respectively. This is attributed to the aeroacoustic coupling between the shear layer and the cavity acoustics, where the effective impingement of the shear layer at the cavity trailing edge gives rise to pronounced cavity acoustic modes. When an elastic panel is introduced at the cavity bottom, it interacts with these cavity acoustic modes, potentially absorbing the energy of the incident acoustic waves and thereby significantly reducing the peak amplitude up to 16.1 dB, as evidenced in the *EP*30 case. By weakening the aeroacoustic coupling through the interaction between the aeroacoustic and structural dynamics—specifically the interplay of shear layer oscillations, acoustic mode resonances, and panel vibrations—the overall acoustic emissions are attenuated. Notably, the *RC*10 and *RC*40 cases do not exhibit hallmark features of aeroacoustic coupling,

resulting in reduced cavity noise emissions compared to the *RC*20 and *RC*30 configurations. Consequently, the implementation of the elastic panel in the *EP*10 and *EP*40 scenarios does not yield reductions in acoustic levels as substantial as those observed in the *EP*20 and *EP*30 cases.

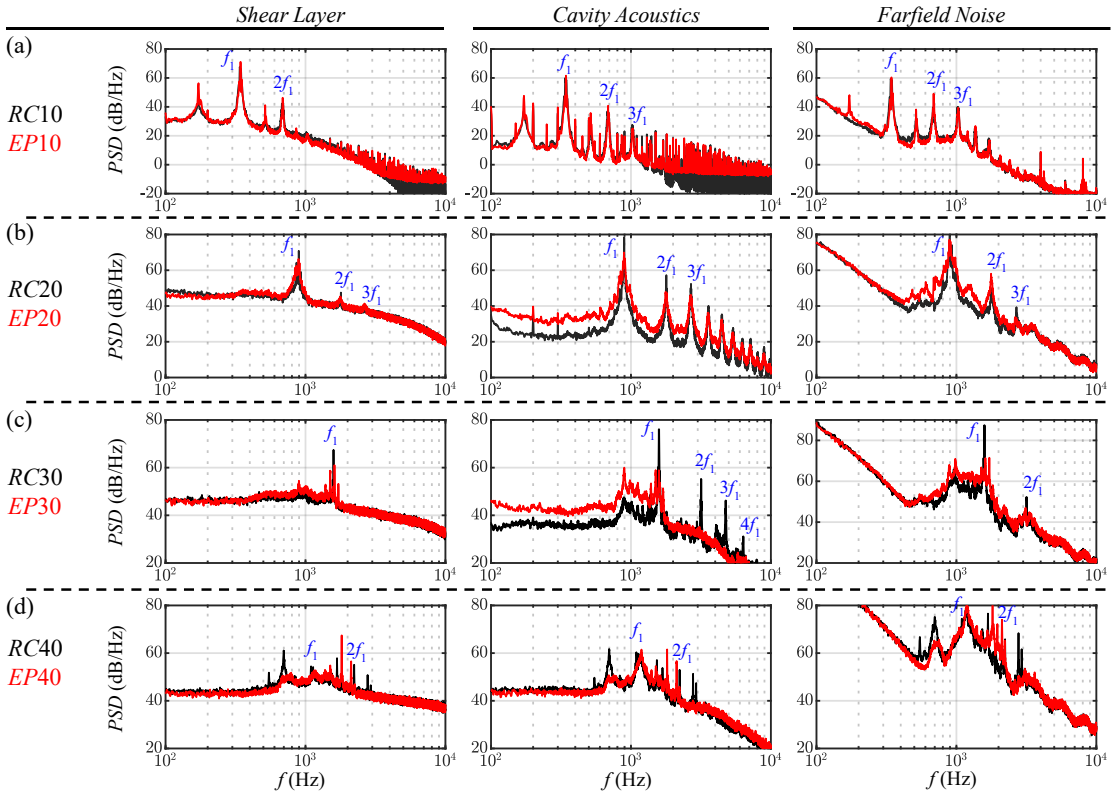

Figure 4.6 Comparison of p' spectra measured at locations *mic*2 (first column), *mic*3 (second column) and *mic*1 (third column); (a) $u_\infty = 10$ ms^{-1}, (b) $u_\infty = 20$ ms^{-1}, (c) $u_\infty = 30$ ms^{-1}, (d) $u_\infty = 40$ ms^{-1}.

4.3 Coherence Analysis

Our findings indicate that the pronounced acoustic response observed in *RC* configurations results from synergistic interactions between the convective shear layer and the cavity acoustic mode. This interaction is characterized by a frequency lock-on effect, which facilitates the transfer of energy from the shear layer to the cavity acoustic field. The extent of energy transfer varies with the freestream flow conditions, as some cases experience fluid resonant and some experience dynamic cavity oscillations. Therefore, the application of elastic panels yields varied levels of effectiveness in reducing the cavity noise. Some panel cases (*EP*20 and *EP*30) effectively reduce the peak spectral tones while maintaining the overall trend, whereas others (*EP*10 and *EP*40) exhibit negligible impact on the shear layer and acoustic spectra. To further investigate the factors contributing to the effectiveness of these panels, we hsave performed a coherence analysis on the pressure signals from the shear layer, cavity acoustic mode, and farfield noise. Figure 4.7 presents the coherence of these pressure signals, calculated using the formula $\gamma^2(f) = |P_{XY}(f)|^2/P_X(f)P_Y(f)$, where $P_X(f)$ and $P_Y(f)$ represent the power spectral densities of the p' signals for any selected pair among the shear layer, acoustic mode and farfield, whereas $P_{XY}(f)$ denotes the cross-power spectral density between the selected pair of signals across the shear layer, cavity acoustics and farfield noise.

For a free stream flow condition with u_∞ = 10 ms^{-1} (Figure 4.7(a)), both the *RC*10 and *EP*10 configurations exhibit strong coherence between the shear layer and the farfield noise at specific spectral peaks across the low-frequency region ($f < 10^3$). A similar coherence trend is also observed between the shear

layer and the cavity acoustics. Additionally, the coherence between cavity acoustics and farfield noise shows strong congruence over a broad lower frequency spectrum ($10^2 < f < 10^3$). Notably, little to no difference is observed in the coherence patterns for *RC*10 and *EP*10, suggesting that the elastic panel did not significantly alter the coherence pattern of the radiating frequency modes among the components responsible for cavity noise emission, which largely remains unaffected.

As the wind speed increases to u_∞= 20 ms^{-1} (Figure 4.7(b)), the coherence between the shear layer and farfield noise is strengthened ($\gamma^2 \sim 0.8$) and concentrated to a solitary spectral peak at f = 895 Hz, similarly the coherence pattern of cavity-acoustics ↔ far-field noise (instead of being scattered as seen in *RC*10) remains concentrated to a solitary spectral peak at f = 895 Hz which is translated into the strongly coherent cavity acoustic mode at the same frequency mode whereas the coherence pattern between cavity acoustics and farfield noise also suggests that both of them remain strongly linked together and an overall cohesive approach which puts *RC*20 into the category of fluid resonant cavity oscillation. When the elastic panel configuration (*EP*20) is introduced under similar conditions, it slightly broadens the coherence spectrum towards the lower frequency region ($f < 10^3$) for both shear layer ↔ cavity acoustics and shear layer ↔ farfield interactions while maintaining strong coherence at f = 895Hz. However, this comes at the expense of diminished coherence at higher spectral peaks ($f > 10^3$) compared to *RC*20. Thus, it can be argued that spreading the influence of favourable coherence, instead of being concentrated at a few spectral peaks, enhances the

broadband component of the signal and thus reduces the tonal noise, as observed in the corresponding *EP*20 spectra shown in Figure 4.6.

Overall, the cases *RC*30 and *EP*30 (Figure 4.7(c)) exhibited trends similar to their *RC*20 and *EP*20 counterparts. For *RC*30, there is a strong coherence between the shear layer and both farfield noise and cavity acoustics, concentrated at the peak frequency of f = 1585 Hz. In contrast, *EP*30 broadens the lower frequency coherence spectrum and reduces the strong coherency at f = 1585 Hz to $\gamma^2 \sim 0.6$, which has evidently resulted in substantial tonal noise reduction, as illustrated in Figure 4.6. The *RC*40 and *EP*40 cases generally follow a similar coherence spectrum trend as the *RC*10 and *EP*10 (Figure 4.7(d)), except the coherence is shifted towards the higher frequency region. The spectra remained scattered, and the installation of the elastic panel, while slightly reducing the coherency, did not significantly affect the ultimate noise radiation.

In essence, it is therefore suggested that fluid dynamic cavity oscillations (*RC*10 and *RC*40) are accompanied by scattered coherence spectra, leading to the emergence of various frequencies in the farfield noise spectrum (Figure 4.7(a) and 4.7(d)). Conversely, the fluid resonant cavity oscillations (*RC*20 and *RC*30) reveal coherence spectra concentrated at a few spectral peaks corresponding to the dominant flow frequencies, as observed in Figure 4.7(b) and 4.7(c). In such cases, the elastic panel is effective as it redistributes the energy of tonal frequencies and consequently reduces the tonal noise radiation associated with fluid resonant cavity oscillations.

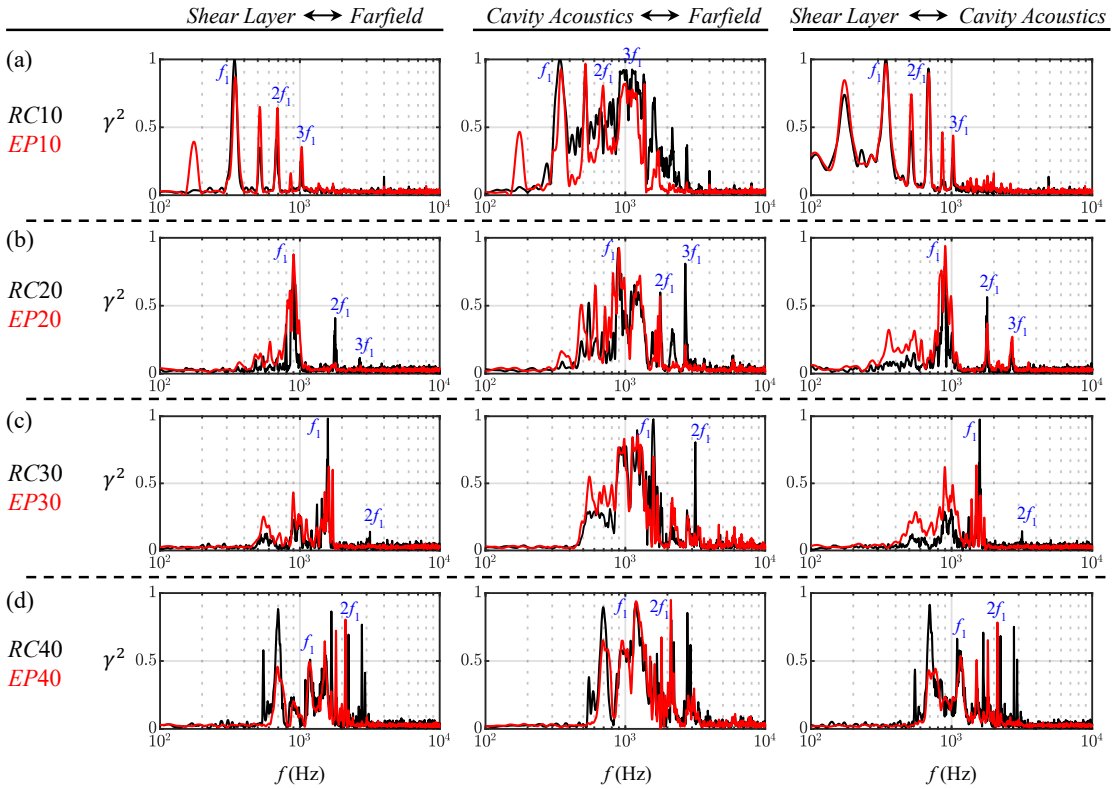

Figure 4.7 Coherence, γ^2 between shear layer and farfield noise (first column), cavity acoustics and farfield noise (second column), shear layer and cavity acoustics (third column). (a) u_∞ = 10 ms^{-1}, (b) u_∞ = 20 ms^{-1}, (c) u_∞ = 30 ms^{-1}, (d) u_∞ = 40 ms^{-1}.

4.4 Transverse Velocity Fluctuation

The transverse velocity fields derived from PIV measurements offer crucial insights into the oscillations of the shear layer over the cavity opening, a critical site for cavity noise generation, as illustrated in Figure 4.8. The velocity snapshots were taken consistently at quarter-period intervals ($T/4$) within a single fluctuation cycle (T) of the dominant frequency. It should be noted that the period T varies and is specified for each tested case. The instantaneous velocity fields reveal the development of vortical structures within the shear layer, which increases in size as they are convected downstream, and their impingement on the cavity trailing edge appears as downwashes against the aft wall of the cavity. For a flow speed of u_∞ = 20 ms^{-1}, the vortical structures are

more distinctly defined across the cavity opening compared to those at u_∞ = 30 ms^{-1}, which are less clear. The PIV measurements suggest that flow velocities exceeding u_∞ = 30 ms^{-1} are not advisable with the current setup due to challenges in stabilizing the flow field. Typically, a flow velocity of u_∞= 20 ms^{-1} achieves optimal particle seeding density, (Maryami *et al.* 2024), enabling accurate and reliable tracking of particles within the fluid, thus ensuring robust flow velocity data. Despite these limitations, we included the *RC*30 and *EP*30 cases to explore any potential insights.

Comparison between the *RC* and elastic panel *EP* configurations reveals subtle yet significant differences in the shear layer dynamics. In the *EP* configurations, the shear layer is slightly thinner and more disrupted compared to the well-defined vortices observed in the *RC* configurations. Moreover, the evolution of the shear layer in *EP* configurations shows notable distinctions; the onset of the shear layer at the cavity leading edge is less vigorous and robust than in *RC* configurations. Additionally, the growth pattern of the shear layer as it convects toward the cavity trailing edge differs markedly from the more regular pattern observed in *RC* cases. Lastly, the impingement of the shear layer in *EP* cases does not produce significant downwash imprints near the aft wall, unlike in *RC* cases. This observation aligns with previous findings (Figure 4.6) that the shear layer impingement in *EP* cases is less effective in transferring significant shear layer energy to the cavity acoustic mode compared to *RC* cases.

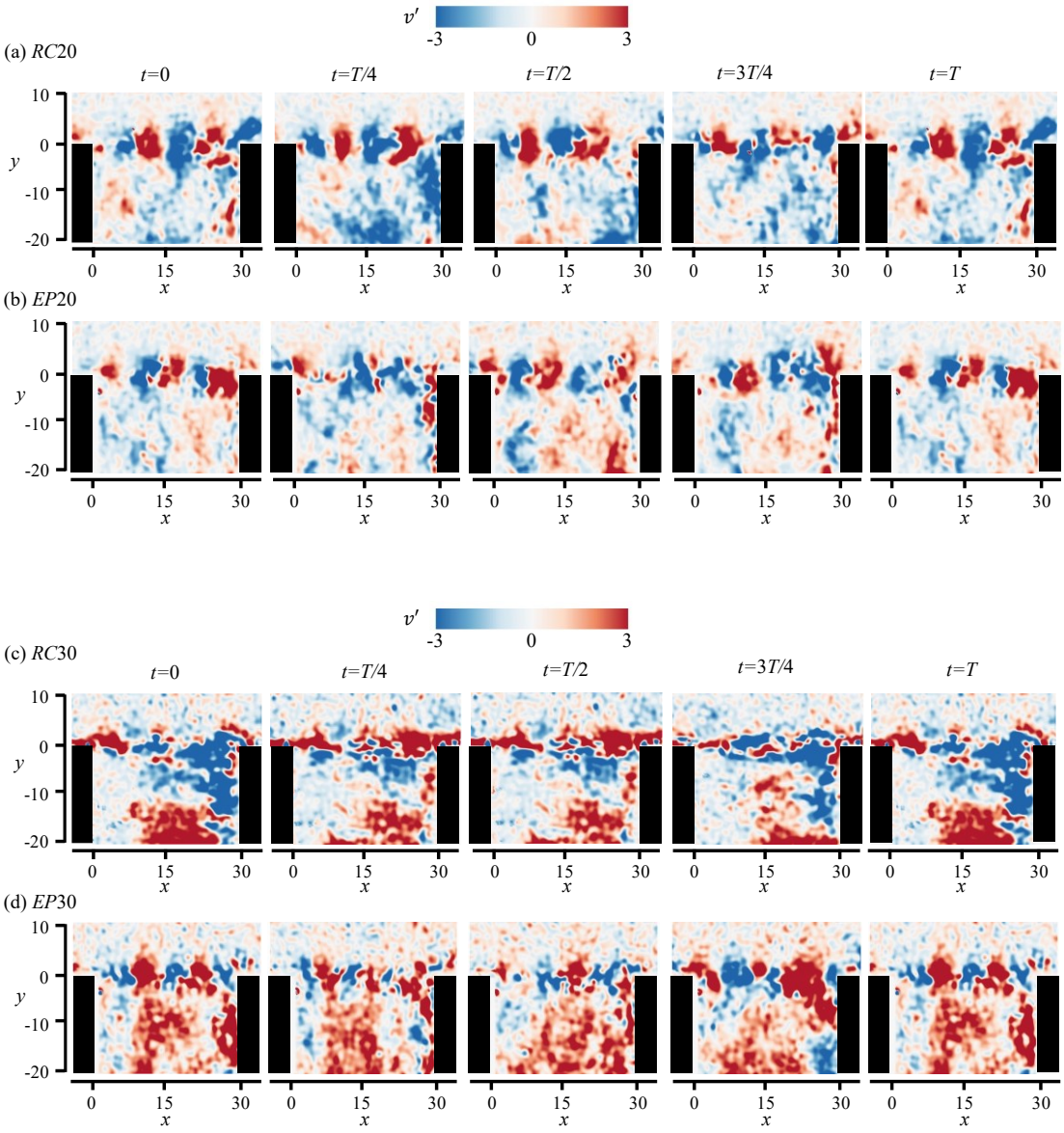

Figure 4.8 Instantaneous transverse velocity fluctuation during one complete oscillation cycle of shear layer growth, followed by the downwash after impingement near the cavity opening region, (a) *RC*20, (b) *EP*20, (c) *RC*30, (d) *EP*30.

4.5 Summary

This chapter details an experimental study aimed at validating and enhancing a novel passive control method using surface compliance to mitigate tonal noise in deep cavities. The strategy involved implementing an elastic panel flush-mounted at the cavity bottom to alter aeroacoustic-structural interactions and reduce acoustic emissions at crucial flow velocities. Conducted within an aeroacoustic wind tunnel, the setup facilitated precise measurements of near and far-field pressures and employed Particle Image Velocimetry (PIV) to effectively capture flow dynamics. The results showed that the compliant panel significantly changed aeroacoustic patterns within the cavity, achieving noise reductions up to 16.1 dB, particularly at flow velocities of 20 and 30 ms^{-1} conditions that typically amplify aeroacoustic resonances in rigid cavity (*RC*) cases. Comparative analysis between the RC configuration and the elastic panel (*EP*) setup highlighted that the panel introduction notably affected the coherence among the cavity acoustic mode, shear layer, and far-field noise, indicating a disruption in typical aeroacoustic coupling processes due to altered shear layer dynamics. Furthermore, PIV imagery revealed that the EP configurations exhibited a thinner and more disrupted shear layer compared to the well-defined vortices of the *RC* setups. Th experimental investigation carried out in this chapter has provided not only the verification and implementation of the proposed concept but also the crucial understanding of the mechanisms of noise generation and reduction.

Chapter 5

Leveraging Cavity Aeroacoustic Suppression using Multiple Elastic Panels

This chapter reports the numerical study of a novel methodology for passive suppression of deep cavity noise by means of strategically designed and arrangements of multiple elastic panels and examines its underlying aeroacoustic-structural interaction physics. The study is conducted with the same operating conditions and numerical scheme as was employed in chapter 3. For each cavity-panel configuration, the fluid-loaded panel natural frequencies are harmonized with the characteristic aeroacoustic processes of the original/modified cavity aeroacoustic feedback loop. This promotes panel aeroacoustic-structural resonance for absorption of feedback flow and acoustic fluctuation energy for achieving less eventual cavity noise. The most effective configuration gives a remarkable noise power reduction by 15 dB from rigid cavity. Inadvertently it reduces cavity drag by almost 15%. Simultaneous

reduction of both cavity noise and drag is unprecedented among similar attempts in literature. In-depth spatio-temporal analyses of aeroacoustic-structural interaction results elucidate the intricate interplay between cavity flow, panel vibration responses, and cavity acoustic modes, leading to noise reduction in all cavity-panel configurations studied. Essentially the vertical panel acts to curtail the efficacy of coupling between growing shear layer and cavity acoustic modes whose sustenance is further impeded by an acoustically induced resonant panel at cavity bottom. The proposed methodology is confirmed to be feasible yet effective, which holds great potential for fluid-moving applications in which a quiet and energy-efficient cavity configuration is desired.

5.1 Computational Settings

We applied Direct Aeroacoustics Simulation (DAS) and Conservation Element and Solution Element (CE/SE) methods to study unsteady aerodynamics and acoustics using a simplified model of an elastic panel. Our focus was on a deep cavity with an L/D ratio of 0.4 at a freestream velocity of 30 ms^{-1}. The computational domain utilized a 2.74 million element grid, detailed in Figure 2.11. For full methodology, readers are referred to Chapter 2. Figure 5.1 illustrates the setup of virtual probe locations critical for analyzing cavity acoustics, structural dynamics and farfield noise. The aeroacoustic characteristics are evaluated using 2430 virtual probes. These probes are strategically placed with a spacing of 0.004 along the cavity walls. Additionally, for the analysis of cavity acoustic radiation, there are probes positioned at a radius r = 10.

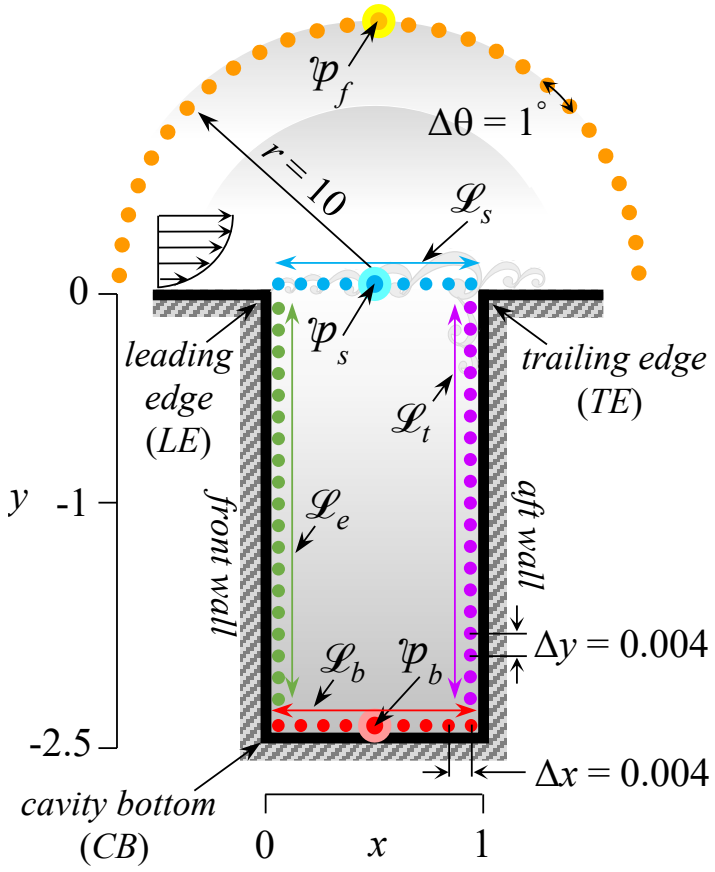

Figure 5.1 Virtual probe locations around the cavity. Checkpoints indicated with distinctive lines i.e. $\mathcal{L}_s$: (0,0) → (1,0), $\mathcal{L}_b$: (0,-2.5) → (1,-2.5), $\mathcal{L}_e$: (0,0) → (0,-2.5), $\mathcal{L}_t$: (1,0) → (1,-2.5). The reference points of correlation analysis in subsequent discussions are $\mathcal{P}_f$: (0.5, 20), $\mathcal{P}_s$: (0.5, 0) and $\mathcal{P}_b$: (0.5, -2.5).

5.2 Cavity – Panel Configurations with Single Panel

5.2.1 Determination of potential panel locations

In order to appropriately mount the elastic panels for the proposed noise suppression approach, it requires certain knowledge of the flow characteristics over the rigid cavity from which the potential panel locations to achieve resonance conditions for modifying the cavity feedback mechanism can be deduced. Our previous numerical study (as discussed in Chapter 3) on the rigid cavity noise outlines the physical processes that lead to the aeroacoustic feedback coupling between the cavity shear layer and the cavity acoustic mode,

responsible for the ultimate intense tonal noise radiation. The results pinpoint that each cavity wall supports a certain physical process that maintains the aeroacoustic feedback coupling. Thus, to modify the identified coupling phenomena for the ultimate noise suppression, we attempted five cavity-panel configurations (Figure 5.2(a)) so that each elastic panel could interact with an aeroacoustic coupling process and absorb the incident flow fluctuation energy to maintain its flow/acoustically induced vibration. The deterministic consideration of this modification strategy is the natural frequency of the elastic panel in the presence of fluid loading, which must be kept the same as the dominant frequency of the rigid cavity (*RC*) flow. In order to achieve the fluid-loaded panel natural vibration with fixed end boundary conditions, we used the equation, $(f_{EPdX})_n = (n/2L_{EP})[(T_{EP}/\rho_{EP}h_{EP})/(1 + L_{EP}/\pi n\rho_{EP}h_{EP})]^{0.5}$. While keeping the panel length same as the cavity length, the thickness and the exerted tension can be altered to match the designed frequency. All panels are assumed to be made up of elastomeric material like silicon rubber following the suggestions of a previous study (Naseer *et al.* 2022). Table 5.1 shows the three panel designs that are considered. Their target designed natural frequencies for the noise control actions are selected to be the third (n = ③) resonant modes of the panels, which are highlighted and shaded in the table. The rationale behind the choice of these three specific natural frequencies will be elaborated upon in the upcoming discussions.

Table 5.1 Three panel designs and the distribution of the first nine resonant modes of each design.

Panel design		*n*-th resonant panel frequency								
	n =	①	②	③	④	⑤	⑥	⑦	⑧	⑨
f_{EPd1}		0.306	0.615	0.925	1.234	1.54	1.852	2.16	2.47	2.78
f_{EPd2}		0.414	0.832	1.25	1.668	2.086	2.5	2.92	3.3	3.75
f_{EPd3}		0.455	0.915	1.375	1.835	2.295	2.75	3.21	3.67	4.13

5.2.2 Cavity Noise Reduction Scheme with Single Panel

Figure 5.2(b) shows the vibratory response of every single panel as it interacts with the cavity flow. The temporal patterns of sustained panel vibration reflect the successful execution of our conceived idea of flow fluctuation energy extraction through flow/acoustically triggered panel vibration. The extent of ultimate noise reduction or amplification varies across different cavity-panel configurations. The *SPL* spectra measured at the far field reveal that the flow-induced resonant panel vibrations mitigate most effectively the cavity tonal noise when the panel is mounted either at the aft or the bottom wall of the cavity as the respective peak *SPL* reduction of 3.8 and 3.6 dB from the *RC* case is observed Figure 5.2(c). The azimuthal *SPL* distribution shows a consistent reduction pattern. It can also be seen that the best performing cases are associated with a shift in the cavity flow dominant frequency from 0.925 to 1.25. For the detailed reasoning of the cavity-panel configuration noise reduction mechanisms, readers are referred to Chapter 3. However, to aid the understanding of the present study, the noise reduction mechanisms are succinctly explained here. The dominant frequency shift in EP_{aft} case is attributed to the energy absorption of the dominant low-frequency mode by the vibrating panel, resulting from the interaction of the shear layer vortices with the aft panel. The dominant frequency shift in EP_{bottom} case is attributed to the energy absorption of the dominant low-frequency modes by the vibrating panel, resulting from the incidence of acoustic waves on the bottom panel. After absorbing the flow excitation energy of the low-frequency mode, the flow-panel interaction shifts the frequency to a higher mode of lesser energy, which emerges as the new flow dominant mode. Further, the interaction also invokes

the phase shift in the coupling between the shear layer and cavity acoustic mode. As a result, when the reflected acoustic waves from the cavity bottom meet the shear layer at the cavity opening, it excites the shear layer according to the shifted mode but it does not support the favourable mutual phase difference ($\Delta\phi \sim 0$) near the cavity leading edge as occurred in *RC* case. These two actions result in a delayed shear layer growth. Hence, the effectively shortened shear layer length also assists the shift in the previously sustained Rossiter frequency of $f = 0.925$ to the higher mode of $f = 1.25$ for EP_{aft} and EP_{bottom} case. In summary, the cavity-panel configuration with single panel has shown its effectiveness in reducing the aeroacoustically generated deep cavity noise, given that the location of the elastic panel is appropriately designed and located.

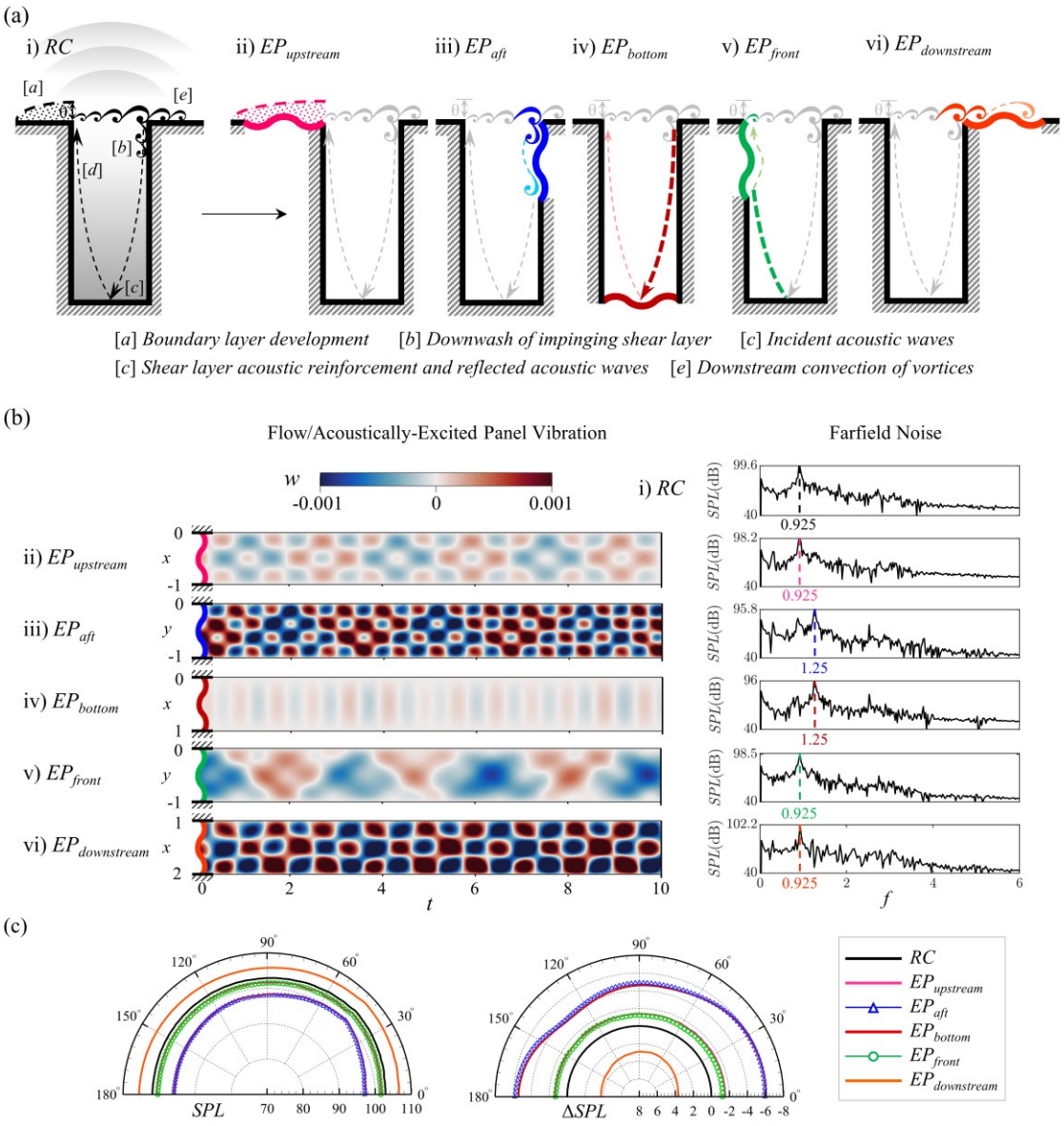

Figure 5.2 Cavity noise suppression with strategic modification of shear layer – acoustic mode coupling using single elastic panel. (a) Identified key physical processes responsible for feedback mechanism (Naseer *et al.* 2023b) and the panels (ii) – (vi) set for the individual processes [a] – [e] for modifying the feedback. (b) Flow/acoustically excited panel vibratory responses exhibiting the significant flow energy extraction and its effect on the far field cavity tone at (x,y) = (6.75, 21.5) and its frequency shift. (c) Azimuthal distributions of *SPL* of different cavity-panel configurations and their noise reduction ΔSPL.

5.3 Cavity – Panel Configuration with Multiple Panels

Cavity-panel configurations with single elastic panels has shown promising noise reduction potential. To leverage further noise suppression, the present study attempts an extended approach based on configurations with multiple panels (Figure 5.3). We first formulate the configurations with double panels (*DEP*) by combining the best-performing single-panel cases in Sec 5.2 with differently designed frequency arrangements. A *DEP* configuration is designed in such a way that an elastic panel is mounted on the aft wall, whereas another panel is mounted at the cavity bottom. Each *DEP* configuration is uniquely assigned a combination of panel natural frequencies based on aeroacoustical physics identified in *RC* case and previously tested cases with single panels. To design the panels for *DEP*, there are two frequencies of interest. The first is the original frequency of *RC* tone (f = 0.925) and the second is the shifted frequency (f = 1.25) which emerges when a single elastic panel operates at either the aft or the cavity bottom wall (as discussed in Sec 5.2). *DEP*1 configuration simply combines the *SEP*1 and *SEP*2 panels whose natural frequencies are tuned to meet the dominant frequency of the *RC* case. The combined actions of the panels on the shear layer and the cavity acoustic mode are envisaged to doubly affect the resultant noise reduction. As seen in Naseer *et al.* (2023b), the panel at the aft or the bottom cavity wall tends to shift the dominant cavity aeroacoustic fluctuation mode from f = 0.925 to f = 1.25. Therefore, another *DEP* configuration has been designed in which one panel is to cater the original *RC* dominant frequency, f = 0.925 and another is for the shifted frequency (f = 1.25). In this way when one panel triggers the frequency shift after pacifying the

energy-enriched content at f = 0.925 of the flow, the other panel should be accordantly designed to interact with the shifted mode. Following this approach, *DEP*2 and *DEP*3 configurations are considered. In *DEP*2, the aft panel is designed to target the original *RC* frequency whereas the bottom panel is tuned to comply with the envisaged shifted frequency. In *DEP*3, the targeted actions of the two panels with respect to the selected frequencies are swapped. To seek further possibility for more cavity noise reduction, a triple elastic panel configuration (*TEP*) is also attempted by mounting one more panel at the cavity front wall in *DEP*2 configuration. Since the dominant frequency observed in *DEP*2 is shifted to f = 1.375, this frequency is designated for the natural frequency of the third panel. As such seven cases are discussed in this study along with the *RC* baseline case.

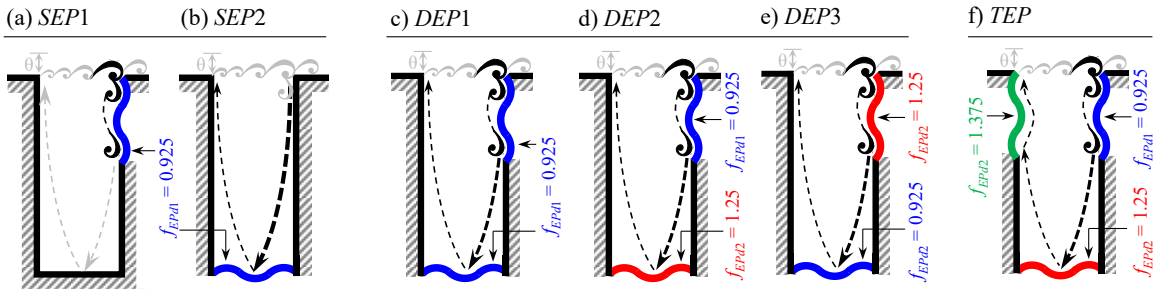

Figure 5.3 Cavity configurations with multiple panels. Note that the EP_{aft} and EP_{bottom} cases in Fig. 4 are renamed as *SEP*1 and *SEP*2 for the sake of consistency of forthcoming discussions. (a) *SEP*1, (b) *SEP*2, (c) *DEP*1, (d) *DEP*2, (e) *DEP*3 (f) *TEP*.

5.4 Modifications of Cavity Aeroacoustics

The temporal evolution of flow pressure fluctuations p' within the cavity of all cases are depicted in Figure 5.4. The figures reveal periodic flow fluctuations both along the shear layer region and inside the cavity. For easy comparison, the series of snapshots in each case commences at the moment of minimum

pressure within the cavity. The subsequent snapshots are consistently taken at time intervals of $T/4$ within a single flow fluctuation period T of the dominant frequency captured at cavity bottom center (x, y) = (0.5, -2.5). Note that the value of T varies and is accordingly shown for the tested cases. Evidently, the p' fluctuates in a clear alternating pattern in time with a spatial extent almost filling up the entire cavity. It is worth highlighting that a notable rarefaction ($p' < 0$) occurs concurrently at the moment ~ $T/4$ when the downwash secondary vortex forms (Figure 5.5) as the flow separates at the cavity trailing edge. Subsequently, a significant compression wave ($p' > 0$) is generated (Figure 4) after these two flow processes conclude (~ $3T/4$). These findings are consistent with the results of a previous numerical investigation of flow past a deep cavity of almost similar size (Ho and Kim, 2021). The fluctuation patterns of p' within the cavity depicted in Figure 5.4, are identified as the cavity acoustic mode (Naseer *et al.* 2023b). When this cavity acoustic mode interacts with the shear layer at the cavity opening, it promotes strong acoustic radiation (Figure 5.6) specifically for the *RC* case. A close examination of Figure 5.4 reveals a strong pressure fluctuation due to cavity mode oscillation in the *RC* case. However, in all the cases with elastic panels, the intensity of these fluctuations is markedly diminished.

In Figure 5.5, we can observe a fluctuating shear layer originating from the cavity leading edge (*LE* in Figure 5.1). This shear layer gives rise to a sequence of substantial vortical flow structures as a result of Kelvin-Helmholtz instabilities that convect downstream. When these streamwise growing vortical structures reach the cavity trailing edge (*TE* in Figure 5.1), their strong vortex-structure interaction results in the emergence of separating flow over the flat

wall downstream of the cavity. Meanwhile the intensified strain rate induced near *TE* generates a series of secondary vortical structures that extends and descends into the cavity. As these secondary vortical structures detach from the *TE*, the strain rate diminishes and the high vorticity region contracts as the flow progresses along the cavity aft wall. Among all the cases under consideration, with or without panels, the oscillation patterns of the shear layers across the cavity opening remains more or less the same. However, a noteworthy observation in comparison to the *RC* case is the delayed shear layer growth in all cases with elastic panels. This delayed growth is not merely a minor variation, but rather a significant one, suggesting a potential alteration in the feedback phenomena in these cases.

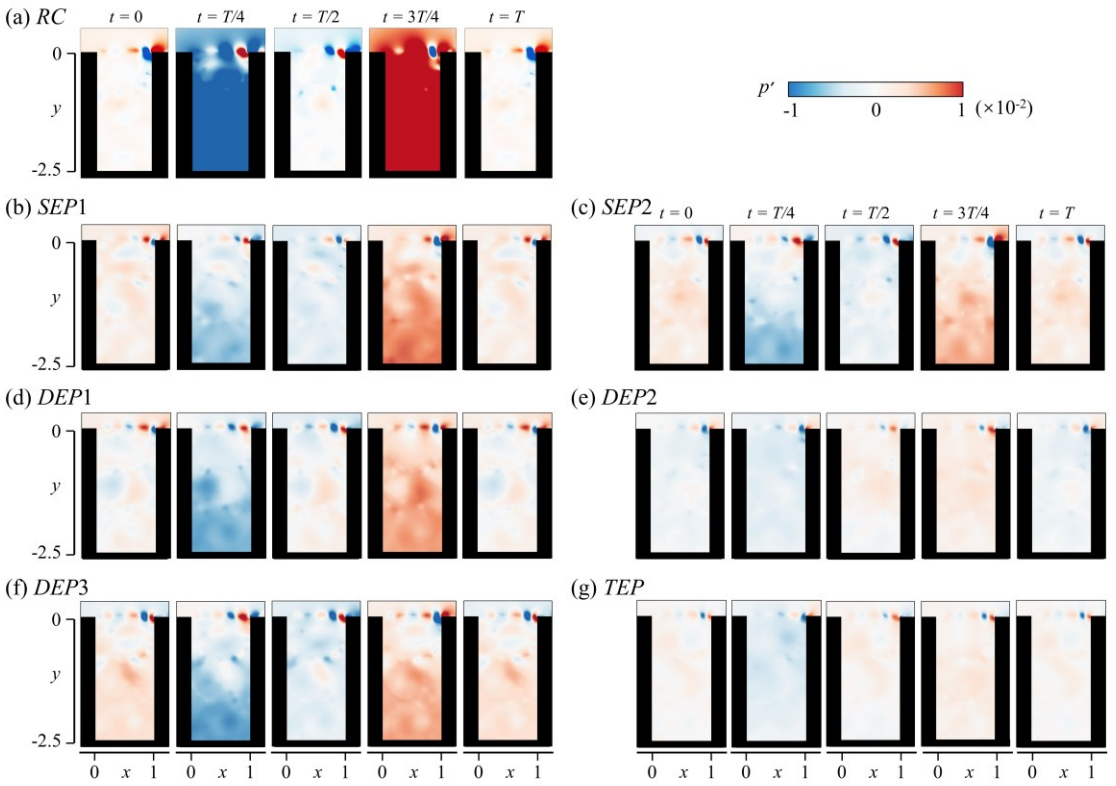

Figure 5.4 Snapshots of instantaneous pressure fluctuation p' for a cycle of cavity mode oscillation, commencing from the moment of shear layer impingement at the downstream edge. (a) *RC*, (b) *SEP*1, (c) *SEP*2, (d) *DEP*1, (e) *DEP*2, (f) *DEP*3 (g) *TEP*.

In Figure 5.6, we can observe the snapshots of instantaneous p' of noise radiation for all configurations, taken at the moment when the acoustic rarefaction impacts the cavity bottom. As depicted, the cavity noise is tonal in nature and resembles the *RC* radiation. However, the magnitude of noise radiation varies substantially across all cases. *DEP*2 and *TEP* cases exhibit the highest acoustic reduction whereas a slight reduction in noise is observed in all the remaining cases.

Figure 5.7 shows a comparison of noise spectra at $\wp_f$ in the far-field and at $\wp_b$ near the cavity bottom, with the power spectral density (*PSD*) of p' at $\wp_s$ within the shear layer. We can see that the *DEP*1 and *DEP*3 cases give the lowest noise reduction from the *RC* case, whereas the *SEP*1 and *SEP*2 cases give moderate reduction and *DEP*2 and *TEP* give the highest reduction. A closer look at the spectra reveals a distinct trend concerning the frequency peaks. A single peak at f = 1.25 dominates the spectra in *SEP*1, *SEP*2, *DEP*1, and *DEP*3 cases regardless of the measurement locations. On the other hand multiple peaks, namely at f = 0.925, 1.25, and 1.375, dominate the spectra across various locations in the *DEP*2 and *TEP* cases. These findings indicate that despite the shift in dominant frequency from f = 0.925 to f = 1.25 in some cases (*SEP*1, *SEP*2, *DEP*1, and *DEP*3), the aeroacoustic coupling between the shear layer fluctuation and the cavity acoustic mode remains intact. This is due to the fact that both the shear layer and acoustic mode are locked-on together and operating at similar frequencies, as evidenced by the corresponding spectra at $\wp_S$ and $\wp_b$. Similar frequency lock-in phenomenon was observed in many studies of rigid cavity flow (East 1966; Yang *et al.* 2009; Yokoyama *et al.* 2017; Ho and Kim 2021).

On the contrary, in the *DEP*2 and *TEP* cases, the aeroacoustic coupling appears to disintegrate entirely. This is reflected from the fact that the shear layer and cavity mode operating at dissimilar frequencies, thereby failing to meet the conditions necessary for shear layer-cavity mode coupling. This results in a significant reduction in cavity tonal noise by 15 dB from the *RC* case. The far-field noise p' spectra of *DEP*2 and *TEP* reveal a mismatch frequency interaction between the shear layer and cavity mode, producing three distinct frequency peaks (f = 0.925, 1.375, and 0.45) of nearly equal magnitude. These peaks originate from the cavity mode, shear layer, and their interaction (f = 0.45 = 1.375 − 0.925), respectively. This suggests that the far-field noise reduction can be best achieved by initially shifting the shear layer frequency to a higher mode via the aft panel, followed by pacifying the shifted cavity mode through the bottom panel using suitably designed panel frequencies. In this context, the *DEP*2 configuration appears to be particularly effective.

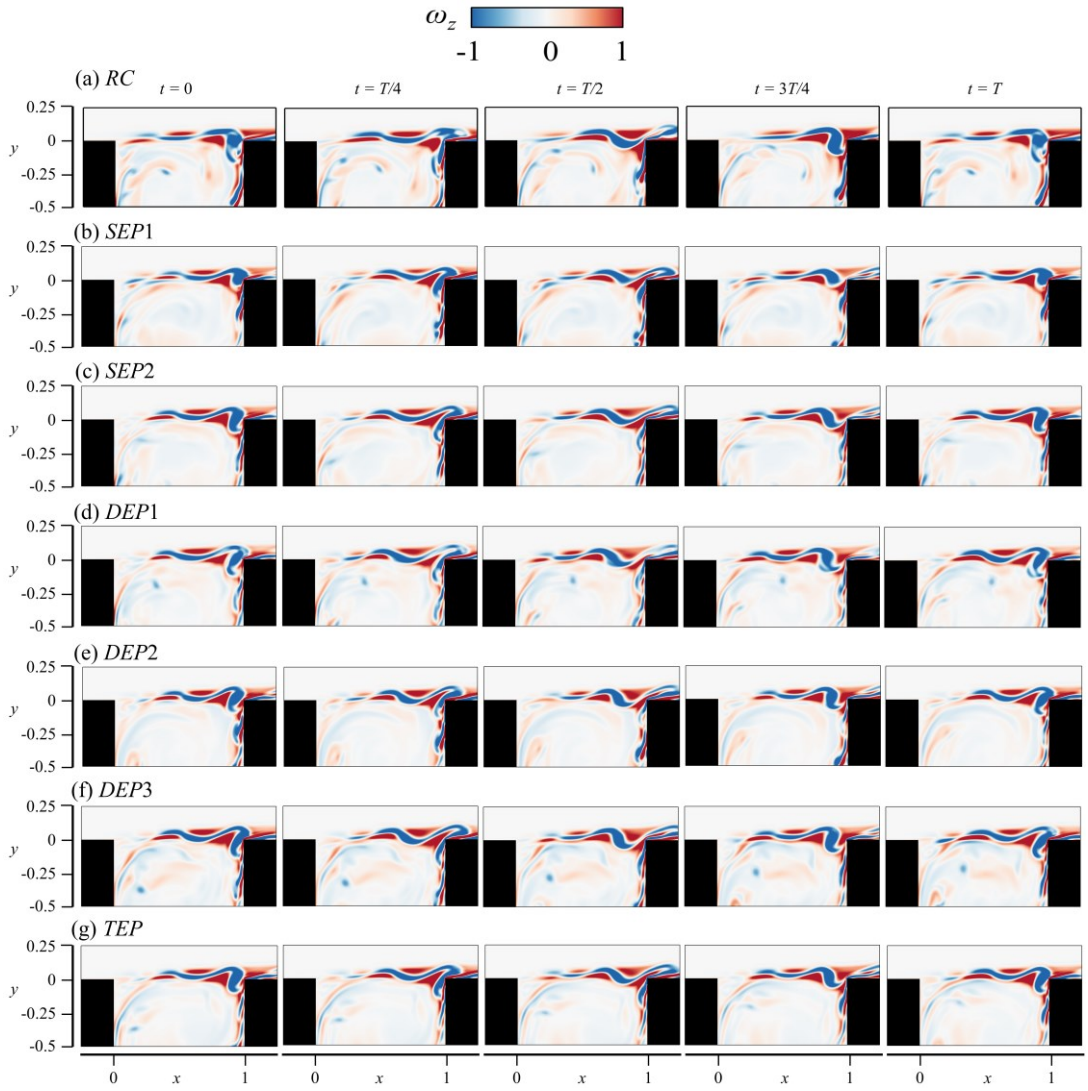

Figure 5.5 Instantaneous vorticity during the shear layer growth, followed by the downwash after impingement near the cavity opening region, spanning a full shear layer oscillation cycle. Snapshots are synchronized with those in Figure 5.4. (a) *RC*, (b) *SEP*1, (c) *SEP*2, (d) *DEP*1, (e) *DEP*2, (f) *DEP*3 (g) *TEP*.

Figure 5.8 shows the azimuthal *SPL* distributions of all the cases extracted at the respective peak frequencies. All the cavity noise directivity patterns closely resemble the *RC* case. Notably, the *SEP*1 and *SEP*2 cases introduce a slight directivity shift which results in a new peak radiation angle at approximately 45° from the downstream horizontal wall. The azimuthal variation of *SPL* in *DEP*1, *DEP*3 and *TEP* exhibit relatively consistent behaviours. However, the extent of noise reduction in *DEP*2 displays high variation across different azimuthal angles. The efficacy of noise reduction by

the elastic panels can be quantified using the change in sound power level $\Delta PWL = 10\log_{10}(W_{EP}/W_{RC})$, in dB, where $W = \int_0^{\pi} p'_{rms}\, d\theta$. Notably, the *SEP*1, *SEP*2 and *DEP*1 cases achieve a mild sound power reduction of nearly 5 dB but the *DEP*2 and *TEP* cases demonstrate a remarkable sound power level reduction of 14.3 dB and 13.6 dB respectively (Figure 5.7(e) and 5.7(g)). In summary, these observations provide robust evidence that the cavity-panel configurations designed with panels of dissimilar resonant frequencies exhibit much more prominent cavity noise reduction than the configurations designed with the same/similar frequencies. The forthcoming sections will delve into the analysis and discussion of the physical mechanisms underlying these phenomena.

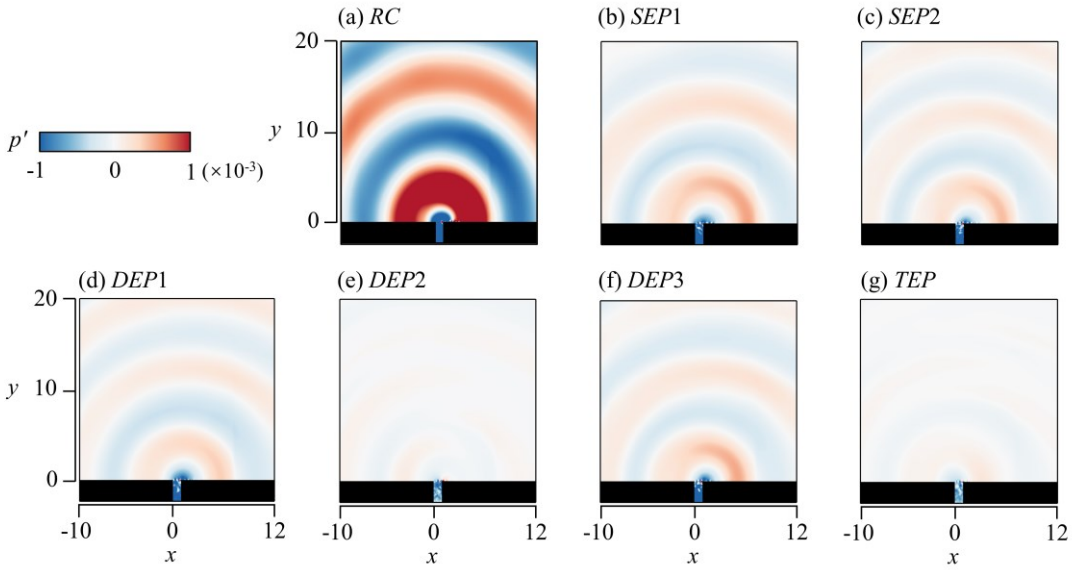

Figure 5.6 Instantaneous noise radiation captured at the instant of cavity mode rarefaction hits the cavity bottom (i.e. at ~ $T/4$ of Figure 5.4). (a) *RC*, (b) *SEP*1, (c) *SEP*2, (d) *DEP*1, (e) *DEP*2, (f) *DEP*3 (g) *TEP*.

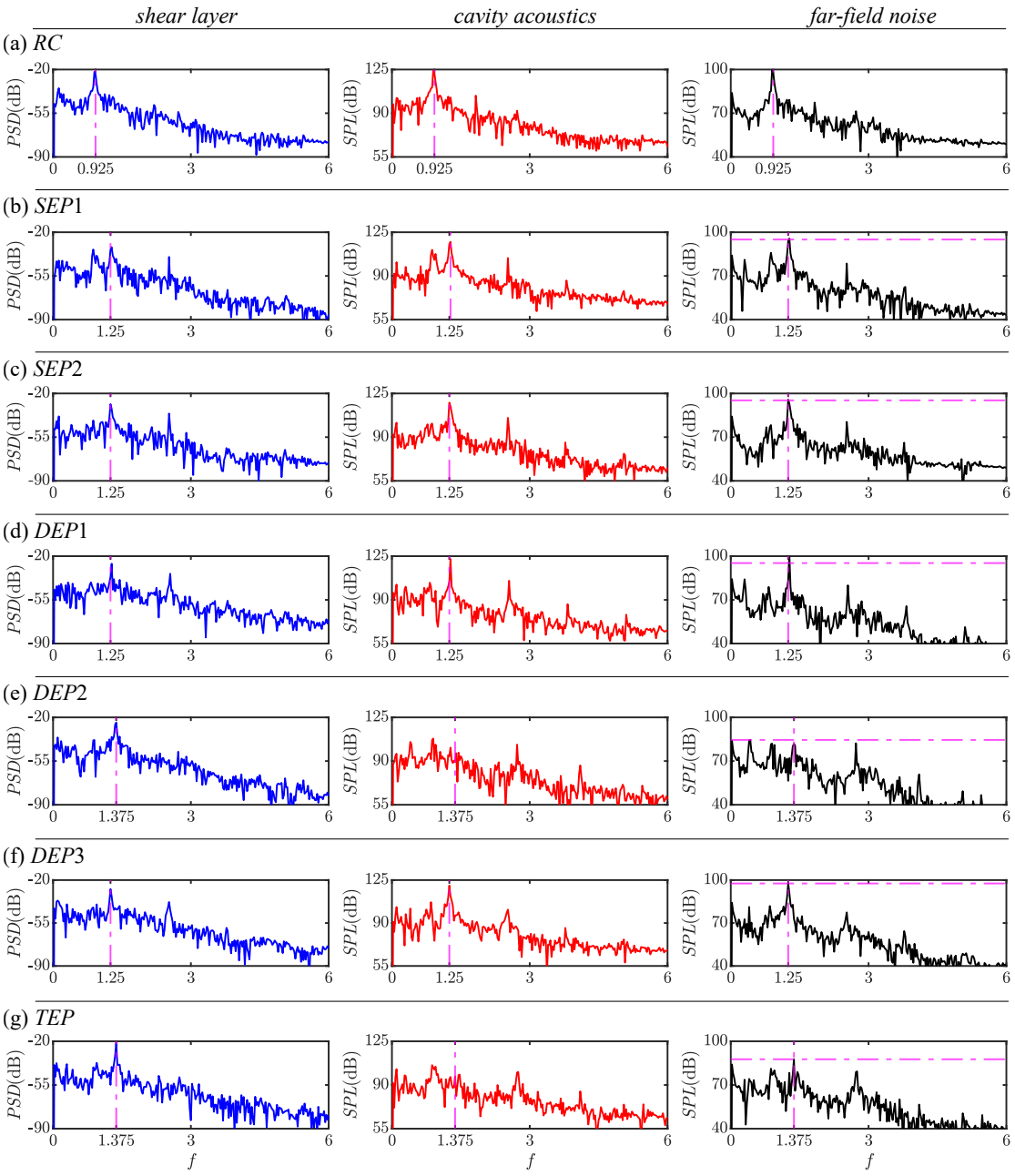

Figure 5.7 Comparison of p' spectra measured at locations $\mathcal{P}_s$ (first column), $\mathcal{P}_b$ (second column) and $\mathcal{P}_f$ (third column). The vertical dashed lines indicate the dominant frequencies trending across different cases and different sample locations. (a) *RC*, (b) *SEP*1, (c) *SEP*2, (d) *DEP*1, (e) *DEP*2, (f) *DEP*3 (g) *TEP*.

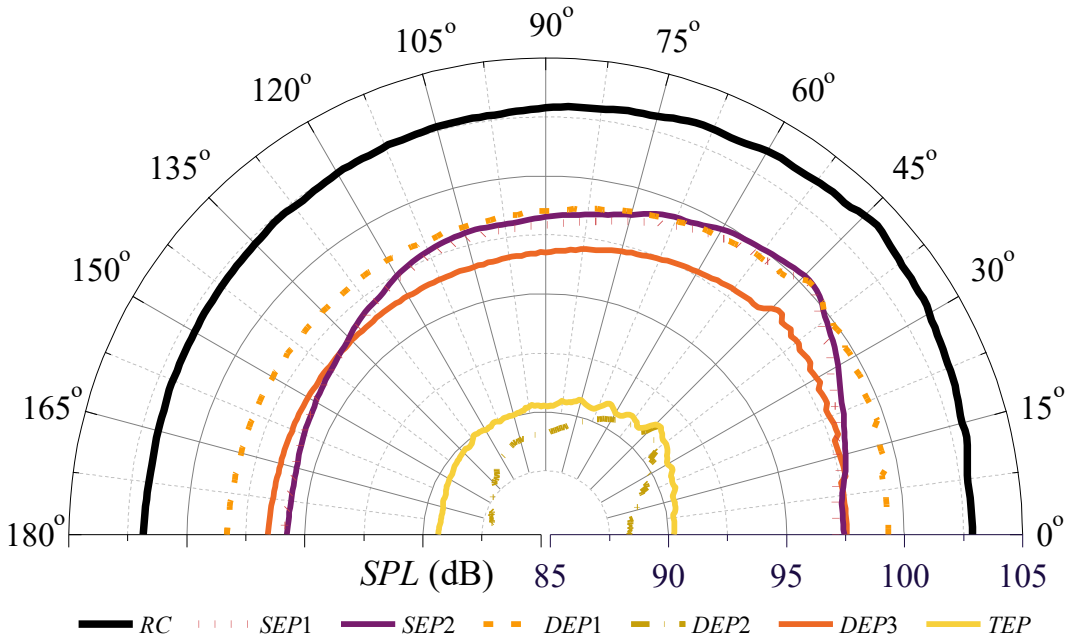

Cases	*SEP*1	*SEP*2	*DEP*1	*DEP*2	*DEP*3	*TEP*
Δ*PWL* (dB)	– 4.6	– 4.8	– 5.1	– 14.3	– 3.2	-13.6

Figure 5.8 Azimuthal distribution of peak *SPL* at r = 10. The table illustrates the changes in sound power level from *RC* case.

It is intriguing to examine the impact of elastic panels on the time-averaged drag experienced by the cavity (Table 5.2), calculated using the method adopted by Gharib and Roshko (1987) as $\bar{C}_D = 2\bar{F}_d/\rho u^2 l_{(x,y)}$, where $\bar{F}_d = \bar{F}_{form} + \bar{F}_{fric}$; $\bar{F}_{form} = -\int_{-2.5}^{0} p(0,y)\,dy + \int_{-2.5}^{0} p(1,y)\,dy$; $\bar{F}_{fric} = \int_0^1 \tau(x,-2.5)\,dx$. Notably, the skin friction drag coefficient $\bar{C}_{D,fric}$ is two orders of magnitude weaker than the form drag coefficient $\bar{C}_{D,form}$ in all cases so the latter is the primary contributor to the total cavity drag $\bar{C}_D$. For all the configurations in the study, a consistent reduction in total drag, up to 20%, from the *RC* case is observed. In particular the quietest *DEP*2 and *TEP* configurations give a total drag reduction of ~16% and ~11% respectively. The use of elastic panels for noise reduction is remarkably accomplished without compromising the cavity aerodynamics. In fact, it offers the advantage of

reduced cavity drag. It is worth noting that similar aeroacoustic benefits have been observed in the context of utilizing flow-induced elastic panels for tonal noise reduction in airfoils (Arif et al., 2022).

Table 5.2 Comparison of skin friction drag $\bar{C}_{D,fric}$, form drag $\bar{C}_{D,form}$, and total drag C_D for all cavity-panel configurations. Values in brackets indicate the percentage deviations from the *RC* case.

	$\bar{C}_{D,fric}$	$\bar{C}_{D,form}$	$\bar{C}_D$
RC	5.68×10^{-5}	1.70×10^{-3}	1.76×10^{-3}
*SEP*1	6.48×10^{-5} (+14.1%)	1.36×10^{-3} (-20.2%)	1.42×10^{-3} (-19.1%)
*SEP*2	5.48×10^{-5} (-3.6%)	1.59×10^{-3} (-6.4%)	1.64×10^{-3} (-6.4%)
*DEP*1	5.56×10^{-5} (-2.1%)	1.64×10^{-3} (-3.5%)	1.69×10^{-3} (-3.9%)
*DEP*2	5.15×10^{-5} (-9.26%)	1.43×10^{-3} (-15.7%)	1.48×10^{-3} (-15.6%)
*DEP*3	5.6×10^{-5} (-1.4%)	1.67×10^{-3} (-2.2%)	1.73×10^{-3} (-1.9%)
TEP	5.66×10^{-5} (-0.3%)	1.51×10^{-3} (-11.4%)	1.57×10^{-3} (-10.9%)

5.5 Noise Suppression Mechanism with Multiple Panels

Figure 5.9 shows the variations of pressure fluctuation p' along the lines $\mathscr{L}_s$ and $\mathscr{L}_b$ (in Figure 5.1) to illustrate the spatial-temporal variations of the shear layer growth across the cavity opening and cavity acoustic mode behaviour at the cavity bottom respectively. The inclined ridges in the first column of Figure 5.9 highlight the downstream convecting shear layer vortices and their convective velocities are estimated by the slope of the dashed lines. By utilizing the estimated values for vortices convection velocity (κ ~ 0.5, 0.67, and 0.72) and the suggested negligible phase delay (α ~ 0) between the impinging vortex and acoustic emission (Forestier *et al.* 2003; Larchevêque *et al.* 2003; El Hassan *et al.* 2008), the modified formula for Rossiter modes, $f = (m - \alpha)/(1/\kappa + M_\infty/[1 + (\gamma - 1)M_\infty^2/2]^{0.5})$ is employed to determine that the second (m = 2) dominant mode dominates the flow regimes across the cases. The resulting

frequencies are f = 0.95, 1.26, and 1.375. These values agree well with the dominant shear layer frequencies observed in the pressure spectra in all the cases (Figure 5.7). This agreement suggests that the cavity-panel configurations do not undergo significant alterations of the fundamental shear layer dynamics and continue to adhere to the inherent cavity flow behaviour. This behaviour can be effectively elucidated and supplemented by the established methodologies.

When the shear layer impinges at the cavity trailing edge, it emits acoustic waves that travel toward the cavity bottom and reflect upward along the cavity to form a standing wave for its acoustic mode whose existence is confirmed in the second column of Figure 5.9. A comparison of the strength of cavity standing waves reveals that the *RC* configuration gives robust internal cavity fluctuations. In contrast, the *DEP*2 configuration appears to significantly reduce the acoustic mode footprints as a result of an effective acoustic energy loss to the resonant panel at the cavity bottom. Other panel configurations appear to keep similar cavity acoustic fluctuations to a certain extent, albeit at significantly lower magnitudes than in the *RC* case.

Upon examining the relationship between the strength of the shear layer (near the cavity trailing edge) and the cavity mode in each case, an inverse correlation is observed: the weaker the cavity mode, the stronger the shear layer. This phenomenon can be explained by the aeroacoustic feedback mechanism proposed by Bruggeman *et al.* (1989). It is conceptualized on the energy transfer between the vortical (hydrodynamic) and potential (acoustic) fields in their study of the noise response of a flow-induced oscillation at low Mach number (0.07) in closed side branches of the gas transport system. In

their theoretical framework, based on the concept of the vortex sound theory (Powell 1964; Howe 2003), Bruggeman *et al.* (1989) presented the feedback mechanism constituted by the following processes: acoustic forcing from the resonance on the shear layer at the upstream corner; formation of coherent vortices by the instabilities in the separated shear layer; transfer of energy from the local flow to the acoustic field by the interaction of convective vorticity and the acoustic resonance; and the net energy transfer to the acoustic field determines the amplitude and the phase of the feedback at the upstream corner. Similar observations have also been reported in other studies (Yang *et al.* 2009; Yamouni *et al.* 2013; Ho and Kim 2021).

As illustrated in Figure 5.9(a), the said feedback mechanism is evident in the *RC* configuration, where the maximum shear layer energy appears to be converted to the acoustic mode at the resonance frequency $f = 0.925$. The superimposed vertical dashed lines indicate the acoustic mode meeting the in-phase shear layer convective ridges on the upstream edge ($x \sim 0$). However, the cavity-panel configurations deviate from this behaviour due to potential phase modifications of the cavity mode induced by the elastic panel. In fact, across the cavity opening, the out-of-phase destructive interference between the growing shear layer and passing acoustic waves appears to delay the shear layer growth in the *DEP*2 and *TEP* configurations. This is evidenced by the observation of a region of stagnant or stationary flow ($p' \sim 0$) around $x \sim 0.3$ in these cases (Figure 5.9(e) and 5.9(g)), where the horizontal dashed lines indicate the interruption of shear layer growth due to destructive interference upon out-of-phase shear layer-cavity mode interaction.

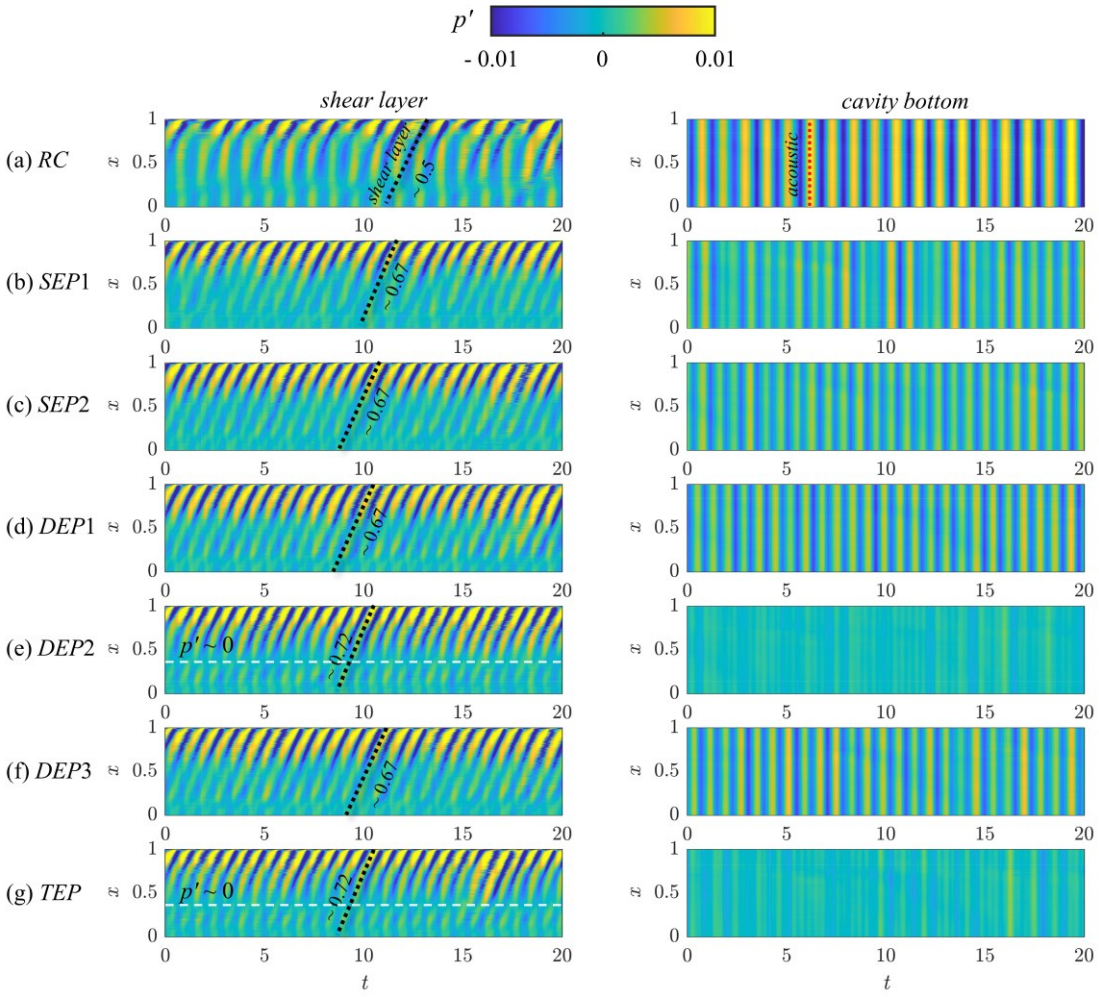

Figure 5.9 Temporal variations of p' across the cavity shear layer ($\mathscr{L}_s$) and along the cavity bottom ($\mathscr{L}_b$). The slope of inclined ridges marked with dashed lines measures the vortex convection velocity, and vertical dashed lines mark the projection of the corresponding cavity mode. (a) *RC*, (b) *SEP*1, (c) *SEP*2, (d) *DEP*1, (e) *DEP*2, (f) *DEP*3 (g) *TEP*.

Our observations indicate that the feedback mechanism driving the deep cavity flow and generating the extreme acoustic response in the *RC* case is a result of the mutual interaction between the convective shear layer and the cavity acoustic mode. This interaction occurs at the same frequency and their favourable phase relationship (a lock-on effect) which facilitates maximum energy conversion from the shear layer to the cavity acoustics. However, in the *SEP*1, *SEP*2, *DEP*1 and *DEP*3 cases, although the shear layer and cavity mode are fluctuating at a similar frequency, their acoustic radiation is slightly reduced

whereas in *DEP*2 and *TEP* cases the significant acoustic reduction is accompanied by the emergence of different shear layer and cavity mode fluctuation frequency as observed in Figure 5.7. To understand the dynamics leading to this acoustics reduction, it is beneficial to examine the spatial distribution of p' spectra within the shear layer (i.e. along the $\mathscr{L}_s$) and on the cavity bottom (i.e. along the $\mathscr{L}_b$). Additionally, it is important to assess the coherence γ^2 between $p'(\mathscr{L}_s)$ and $p'(\mathscr{p}_b)$ calculated as $\gamma^2(f) = |P_{sb}(f)|^2 / P_s(f)P_b(f)$, where $P_s(f)$ and $P_b(f)$ are the power spectral densities of p'signals for the shear layer and the acoustic mode respectively, and $P_{sb}(f)$ is the cross power spectral density between the signals. It is also prudent to evaluate the phase difference $\Delta\phi$ between $p'(\mathscr{L}_s)$ and $p'(\mathscr{L}_b)$ along the same streamwise location (i.e. same x) (Figure 5.10).

In the *RC* case, the shear layer impingement excites a range of frequencies near the cavity trailing edge and produces a relatively wide spectrum. However, only one frequency, f = 0.925, is amplified and locked-on between the growing shear layer and cavity acoustic mode for their strong mutual synchronization, $\gamma^2(0.925) \sim 1$, and in-phase excitation, $\Delta\phi(0.925) \sim 0$. This perfect condition for aeroacoustic resonance allows the acoustic field to draw maximum energy from the growing shear layer, as evidenced by the higher magnitude of the acoustic spectrum at the cavity bottom. Having understood the conditions of the feedback coupling mechanism in the *RC* case, we can now establish a criterion based on four quantifiable conditions derived from the *RC* case and compare them in the cases with panels.

C1. Frequency lock-on ($f_{shear\ layer} = f_{acoustic\ mode} = f_1$);

C2. Strong synchronization ($\gamma^2(f_1) \sim 1$);

C3. Favourable phase difference ($\Delta\phi(f_1) \sim 0$);

C4. Energy conversion from shear layer to acoustic field ($|p'(\mathscr{L}_b, f_1)| > |p'(\mathscr{L}_s, f_1)|$).

Interestingly, the *SEP*1, *SEP*2, *DEP*1, and *DEP*3 cases meet two of the four conditions as their respective shear layer and cavity mode share the same frequency ($f = 1.25$) and strong synchronization ($\gamma^2(1.25) \sim 1$). However, they fail to maintain a favourable phase difference at the dominant frequency, preventing efficient energy transfer to the acoustic mode upon shear layer impingement. As a result, the shear layer remains concentrated near the downstream edge. In the *DEP*2 and *TEP* cases, none of the four conditions are met, indicating a complete decoupling of the feedback mechanism and resulting in the highest noise reduction. Other cases with elastic panel partially follow the feedback process so slight noise reduction is resulted.

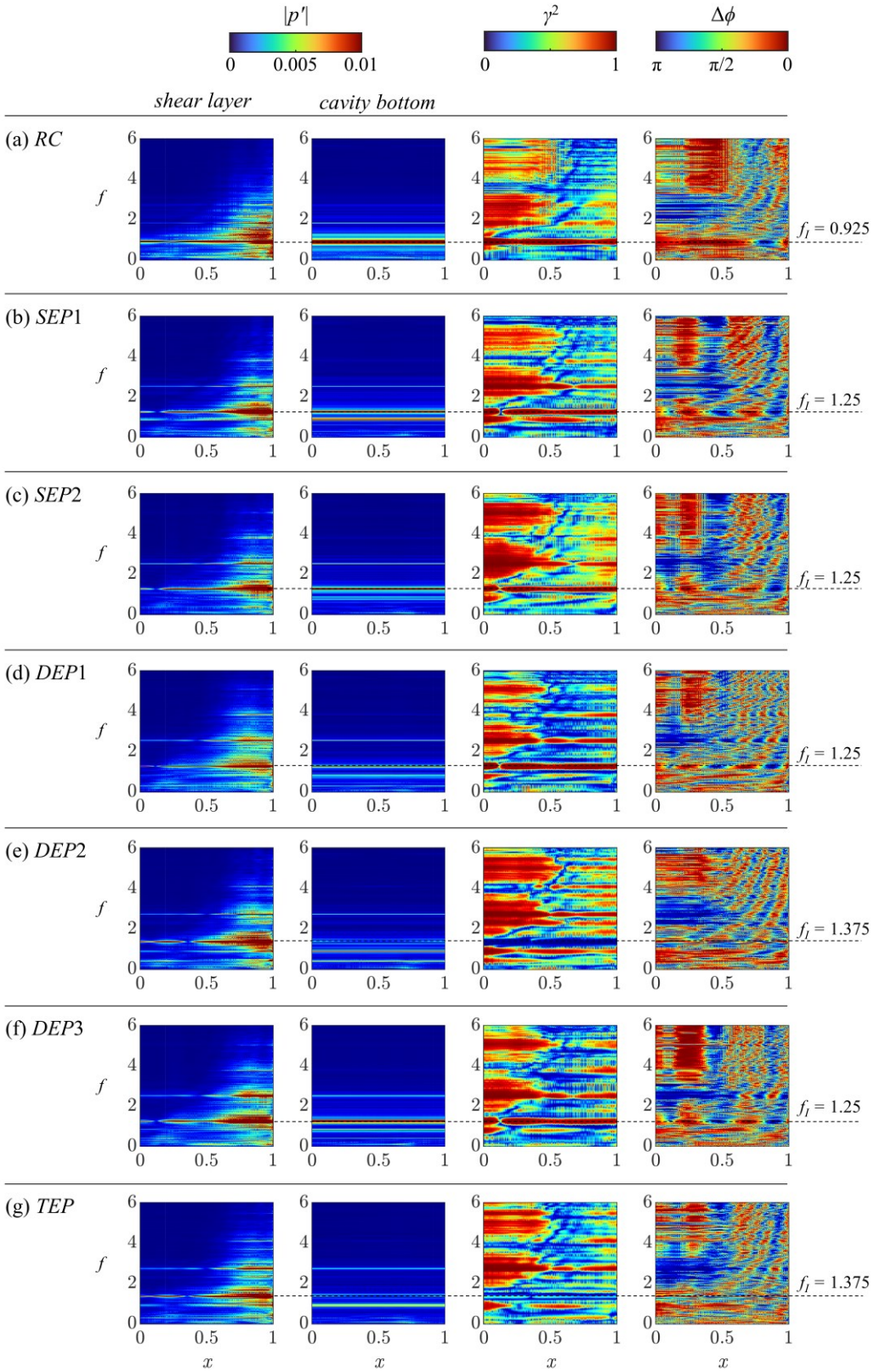

Figure 5.10 First column: variation of FFT transformed $p'(\mathscr{L}_s)$ magnitude across cavity opening. Second column: variation of FFT transformed $p'(\mathscr{L}_b)$ magnitude across the cavity bottom ($\mathscr{L}_b$). Third column: coherence, γ^2 between shear layer pressure $p'(\mathscr{L}_s)$ across cavity opening and acoustic pressure at cavity bottom center $p'(\mathscr{p}_b)$. Fourth column: phase difference, $\Delta\phi$ between $p'(\mathscr{L}_s)$ and $p'(\mathscr{L}_b)$. (a) *RC*, (b) *SEP*1, (c) *SEP*2, (d) *DEP*1, (e) *DEP*2, (f) *DEP*3 (g) *TEP*.

The *p'* magnitudes at the dominant frequencies of the spectra in Figure 5.10 are consolidated to provide further insight into the variations of the coupling patterns between the shear layer growth and the cavity acoustics (Figure 5.11). In the *RC* case, the *p'* magnitude gradually increases from cavity leading edge up to $x = 0.8$ and beyond which it suddenly rises by almost 160% at cavity trailing edge (Figure 5.11(a)). However, the presence of elastic panels in all configurations seems to significantly alter the evolution of *p'* along the cavity shear layer. Most notably, the pressure fluctuations in the shear layer appear to decay downstream, nearly diminishing (i.e., $p' \sim 0$) at certain streamwise locations, and then increase rapidly towards the trailing edge, surpassing the *RC* case at $x > 0.6$. Interestingly, the *p'* values of all configurations, except for *DEP* and *TEP*, completely decay to zero at $x \sim 0.13$. The *p'* values of *DEP*2 and *TEP* become zero at a further downstream position, around $x \sim 0.36$. The distributions of *p'* magnitude along the cavity bottom in Figure 5.11(b) reveal that the presence of elastic panels tends to suppress the development of cavity acoustics in all configurations, with the *RC* case exhibiting the strongest cavity acoustics. The elastic panels are capable of reducing the acoustic *p'* at the cavity bottom by at least half. In particular, those in *DEP*2 and *TEP* can nullify the acoustic *p'*, possibly due to the highly effective energy absorption by the resonant vibration of the panels at the cavity bottom.

To gain a better understanding of the aforementioned observations, it is more informative to study the coherence (γ^2) and the phase difference ($\Delta\phi$) of *p'* at the dominant frequencies, at the same streamwise locations (i.e., at the same x) along both the cavity opening and the bottom (Figure 5.11(c) and 5.11(d)). For the *RC* case, $\gamma^2 \sim 1$ and $\Delta\phi \sim 0$ up to $x \sim 0.6$, indicating a strong

coupling between the shear layer growth and the cavity acoustics. The coupling is modified at $x > 0.6$ due to the influence of shear layer impingement at the trailing edge, as evidenced by significant variations in $\Delta\phi$. However, the impingement flow is still synchronized with the cavity acoustics, as indicated by the consistent $\gamma^2 \sim 1$ in that region. For all cavity-panel configurations, except *DEP*2 and *TEP*, the value of γ^2 generally remains close to unity, indicating that their shear layer growth and the cavity acoustics are still synchronized. However, the elastic panels appear to modify and weaken the coupling of two processes to varying degrees, as seen in the fluctuations of $\Delta\phi$. The loss of coupling is most pronounced at $x \sim 0.13$, where the shear layer growth and the cavity acoustics tend to counteract each other, resulting in $\Delta\phi \sim \pi/2$. All these facts strongly support the notion that the chosen elastic panels inside the cavity act to weaken the original coupling observed in the *RC* case, leading to a reduction in overall cavity noise generation. A similar weakening of the coupling is observed in *TEP*, but its γ^2 remains below 0.5 across the length of the cavity, reaching its minimum at $x \sim 0.24$. As a result, the shear layer growth in *TEP* becomes much less synchronized with the cavity acoustics compared to all the cavity-panel configurations just discussed and the two processes are considered to be effectively decoupled. *TEP* generates much less noise as a consequence. A more complete decoupling of a similar kind is observed in *DEP*2 in which its γ^2 consistently diminishes across the cavity length regardless of the $\Delta\phi$ values. As a result, *DEP*2 exhibits the lowest level of cavity noise compared to all other configurations.

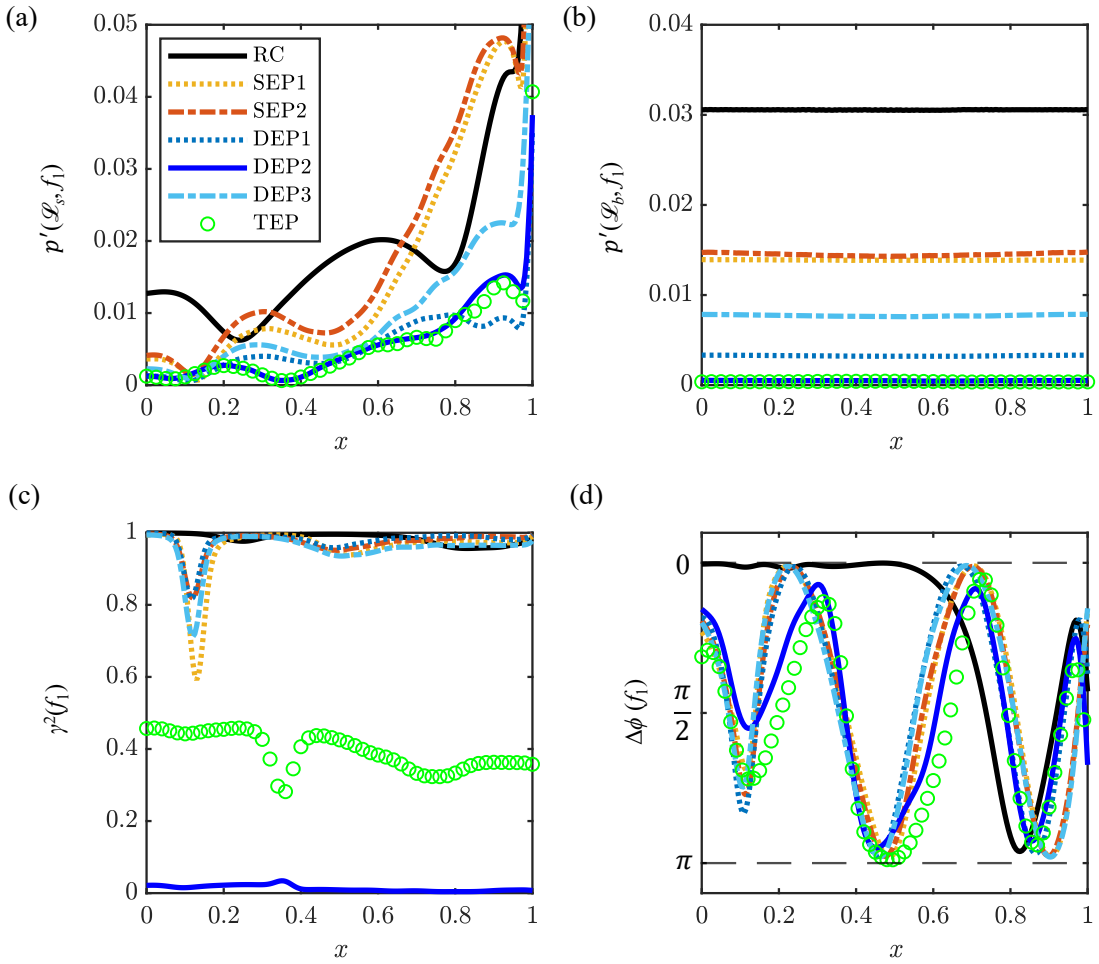

Figure 5.11 (a) Variation of FFT transformed peak $p'(\mathscr{L}_s, f_1)$ magnitude across cavity opening. (b) Variation of FFT transformed peak $p'(\mathscr{L}_s, f_1)$ magnitude across the cavity bottom. (c) Coherence between shear layer pressure $p'(\mathscr{L}_s)$ across cavity opening and acoustic pressure $p'(\mathscr{p}_b)$ at cavity bottom center. (d) Phase difference between $p'(\mathscr{L}_s, f_1)$ and $p'(\mathscr{L}_b, f_1)$.

In the *SEP*1 and *SEP*2 configurations, the presence of the elastic panel introduces a phase shift between the shear layer impingement notches and the resulting cavity acoustic modes, causing them to be misaligned (Figure 5.12(b) and 5.12(c)). This phase shift extends well beyond $\pi/3$ (see Figure 5.11(d)), resulting in ineffective synchronized interference between the p' fluctuations from the growing shear layer and the cavity acoustic waves, regardless of whether the elastic wall is positioned near the *LE* or at the bottom of the cavity. Consequently, the cavity acoustic mode in these configurations is weaker

compared to the *RC* case. Surprisingly, the dual-panel configuration, *DEP*1, which combines the design elements of *SEP*1 and *SEP*2, behaves in a similar fashion (Figure 5.12(d)). The same phenomenon persists even when the resonant frequency of the elastic panel on the aft wall is adjusted to form *DEP*3 (Figure 5.12(f)). However, if a properly designed natural frequency is used for the bottom panel to enhance energy absorption (i.e., *DEP*2), more energy loss occurs, thereby maintaining the feedback loop for the synchronization of shear layer growth. This results in the weakest corresponding cavity acoustic mode. On the other hand, introducing an additional elastic panel on the front wall (i.e., *TEP*) does not provide any additional energy contribution, resulting in p' fluctuations that exhibit patterns and magnitudes similar to those observed in *DEP*2. As a result, the level of noise reduction achieved in both *DEP*2 and *TEP* cases is comparable (Figure 5.11).

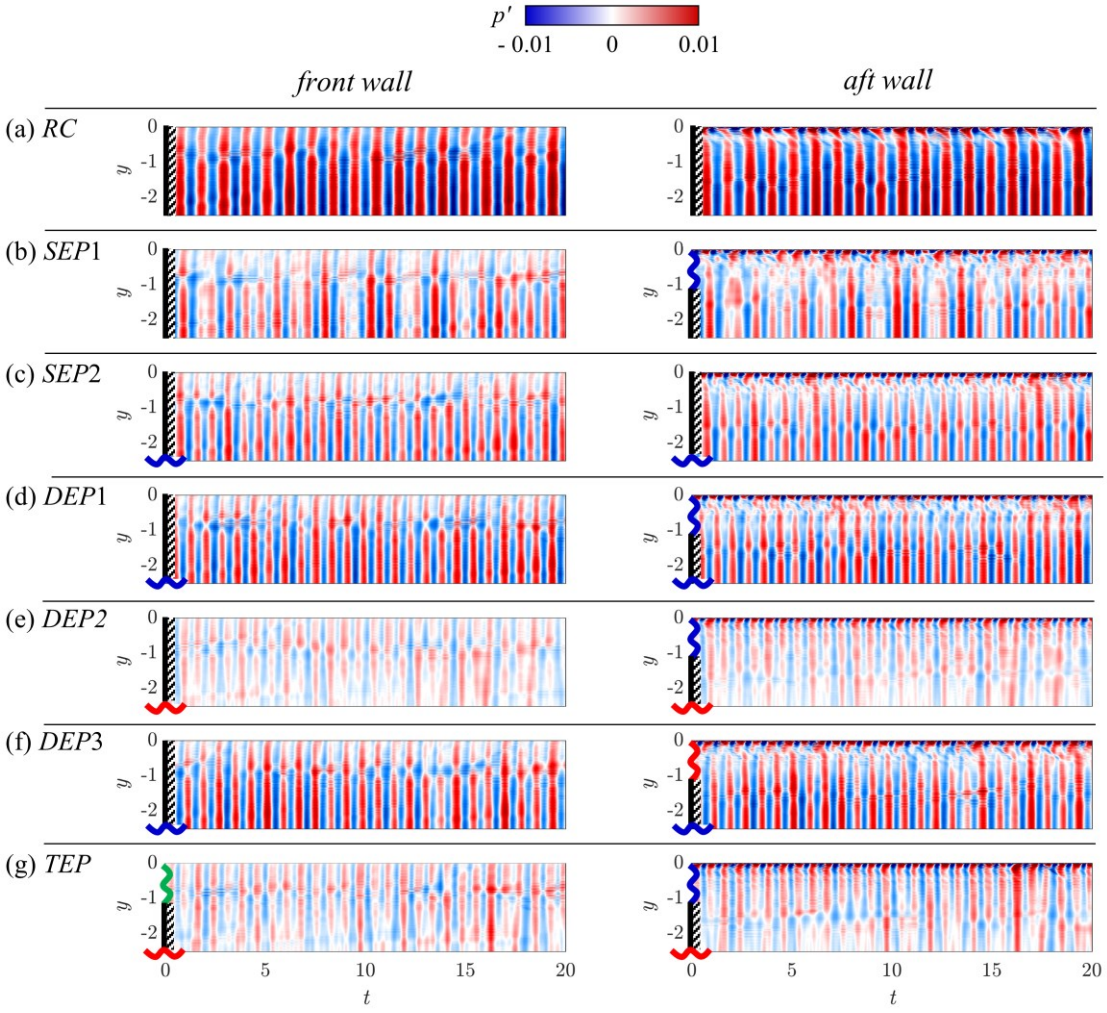

Figure 5.12 Spatio-temporal variation of p' across the cavity side walls (along $\mathscr{L}_e$ and $\mathscr{L}_t$) illustrating the targeted effect of panel vibrations on the localized flow pattern modification across the respective panel locations. The specific panel locations are marked with flexible wavy icons on the aft or front walls. The operation of the bottom wall panel is indicated with a squared box pinned at the cavity base. The panel color indicates the assigned panel frequency arrangement as in Figure 5.3 (a) *RC*, (b) *SEP*1, (c) *SEP*2, (d) *DEP*1, (e) *DEP*2, (f) *DEP*3 (g) *TEP*.

Figure 5.13 illustrates the distribution of p' spectra recorded along the front and aft walls of the cavity. In the *RC* case, a single dominant frequency f = 0.925 of the flow and its first harmonic on both walls are clearly evident (Figure 5.13(a)). On the front wall, there are observable p' fluctuations at lower frequencies f < 0.55 within -1.0 < y < -0.5, corresponding to the upwash entrainment of vorticity induced by the shear layer (Figure 5.5(a)). On the aft

wall, the shear layer impingement results in a broadband p' fluctuation at the cavity trailing edge. Its subsequent downwash creates a low-frequency p' fluctuation at $f \sim 1.6$. As discussed previously, an effective cavity aeroacoustic resonance occurs in *RC* case due to the proper phase-matching of the dominant shear layer fluctuations and the cavity acoustic mode with the chosen L/D, both at $f = 0.925$. Significant differences arise after the installation of elastic panels. In each of the *SEP*1, *SEP*2, *DEP*1, and *DEP*3 cases, the presence of elastic panel(s) re-distributes the dominant flow fluctuation energy and splits them into two new modes of narrower bands but weaker magnitudes. The broadband p' fluctuations caused by shear layer impingement at the trailing edge are generally weaker compared to the *RC* case. Similar types of p' fluctuations due to upwash and downwash persist on the front and aft walls respectively, but they are generally weaker and more dispersed than those in the *RC* case. These phenomena can be attributed to the fact that the frequencies of the two new modes do not provide a favorable phase-matching condition for cavity flow feedback and synchronization, unlike in the *RC* case. Consequently, the cavity aeroacoustic resonance is greatly weakened, resulting in reduced flow unsteadiness and moderate noise reduction in these cases. The splitting of the dominant flow fluctuation mode is more pronounced in the p' spectra of *DEP*2 and *TEP*. Each of these cases allows for a redistribution of flow fluctuation energy into three new modes, each with a narrower band and significantly reduced magnitude. Their upwash on the front wall, downwash on the aft wall, and the shear layer impingement at the trailing edge are highly suppressed as well. This can be attributed to the more unfavorable phase-matching conditions in these two cases, due to their considerably reduced overall p' fluctuations (Figure 5.13) and exceptionally higher cavity noise reduction.

Similar emergence of new modes in controlled cavity flows has been reported in experimental active control studies of subsonic flows past open shallow cavities ($L/D > 1$) by Samimy *et al.* (2007) and Douay *et al.* (2016). They observed that the application of active control action leads to the generation of new flow modes that interact with the original mode. However, their different relative phase differences result in a resultant flow fluctuation with a modulated magnitude, which can be either stronger or weaker than the original mode depending on the freestream Mach number and cavity dimensions. Their finding supports the observed fact with the proposed noise control idea that the weakening of the original cavity aeroacoustic resonance is facilitated by the introduction of new flow modes induced by the panel compliance. The new flow modes at multiple frequencies interact with one another, ultimately resulting in modulated resultant flow pressure fluctuation *p'* weaker than the original *RC* case (Figure 5.13(h)). As a result, all cases with elastic panel(s) consistently exhibit lower cavity noise generation to varying extents.

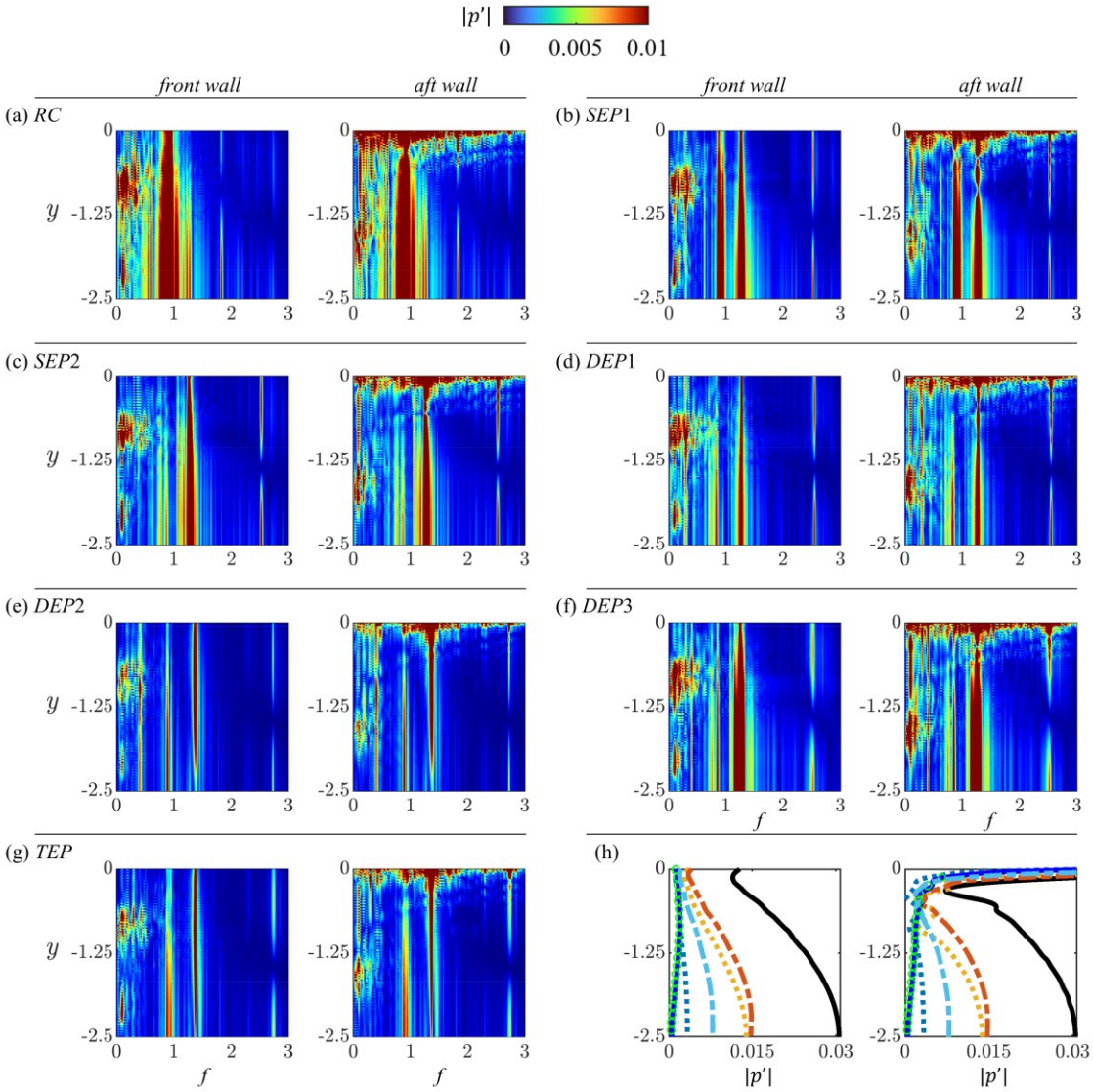

Figure 5.13 Distribution of p' along cavity front and aft walls. (a) *RC*, (b) *SEP*1, (c) *SEP*2, (d) *DEP*1, (e) *DEP*2, (f) *DEP*3 (g) *TEP* (h) Magnitudes of p' along the respective spectra peaks; ——— , *RC*; ····· , *SEP*1; – – – , *SEP*2; ····· , *DEP*1; ——— , *DEP*2; – – – , *DEP*3; – – – , *TEP*.

5.6 Aeroacoustic-Structural Interaction of Panels

It is intriguing to observe the influence of aeroacoustically, or acoustically, induced vibratory responses of elastic panels on the modification of the coupling between developing shear layers and cavity acoustic modes in all cases. Figure 5.14 portrays the temporal progression of vibratory displacements w along the elastic panels as observed across all cases. Generally, each panel exhibits a continuous bending wave pattern over time; however, the specific type of panel bending wave it sustains is contingent upon the panel orientation. For vertical panels, transverse bending wave propagation predominates, whereas horizontal panels solely support standing bending waves. This distinction can be attributed to the varying pressure fluctuations exerted on the panel surfaces due to diverse types of aeroacoustic-structural interactions within each case.

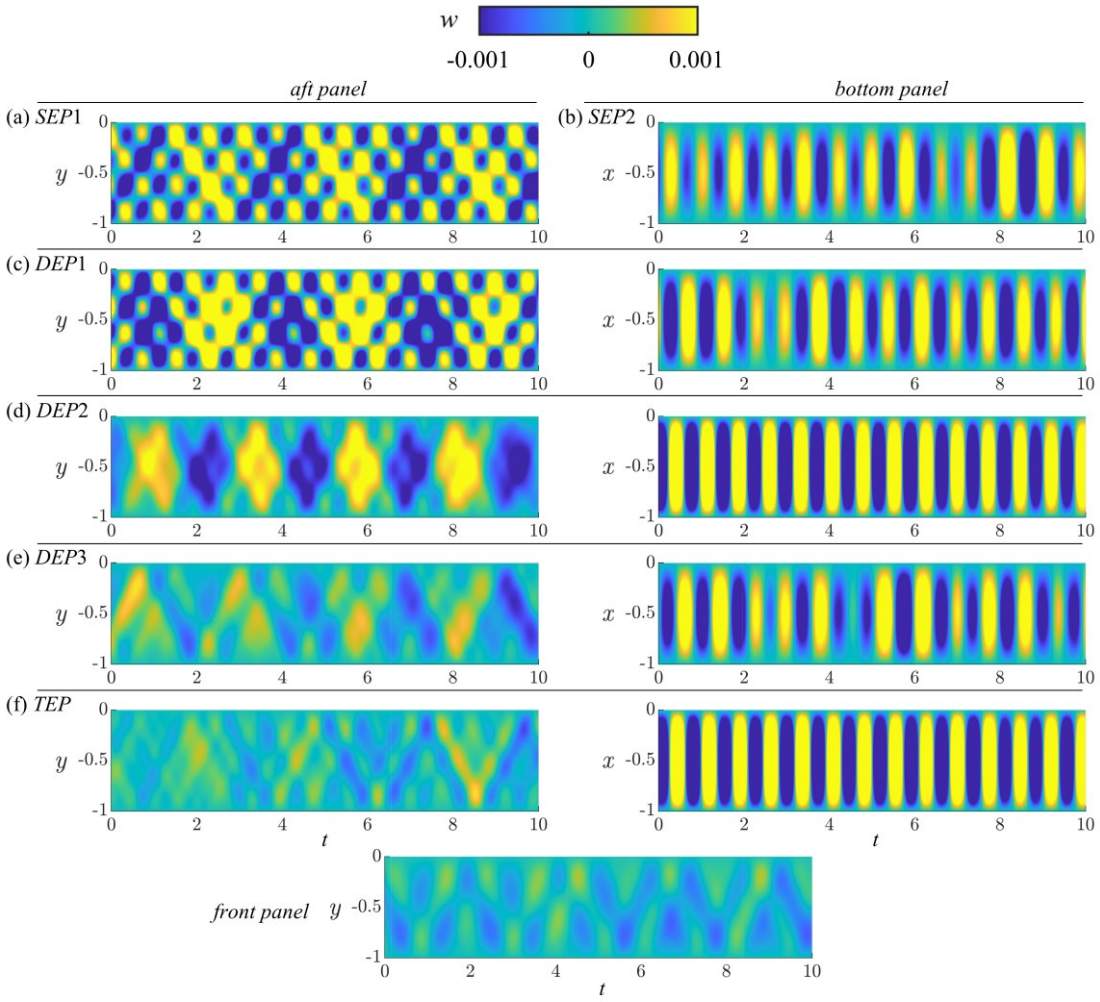

Figure 5.14 Spatio-temporal panel vibratory responses. (a) *SEP*1, (b) *SEP*2, (c) *DEP*1, (d) *DEP*2, (e) *DEP*3 (f) *TEP*.

Figure 5.15 depicts the vibratory acceleration $|\ddot{w}|$ spectra at the mid-points of the panels across various cases. In order to aid the discussions, blue, red and green lines are used to indicate panel designs with designed natural frequencies ($f_{EPd1}, f_{EPd2}, f_{EPd3}$) = (0.925, 1.25, 1.375) at their third (n = ③) panel modes. In the *SEP*1 case, since the panel is situated near the cavity opening, it directly experiences p' which is of an aeroacoustic nature (Naseer *et al.* 2023b). This p' comprises fluctuations from the developing shear layer and incident acoustic fluctuations originating from the cavity bottom. It is intriguing to note that the resulting aeroacoustic-structural interaction, involving the shear layer impingement, its subsequent unsteady downwash, and the vibrating panel,

leads to structural resonance at panel vibration modes n = ①, ②, ④, ⑦, ⑧, and ⑨ (Table I). This highly nonlinear interaction induces p' excitation with magnitudes and phases spreading across a broad frequency range, thereby favourably exciting multiple panel vibration modes simultaneously. All the excited panel vibration modes compete to absorb the energy of the p' excitation at their resonant frequencies, consequently leaving less flow fluctuation energy available for cavity resonance as compared to the *RC* case. It is surprising to observe that the dominant panel structural resonance occurs at the fourth (n = ④) vibration mode, rather than the third (n = ③) mode specified in the panel design. This particular structural resonance is believed to contribute to setting the final frequency f = 1.25 for p', which is taken up by the developing shear layer and the cavity acoustic mode of the entire cavity-panel system (Figure 5.7(b)). In the *SEP*2 case, the panel located at the bottom of the cavity is subjected to p' solely due to the cavity acoustic resonant mode. As a result, the excitation of the panel is primarily of an acoustic nature (Naseer *et al.* 2023b). The cavity mode standing wave characteristics generate a p' with a much narrower spectral magnitude distribution than that generated in *SEP*1 by impinging the shear layer. This fact leads to the excitation of fewer panel vibration modes compared to the *SEP*1 case. Only vibration modes n = ④ and ⑧ are excited. The resultant acoustic-structural interaction of the entire cavity-panel system selects the dominant structural resonance at the fourth (n = ④) panel vibration mode, although a weak excitation at the designed third (n = ③) mode still persists. Similar to the *SEP*1 case, the bottom panel structural resonance determines the dominant frequencies of the developing shear layer and the cavity acoustic mode of the entire cavity-panel system.

In the *DEP*1 configuration, both panels from the *SEP*1 and *SEP*2 cases are installed (Figure 5.3). It is interesting to note that the structural resonance of the panels exhibits a high degree of similarity to those observed in the individual *SEP*1 or *SEP*2 cases. The only notable distinction is that the *DEP*1 aft panel demonstrates a weaker response at the favoured fourth (n = ④) mode but a stronger response at the designed third (n = ③) mode. This difference is believed to facilitate more effective absorption of p' energy within the cavity, as compared to the *SEP*1 or *SEP*2 cases. As discussed before, in the *DEP*2 case, the bottom panel design is changed to absorb the dominance of p' fluctuation at f = 1.25 inside the cavity as observed in *SEP*1, *SEP*2 and *DEP*1 cases. The combination of different panel designs into the cavity appears to result in a completely distinct type of aeroacoustic- and acoustic-structural interactions from previous cases. Now the *DEP*2 aft panel shows structural resonance at panel vibration modes n = ①, ④, ⑦ and ⑨ but the bottom panel does not have any of its own vibration modes excited. It is surprising to observe that the bottom panel shows a particularly strong forced vibration response at f = 1.375 which does not coincide with any of vibration modes of the two panels. Such forced vibration response may disturb the fluid above the bottom panel and radiate a p' component at the same f = 1.375. This extra p' component is observed to propagate towards the aft panel and set it to vibrate with a response comparable to the excited n = ④ of the aft panel. The two panels appear to show a cross-talk to one another. Similar phenomenon of cross-talk is also evident with bottom panel vibration for the emergence of two weak acceleration peaks at the 3rd and 9th modes of the aft panel. This dominant frequency f = 1.375 is considered an evidence for the specific cavity-panel system exhibiting

synchronization between the unsteady aeroacoustics and the nonlinear dynamics of the panels. Such form of synchronization is not observed in literature of cavity aeroacoustics. It can be considered as a form of aeroacoustic-structural resonance for the different panels in cavity configuration design. It must be noted that aeroacoustic-structural resonance does not show up in *DEP*1 case whose both panels are the same (Figure 5.15(c)).

As previously discussed, in the *DEP*2 case, the design of the bottom panel has been modified to address the dominant fluctuations of p' at $f = 1.25$ within the cavity, as observed in the *SEP*1, *SEP*2, and *DEP*1 cases. The combination of different panel designs within the cavity appears to result in a completely distinct type of aeroacoustic and acoustic-structural interactions compared to the previous cases. In the *DEP*2 configuration, the aft panel exhibits structural resonance at panel vibration modes n = ①, ④, ⑦ and ⑨, while the bottom panel does not have any of its own vibration modes excited. It is surprising to note that the bottom panel displays a particularly strong forced vibration response at $f = 1.375$, which does not correspond to any of the vibration modes of the two panels. This forced vibration response may disrupt the fluid above the bottom panel and generate a component of p' at the same frequency of f = 1.375. This additional p' component is observed to propagate towards the aft panel, causing it to vibrate with a response comparable to the excited $n = 4$ mode of the aft panel. The two panels seem to exhibit a cross-talk effect, influencing the vibrations of each other. A similar phenomenon of cross-talk is also evident with the vibration of the bottom panel, resulting in the emergence of two weak acceleration peaks at the third (n = ③) and ninth (n = ⑨) modes of the aft panel. The dominant frequency of $f = 1.375$ is considered as evidence

of the specific cavity-panel system *DEP*2 exhibiting synchronization between the unsteady aeroacoustics and the nonlinear dynamics of the panels. Such a form of synchronization has not been observed in the existing literature on cavity aeroacoustics. It can be regarded as a manifestation of aeroacoustic-structural resonance in the cavity configuration design with different panels. It is important to note that aeroacoustic-structural resonance is not observed in the *DEP*1 case, where both panels are identical (Figure 5.15(c)). In the *DEP*3 case, the two panels exhibit similar vibratory responses as observed in the *DEP*2 case, albeit with their positions swapped. Although aeroacoustic-structural resonance is still present, its impact is not as pronounced as in the *DEP*2 case. The bottom panel demonstrates high vibration responses at n = ④ and ⑧ modes, while the aft panel exhibits significant vibration responses at n = ①, ③, and ⑦ (Figure 5.15(d)). Additionally, there is cross-talk occurring at the frequency corresponding to the n = ⑧ mode of the bottom panel. However, the magnitudes of the responses of both panels are generally weaker compared to those in the *DEP*2 case, indicating a reduced energy absorption of p' within the cavity. In the *TEP* case, a front panel is incorporated into the *DEP*2 configuration. This panel is purposefully designed to absorb the observed aeroacoustic-structural resonance at f = 1.375 by resonating at its own third (n = ③) mode. While the front panel exhibits substantial responses at its n = ②, ③, and ⑥ modes, its inclusion does not significantly modify the vibratory responses of the aft and bottom panels. These panels continue to display more or less the same levels of vibratory responses as in the *DEP*2 case (Figure 5.15(e)), suggesting a similar ability to absorb energy from p' within the cavity.

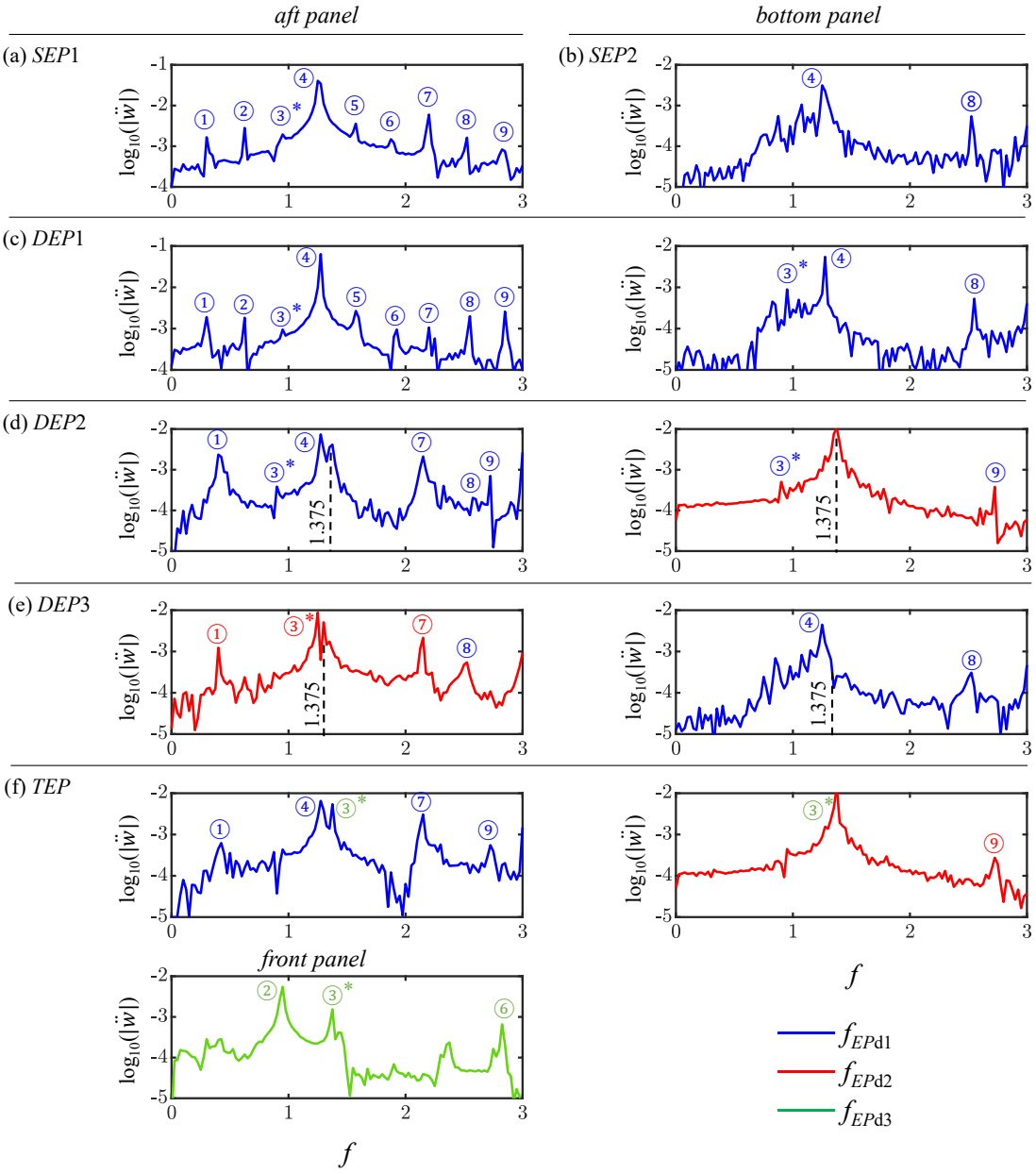

Figure 5.15 Modal response of panel acceleration $|\ddot{w}|$. Spectral peaks are tagged with the modes given in Table I. The asterisk '*' means the primary designed panel natural frequencies shaded in Table I. (a) *SEP*1, (b) *SEP*2, (c) *DEP*1, (d) *DEP*2, (e) *DEP*3 (f) *TEP*.

Figure 5.15 clearly shows that the panels in all cases are capable of entering different structural resonance at various panel vibration modes depicted in Table 5.1. The first and third columns in Figure 5.16 display the distributions of the panel acceleration $\ddot{w}$ spectra along the length of the panels in all cases. Clearly, whenever a panel is oriented vertically (i.e. the aft and front panels), all the panel resonant frequencies identified in Figure 5.15 develop into their corresponding vibration mode shapes fully along the panel. The emergence of complete mode shapes provides further support for the resonant responses of the panels. However, the vibratory responses of all bottom panels exhibit different behaviours. In every case, no full vibration mode shape is observed along the bottom panel, even when the frequencies of the vibratory responses match the natural frequencies depicted in Table 5.1. Instead, the entire bottom panel seems to respond to the imposed p' in a manner similar to the forced vibration of the first mode. The particular forced vibration behaviour is likely due to the specific type of acoustic-panel interaction that is driven by the cavity acoustic mode at the bottom of the cavity. The standing wave of the cavity acoustic mode may expose an acoustic p' excitation whose phase is constant along the length of the bottom panel. The constant excitation phase may not favour the development of spatial vibratory responses into their full mode shapes. On the contrary, all the vertical panels are excited by aeroacoustic p' excitation with distributed phases over a wide range of frequencies, resulting from shear layer impingement and its downwash, which favours the simultaneous development of all mode shapes fully along the bottom panel. The different characteristics of p' excitation phases on the vertical and bottom panels are believed to be responsible for the emergence of their different sustained bending wave patterns in Figure 5.14.

Furthermore, it could be argued that while a panel absorbs p' energy inside the cavity through its different resonant vibration modes, the resonant vibratory accelerations may generate additional p' components which may eventually contribute to the cavity noise radiation in the far field location $\wp_f$. To address this concern, the coherence between the noise radiation at $\wp_f$ and the p' acting on the panel surface is calculated using a similar procedure as discussed in Sec 5.5, and its variation across each panel is determined (the second and fourth columns in Figure 5.16). A careful comparison of the spectral distributions of the coherence and vibration acceleration reveals that not all the resonant panel vibration responses contribute to the eventual cavity noise radiation. Some resonant responses show a very high level of coherence ($\gamma^2 \rightarrow 1$) with noise radiation (marked with red double arrows), while others show an extremely low coherence ($\gamma^2 \rightarrow 0$) (marked with black double arrows) (Figure 5.16). It is interesting to note that in the *DEP*2 and *TEP* cases, almost all of their strong panel acceleration peaks do not contribute to the eventual cavity noise radiation due to their almost zero coherence. There are mild contributions from a few peaks, but their panel accelerations are several orders of magnitude weaker than the strong peaks. Therefore, most panel responses in the *DEP*2 and *TEP* cases essentially act to absorb p' energy in the cavity-panel system only and do not contribute to the far-field noise radiation. This observation not only explains the root cause of the exceptionally low level of cavity noise radiation in these two cases but also further substantiates the possibility of effectively suppressing cavity noise radiation through the aeroacoustic-structural resonance of two properly designed panel inside the cavity.

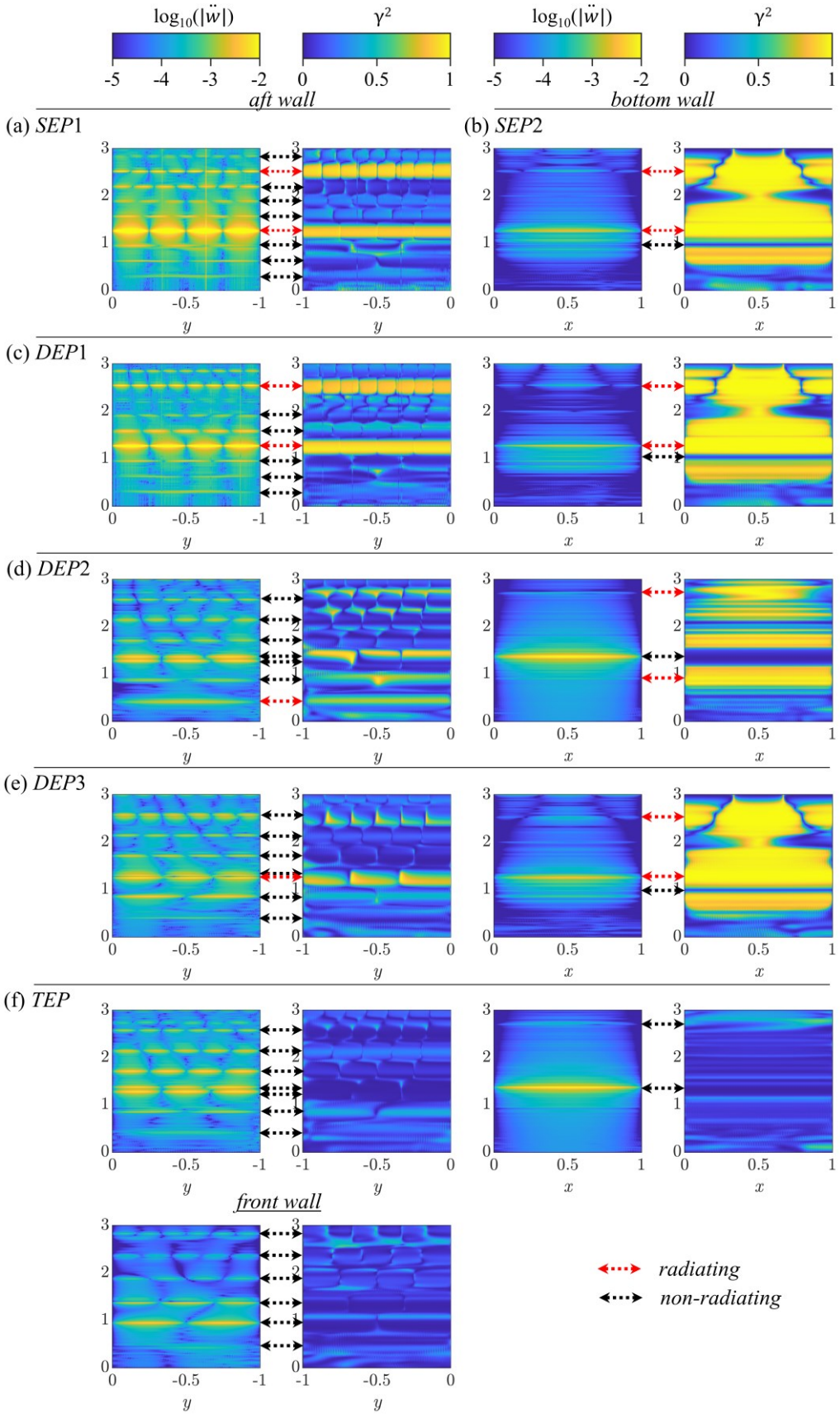

Figure 5.16 First column and third column: variation of FFT transformed of aft and bottom panel acceleration; second and fourth column: spectra of magnitude-squared coherence γ^2 between the acoustic signal at p_f and pressure signals along the respective panel surface. (a) *SEP*1, (b) *SEP*2, (c) *DEP*1, (d) *DEP*2, (e) *DEP*3 (f) *TEP*.

5.7 Implementation guidelines of the proposed Noise Reduction Concept

To concisely explain the proposed cavity noise suppression concept that leverages multiple elastic panels, implementation guidelines are outlined here based on the insights gained from our recent and previously performed studies (Naseer *et al.* 2023b, Naseer *et al.* 2024 and Naseer *et al.* 2025).

[i] Thorough analysis of rigid cavity flow characteristics

- The analysis aims to identify all locations on the cavity walls that support the flow processes responsible for cavity aeroacoustic feedback. These locations are the ideal positions for the placement of elastic panels to modify the identified flow processes. It is crucial to determine the dominant frequencies of the flow processes, as they will be the defining physical parameters for the structural designs of the panels.

[ii] Specification of elastic panel

- Each elastic panel is expected to extract the flow fluctuation energy of a particular aeroacoustic feedback process identified in [i] through its resonant vibration excited by the flow and acoustic excitation naturally occurring in the cavity flow. To achieve this, the fluid-loaded natural frequency of an elastic panel is selected as the working frequency, which must match an identified flow frequency.
- The setting of the working frequency of a panel is guided by Eq. 3.1. The length, thickness, tension, and material properties are considered as the adjustable parameters for the working frequency. The panel length is typically constrained by the flow problem. The panel tension is usually

set to a small value for ease of its application in practical applications. The panel thickness and material properties are the more convenient parameters for adjustment.

[iii] Setting of cavity-panel configurations

- It begins with the modification using a single elastic panel. The setting of this panel may proceed in the same manner as reported in Section 5.2. Typically, the modification targets the more energetic aeroacoustic feedback process, followed by the processes with weaker energy content. Special attention must be paid to any shift in the dominant frequencies of the modified flow.
- If stronger cavity noise suppression is desired, configurations with multiple elastic panels can be explored. However, one must be cautious that the new elastic panels may be designed based on the dominant frequencies of the modified flow, rather than the original ones with the rigid cavity flow. The configuration can proceed in a similar manner as reported in Section 5.3.

5.8 Summary

In this paper, we have meticulously explored a unique passive approach for suppressing the deep cavity noise, employing a distributed surface compliance mechanism via a strategic designs and arrangements of multiple elastic panels. The study involves a detailed numerical analysis on a two-dimensional flow past deep cavity characterized by a length-to-depth ratio of 0.4, exposed to the low Mach number flow (M = 0.09) and a Reynolds number $Re = 4\times10^4$ based on cavity length. The focus of the study delves into the complex dynamics of cavity

flows, scrutinizing the intricacies of noise generation processes influenced by the placement of single, double and triple panels at various cavity wall locations. Our initial analysis encompasses both a rigid cavity and five distinct cavity-panel configurations with a single panel which provide critical insights into flow characteristics. These findings inform the development of five novel cavity-panel arrangements, featuring double and triple panel configurations, aimed at accentuating the maximum cavity noise reduction. The design rationale for these multiple panel configurations is grounded in two fundamental observations: the predominance of shear layer fluctuations near the cavity aft wall adjacent to the cavity trailing edge, and the dominant acoustic modes operating at the cavity bottom. By meticulously targeting these pivotal aspects of the cavity aeroacoustic mechanism with strategically designed elastic panels, the proposed approach is envisaged to significantly influence, and thereby mitigate, the noise generation processes.

In assessing the efficacy of the novel cavity-panel configurations for noise suppression, we solve the cavity aeroacoustics by means of Direct Aeroacoustic Simulation (DAS) coupled with panel structural dynamics solver in monolithic fashion. Among these, a double panel configuration, namely the *DEP*2 case, emerges as the most effective in mitigating cavity tonal noise by almost 15 dB. This particular arrangement strategically employs aft and bottom wall panels, where fluid-loaded natural frequencies are precisely tuned to target specific dominant flow frequencies. The success of *DEP*2 case can be attributed to its adept harnessing of aeroacoustic-structural interactions of panels for effective suppressing the flow and acoustic fluctuation energy of the cavity. Other double panel configurations also demonstrate a certain level of noise reduction, but

their effectiveness varies. Interestingly, the triple panel configuration *TEP*, which builds upon the same principles as the *DEP2* setup, does not yield extra noise reduction benefits of a third panel on the cavity front wall. This outcome underscores the complexity of aeroacoustic interactions and the challenge of optimizing panel arrangements for maximal noise suppression.

Extensive analyses of numerical results reveal that employing strategically designed elastic panels in various configurations can alter the aeroacoustic feedback mechanisms responsible for fluid-resonant oscillations in deep cavities in different fashion. A notable observation is the high contrast in the energy transfer dynamics between the growing shear layer and cavity acoustic modes exhibited in the baseline rigid cavity case (*RC*) and various cavity-panel configurations. In the *RC* case, the energy of flow fluctuation due to shear layer impingement at cavity trailing edge is efficiently channelled to generate a strong cavity acoustic mode. However, this dynamics behaves significantly different in the cavity-panel configurations, where the interaction of the shear layer with the cavity aft wall only leads to a weak cavity acoustic mode. The detailed study of the spectral and phase information of shear layer flow and cavity acoustic mode fluctuations in the *DEP2* case shows a distinct deviation from the *RC* case. In *DEP2* case, the shear layer fluctuation and cavity acoustic mode operate at different frequencies and are completely out-of-phase, exhibiting a total distortion in their coherence. This indicates that the critical locked-on condition, defined in the *RC* case by the criteria of $f_1 = f_{shear\ layer} = f_{acoustic\ mode}$, $\gamma^2(f_1) \sim 1$ and $\Delta\phi(f_1) \sim 0$, is significantly disrupted with the multiple elastic panels introduced. Moreover, the analysis of frequency modulation along the cavity front and aft walls elucidates that the original *RC* dominant frequency is

split into the multiple cavity acoustic modes in the cavity-panel configuration. Therefore, this constitutes a re-distribution of flow/acoustic fluctuation energy across multiple cavity modes, which may interact with each other with different relative phases, and play a pivotal role in modulating the ultimate cavity noise radiation.

The aeroacoustic-structural interaction of panels within deep cavities has provided a good insight into effective noise reduction mechanisms. Our study reveals that the flow-induced elastic panels significantly influence the coupling between developing shear layers and cavity acoustic modes. Each panel dictates its specific bending wave pattern with respect to its orientation. Vertical panels predominantly exhibit transverse bending wave propagation while horizontal panels support standing bending waves. Such kind of preference is attributed to different aeroacoustic-structural interactions marked by distinct pressure fluctuations. The panels in structural resonance interact with the flow and acoustic fluctuation in unique ways and lead to significant alterations in cavity noise generation characteristics. Notably, in *DEP*2 and *TEP* cases, the panels do not contribute to far-field noise radiation despite their strong vibratory responses, indicating their primary role in absorbing flow fluctuation energy within the cavity-panel systems. The observation of this new phenomenon of aeroacoustic-structural resonance in multiple panel configurations highlights the potential of the proposed passive approach for effectively suppressing cavity noise radiation.

Another unique aspect of the proposed approach lies in the minimal distortion of the original flow characteristics. It is achieved by maintaining the resonant vibratory panel displacement smaller than the typical cavity

dimensions and utilizing the reactive nature of structural resonance for energy absorption rather than traditional dissipative methods. More important to note is that the flow dynamic consequences of the proposed passive approach gives an unintended advantage of remarkable drag reduction (as much as 15% in *DEP*2 case) providing crucial attractiveness of implementing the proposed noise suppression technique in engineering applications. Last but not the least, the present study contributes a novel, effective, yet minimally invasive approach to cavity noise suppression. The physical insights gained from the study are expected to guide future research and development in noise control strategies with similar advantages, especially in engineering applications where the flow-induced cavity noise is a critical concern.

Chapter 6

Conclusions

This thesis has consolidated and expanded upon a series of experimental and numerical studies focusing on the suppression of tonal noise in deep cavities using surface compliance. Through the strategic deployment of elastic panels within cavity walls, this research has introduced a novel passive control concept that has proven effective in modifying the fundamental mechanisms of deep cavity tonal noise, as well as achieving reductions in drag.

6.1 Summary and Research Achievements

Chapter 3 of this thesis documented the unique passive control strategy for reducing deep cavity noise through localized surface compliance, leveraging the flow-induced structural resonance of an elastic panel integrated within cavity walls. This strategy was rigorously evaluated under conditions characterized by a Mach number of 0.09 and a Reynolds number of $Re = 4 \times 10^4$, focusing on a cavity with a length-to-depth ratio of 0.4. Utilizing the direct aeroacoustic simulation, the study analyzed the spatio-temporal interactions between the

elastic panel and fluid fluctuations within the cavity. This numerical exploration was validated against existing experimental data and involved detailed wavenumber-frequency analyses to understand the dynamics between the developing shear layer and cavity acoustic modes. Five key processes central to cavity aeroacoustic feedback were identified and studied: boundary layer growth at the cavity leading edge, shear layer growth driven by acoustic excitation, formation of cavity acoustic standing waves, excitation of cavity modes by shear layer impingement at the trailing edge, and the highly unsteady flow post-shear layer impingement. The elastic panel, crafted from an elastomeric material, was designed to resonate at a frequency matching the dominant frequency of the cavity flow fluctuations. This strategic positioning allowed the panel to interact with each identified flow process, significantly altering the aeroacoustic interactions and leading to varying degrees of noise suppression. The most substantial noise reduction was observed when the panel influenced the formation of standing waves and the excitation of cavity modes by shear layer impingement at the trailing edge, achieving reductions in sound power level up to 3.8 dB and 4.8 dB, respectively. Further investigations into the physical mechanisms behind these observations revealed that the presence of panel disrupted the coherency between the shear layer growth and cavity mode acoustics observed in rigid cavities. This disruption shifted the dominant frequency of cavity aeroacoustic feedback upwards and delayed the growth of the shear layer, effectively narrowing the effective cavity size for aeroacoustic feedback. Such alterations were facilitated by the vibrating panel, which absorbed both flow and acoustic energy fluctuations, thereby reducing overall cavity noise. An unintended beneficial consequence of this approach was a significant reduction in cavity drag—almost 19% compared to the rigid cavity

configuration. This reduction highlights the dual benefits of the strategy, not only in noise suppression but also in enhancing the energetic efficiency of the cavity flow. In summary, the Chapter 3 confirms the effectiveness and feasibility of using strategically placed surface compliance to modify fundamental noise mechanisms in deep cavities. This approach not only achieves significant noise and drag reduction but does so while maintaining the cavity basic geometric integrity, making it a valuable strategy for practical applications where the strong pressure pulsation and ultimate noise emissions are critical concerns.

Chapter 4 of this thesis detailed a successful experimental campaign that built upon previous numerical research to validate and enhance a novel passive control method using surface compliance for suppressing tonal noise in deep cavities. This prevalent issue in various aeroacoustic applications was addressed by implementing an elastic panel flush-mounted at the cavity bottom, aimed at modifying aeroacoustic-structural interactions and reducing acoustic emissions at critical flow velocities. The experimental setup, conducted within an aeroacoustic wind tunnel, included precise measurements of near and far-field pressures and utilized Particle Image Velocimetry (PIV) to capture the dynamics of the flow. The introduction of the compliant panel resulted in significant alterations to the aeroacoustic patterns within the cavity, leading to notable reductions in tonal noise by up to 16.1 dB, particularly effective at flow velocities of 20 and 30 ms^{-1}. These velocities are significant as they correspond to conditions that typically amplify aeroacoustic resonances in the rigid cavity (*RC*) configurations. A comparison between the *RC* setup and the experimental panel (*EP*) configuration revealed that the panel significantly disrupted the typical coherence observed among the cavity acoustic mode, shear layer, and

far-field noise, specifically at the dominant frequency. This disruption led to a substantial reduction in peak noise levels, suggesting a fundamental alteration in the aeroacoustic coupling processes due to the modified dynamics of the shear layer and its interaction with the cavity acoustic mode. Further insights were gained from PIV images, which illustrated the dynamics of the shear layer over the cavity opening. The images showed that the *EP* configurations presented a thinner and more disrupted shear layer compared to the *RC* setups, where the shear layer vortices are usually well-defined and larger as they convect downstream. In *RC* cases, the vigorous impingement of the shear layer at the cavity trailing edge typically facilitates an effective energy transfer to the cavity acoustic mode. However, this dynamic was notably different in *EP* cases, highlighting the distinct mechanisms of noise generation and reduction in the respective configurations. In conclusion, Chapter 4 confirms the effectiveness of the elastic panel in altering the internal dynamics of cavity flows, significantly reducing noise output and disrupting traditional aeroacoustic interactions. This experimental validation underscores the potential of surface compliance as a practical and innovative approach to noise suppression in aeroacoustic applications.

Chapter 5 of this thesis explores and advances the passive noise suppression approach based on the flow-complaint elastic surface by employing a strategic design and arrangement of multiple elastic panels across the different cavity walls. This study extends the foundational concepts discussed in previous chapters by implementing distributed surface compliance mechanisms to influence complex cavity dynamics further. The focus was on a two-dimensional flow past a deep cavity with a length-to-depth ratio of 0.4,

subjected to a low Mach number (M = 0.09) and a Reynolds number ($Re = 4 \times 10^4$). The detailed numerical analysis investigated the effects of single, double, and triple panel configurations on the noise suppression by targeting the key cavity aeroacoustic processes. The design of the panel configurations was informed by an initial analysis that highlighted the critical roles of shear layer impingement near the cavity aft wall and the dominant acoustic modes at the cavity bottom. The Direct Aeroacoustic Simulation (DAS) coupled with a panel structural dynamics solver was used to assess the efficacy of various panel arrangements. Among the various cavity-panel configurations with multi panel arrangements, a double panel configuration, identified as *DEP*2, was notably effective, reducing cavity tonal noise by almost 15 dB. This configuration strategically positioned panels at the aft and bottom walls of the cavity, with fluid-loaded natural frequencies finely tuned to target specific dominant flow frequencies. While other double panel configurations also demonstrated noise reduction, their effectiveness varied. Intriguingly, the addition of a third panel in the triple panel configuration (*TEP*) did not provide additional noise reduction benefits, underscoring the complexity and challenge of optimizing panel arrangements for maximal noise suppression. This outcome emphasizes the nuanced interplay of aeroacoustic interactions in cavity noise control. Numerical results of Chapter 5 revealed significant alterations in the aeroacoustic feedback mechanisms, particularly how energy is transferred between the growing shear layer and cavity acoustic modes. Unlike the baseline rigid cavity configuration, where shear layer impingement robustly channels energy into a strong acoustic mode, the panel configurations led to a weaker interaction and a significant deviation in the coherence between these elements. In the DEP2 case, for example, the shear layer and cavity acoustic modes

operated at distinctly different frequencies and were completely out-of-phase. This disintegration of the critical locked-on condition previously defined in rigid cavities demonstrates the effectiveness of using multiple panels to redistribute flow and acoustic energy across various cavity modes. This redistribution plays a crucial role in modulating cavity noise radiation. Moreover, the specific bending wave patterns dictated by the panels orientation—transverse in vertical panels and standing in horizontal panels—highlight the unique aeroacoustic-structural interactions that contribute to effective noise reduction. The structural resonance of these panels, while minimally distorting the original flow characteristics, provides an unexpected benefit of significant drag reduction, enhancing the practical appeal of this noise suppression technique. Ultimately, the insights gained from this comprehensive analysis underscore the potential of this novel, minimally invasive approach for effectively suppressing cavity noise radiation in engineering applications where reducing flow-induced noise is paramount. This chapter, therefore, contributes critical knowledge to the ongoing development of noise control strategies, offering valuable guidance for future research in this field.

6.2 Limitations and Future Works

6.2.1 Limitations

The numerical component of this thesis employed Direct Aeroacoustic Simulation (DAS) to explore cavity tonal noise reduction through fluid-structure interactions with an elastic panel. Given the intensive computational resources and time required for DAS, this study was confined to two-dimensional analyses. While two-dimensional conditions adequately represented our specific flow scenarios and the effectiveness of the cavity-panel configuration was verified through experimental investigations, the inherent limitations, such as the wealth of detailed spatial and temporal information offered by three dimensional numerical investigation, preclude insights into three-dimensional phenomena which include spanwise development or distortion of the shear layer and any potential centrifugal instabilities. A transition to three-dimensional numerical investigations could thus provide deeper understanding and enhance the fidelity of the cavity noise generation/suppression .

6.2.2Future Works

Expansion to Different Flow Regimes:

The current study concentrated on low Mach number conditions. Extending this noise suppression concept to high subsonic and transonic flow regimes, as well as exploring different cavity aspect ratios, could broaden the applicability of our findings. Although the fundamental cavity flow phenomena driving the

aeroacoustic mechanisms remain consistent, testing the effectiveness of the elastic panel deployment across varying conditions would be prudent.

Broadening the Applications:

Implementing this study findings in real-world scenarios involving tandem cavity configurations, such as gaps over train cars or gas transport infrastructures with various fittings, could prove fruitful. Studying cavities in tandem configurations, where additional modes might emerge due to the introduction of another cavity, offers an exciting area for practical application and further research.

Experimental Extensions:

Although the current experimental setup utilized a bottom-mounted elastic panel, recent numerical findings suggest that using dual panels—one at the aft wall and another at the cavity bottom—could enhance noise reduction. Future experimental work should consider employing this dual panel scheme to validate and potentially augment the noise suppression capabilities demonstrated numerically.

Material Innovations:

While silicone rubber was used for the elastic panels in this study, exploring other materials such as Kevlar, known for its acoustic transparency, could offer alternative mechanisms for suppressing cavity aeroacoustics. A Kevlar panel at the cavity bottom might effectively obscure cavity acoustic modes, altering aeroacoustic phenomena for enhanced noise suppression.

Combination with Other Noise Control Techniques:

The utility of elastic panels could be combined with other noise control methods, such as introducing porosities at the cavity leading or trailing edges. This could further dampen aeroacoustic processes and reduce noise emissions, broadening the scope of effective noise control strategies.

Advanced Stability Investigation:

With advancements in stability techniques such as biglobal, triglobal, and higher-order spectral methods, future studies could delve further deeper into the transition dynamics of the shear layer from rigid cavity configurations to those with elastic panels. This could further elucidate the modified interactions between the shear layer and cavity acoustic modes, contributing to noise reduction.

References

Abdelmwgoud, M. and Mohany, A. (2021), "Control of the self-sustained shear layer oscillations over rectangular cavities using high-frequency vortex generators", *Physics of Fluids,* 33 (4), 045115.

Anderson, J. D. (2009), "Computational Fluid Dynamics", *Springer, Berlin, Heidelberg*, edited by Wendt, J. F., 3rd Edition.

Angland, D., Zhang, X., and Goodyer, M. (2012), "Use of Blowing Flow Control to Reduce Bluff Body Interaction Noise", *AIAA Journal,* 50 (8), 1670-1684.

Arif, I., Wu, D., Lam, G. C. Y., and Leung, R. C. K. (2020a), "Exploring Airfoil Tonal Noise Reduction with Elastic Panel Using Perturbation Evolution Method", *AIAA Journal,* 58 (11), 4958-4968.

Arif, I., Lam, G. C. Y., Wu, D., and Leung, R. C. K. (2020b), "Passive airfoil tonal noise reduction by localized flow-induced vibration of an elastic panel", *Aerospace Science Technology,* 107, 106319.

Arif, I., Lam, G. C. Y., Leung, R. C. K., and Naseer, M. R. (2022), "Distributed surface compliance for airfoil tonal noise reduction at various loading conditions", *Physics of Fluids,* 34 (4), 046113.

Arunajatesan, S., Sinha, N., and Seiner, J. (2003), "Mechanisms in high-frequency control of cavity flows", *41st Aerospace Sciences Meeting and Exhibit* (Aerospace Sciences Meetings: American Institute of Aeronautics and Astronautics).

Arunajatesan, S., Kannepalli, C., Sinha, N., Sheehan, M., Alvi, F., Shumway, G., and Ukeiley, L. (2009), "Suppression of Cavity Loads Using Leading-Edge Blowing", *AIAA Journal,* 47 (5), 1132-1144.

Arya, N. and De, A. (2021), "Effect of vortex and entropy sources in sound generation for compressible cavity flow", *Physics of Fluids,* 33 (4), 046107.

Bacci, D. and Saddington, A. J. (2022), "Hilbert–Huang spectral analysis of cavity flows incorporating fluidic spoilers", *AIAA Journal,* 61 (1), 271-284.

Bacci, D. and Saddington, A. J. (2023), "Influence of door gap on aeroacoustics and structural response of a cavity", *AIAA Journal,* 62 (3), 1021-1036.

Berglund, B., Hassmén, P., and Job, R. F. S. (1996), "Sources and effects of low-frequency noise", *The Journal of the Acoustical Society of America,* 99 (5), 2985-3002.

Bies, D. A., Hansen, C. H., and Howard, C. Q. (2017), *Engineering noise control* (4th edn.: CRC press).

Björk, E. A. (1986), "Laboratory annoyance and skin conductance responses to some natural sounds", *Journal of Sound and Vibration,* 109 (2), 339-345.

Blevins, R. D. (2015), *Formulas for dynamics, acoustics and vibration* (John Wiley & Sons).

Bourquard, C. (2021), 'Acoustic damping and aeroacoustic instabilities of cavities subject to bias and grazing flows', (ETH Zurich).

Bres, G. A. and Colonius, T. (2008), "Three-dimensional instabilities in compressible flow over open cavities", *Journal of Fluid Mechanics* 599, 309-339.

Bruggeman, J. C., Hirschberg, A., van Dongen, M. E. H., Wijnands, A. P. J., and Gorter, J. (1989), "Flow Induced Pulsations in Gas Transport Systems: Analysis of the Influence of Closed Side Branches", *Journal of Fluids Engineering,* 111 (4), 484-491.

Bruggeman, J. C., Hirschberg, A., van Dongen, M. E. H., Wijnands, A. P. J., and Gorter, J. (1991), "Self-sustained aero-acoustic pulsations in gas transport systems: Experimental study of the influence of closed side branches", *Journal of Sound and Vibration,* 150 (3), 371-393.

Burgio, L., Scilley, K., Hardin, J. M., Hsu, C., and Yancey, J. (1996), "Environmental “White Noise”: An Intervention for Verbally Agitated Nursing Home Residents", *The Journals of Gerontology: Series B,* 51B (6), P364-P373.

Carpenter, P. W., Lucey, A. D., and Davies, C. (2001), "Progress on the Use of Compliant Walls for Laminar-Flow Control", *Journal of Aircraft,* 38 (3), 504-512.

Cattafesta III, L. N., Song, Q., Williams, D. R., Rowley, C. W., and Alvi, F. S. (2008), "Active control of flow-induced cavity oscillations", *Progress in Aerospace Sciences,* 44 (7-8), 479-502.

Chang, S.-C. (1995), "The Method of Space-Time Conservation Element and Solution Element—A New Approach for Solving the Navier-Stokes and Euler Equations", *Journal of Computational Physics,* 119 (2), 295-324.

Chang, S.-C., Wang, X.-Y., and Chow, C.-Y. (1999), "The Space-Time Conservation Element and Solution Element Method: A New High-Resolution and Genuinely Multidimensional Paradigm for Solving Conservation Laws", *Journal of Computational Physics,* 156 (1), 89-136.

Chang, S. and Wang, X. (2002), 'Courant Number Insensitive CE/SE Euler Scheme', *38th AIAA/ASME/SAE/ASEE Joint Propulsion Conference & Exhibit* (Joint Propulsion Conferences: American Institute of Aeronautics and Astronautics).

Choy, Y. S. and Huang, L. (2005), “Effect of Flow on the Drumlike Silencer,” *The Journal of the Acoustical Society of America*, Vol. 118, No. 5, pp. 3077–3085.

Covert, E. E. (1970), "An approximate calculation of the onset velocity of cavity oscillations", *AIAA Journal,* 8 (12), 2189-2194.

Crighton, D. G. (1981), "Acoustics as a branch of fluid mechanics", *Journal of Fluid Mechanics,* 106, 261-298.

Desquesnes, G., Terracol, M., and Sagaut, P. (2007), "Numerical investigation of the tone noise mechanism over laminar airfoils", *Journal of Fluid Mechanics,* 591, 155-182.

Douay, C. L., Pastur, L. R., and Lusseyran, F. (2016), "Centrifugal instabilities in an experimental open cavity flow", *Journal of Fluid Mechanics,* 788, 670-694.

Dowell, E. H. (1974), "Aeroelasticity of plates and shells", *Springer Science & Business Media*, vol. 1.

Dowling, A. P. and Williams, J. E. F. (1983), *Sound and Sources of Sound* (E. Horwood).

East, L. F. (1966), "Aerodynamically induced resonance in rectangular cavities", *Journal of Sound Vibration,* 3 (3), 277-287.

El Hassan, M., Keirsbulck, L., and Labraga, L. (2008), "Aero-acoustic coupling Inside large deep cavities at low-subsonic speeds", *Journal of Fluids Engineering,* 131 (1).

Elder, S. A. (1978), "Self-excited depth-mode resonance for a wall-mounted cavity in turbulent flow", *Journal of the Acoustical Society of America,* 64 (3), 877-890.

European, C. and Directorate-General for, E. (2018), *What are the health costs of environmental pollution?* (Publications Office).

Fan, H. K., Leung, R. C. K., and Lam, G. C. Y. (2015), "Numerical analysis of aeroacoustic-structural interaction of a flexible panel in uniform duct flow", *The Journal of the Acoustical Society of America,* 137 (6), 3115-3126.

Fan, H. K., Leung, R. C. K., Lam, G. C. Y., Aurégan, Y., and Dai, X. (2018), "Numerical coupling strategy for resolving in-duct elastic panel aeroacoustic/structural interaction", *AIAA Journal,* 56 (12), 5033-5040.

Fan, K. H., "Computational aeroacoustic-structural interaction in internal flow with CE/SE method," Ph.D. thesis (The Hong Kong Polytechnic University, 2018).

Forestier, N., Jacquin, L., and Geffroy, P. (2003), "The mixing layer over a deep cavity at high-subsonic speed", *Journal of Fluid Mechanics,* 475, 101-145.

Gad-el-Hak, M. (2002), "Compliant coatings for drag reduction", *Progress in Aerospace Sciences,* 38 (1), 77-99.

Gharib, M. and Roshko, A. (1987), "The effect of flow oscillations on cavity drag", *Journal of Fluid Mechanics,* 177, 501-530.

Gloerfelt, X., Bailly, C., and Juvé, D. (2003), "Direct computation of the noise radiated by a subsonic cavity flow and application of integral methods", *Journal of Sound and Vibration,* 266 (1), 119-146.

Greenshields, C. J. and Weller, H. G. (2005), "A unified formulation for continuum mechanics applied to fluid–structure interaction in flexible tubes", *International Journal for Numerical Methods in Engineering,* 64 (12), 1575-1593.

Han, S., Luo, Y., Li, H., Wu, C., Liu, X., and Zhang, S. (2022), "Data-driven and physical property-based hydro-acoustic mode decomposition", *Physics of Fluids,* 34 (2), 026102.

Harding, A. H., Frost, G. A., Tan, E., Tsuchiya, A., and Mason, H. M. (2013), "The cost of hypertension-related ill-health attributable to environmental noise", *Noise Health,* 15 (67), 437-445.

Hayek, S. I. (2010), "Advanced Mathematical Methods in Science and Engineering", *Chapman and Hall/CRC*, 2nd edition.

He, Y., Thompson, D., and Hu, Z. (2024), "Aerodynamic noise from a high-speed train bogie with complex geometry under a leading car", *Journal of Wind Engineering and Industrial Aerodynamics,* 244, 105617.

Heller, H. H. and Bliss, D. B. (1975), "Aerodynamically induced pressure oscillations in cavities - physical mechanisms and suppression concepts", *AF Flight Dynamics Laboratory, (FY), Wright-Patterson AFB, Ohio*, Technical Report No. AFFDL-TR-74-133.

Ho, Y. W. and Kim, J. W. (2021), "A wall-resolved large-eddy simulation of deep cavity flow in acoustic resonance", *Journal of Fluid Mechanics,* 917.

Howe, M. S. (2003), *Theory of vortex sound* (Cambridge university press).

Huang, L. (1999), “A Theoretical Study of Duct Noise Control by Flexible Panels,” *The Journal of the Acoustical Society of America*, Vol. 106, No. 4, pp. 1801–1809.

Jones, L. E. (2008), "Numerical studies of the flow around an airfoil at low Reynolds number", *School of Engineering Sciences, University of Southampton, Doctoral Thesis*, 229p.

Jones, L. E., Sandberg, R. D., and Sandham, N. D. (2010), "Stability and receptivity characteristics of a laminar separation bubble on an aerofoil", *Journal of Fluid Mechanics,* 648, 257-296.

Kato, C. and Ikegawa, M. (1991), "Large eddy simulation of unsteady turbulent wake of a circular cylinder using the finite element method", *Advances in Numerical Simulation of Turbulent Flows*, 49-56.

Kight, C. R. and Swaddle, J. P. (2011), "How and why environmental noise impacts animals: an integrative, mechanistic review", *Ecol Lett,* 14 (10), 1052-1061.

Kook, H. and Mongeau, L. (2002), "Analysis of the periodic pressure fluctuations induced by flow over a cavity", *Journal of Sound and Vibration,* 251 (5), 823-846.

Kusano, K., Yamada, K., and Furukawa, M. (2020), "Aeroacoustic simulation of broadband sound generated from low-Mach-number flows using a lattice Boltzmann method", *Journal of Sound and Vibration,* 467, 115044.

Lai, H. and Luo, K. H. (2008), "A Conceptual Study of Cavity Aeroacoustics Control Using Porous Media Inserts", *Flow, Turbulence and Combustion,* 80 (3), 375-391.

Lam, G. C. Y. (2012), "Aeroacoustics of merging flows at duct junctions", *Department of Building Services Engineering, The Hong Kong Polytechnic University, Doctoral Thesis*, 204p.

Lam, G. C. Y. and Leung, R. C. K. (2018), "Aeroacoustics of NACA 0018 airfoil with a cavity", *AIAA Journal,* 56 (12), 4775-4786.

Lam, G. C. Y., Leung, R. C. K., and Tang, S. K. (2013), "Aeroacoustics of T-junction merging flow", *The Journal of the Acoustical Society of America,* 133 (2), 697-708.

Lam, G. C. Y., Leung, R. C. K., and Tang, S. K. (2014a), "Aeroacoustics of duct junction flows merging at different angles", *Journal of Sound Vibration,* 333 (18), 4187-4202.

Lam, G. C. Y., Leung, R. C. K., Seid, K. H., and Tang, S. K. (2014b), "Validation of CE/SE scheme in low mach number direct aeroacoustic simulation", *International Journal of Nonlinear Sciences Numerical Simulation,* 15 (2), 157-169.

Lang, A. and Johnson, T. (2010), "Drag reduction over embedded cavities in Couette flow", *Mechanics Research Communications,* 37 (4), 432-435.

Larchevêque, L., Sagaut, P., Mary, I., Labbé, O., and Comte, P. (2003), "Large-eddy simulation of a compressible flow past a deep cavity", *Physics of fluids,* 15 (1), 193-210.

Lawson, S. J. and Barakos, G. N. (2009), "Assessment of passive flow control for transonic cavity flow using detached-eddy simulation", *Journal of Aircraft,* 46 (3), 1009-1029.

Lawson, S. J. and Barakos, G. N. (2011), "Review of numerical simulations for high-speed, turbulent cavity flows", *Progress in Aerospace Sciences,* 47 (3), 186-216.

Lee, B. (2010), "Effect of a Perturbed Shear Layer on Cavity Resonance", *Journal of Aircraft,* 47 (1), 343-345.

Leung, R. C. K., So, R., Wang, M., and Li, X. (2007), "In-duct orifice and its effect on sound absorption", *Journal of Sound and Vibration,* 299 (4-5), 990-1004.

Liu, Q. and Gómez, F. (2019), "Role of trailing-edge geometry in open cavity flow control", *AIAA Journal,* 57 (2), 876-878.

Liu, Q. and Gaitonde, D. (2021), "Acoustic response of turbulent cavity flow using resolvent analysis", *Physics of Fluids,* 33 (5), 056102.

Liu, Y., Chen, B., Shi, Y., and Rong, A. (2024), "Visualization of pressure fluctuation characteristics of weapon bay on unmanned aerial vehicle using delayed detached eddy simulation", *Journal of Visualization,* 27 (1), 75-87.

Liu, Y., Liu, P., Guo, H., Hu, T., and Zhang, J. (2023), "Investigation of the dominant Rossiter modal tones at the locked-on state", *Journal of Sound and Vibration,* 556, 117741.

Loh, C. (2003), 'On a Non-Reflecting Boundary Condition for Hyperbolic Conservation Laws', *16th AIAA Computational Fluid Dynamics Conference* (Fluid Dynamics and Co-located Conferences: American Institute of Aeronautics and Astronautics).

Loh, C., Hultgren, L., and Jorgenson, P. (2001), 'Near field screech noise computation for an underexpanded supersonic jet by the CE/SE method', *7th AIAA/CEAS Aeroacoustics Conference and Exhibit* (Aeroacoustics Conferences: American Institute of Aeronautics and Astronautics).

Loh, C. Y. and Hultgren, L. S. (2006), "Jet Screech Noise Computation", *AIAA Journal,* 44 (5), 992-998.

Lucas., M. J., Noreen, R., Southerland, L. D., Cole III, J., and Junger, H. (1995), "The Acoustic Characteristics of Turbomachinery Cavities", *Marshall Space Flight Center, Alabama* NASA Contractor Report 4671.

Luk, K. F., So, R. M. C., Leung, R. C. K., Lau, Y. L., and Kot, S. C. (2004), "Aerodynamic and Structural Resonance of an Elastic Airfoil Due to Oncoming Vortices", *AIAA Journal,* 42 (5), 899-907.

Maryami, R. and Liu, Y. (2024), "Cylinder flow and noise control by active base blowing", *Journal of Fluid Mechanics,* 985, A10.

Maryami, R., Arcondoulis, E. J. G., and Liu, Y. (2024), "Flow and aerodynamic noise control of a circular cylinder by local blowing", *Journal of Fluid Mechanics,* 980, A56.

Maury, C., Bravo, T., and Mazzoni, D. (2019), "The use of microperforations to attenuate the cavity pressure fluctuations induced by a low-speed flow", *Journal of Sound and Vibration,* 439, 1-16.

Mendoza, J. M. (1997), *Effects of cavity dimensions, boundary layer, and temperature on cavity noise generation and control* (Georgia Institute of Technology).

Milne, G. J., Thieman, C. C., and Vakili, A. (2013), 'An Experimental Investigation of Supersonic Cavity Flow Control with Vertical Cylinders', *43rd Fluid Dynamics Conference* (Fluid Dynamics and Co-located Conferences: American Institute of Aeronautics and Astronautics).

Moreau, D. J., Brooks, L. A., and Doolan, C. J. (2012), "The effect of boundary layer type on trailing edge noise from sharp-edged flat plates at low-to-

moderate Reynolds number", *Journal of Sound and Vibration,* 331 (17), 3976-3988.

Mourão Bento, H. F., VanDercreek, C. P., Avallone, F., Ragni, D., and Snellen, M. (2022), "Lattice Boltzmann very large eddy simulations of a turbulent flow over covered and uncovered cavities", *Physics of Fluids,* 34 (10), 105120.

Narasimha, R. and Prasad, S. N. (1994), "Leading edge shape for flat plate boundary layer studies", *Experiments in Fluids,* 17 (5), 358-360.

Naseer, M. R., Arif, I., and Leung, R. C. K. (2023a), "Utilization of Embedded Surface Compliance for Suppression of Deep Cavity Flow Noise", *INTER-NOISE and NOISE-CON Congress and Conference Proceedings,* 268 (3), 5323-5334.

Naseer, M. R., Arif, I., Lam, G. C. Y., and Leung, R. C. K. (2022), "Effect of Flow-Induced Surface Vibration on Deep Cavity Aeroacoustics", *28th AIAA/CEAS Aeroacoustics 2022 Conference*, AIAA Paper No, 2022-2958.

Naseer, M. R., Arif, I., Leung, R. C. K., and Lam, G. C. Y. (2023b), "Suppression of deep cavity aeroacoustics at low Mach number by localized surface compliance", *Physics of Fluids,* 35 (5).

Naseer, M. R., Arif, I., Leung, R. C. K., and Abdullah, A. (2024), "Deep cavity noise suppression by exploiting aeroacoustic–structural interaction of multiple elastic panels". *Physics of Fluids*, 36 (5): 057141.

Naseer, M.R., Arif, I., Leung, R.C.K. (2025). "Mitigation of Cavity Noise with Aeroacoustically Excited Surface Panels" In: Doolan, C., Moreau, D.,

Wills, A. (eds) Flinovia—Flow Induced Noise and Vibration Issues and Aspects—IV. FLINOVIA 2023. Springer.

Pawłaczyk-Luszczyńska, M., Dudarewicz, A., Waszkowska, M., and Sliwińska-Kowalska, M. (2003), "Assessment of annoyance from low frequency and broadband noises", *Int J Occup Med Environ Health,* 16 (4), 337-343.

Pirrera, S., De Valck, E., and Cluydts, R. (2010), "Nocturnal road traffic noise: A review on its assessment and consequences on sleep and health", *Environ Int,* 36 (5), 492-498.

Plentovich, E. B., Stallings Jr, R. L., and Tracy, M. B. (1993), 'Experimental cavity pressure measurements at subsonic and transonic speeds. Static-pressure results'.

Plumblee, H. E., Gibson, J. S., and Lassiter, L. W. (1962), 'A theoretical and experimental investigation of the acoustic response of cavities in an aerodynamic flow', (LOCKHEED AIRCRAFT CORP MARIETTA GA), 164.

Powell, A. (1964), "Theory of Vortex Sound", *The Journal of the Acoustical Society of America,* 36 (1), 177-195.

Rausch, V. H., Bauch, E. M., and Bunzeck, N. (2014), "White noise improves learning by modulating activity in dopaminergic midbrain regions and right superior temporal sulcus", *J Cogn Neurosci,* 26 (7), 1469-1480.

Rebholz, P. S., Krebietke, S., Abhari, R. S., and Kalfas, A. I. (2016), "Turbine Aerodynamic Low-Frequency Oscillation and Noise Reduction Using Partial Shrouds", *Journal of Propulsion and Power,* 32 (5), 1067-1076.

Rockwell, D. and Naudascher, E. (1978), "Review—Self-sustaining oscillations of flow past cavities", *Journal of Fluids Engineering,* 100 (2), 152-165.

Rossiter, J. E. (1964), "Wind-tunnel experiments on the flow over rectangular cavities at subsonic and transonic speeds", *Aeronautical Research Council*, Reports and Memoranda No. 3438.

Rossiter, J. E. (1967), *Wind-tunnel Experiments on the Flow Over Rectangular Cavities at Subsonic and Transonic Speeds* (H.M. Stationery Office).

Rowley, C. W. and Williams, D. R. (2006), "Dynamics and Control of High-Reynolds-Number Flow over Open Cavities", *Annual Review of Fluid Mechanics,* 38 (Volume 38, 2006), 251-276.

Rowley, C. W., Colonius, T., and Basu, A. J. (2002), "On self-sustained oscillations in two-dimensional compressible flow over rectangular cavities", *Journal of Fluid Mechanics,* 455, 315-346.

Saddington, A. J., Thangamani, V., and Knowles, K. (2016), "Comparison of passive flow control methods for a cavity in transonic flow", *Journal of Aircraft,* 53 (5), 1439-1447.

Samimy, M., Debiasi, M., Caraballo, E., Serrani, A., Yuan, X., Little, J., and Myatt, J. H. (2007), "Feedback control of subsonic cavity flows using reduced-order models", *Journal of Fluid Mechanics,* 579, 315-346.

Sanmiguel-Rojas, E., Jiménez-González, J., Bohorquez, P., Pawlak, G., and Martínez-Bazán, C. (2011), "Effect of base cavities on the stability of the wake behind slender blunt-based axisymmetric bodies", *Physics of Fluids,* 23 (11), 114103.

Sarohia, V. (1977), "Experimental Investigation of Oscillations in Flows Over Shallow Cavities", *AIAA Journal,* 15 (7), 984-991.

Sato, M., Asada, K., Nonomura, T., Aono, H., Yakeno, A., and Fujii, K. (2019), "Mechanisms for turbulent separation control using plasma actuator at Reynolds number of 1.6× 106", *J Physics of Fluids,* 31 (9), 095107.

Schmit, R. F. and Raman, G. (2006), "High and Low Frequency Actuation Comparison for a Weapons Bay Cavity", *International Journal of Aeroacoustics,* 5 (4), 395-414.

Schumacher, K. L., Doolan, C. J., and Kelso, R. M. (2014), "The effect of a cavity on airfoil tones", *Journal of Sound and Vibration,* 333 (7), 1913-1931.

Shaw, L. L. (1979), "Suppression of aerodynamically induced cavity pressure oscillations", *The Journal of the Acoustical Society of America,* 66 (3), 880-884.

Singer, B. A., Brentner, K. S., Lockard, D. P., and Lilley, G. M. (2000), "Simulation of acoustic scattering from a trailing edge", *Journal of Sound and Vibration,* 230 (3), 541-560.

Singh, N. and Davar, S. C. (2004), "Noise Pollution-Sources, Effects and Control", *Journal of Human Ecology,* 16 (3), 181-187.

So, R. M. C., Liu, Y., and Lai, Y. G. (2003), "Mesh shape preservation for flow-induced vibration problems", *Journal of Fluids and Structures,* 18 (3), 287-304.

Söderlund, G. B. W., Sikström, S., Loftesnes, J. M., and Sonuga-Barke, E. J. (2010), "The effects of background white noise on memory performance

in inattentive school children", *Behavioral and Brain Functions,* 6 (1), 55.

Stansfeld, S. A. and Matheson, M. P. (2003), "Noise pollution: non-auditory effects on health", *British Medical Bulletin,* 68 (1), 243-257.

Sun, Y., Taira, K., Cattafesta, L. N., and Ukeiley, L. S. (2017), "Biglobal instabilities of compressible open-cavity flows", *Journal of Fluid Mechanics,* 826, 270-301.

Sun, Y., Liu, Q., Cattafesta III, L. N., Ukeiley, L. S., and Taira, K. (2019), "Effects of sidewalls and leading-edge blowing on flows over long rectangular cavities", *AIAA journal,* 57 (1), 106-119.

Talotte, C. (2000), "Aerodynamic noise: A critical survey", *Journal of Sound and Vibration,* 231 (3), 549-562.

Tam, C. K. W. and Block, P. J. W. (1978), "On the tones and pressure oscillations induced by flow over rectangular cavities", *Journal of Fluid Mechanics,* 89 (2), 373-399.

Tang, Y.-P. and Rockwell, D. (1983), "Instantaneous pressure fields at a corner associated with vortex impingement", *Journal of Fluid Mechanics,* 126, 187-204.

Ukeiley, L., Seiner, J., Ponton, M., and Jansen, B. (2003), 'Suppresion of Pressure Loads in Resonating Cavities Through Blowing', *41st Aerospace Sciences Meeting and Exhibit* (Aerospace Sciences Meetings: American Institute of Aeronautics and Astronautics).

Ukeiley, L. S., Ponton, M. K., Seiner, J. M., and Jansen, B. (2004), "Suppression of Pressure Loads in Cavity Flows", *AIAA Journal,* 42 (1), 70-79.

Vemuri, S. S., Liu, X., Zang, B., and Azarpeyvand, M. (2020), "On the use of leading-edge serrations for noise control in a tandem airfoil configuration", *Physics of Fluids,* 32 (7), 077102.

Venkatachari, B. S., Cheng, G. C., Soni, B. K., and Chang, S. C. (2008), "Validation and verification of Courant number insensitive CE/SE method for transient viscous flow simulations", *Mathematics and Computers in Simulation,* 78 (5), 653-670.

Visbal, M. R. and Gordnier, R. E. (2004), "Numerical simulation of the interaction of a transitional boundary layer with a 2-D flexible panel in the subsonic regime", *Journal of Fluids and Structures,* 19 (7), 881-903.

Vitturi, M. d. M., Esposti Ongaro, T., Neri, A., Salvetti, M. V., and Beux, F. (2007), "An immersed boundary method for compressible multiphase flows: application to the dynamics of pyroclastic density currents", *Computational Geosciences,* 11 (3), 183-198.

Wang, P., Jia, S., He, Z., He, C., Sung, H. J., and Liu, Y. (2024), "Flow–acoustic resonance mechanism in tandem deep cavities coupled with acoustic eigenmodes in turbulent shear layers", *Journal of Fluid Mechanics,* 984, A19.

Yamouni, S., Sipp, D., and Jacquin, L. (2013), "Interaction between feedback aeroacoustic and acoustic resonance mechanisms in a cavity flow: a global stability analysis", *Journal of Fluid Mechanics,* 717, 134-165.

Yang, Y., Rockwell, D., Lai-Fook Cody, K., and Pollack, M. (2009), "Generation of tones due to flow past a deep cavity: Effect of streamwise length", *Journal of Fluids and Structures,* 25 (2), 364-388.

Yang, Y., Liu, Y., Liu, R., Shen, C., Zhang, P., Wei, R., Liu, X., and Xu, P. (2021), "Design, validation, and benchmark tests of the aeroacoustic wind tunnel in SUSTech", *Applied Acoustics,* 175, 107847.

Yen, J. and Wagner, D. (2005), 'Computational Aeroacoustics Using a Simplified Courant Number Insensitive CE/SE Method', *11th AIAA/CEAS Aeroacoustics Conference* (Aeroacoustics Conferences: American Institute of Aeronautics and Astronautics).

Yokoyama, H., Odawara, H., and Iida, A. (2016), "Effects of freestream turbulence on cavity tone and sound source", *International Journal of Aerospace Engineering,* 2016, 7347106.

Yokoyama, H., Tanimoto, I., and Iida, A. (2017), "Experimental tests and aeroacoustic simulations of the control of cavity tone by plasma actuators", *Applied Sciences,* 7 (8), 790.

Yokoyama, H., Otsuka, K., Otake, K., Nishikawara, M., and Yanada, H. (2020), "Control of cavity flow with acoustic radiation by an intermittently driven plasma actuator", *Physics of Fluids,* 32 (10), 106104.

Ziada, S. (2010), "Flow-excited acoustic resonance in industry", *Journal of Pressure Vessel Technology,* 132 (1), 015001.

Ziada, S. and Bühlmann, E. T. (1992), "Self-excited resonances of two side-branches in close proximity", *Journal of Fluids and Structures,* 6 (5), 583-601.

Ziada, S., Oengören, A., and Vogel, A. (2002), "Acoustic resonance in the inlet scroll of a turbo-compressor", *Journal of Fluids and Structures,* 16 (3), 361-373.